

Quantitative Analysis of Haptotactic Cell Migration

by

Jan Schwarz


July 2016

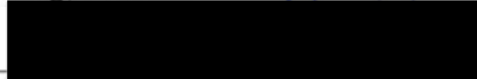
*A thesis presented to the
Graduate School
of the
Institute of Science and Technology Austria, Klosterneuburg, Austria
in partial fulfillment of the requirements
for the degree of
Doctor of Philosophy*



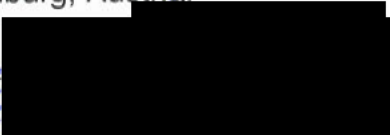
Institute of Science and Technology


The thesis of Jan Schwarz, titled "Quantitative Analysis of Haptotactic Cell Migration", is approved by:

Supervisor: Prof. Dr. **Michael Sixt**, IST Austria, Klosterneuburg, Austria.
Signature: 

Committee member: Prof. Dr. **Daria Siekhaus**, IST Austria, Klosterneuburg, Austria.
Signature: 

Committee member: Prof. Dr. **Daniel Legler**, Biotechnology Institute Thurgau at the University of Konstanz, Kreuzlingen, Switzerland.
Signature: 

Committee member: Prof. Dr. **Harald Janovjak**, IST Austria, Klosterneuburg, Austria.
Signature: 

Defense Chair: Prof. Dr. **Uli Wagner**, IST Austria, Klosterneuburg, Austria.
Signature: 

© by Jan Schwarz July 2016

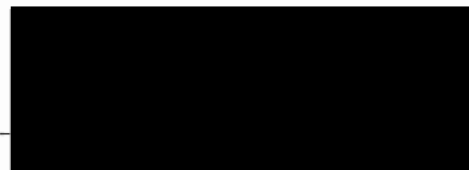
All Rights Reserved

I hereby declare that this thesis is my own work and that it does not contain other people's work without this being so stated; this thesis does not contain my previous work without this being stated, and the bibliography contains all the literature that I used in writing the dissertation.

I declare that this is a true copy of my thesis, including any final revisions, as approved by my thesis committee, and that this thesis has not been submitted for a higher degree to any other university or institution.

I certify that any republication of materials presented in this thesis has been approved by the relevant publishers and co-authors.

Signature: _____



Jan Schwarz

Biographical sketch

Jan Schwarz studied chemistry and biochemistry at the Ludwig Maximilian University of Munich (LMU). After finishing his bachelor's studies, he focused on the interface between organic chemistry and biology and developed chemical tools to address biological questions. During his master studies, Jan designed and synthesized dopamine agonists with photo-switchable receptor affinity in the research group of Dirk Trauner at LMU Munich.

After graduating with majors in organic chemistry and biochemistry, Jan decided to shift his focus to cell biology. Since 2011, he has been conducting his doctoral studies in Michael Sixt's research group at IST Austria. He uses chemical surface functionalization and micro-fabrication as tools to answer basic questions regarding chemokine sensing and directed cell migration. His work was funded by a Boehringer Ingelheim Fonds PhD fellowship.

List of publications

1. **J. Schwarz**, and M. Sixt. 2016. Quantitative Analysis of Dendritic Cell Haptotaxis. In *Methods in Enzymology*. *Methods in Enzymology* vol. 570. Elsevier. 567–581.
2. Weber, M., R. Hauschild, **J. Schwarz**, C. Moussion, I. de Vries, D. F. Legler, S. A. Luther, T. Bollenbach, and M. Sixt. 2013. Interstitial Dendritic Cell Guidance by Haptotactic Chemokine Gradients. *Science* 339: 328–332.
3. **J. Schwarz**, J. Merrin, T. Frank, R. Hauschild, V. Bierbaum, T. Bollenbach, S. Tay, M. Sixt and M. Mehling. A microfluidic device for measuring cell migration towards substrate bound and soluble chemokine gradients. *in submission*
4. A. Leithner, A. Eichner, J. Müller, A. Reversat, M. Brown, **J. Schwarz**, J. Merrin, D. de Gorter, F. Schur, J. Bayerl, I. de Vries, S. Wieser, R. Hauschild, F. P. L. Lai, M. Moser, D. Kerjaschki, K. Rottner, J. V. Small, T. E. B. Stradal and M. Sixt. Lamellipodia and filopodia promote environmental exploration but are dispensable for locomotion of leukocytes. *in revision*
5. M. Morri, C. Fourcade, **J. Schwarz** and H. Janovjak. Optical functionalization of human class A orphan G-protein coupled receptors. *in submission*

In preparation

1. **J. Schwarz**, V. Bierbaum, K. Vaathomeri, R. Hauschild, M. Brown, A. Leithner, A. Reversat, T. Tarrant, T. Bollenbach and M. Sixt. Dendritic cells interpret interstitial CCL21 gradients in a signal-to-noise ratio governed, GRK6 dependent manner. *in preparation*
2. **J. Schwarz**, M. Nemethova, R. Chait, R. Hauschild, C. Guet and M. Sixt. Covalent, adapter based protein patterning by photobleaching. *in preparation*

Acknowledgement

Many people influenced my work and me during the last five years and encouraged me in many different ways. In the following paragraphs I want to acknowledge at least some of them.

First, I would like to thank Michael Sixt for being a great supervisor, mentor and scientist. I highly appreciate his guidance and continued support. Furthermore, I am very grateful that he gave me the exceptional opportunity to pursue many ideas of which some managed to be included in this thesis.

I owe sincere thanks to the members of my PhD thesis committee, Daria Siekhaus, Daniel Legler and Harald Janovjak. Especially I would like to thank Daria for her advice and encouragement during our regular progress meetings. I also want to thank the team and fellows of the Boehringer Ingelheim Fond (BIF) PhD Fellowship for amazing and inspiring meetings and the BIF for financial support.

Important factors for the success of this thesis were the warm, creative and helpful atmosphere as well as the team spirit of the whole Sixt Lab. Therefore I would like to thank my current and former colleagues Frank Assen, Markus Brown, Ingrid de Vries, Michelle Duggan, Alexander Eichner, Miroslav Hons, Eva Kiermaier, Aglaja Kopf, Alexander Leithner, Christine Mousson, Jan Müller, Maria Nemethova, Jörg Renkawitz, Anne Reversat, Kari Vaahtomeri, Michele Weber and Stefan Wieser. We had an amazing time with many legendary evenings and events. Along these lines I want to thank the *in vitro* crew of the lab, Jörg, Anne and Alex, for lots of ideas and productive discussions. I am sure, some day we will reveal the secret of the ‘splodge’.

I want to thank the members of the Heisenberg Lab for a great time and thrilling kicker matches. In this regard I especially want to thank Maurizio ‘Gnocci’ Monti, Gabriel Krens, Alex Eichner, Martin Behrndt, Vanessa Barone,

Philipp Schmalhorst, Michael Smutny, Daniel Capek, Anne Reversat, Eva Kiermaier, Frank Assen and Jan Müller for wonderful after-lunch matches.

I would not have been able to analyze the thousands of cell trajectories and probably hundreds of thousands of mouse clicks without the productive collaboration with Veronika Bierbaum and Tobias Bollenbach. Thanks Vroni for countless meetings, discussions and graphs and of course for proofreading and advice for this thesis. For proofreading I also want to thank Evi, Jörg, Jack and Anne.

I would like to acknowledge Matthias Mehling for a very productive collaboration and for introducing me into the wild world of microfluidics. Jack Merrin, for countless wafers, PDMS coated coverslips and help with anything micro-fabrication related. And Maria Nemethova for establishing the 'click' patterning approach with me. Without her it still would be just one of the ideas...

Many thanks to Ekaterina Papusheva, Robert Hauschild, Doreen Milius and Nasser Darwish from the Bioimaging Facility as well as the Preclinical and the Life Science facilities of IST Austria for excellent technical support. At this point I especially want to thank Robert for countless image analyses and technical ideas. Always interested and creative he played an essential role in all of my projects.

Additionally I want to thank Ingrid and Gabby for welcoming me warmly when I first started at IST, for scientific and especially mental support in all those years, countless coffee sessions and Heurigen evenings.

Last but not least I would like to thank my family. My parents and siblings who always supported me and my decisions and of course my wife Isabell for her love and support.

Abstract

Directed cell migration is a hallmark feature, present in almost all multi-cellular organisms. Despite its importance, basic questions regarding force transduction or directional sensing are still heavily investigated. Directed migration of cells guided by immobilized guidance cues - *haptotaxis* - occurs in key-processes, such as embryonic development and immunity (Middleton et al., 1997; Nguyen et al., 2000; Thiery, 1984; Weber et al., 2013). Immobilized guidance cues comprise adhesive ligands, such as collagen and fibronectin (Barczyk et al., 2009), or chemokines - the main guidance cues for migratory leukocytes (Middleton et al., 1997; Weber et al., 2013). While adhesive ligands serve as attachment sites guiding cell migration (Carter, 1965), chemokines instruct haptotactic migration by inducing adhesion to adhesive ligands and directional guidance (Rot and Andrian, 2004; Schumann et al., 2010). Quantitative analysis of the cellular response to immobilized guidance cues requires *in vitro* assays that foster cell migration, offer accurate control of the immobilized cues on a subcellular scale and in the ideal case closely reproduce *in vivo* conditions. The exploration of haptotactic cell migration through design and employment of such assays represents the main focus of this work.

Dendritic cells (DCs) are leukocytes, which after encountering danger signals such as pathogens in peripheral organs instruct naïve T-cells and consequently the adaptive immune response in the lymph node (Mellman and Steinman, 2001). To reach the lymph node from the periphery, DCs follow haptotactic gradients of the chemokine CCL21 towards lymphatic vessels (Weber et al., 2013). Questions about how DCs interpret haptotactic CCL21 gradients have not yet been addressed. The main reason for this is the lack of an assay that offers diverse haptotactic environments, hence allowing the study of DC migration as a response to different signals of immobilized guidance cue.

In this work, we developed an *in vitro* assay that enables us to quantitatively assess DC haptotaxis, by combining precisely controllable chemokine photo-patterning with physically confining migration conditions. With

this tool at hand, we studied the influence of CCL21 gradient properties and concentration on DC haptotaxis. We found that haptotactic gradient sensing depends on the absolute CCL21 concentration in combination with the local steepness of the gradient. Our analysis suggests that the directionality of migrating DCs is governed by the signal-to-noise ratio of CCL21 binding to its receptor CCR7. Moreover, the haptotactic CCL21 gradient formed *in vivo* provides an optimal shape for DCs to recognize haptotactic guidance cue.

By reconstitution of the CCL21 gradient *in vitro* we were also able to study the influence of CCR7 signal termination on DC haptotaxis. To this end, we used DCs lacking the G-protein coupled receptor kinase GRK6, which is responsible for CCL21 induced CCR7 receptor phosphorylation and desensitization (Zidar et al., 2009). We found that CCR7 desensitization by GRK6 is crucial for maintenance of haptotactic CCL21 gradient sensing *in vitro* and confirm those observations *in vivo*.

In the context of the organism, immobilized haptotactic guidance cues often coincide and compete with soluble chemotactic guidance cues. During wound healing, fibroblasts are exposed and influenced by adhesive cues and soluble factors at the same time (Wu et al., 2012; Wynn, 2008). Similarly, migrating DCs are exposed to both, soluble chemokines (CCL19 and truncated CCL21) inducing chemotactic behavior as well as the immobilized CCL21. To quantitatively assess these complex coinciding immobilized and soluble guidance cues, we implemented our chemokine photo-patterning technique in a microfluidic system allowing for chemotactic gradient generation. To validate the assay, we observed DC migration in competing CCL19/CCL21 environments.

Adhesiveness guided haptotaxis has been studied intensively over the last century. However, quantitative studies leading to conceptual models are largely missing, again due to the lack of a precisely controllable *in vitro* assay. A requirement for such an *in vitro* assay is that it must prevent any uncontrolled cell adhesion. This can be accomplished by stable passivation of the surface. In addition, controlled adhesion must be sustainable, quantifiable and dose dependent in order to create homogenous gradients. Therefore, we developed

a novel covalent photo-patterning technique satisfying all these needs. In combination with a sustainable poly-vinyl alcohol (PVA) surface coating we were able to generate gradients of adhesive cue to direct cell migration. This approach allowed us to characterize the haptotactic migratory behavior of zebrafish keratocytes *in vitro*. Furthermore, defined patterns of adhesive cue allowed us to control for cell shape and growth on a subcellular scale.

Table of contents

Biographical sketch	iv
List of publications	v
Acknowledgement	vi
Abstract	viii
Table of contents	xi
Lists	xv
Figures	xv
Supplemental figures	xvi
Tables	xvi
Abbreviations	xvii
1. Introduction	1
1.1. Eukaryotic cell migration	1
1.2. Cell guidance	4
1.2.1. Haptotaxis	5
1.2.1.1. Haptotactic guidance by integrin ligands	5
1.2.1.2. Haptotactic guidance by chemokines	6
1.2.2. Intracellular chemotactic and haptotactic signaling	7
1.2.2.1. Heterotrimeric G-protein dependent receptor signaling	8
1.2.2.2. Heterotrimeric G-protein independent receptor signaling and signal termination	12
1.2.3. Signal detection and interpretation.....	15
1.2.3.1. Signal detection	15
1.2.3.2. Signal interpretation models	17
1.2.3.3. Signal interpretation strategies	20
1.2.4. Gradient generation <i>in vivo</i>	21
1.3. Dendritic cells as a model for chemokine guided haptotaxis	23
1.3.1. Dendritic cell lifecycle	23
1.3.2. CCR7 and its ligands - chemokines CCL19 and CCL21	24
1.3.2.1. Chemokine guided haptotaxis	24
1.3.2.2. CCR7 signaling and desensitization	25
1.4. In vitro assay systems	28
1.4.1. Dendritic cell migration in confined environments	28
1.4.2. Diffusion-based gradients	30
1.4.3. Microfluidics	31
1.4.3.1. Soluble gradient generation using microfluidic systems	34
1.4.4. Immobilized guidance cues	36
1.4.4.1. Micropatterning	37
1.4.4.2. Surface activation	37
1.4.4.3. Passivation of activated surfaces	39
1.4.4.4. Functionalization of activated surfaces	40
1.4.4.5. Patterning by photobleaching	43
2. Project description	48
3. Results	50
3.1. Quantitative analysis of dendritic cell haptotaxis	50

3.1.1.	Abstract.....	50
3.1.2.	Introduction	50
3.1.3.	Methods	53
3.1.3.1.	A. Lower surface preparation	55
3.1.3.2.	B. Upper surface preparation	58
3.1.3.3.	C. Haptotaxis chamber assembly.....	61
3.1.4.	Troubleshooting	64
3.1.4.1.	The haptotaxis chamber	64
3.1.4.2.	Cell treatment	64
3.1.4.3.	LAPAP/chemokine presentation.....	65
3.1.5.	Perspectives	66
3.1.6.	Acknowledgements.....	66
3.2.	Dendritic cells interpret interstitial CCL21 gradients in a signal-to-noise ratio governed, GRK6 dependent manner.	67
3.2.1.	Abstract.....	67
3.2.2.	Introduction	68
3.2.3.	Results	70
3.2.3.1.	Characterization of immobilized CCL21 gradients in vivo	70
3.2.3.2.	Haptotaxis Assay.....	70
3.2.3.3.	Characterization of DC migration in haptotaxis assays	75
3.2.3.4.	Gradient shape and steepness influences recognition of haptotactic CCL21 gradients 78	
3.2.3.5.	Dendritic cell haptotaxis reflects signal-to-noise-ratio of immobilized chemokine gradient.....	79
3.2.3.6.	Influence of immobilized CCL21 gradients on cell speed	82
3.2.3.7.	G-protein coupled receptor kinase 6 is important for shallow haptotactic gradient sensing.....	84
3.2.3.8.	G-protein coupled receptor kinase 6 is important for shallow haptotactic gradient sensing in vivo.	86
3.2.4.	Discussion.....	88
3.2.5.	Supplemental figures	91
3.2.6.	Materials and methods.....	94
3.2.6.1.	Cell culture.....	94
3.2.6.2.	Mice	94
3.2.6.3.	GRK6 ^{-/-} bone marrow chimera generation.....	94
3.2.6.4.	Chemokine	95
3.2.6.5.	Haptotaxis chamber production.....	95
3.2.6.6.	Laser writing and mCCL21 24-98 bio immobilization	97
3.2.6.7.	Imaging.....	99
3.2.6.8.	Antibody staining (immobilized mCCL21 24-98 bio).....	99
3.2.6.9.	Collagen migration assays	100
3.2.6.10.	Adhesion assays	100
3.2.6.11.	In vivo staining of interstitial CCL21 gradients.....	100
3.2.6.12.	Image analysis of in vivo and in vitro gradients	101
3.2.6.13.	Ex vivo crawl in assay (endpoint analysis)	101
3.2.6.14.	In vivo migration assay	102
3.2.6.15.	Cell tracking.....	103
3.2.6.16.	Statistical analysis	103
3.2.7.	Author contributions	104
3.2.8.	Acknowledgements.....	105
3.3.	A microfluidic device for measuring cell migration towards substrate bound and soluble chemokine gradients.....	106
3.3.1.	Abstract.....	106
3.3.2.	Introduction	107
3.3.3.	Results and discussion	109

3.3.3.1.	Microfluidic system to probe chemotactic and haptotactic migration at the single cell level.....	109
3.3.3.2.	Immobilized CCL21 gradients induce DC haptotaxis in a microfluidic migration chamber	113
3.3.3.3.	CCL19 gradients induce DC chemotaxis in a microfluidic migration chamber 115	
3.3.3.4.	Migration of DC in competing chemotactic and haptotactic chemokine gradients	118
3.3.4.	Conclusion	120
3.3.5.	Material and methods.....	121
3.3.5.1.	Design and fabrication of microfluidic chips.....	121
3.3.5.2.	Chip set-up, operation and control.....	122
3.3.5.3.	Generation of stable soluble chemokine gradients	122
3.3.5.4.	Generation of bound chemokine gradients by laser-assisted adsorption by photobleaching.....	123
3.3.5.5.	Mice, dendritic cell isolation, culture and maturation	124
3.3.5.6.	Imaging, Cell-tracking and data analysis	124
3.3.5.7.	Statistical analysis	125
3.3.6.	Author contributions	125
3.3.7.	Acknowledgement.....	126
3.3.8.	Supplemental movies	126
3.4.	Covalent, adapter based protein patterning by photobleaching	127
3.4.1.	Abstract.....	127
3.4.2.	Introduction	127
3.4.3.	Results and discussion	128
3.4.4.	Materials and methods.....	137
3.4.4.1.	PVA coating	137
3.4.4.2.	Photo-immobilization of FAM-alkyne	138
3.4.4.3.	1,3 dipolar cycloaddition	139
3.4.4.4.	Quantification of immobilization efficiency	140
3.4.4.5.	Design and fabrication of the PDMS chamber.....	140
3.4.4.6.	Cell culture and primary cells.....	141
3.4.4.7.	Adhesion assays and migration assays	141
3.4.4.8.	Imaging.....	142
3.4.4.9.	Cell tracking, image processing and statistical analysis.....	142
3.4.5.	Supplemental movies	143
3.4.6.	Author contributions	144
3.4.7.	Acknowledgements	144
4.	Discussion	145
4.1.	DC haptotaxis assay	145
4.1.1.	Photo-patterning.....	145
4.1.2.	CCL21 modification.....	147
4.1.3.	DC migration conditions	147
4.2.	DC haptotaxis and CCR7 desensitization.....	148
4.2.1.	CCL21 gradient <i>in vivo</i>	148
4.2.2.	DC haptotaxis.....	149
4.2.3.	Influence of chemokine immobilization on signal desensitization and haptotaxis.....	150
4.2.4.	Influence of CCR7 desensitization on haptotactic gradient sensing <i>in vitro</i> 151	
4.2.5.	Influence of CCR7 desensitization on haptotactic gradient sensing - <i>in vivo</i> 152	
4.2.6.	Kinetic effects of CCL21 immobilization and impaired desensitization ..	153
4.3.	Coinciding soluble and immobilized guidance cues	154

4.3.1. Microfluidic chip.....	154
4.3.2. DC migration in flow free 2D environments.....	155
4.3.3. Competing gradients of soluble CCL19 and immobilized CCL21	156
4.4. Spatial control over cell adhesion and integrin guided haptotaxis.....	157
4.4.1. Method and outlook.....	157
4.4.2. Outlook haptotactic mesenchymal cell migration	160
5. Appendix	163
6. Bibliography	164

Lists

Figures

Figure 1.: Lamellipodial architecture and the adhesion lifecycle.....	1
Figure 2.: Integrin linkage couples intracellular actin polymerization to cell protrusion.....	2
Figure 3.: Cell migration modes.	3
Figure 4.: Haptotactic cell guidance.	5
Figure 5.: Chemotaxis signaling pathways.	8
Figure 6.: GPCR signal termination.	13
Figure 7.: Signal detection.	16
Figure 8.: Conceptual and mathematical models for chemotaxis.	18
Figure 9.: Concentration gradient generation <i>in vivo</i>	21
Figure 10.: DC lifecycle.	23
Figure 11.: Chemokine dependent CCR7 signal termination.	25
Figure 12.: Interstitial DC migration as an inspiration for <i>in vitro</i> migration assays.	28
Figure 13.: Examples for diffusion generated gradients of guidance cue.	30
Figure 14.: Fluid flow patterns.....	32
Figure 15.: Microfluidic chip production.....	33
Figure 16.: Microfluidic gradient generation.	35
Figure 17.: Micropatterning.	37
Figure 18.: Surface functionalization.....	38
Figure 19.: Micropatterning techniques.....	41
Figure 20.: Photopatterning reagents and techniques.	42
Figure 21.: Protein immobilization by photobleaching.....	44
Figure 22.: Examples for adapter-connector pairs.	46
Figure 23.: 3D migration assays.	51
Figure 24.: Chemokine micropatterning.	53
Figure 25.: Haptotaxis chamber.....	54
Figure 26.: Production of the CCL21 24-98 bio patterned glass-bottom dish.	57
Figure 27.: Lid production.	60
Figure 28.: Haptotaxis chamber assembly.....	63
Figure 29.: Visualization and quantification of the interstitial CCL21 gradient.	71
Figure 30.: Haptotaxis assay.	72
Figure 31.: Analysis of surface immobilized CCL21 24-98 bio and <i>in vitro</i> reconstruction of the interstitial CCL21 gradient.....	74

Figure 32.: Analysis of dendritic cell haptotaxis on defined gradients of surface immobilized CCL21.....	77
Figure 33.: Dendritic cell haptotaxis reflects SNR of immobilized chemokine gradient.	80
Figure 34.: Influence of immobilized CCL21 gradients on cell speed.	83
Figure 35.: CCL21 guided DC haptotaxis is GRK6 dependent <i>in vitro</i>	85
Figure 36.: DC haptotaxis on <i>in vivo</i> CCL21 gradients is GRK6 dependent.....	87
Figure 37.: Overview of the set up and functionality of the microfluidic migration device.	111
Figure 38.: Manufacturing of haptotactic chemokine gradients in a microfluidic migration chamber.....	112
Figure 39.: DCs migrating on immobilized CCL21 24-98 bio.....	114
Figure 40.: CCL19 gradients induce DC chemotaxis in a microfluidic migration chamber.	116
Figure 41.: Velocities of DCs for different conditions.	117
Figure 42.: DCs migrating on opposing chemotactic CCL19 and haptotactic CCL21 gradients.	118
Figure 43.: Covalent protein patterning by photobleaching.	129
Figure 44.: Characterization of RGD-HF555 photopatterning on passivating PVA coating.	131
Figure 45.: Covalent, low background protein patterning as tool for probing haptotaxis and cell migration.	134
Figure 46.: Zebrafish keratocyte haptotaxis.....	161
Figure 47.: Appendix.....	163

Supplemental figures

Supplemental Figure 1.: CCL21 24-98 bio.....	91
Supplemental Figure 2.: Velocity as a function of haptotactic index.....	92
Supplemental Figure 3.: GRK6 ^{-/-} DCs do not show impaired entry into the lymphatic vessels or <i>intra nodal</i> migration <i>in vivo</i>	93
Supplemental Figure 4.: Azide-Hilyte555-GRGDS photo-patterning.	136

Tables

Table 1.: Surface passivation reagents.....	39
Table 2.: Biotinylated, truncated murine CCL21 (CCL21 24-98 bio).....	95
Table 3.: Click reaction mixture.....	139

Abbreviations

-/-	Knockout
°C	Degree celsius
2D	Two-dimensional
3D	Three-dimensional
aa	Amino acid(s)
Ab	Antibody
AF	Alexa Fluor
Ag	Antigen
APC	Antigen presenting cell
ATPase	Adenylpyrophosphatase
B4F	Biotin-4-fluorescein
BF	Brightfield
BSA	Bovine serum albumin
c	concentration
C-terminal, C-terminus	Carboxy-terminus, carboxy-terminal
C57BL/6	Inbred mouse strain "C57 black 6"
cAMP	Cyclic adenosine monophosphate
CCL	CC- or β -chemokine
CCR	CC- or β -chemokine receptor
CD	Cluster of differentiation
CD11c	Integrin alfa X
CFSE	Carboxyfluorescein succinimidyl ester
ctrl	Control
Cy3	Cyanine 3 dye
D10	DMEM supplemented with glutamine and 10% FCS
	fetal calf serum
Da/kDa	Dalton/kilodaltons
DAG	Diacylglycerol
DC(s)	Dendritic cell(s)
ddH ₂ O	Double distilled water
DMEM	Dulbecco's Modified Eagle Medium
DMSO	Dimethyl sulfoxide
ECM	Extracellular matrix
EDTA	Ethylenediaminetetraacetic acid
EMCCD	Electron multiplying charge coupled device
FA	Focal adhesion
FACS	Fluorescence-activated cell sorting
FAM	Carboxyfluorescein
FCS	Fetal calf serum
Fig.	Figure
FITC	Fluorescein isothiocyanate
fMLP	<i>N</i> -Formylmethionyl-leucyl-phenylalanine
FRC	Fibroblastic reticulum cells
GAP	GTPase activating protein
GDI	GDP dissociation inhibitor
GDP	Guanosine-5'-diphosphate

GEF	Guanine nucleotide exchange factor
GFP	Green fluorescent protein
GM-CSF	Granulocyte-macrophage colony-stimulating factor
gof	Goodness of fit
GPCR	G protein-coupled receptor
GRGDS	cell binding RGD motif containing peptide
GRK	G-Protein coupled receptor kinase
GTP	Guanosine-5'-triphosphate
GTPase	Guanosine-5'-triphosphatase
HBSS	Hank's buffered salt solution
HEK	Human Embryonic Kidney 293 cells
HEPES	N-(2-hydroxyethyl)-piperazine-N'-2-ethanesulfonic acid
HEV	High endothelial venules
HF	Hilyte Fluor
HI	Haptotactic index
hr(s)	Hour(s)
HUVEC	Human umbilical vein endothelial cells
hν	Photon
Ig	Immunoglobulin
IL	Interleukin
IP ₃	Inositol trisphosphate
K _d	Dissociation constant
KO	Knockout
LAPAP	Laser assisted protein adsorption by photobleaching
λ	Wavelength
LED	Light emitting diode
LN	Lymph node
LPS	Lipopolysaccharide
LYVE-1	Lymphatic vessel endothelial hyaluronan receptor
m/v	Mass/volume
MAPK	Mitogen-activated protein kinases
MAX	maximal
MEF	Mouse embryonic fibroblast
MEM	Minimum essential medium
MHC	Major histocompatibility complex
mole	$6.022140858 \times 10^{23}$
MIN	minimal
min	Minutes
mm	Millimeter
mL	Milliliter
MΩ	Mega Ohm
N-terminal, N-terminus	Amino-terminus, amino-terminal
n.s.	Not significant
nm	Nanometer
ng	Nanogram
nM	Nanomolar
P/S	Penicillin / Streptomycin

PBS	Phosphate buffered saline
PDMS	Polydimethylsiloxane
PEG	Polyethylene glycol
PH	Pleckstrin homology
pH	Power of hydrogen
P	Inorganic phosphate
PI ₃ K	Phosphatidylinositide 3-kinase
PLL	Poly-L-lysine
PtdIns(3,4,5)P ₃ /PIP ₃	Phosphatidylinositol-3,4,5-trisphosphate
PtdIns(4,5)P ₂ /PIP ₂	Phosphatidylinositol-4,5-bisphosphate
PVA	Polyvinyl alcohol
R	Reynolds number
R10/20	RPMI supplemented with glutamine, penicillin/streptomycin and 10% or 20% FCS, respectively
RGD	Arginylglycylaspartic acid
rpm	Revolutions per minute
RPMI	Roswell Park Memorial Institute medium
RT	Room temperature
SA	Streptavidin
SAM	Self assembled monolayer
SEM	Standard error of the mean
SH2/3	Src Homology 2/3 domain
SLO	Secondary lymphoid organ
SNR	Signal-to-noise ratio
TAMRA	5-Carboxytetramethylrhodamine
t	Time
T cell	T helper cell
TIRF	Total internal reflection fluorescence
U/mL	Units per volume
UV	Ultra violet
WT	Wild type
μL	Microliter
μm	Micrometer
μM	Micromolar

1. Introduction

1.1. Eukaryotic cell migration

The ability to move represents a fundamental cellular feature, fostering the development and survival of organisms in all biological domains. It allows unicellular organisms to react to beneficial or detrimental environments. For example, single cells of the eukaryotic slime mold *Dictyostelium discoideum* follow bacteria to forage or each other to aggregate under disadvantageous conditions (Manahan et al., 2004). During development of multicellular organisms, single cells or clusters of cells migrate towards their designated position (Thiery, 1984). In order to protect the organism from endo- and exogenous threats, immune cells efficiently traverse diverse cellular environments (Franz et al., 2002; Yang and Weinberg, 2008).

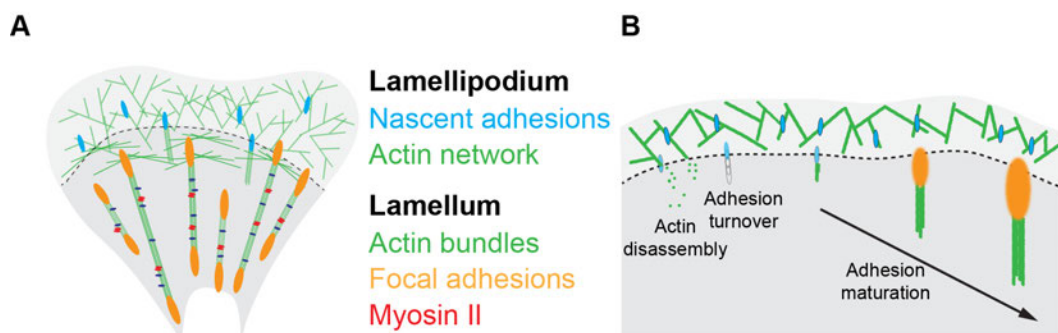


Figure 1.: Lamellipodial architecture and the adhesion lifecycle. Partially adapted from Vicente-Manzanares et al. (Vicente-Manzanares et al., 2008). A) Lamellipodium and lamellum of a sheet-like protruding cell area. Branched actin (green) in the thin lamellipodium merges to actin bundles (green) in the thicker lamellum. B) Adhesion turnover. Nascent adhesions (blue) form in the lamellipodium, disassemble or mature to form mature focal adhesions (FAs, orange).

Migrating eukaryotic cells feature similar, sheet-like membrane protrusions in advancing cell areas, termed *lamellipodia* (Figure 1A) (Abercrombie, 1961). Those membrane sheets consist of an actin network polymerizing against the advancing cell edge (Small et al., 1978). During protrusion, new actin monomers (G-actin) are incorporated in the polymerizing actin fiber (F-actin) close to the membrane. With progressing polymerization, newly incorporated actin monomers translocate towards the center of the cell (retrograde actin flow, Figure 2A) (Wang, 1985). There, the thin *lamellipodium* converges to the much

thicker and less flexible *lamellum* (Figure 1A). In the lamellum, actin fibers form bundles that mechanically interact with substrate adhesion sites (Abercrombie et al., 1971; Ponti, 2004). The mechanical connection of intracellular actin bundles and the extracellular substrate is mainly mediated by heterodimeric transmembrane receptors termed integrins (Hynes, 1992). All integrin dimers comprise an α - and a β -subunit. In total, 24 different $\alpha\beta$ dimer pairs are known, varying in ligand specificity or intracellular signaling (Barczyk et al., 2009). The intracellular c-termini of integrin hetero-dimers bind to and are thereby activated by intracellular adapter molecules like talin or kindlin which in turn connect to F-actin bundles (Barczyk et al., 2009). Those intracellularly activated integrin dimers are primed to bind adhesion sites of the extracellular matrix (ECM), like fibronectin, collagens or laminins (Hynes, 1992).

Small lamellipodial adhesion sites (nascent adhesions, Figure 1A and B) contain only weak integrin clusters but allow for binding of a plethora of scaffolding and signaling proteins (Geiger et al., 2009). If not stabilized by actin bundle formation or tensile forces, nascent adhesions are disassembled with actin network depolymerization at the transition between lamellipodium and lamellum (Figure 1B) (Choi et al., 2008). Stabilized adhesions however, can mature and form focal adhesions (FA, Figure 1B). Growing in the direction of retrograde actin flow, FAs consist of hundreds of proteins regulating and promoting actin binding, force transduction and integrin signaling (Case and Waterman, 2010).

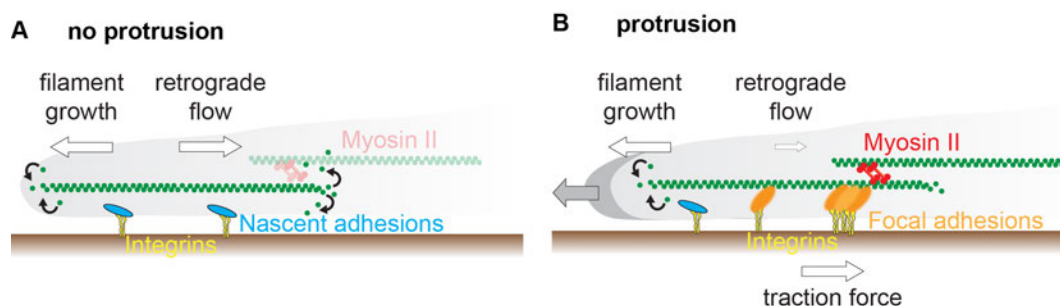


Figure 2.: Integrin linkage couples intracellular actin polymerization to cell protrusion. - molecular clutch. A) Nascent adhesions are not linked to the polymerizing actin filament. Polymerization cannot exert protruding force against the cell membrane and newly incorporated actin monomers flow back within the actin fiber-retrograde flow. Myosin II coupling and contractile forces enhance retrograde actin flow. B) Polymerizing actin fibers are coupled to the extracellular substrate via FAs. Polymerization can exert protruding force against the cell membrane. The cell is protruding, retrograde actin flow is minimal and traction forces onto the

substrate maximal. Myosin II coupling to static filaments further stabilizes protruding actin fibers and retracts the cell body.

Myosin II is an F-actin binding motor protein that, upon phosphorylation, dimerizes in a tail to tail fashion (Vicente-Manzanares et al., 2009). The actin binding head domains promote F-actin bundling at maturing adhesions (Choi et al., 2008). Additionally, myosin II dimers contract actin filaments and bundles against each other to enforce retrograde actin flow (Figure 2A). If mechanically coupled to the substrate via FAs, growing actin filaments push the cell front forward (molecular clutch, Figure 2B) (Mitchison and Kirschner, 1988; Theriot and Mitchison, 1991). Myosin II driven contraction of cell spanning actin bundles then retracts the lagging cell body and the whole entity of the cell is dislocated.

Weakly polarized mesenchymal cell types like fibroblasts follow this classical adhesion based cell migration model (Figure 3A). Rapidly amoeboid migrating cell types, like leukocytes, however, differ in their adhesion and therefore migration characteristics (Friedl, 2004). Lacking prominent actin bundles, they do not form large FA structures within the lamellum and localize active integrin dependent adhesion sites to a focal zone at the cell body (Figure 3B) (Smith et al., 2005).

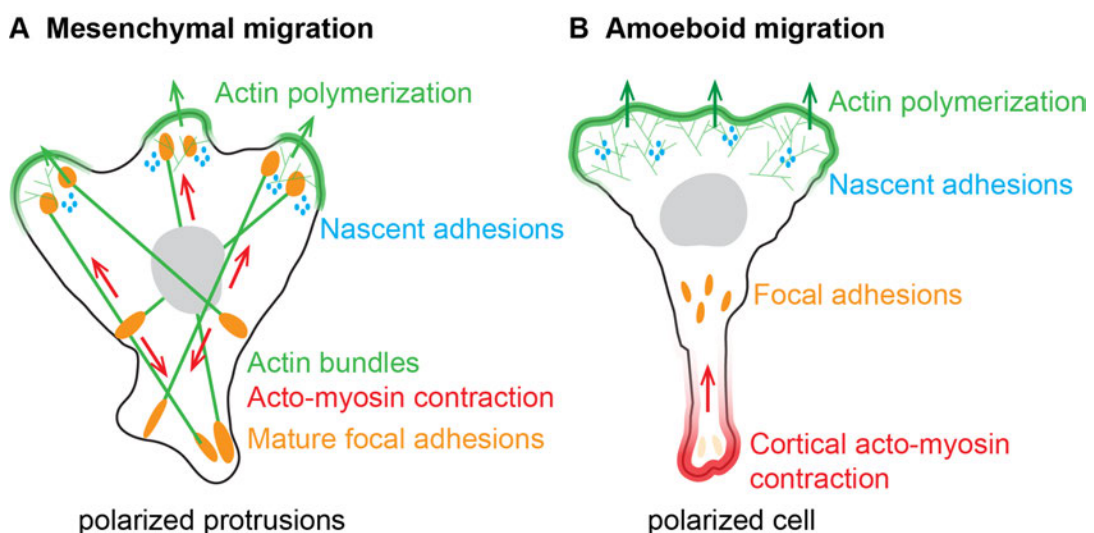


Figure 3.: Cell migration modes. A) Mesenchymal, adhesion-based migration: Local protrusions explore the environment. New FAs form in the lamellum. Myosin driven contraction of actin stress-fibers determines cell shape and migration. No global cell polarity. B) Amoeboid migration: Cells are highly polarized. One prominent actin polymerization based protrusion (leading edge). FA structures in 'focal zones'. Cortical actomyosin contraction at the 'uropod'. Illustration adapted from Bear *et al.* (Bear and Haugh, 2014).

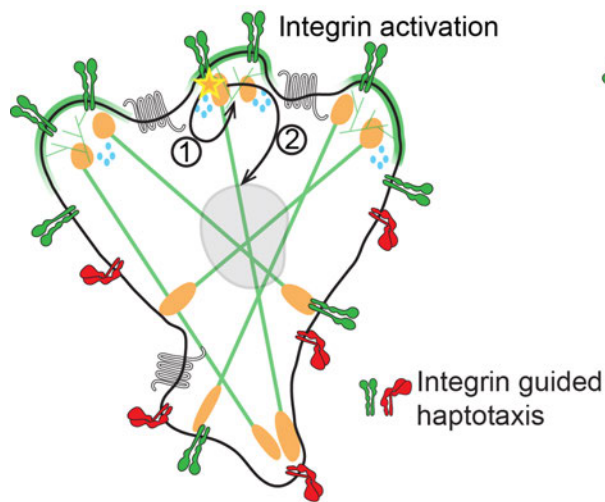
In adhesive environments, force transduction is integrin dependent and amoeboid migrating cells generate traction by the molecular clutch model. However, in contrast to weakly polarized mesenchymal cells, which allow multiple independent protrusions (Figure 3A), protrusion formation is only allowed in the front of the polarized cell (Figure 3B). Therefore, amoeboid migrating cells exhibit a single, characteristic lamellipodium termed the 'leading edge' (Figure 3B). Myosin II activity and cortical acto-myosin contraction is mainly localized at the back of the polarized cell, termed 'uropod' (Friedl et al., 2001). In confined environments like the dense cell and fiber network of the interstitium, integrin dependent substrate adhesion is dispensable for amoeboid cell migration. Here, cells can migrate by squeezing through confined spaces and pores relying exclusively on cortical back contraction and actin polymerization (Lämmermann et al., 2008). The mode of migration is governed by the environmental properties an amoeboid migrating cell is experiencing. It is tightly controlled and can be switched rapidly to maintain cell polarization and velocity (Renkawitz et al., 2009).

1.2. Cell guidance

In contrast to adhesion independent (amoeboid) migrating cells, adhesion dependent (mesenchymal) migrating cells are strongly dependent on the interplay between actin dynamics and FAs. Retrograde actin flow for example is directly linked to traction force exerted on the extra cellular matrix (ECM) by FAs (Gardel et al., 2008). This tight connection between cell adhesion and actomyosin dynamics suggests a direct influence of the mechanical environment on migration efficiency and the directionality of adhesive migrating cells. In areas of stronger substrate adhesion, those cells can exert more traction force and hence migrate more efficiently (Lo et al., 2000). Depending on the rigidity of the substrate they are migrating on, FAs exhibit fluctuations in pulling forces that are reminiscent to attempts to probe local stiffness (Plotnikov et al., 2012). Here, FAs act as rigidity sensors guiding effective migration in the direction of stiffer substrate (*durotaxis*). Similarly to presentation of adhesive ligands, ligand concentration influences migration efficiency and directionality.

1.2.1. Haptotaxis

A Guidance by integrin ligands



B Guidance by GPCR ligands

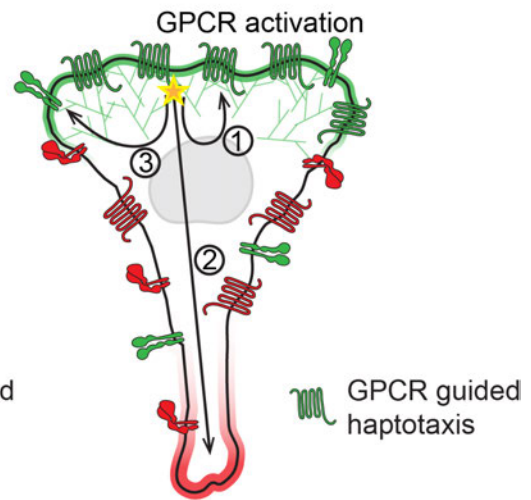


Figure 4.: Haptotactic cell guidance. A) Haptotactic guidance by integrin ligands: Integrin activation induces (A.1.) local protrusions and (A.2.) actomyosin contraction leading to directional migration B) Haptotactic guidance by GPCR ligands: GPCR activation induces (B.1.) protrusion of the lamellipodium and (B.2.) uropod retraction leading to polarization and migration. (B.3.) GPCR induced integrin activation reinforces substrate adhesion.

1.2.1.1. Haptotactic guidance by integrin ligands

In 1965, Carter observed murine fibroblasts migrating on substrates offering different adhesiveness (Carter, 1965). On plain, cell repellent cellulose acetate, cells were not able to adhere and accordingly not able to migrate. However, palladium vaporized cellulose acetate restored spreading and migration. When Carter shadowed parts of the cellulose acetate during palladium vacuum coating, thereby creating a gradient of adhesion sites, cells started to migrate in direction of higher adhesiveness. He termed this phenomenon *haptotaxis*. Carter generalized his observations and claimed that cell adhesion and migration are “interrelated”, meaning the movement of a cell is “controlled by the relative strength of its peripheral adhesions”.

For efficient migration, substrate adhesion needs to be firm, but tightly controlled in order to create new, force generating nascent adhesions and disassemble mature, anchoring FAs (Beningo et al., 2001). The formation of

nascent adhesions is influenced by the availability of integrin ligands on the substrate. The more integrin ligands are available, the stronger the cells can adhere. However, due to the tight coupling of adhesion and mesenchymal migration efficiency, only an ideal, balanced adhesiveness of the substrate promotes maximal velocity (Palecek et al., 1998; Wu et al., 2012). This phenomenon can be termed mesenchymal *haptokinesis* (Friedl et al., 2001). Inhomogeneity of integrin ligand distribution on the substrate can lead to inhomogeneous migration efficiency within the cell and therefore already bias migration towards higher adhesiveness and thereby promote haptotaxis. In this case integrin ligands act as *anchoring sites* biasing random migration. Additionally, integrin activation during nascent adhesion formation locally activates intracellular signaling pathways leading to local protrusions (Figure 4A.1) and global actomyosin contraction (Figure 4A.2) (King et al., 2016). Therefore, integrin signals can evoke *instructive signals* as well, guiding protrusion formation and migration of mesenchymal cells.

1.2.1.2. Haptotactic guidance by chemokines

Mechanical guidance is theoretically limited to environmental features, such as topology, rigidity or adhesiveness. Decoupling guidance or signal transduction from migration mechanics by introducing a control layer that is acting on top of cellular migration mechanics permits control of the migration machinery with any perceivable signal. Hereby, soluble, *chemotactic* extracellular signaling molecules represent the dominant class of cell guidance molecules. Chemotactic ligands vary from molecules like folic acid (Bagorda and Parent, 2008) to proteins like chemotactic cytokines (chemokines) (Thelen, 2001).

Amoeboid migrating cells, e.g. leukocytes, are mainly guided by chemotaxis receptors of the GPCR class and their soluble ligands (Parent, 1999). Haptotactic, integrin dependent guidance as seen in mesenchymal cell types, has not yet been observed for amoeboid migrating leukocytes. However, some chemokines carry highly charged domains which facilitate binding to charged components of the ECM, such as heparan sulfates (Bao et al., 2010; de Paz et al., 2007; Middleton et al., 1997). Those electrostatically immobilized

chemokines can influence amoeboid cell migration by altering adhesion and migration (Sarris et al., 2012; Schumann et al., 2010). As for soluble chemokines, receptor activation by immobilized chemokines induces actin polymerization in the lamellipodium and cortical contraction in the uropod (Figure 4B.1 and B.2). Additionally, chemokine induced integrin activation can enhance binding to integrin ligands (Figure 4B.3) (Rot and Andrian, 2004; Schumann et al., 2010). Hereby, the chemokine can act as *instructive* haptotactic signal guiding cell adhesion and migration (Weber et al., 2013) or can induce adhesion while directional guidance is offered by other, soluble offered, *chemotactic* GPCR ligands (Schumann et al., 2010). How amoeboid migrating cells interpret haptotactically presented guidance cues has not been addressed.

1.2.2. Intracellular chemotactic and haptotactic signaling

Chemotactic and chemokine guided haptotactic gradient sensing require three stages of signal processing in order to influence the mechanical machinery of a cell to polarize and bias migration into a specific direction. Activated by their ligands, G protein coupled receptors undergo dramatic conformational changes (Rasmussen et al., 2011). In this activated state, they are primed to bind a heterotrimeric G-protein ($G\alpha\beta\gamma$) and induce nucleotide exchange in its $G\alpha$ GTPase subunit. Specifically, GTP (Guanosine 5'-triphosphate) binding induces conformational changes in the heterotrimeric G-protein, thereby separating the $G\beta\gamma$ subunit from the $G\alpha$ GTPase subunit. Subsequently, heterotrimeric G-protein subunits dissociate from the receptor, leaving its c-terminus exposed for phosphorylation (Figure 5, receptor level, highlighted in green). Each released receptor component is able to activate signaling cascades of the signal transduction network of the cell (Figure 5, signal transduction network, highlighted in grey). Here, small GTPases (Figure 5, red) act as central hubs to influence actin remodeling, acto-myosin contraction and adhesion in the cytoskeletal network (Figure 5, cytoskeletal network, highlighted in blue). Similarly, extracellular mechanical input (e.g. via nascent adhesions) can influence the cytoskeletal network in order to induce mechanical guidance.

1.2.2.1. Heterotrimeric G-protein dependent receptor signaling

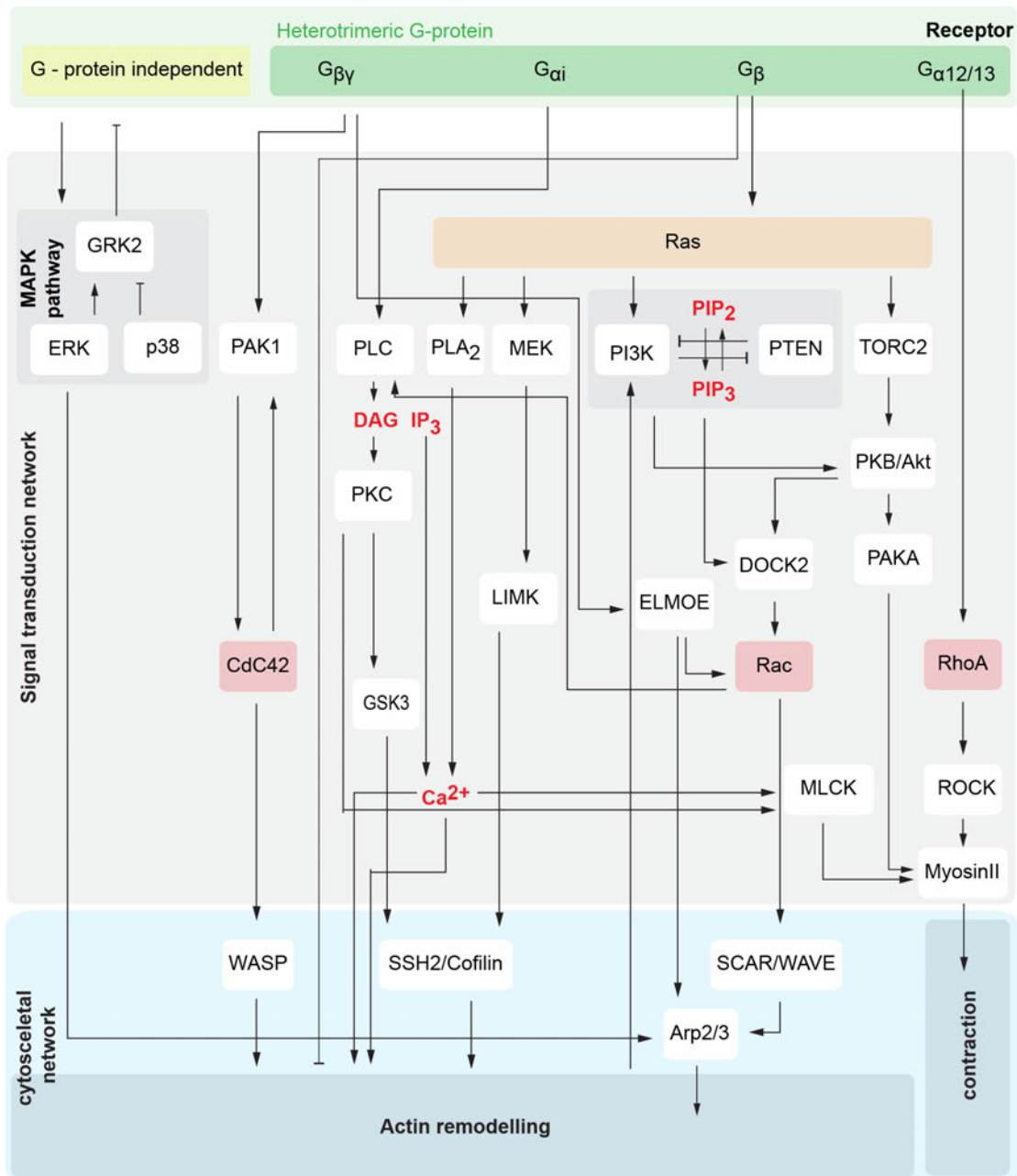


Figure 5.: Chemotaxis signaling pathways. Three main layers of intracellular chemotactic signal processing: 1) Receptor activation (green background). GPCR activation evokes G-protein dependent and independent intracellular signaling cascades. 2) Signal transduction network (STN, grey background). Receptor activation induces amplification and specification of intracellular signaling pathways (white boxes). Here, small GTPases (red, orange boxes) act as central hubs, coordinating a plethora of completed signaling pathways. Second messenger molecules (red font) allow for spatial organization 3) Cytoskeletal network (CN, blue background). Signal processing and amplification in the STN controls actin remodeling and acto-myosin contraction, eventually leading to changes in the morphology of the cell. Feedback from the CN can amplify or dampen STN cascades.

Mainly fast amoeboid migrating cells, like leukocytes and the amoeba *D. discoideum* have been utilized to study signal cascades and hierarchies of the

chemotactic signal network. Despite their phylogenetic distance, similar chemotactic pathways following receptor activation have been identified (Nichols et al., 2015). Predominantly guided by receptor tyrosine kinases, mesenchymal cells like fibroblasts (Singer and Clark, 1999) or epithelial cells like human umbilical vein endothelial cells (HUVECs) (Tsai et al., 2014) utilize the same intracellular signal molecules as chemotactic amoeboid cells, however, differences in signal interpretation have been described (Machacek et al., 2009; Yang et al., 2016).

Chemotactic signaling, like many other cellular processes is controlled by small GTPases due to their function as molecular switches (Wennerberg et al., 2005). Depending on the phosphorylation state of the associated guanine nucleotide (Guanosin 5'-triphosphate, GTP or guanosine diphosphate, GDP+P) the GTPase adopts an active, effector binding (GTP) or an inactive (GDP+P) conformation. Binding, hydrolyzation and dissociation of the guanine nucleotide hereby is influenced by guanine nucleotide exchange factors (GEFs), GTPase activating proteins (GAPs) and guanine nucleotide dissociation inhibitors (GDIs), allowing for control and modulation of the GTPase molecular switch activity. Members of the Ras and Rho subfamilies of small GTPases control cellular processes like proliferation, migration and chemotaxis (Jaffe and Hall, 2005).

Polarization and migration of amoeboid-migrating cells is critically dependent on the Rho-GTPase Cdc42. Cdc42 determines the putative front of the polarized cell, peaking in activity already before protrusion formation (Yang et al., 2016). p21-activated kinase (PAK1) and Cdc42 localize to the plasma membrane either spontaneously or get activated via the G $\beta\gamma$ subunit of the heterotrimeric G-Protein. There activated Cdc42 induces Wiskott-Aldrich symptom protein (WASP (Rohatgi et al., 1999)) and formin (mDia (Peng et al., 2003)) dependent filopodia formation. Filopodia are actin bundled structures exceeding the lamellipodium for probing the cellular environment. For mesenchymal cell migration, filopodia play crucial roles in probing substrate rigidity (Wong et al., 2014) and adhesiveness (Johnson et al., 2015). For amoeboid migrating cells like leukocytes, Cdc42 dependent actin remodeling in

the lamellipodium is crucial for leading edge coordination (Lämmermann et al., 2009). Here, cofilin dependent actin disassembly in the lamellipodium allows for protrusion prioritization and therefore for migration in complex 3D environments.

In protruding or future protruding areas, Cdc42 inhibits the Rho GTPase RhoA, thereby confining basal RhoA activity to the trailing edge of the cell (Yang et al., 2016). There, RhoA induced myosin II phosphorylation by Rho dependent protein kinase (ROCK) leads to cortical actomyosin contraction. Additionally, following chemotaxis receptor activation, RhoA activity is specifically induced via the alternative Gα GTPase subunit Gα_{12/13} (Xu et al., 2003). As for basally active RhoA, Cdc42 activity in the leading edge might limit RhoA activity and actomyosin contraction to the trailing edge.

Weakly polarized and strongly adhesive migrating mesenchymal cell types show different kinetics for the Rho-GTPases Cdc42 and RhoA (Machacek et al., 2009). Here, RhoA instead of Cdc42 spatiotemporally correlates with membrane protrusion. Cdc42 is lagging behind peaking only after retraction of the former protruding area. RhoA activity localizes near FA sites in the lamellum of adhesive migrating cells. Therefore, mechanical disruption of old, mature adhesions in the newly protruding areas seems necessary for effective adhesive migration, explaining the difference in RhoA kinetics compared to amoeboid migrating cells.

Following Cdc42 or RhoA activation, Ras activity increases in a polarized manner (Machacek et al., 2009; Sasaki, 2004; Yang et al., 2016). Induced by Gβγ signaling, Ras GTPases activate a plethora of signaling cascades including phosphoinositide 3-kinase (PI₃K) pathways. PI₃K phosphorylates the membrane lipid phosphatidylinositol (4,5)-bisphosphate (PIP₂) forming the second messenger lipid phosphatidylinositol (3,4,5)-triphosphate (PIP₃). Inhibited by PI₃K in the “front” of the polarized cell, phosphatase and tensin homolog (PTEN) dephosphorylates PIP₃ in the retracting back of the cell promoting a steep PIP₃ gradient within the cell (Sasaki, 2004; Servant, 2000). This steep intracellular gradient is mandatory for induction and maintenance of cell polarity, however dispensable for chemotactic gradient sensing (Andrew and Insall, 2007; Hoeller and Kay, 2007). Lamellipodium organizing factors can be

localized to the putative cell front by the PIP₃ gradient via their PIP₃ binding PH domains.

An important downstream target of PI₃K is the small GTPase Rac1 which peaks in activity with its upstream activator Ras in leukocytes (Yang et al., 2016) and with Cdc42 in fibroblasts (Machacek et al., 2009). Activated by GEFs (e.g. DOCK2 in lymphocytes (Fukui et al., 2001)) Rac1 enforces actin polymerization and remodeling in the leading edge of the cell. Like WASP, the Rac1 activated Scar1/WAVE complex recruits the actin nucleator and branching complex Arp2/3 (Machesky and Insall, 1998). However, Scar1/WAVE dependent Arp2/3 activation leads to branched actin networks and lamellipodium formation instead of actin bundle formation (Pollard and Borisy, 2003). Rac1 induced lamellipodium remodeling additionally is influenced via formin (mDia) dependent nucleation or cofilin dependent actin bundle severing (Tang et al., 2011).

Actin polymerization itself induces PI₃K activity as well and therefore activates Rac1 in a local feedback cycle (Inoue and Meyer, 2008). Hence, cell polarity is influenced mechanically via integrin signaling and is maintained without receptor activation. For instance, integrin activity in nascent adhesions induces heterotrimeric G-protein activation and PI₃K activity similar to chemotaxis receptors via the non-receptor GEF Girdin (Leyme et al., 2015). Mature FAs, which are absent in lamellipodia, are not able to induce similar signaling. Integrin dependent Src kinase and Rac1 activation locally induces Arp2/3 dependent branched actin polymerization and local protrusion formation (Figure 4) (King et al., 2016; Wu et al., 2012). On intermediate adhesive substrates, integrin dependent RhoA activation leads to myosin II dependent stress fiber contraction and movement of the cell body following the Rac1 induced protrusions (Cox et al., 2001).

Myosin II dependent actomyosin contraction at the back of a polarized cell is controlled by the intracellular PIP₃ gradient as well. In *D. discoideum*, protein kinase B (PKB or Akt), a PH-domain carrying kinase, is localizing PAKa and thereby myosin II phosphorylation to the putative cell back (Chung et al., 2001). The kinase TORC2 can phosphorylate PKB in a PI₃K-PIP₃ independent

pathway induced by a different *D. discoideum* Ras variant (RasC) (Cai et al., 2010). However, the mechanisms underlying both pathways are unknown.

Like PIP₃, Ca²⁺ is considered an important intracellular 2nd messenger associated with chemotactic signaling. With basal cytosolic Ca²⁺ concentrations of ≤ 100 nM (Gilbert et al., 1994) already small fluctuations of intracellular Ca²⁺ concentration can be sensed by cellular Ca²⁺ sensors. To maintain sensitivity, intracellular Ca²⁺ levels are constantly reduced by Ca²⁺ ATPases (Clapham, 2006). In addition, in HUVEC leader cells, the ATPase PMCA (Plasma membrane Ca²⁺ ATPase) is polarized towards the leading edge of the cell creating an inverse Ca²⁺ gradient (Tsai et al., 2014). Therefore the leading edge shows higher sensitivity towards local Ca²⁺ pulses associated with chemotactic signaling. Activated by RTKs in epithelial or mesenchymal cells or G α GTPase subunits in *D. discoideum* or leukocytes, phospholipases (PL-C subtypes) cleave PIP₂ to generate the 2nd messengers diacylglycerol (DAG) and inositol triphosphate (IP₃). In turn, soluble IP₃ locally releases Ca²⁺ from the endoplasmatic reticulum of HUVEC leader cells, stimulating local myosin II activation and FA remodeling in the lamellum (Franco et al., 2004; Tsai and Meyer, 2012). Protein Kinase C subtypes (PKCs) induced by the membrane bound DAG inhibit myosin II in mesenchymal cells or induce cofilin mediated lamellipodium remodeling in granulocytes (Asokan et al., 2014).

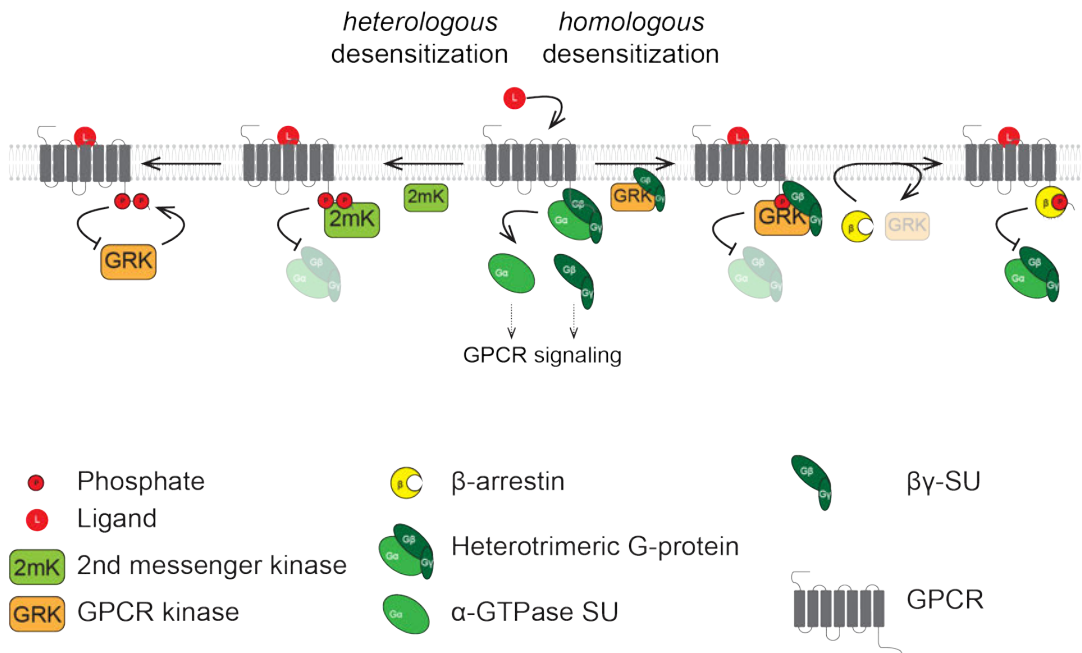
Like G α GTPase subunits of the heterotrimeric G-protein, the G $\beta\gamma$ and G β subunits can bypass Ras GTPase activation and directly induce lamellipodial dynamics during amoeboid chemotaxis (Hoeller et al., 2016; Yan et al., 2012).

1.2.2.2. Heterotrimeric G-protein independent receptor signaling and signal termination

The chemotaxis receptor itself can facilitate or modulate intracellular signaling while bypassing classical, GTPase dominated signaling routes. To adapt for constant stimulation e.g. by rising ligand concentration and thus avoiding persistent receptor activity, signaling needs to be terminated. GPCR signal

termination can occur via two mechanisms: *desensitization* or *receptor down regulation* (Figure 6).

A Desensitization



B Down regulation

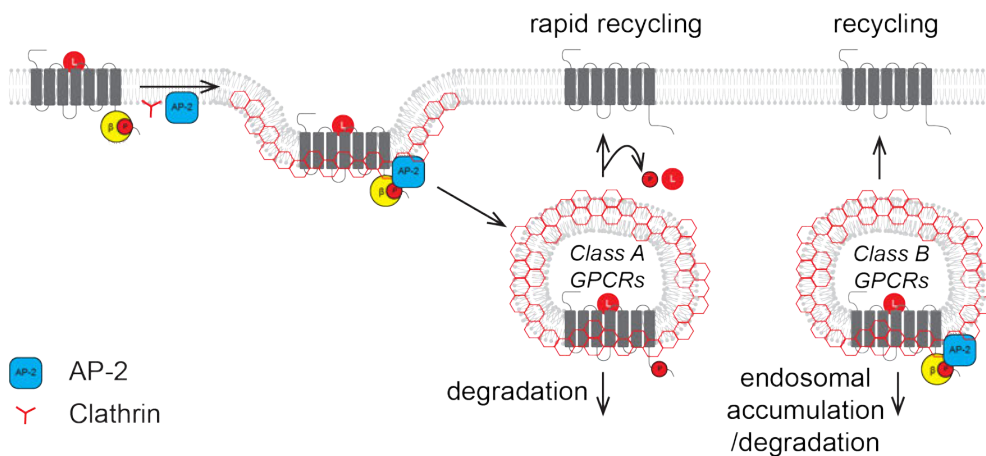


Figure 6.: GPCR signal termination. A) Receptor desensitization: Heterologous GPCR desensitization by 2nd messenger activated kinases; Homologous desensitization by GPCR kinases. B) Receptor down regulation by clathrin/AP-2 dependent internalization: Class A GPCRs weakly bind β -arrestin and therefore rapidly recycle to the plasma membrane. Class B GPCRs strongly bind β -arrestin and are targeted for endosomal degradation.

Desensitization occurs after phosphorylation of the intracellular loops and the c-terminus of the GPCR by either G-protein coupled receptor kinases (GRKs, homologous desensitization, Figure 6A) or 2nd messenger activated kinases, such as PLC activated PKC or Src (heterologous desensitization, Figure 6A) (Benovic et al., 1985; Fan et al., 2001; Pitcher et al., 1998). For GRK dependent

desensitization, GRKs need to localize to the membrane in close proximity to the activated receptor. Of the seven GRK subtypes, five are constantly membrane anchored (GRK1, -4, -5, -6 and -7). Two, GRK2 and GRK3, localize to the membrane transiently by G β γ binding after receptor activation (Kohout and Lefkowitz, 2003). Fast and transient desensitization is achieved by binding of GRKs or arrestins to the phosphorylated receptor thereby blocking G-protein binding and subsequent G-protein signaling (Figure 6A). Arrestins are adapter proteins which can form scaffolds for structural proteins or concentrate signaling proteins, like kinases (Luttrell and Lefkowitz, 2002). Four main classes of arrestins have been identified, of which visual arrestins (-1 and -4) are expressed only in the retina. In contrast arrestin-2 and -3 (β -arrestin1 and -2) are ubiquitously expressed (Lefkowitz et al., 2006). 2nd messenger activated kinases can phosphorylate and thus induce desensitization even without the receptor being activated. Therefore, 2nd messenger activated kinases can modulate the GPCR signaling of other signaling pathways (Luttrell and Lefkowitz, 2002). Receptor phosphorylation can also modulate receptor accessibility for other kinases. In this context, p38 kinase phosphorylation of the granulocyte formyl peptide receptor inhibits GRK2 binding and desensitization. In contrast ERK phosphorylation of the receptor induces GRK2 binding and consequently desensitization. This modulation of receptor activity was shown to account for a 'stop and go' migration pattern in chemotactic neutrophils (Liu et al., 2012).

Beside desensitization, arrestin binding to the phosphorylated receptor can initiate sequestering and thereby down regulate receptor levels (Figure 6B). For sequestration, arrestins recruit clathrins via their adapter proteins AP-2 to the membrane surrounding the arrestin targeted receptor, thereby forming clathrin coated endosomal vesicles (Goodman et al., 1996; Kirchhausen, 1999). Class A GPCRs only transiently bind to arrestins and therefore rapidly dissociate from arrestins in endocytic vesicles (Figure 6B). Without arrestins, class A GPCRs containing endocytic vesicles are acidified, the receptors are dephosphorylated and get rapidly recycled to the plasma membrane (Zhang et al., 1999). Class B GPCRs stably bind arrestins (Figure 6B). Therefore

receptor-arrestin complexes accumulate in endocytic vesicles and are targeted for slow recycling or degradation (Oakley et al., 1999).

Similarly to scaffolding proteins, arrestin can concentrate kinases at endocytic vesicles and therefore mediate G-protein independent signaling cascades (Figure 5). Hereby, arrestins orchestrate signaling cascades induced by receptor stimulation (Lefkowitz et al., 2006). Src kinase for example binds to the desensitized β -arrestin-receptor complex and recruits and activates the MAP kinases ERK1 and ERK2 (Luttrell, 1999). Additionally, as 2nd messenger activated kinase, Src can phosphorylate the receptor to recruit SH2-domain effector proteins. In leukocytes, Src is recruited arrestin independently by receptor oligomerization (Hauser et al., 2016). Accordingly, GPCR clustering represents another layer of G-protein independent GPCR signaling. (reviewed in (Palczewski, 2010)).

1.2.3. Signal detection and interpretation

Chemo- or haptotactic signal detection is a highly dynamic process involving presentation and properties of the guidance cue as well as receptor properties, such as ligand affinity, its availability or kinetics. Similarly, intracellular signaling pathways and cascades follow specific kinetics, spatial distributions and amplification cycles in order to evoke the correct global cellular responses. To understand whether and how cell directionality can be traced back to fundamental principles of sensing such as Weber's law (Ferrell, 2009), or how complex networks can explain signaling properties, has been addressed in theoretical models of *signal detection* and *interpretation*.

1.2.3.1. Signal detection

Cell surface receptors are the first level of chemotactic signal detection and correspondingly represent a first layer of signal modulation. For example, adjusting receptor affinity, accessibility or distribution can influence the sensitivity towards an extracellular gradient of guidance cue. The amount of available receptor depends on the expression level and the kinetics of recycling of activated receptors. In some chemotaxis systems, receptor recycling is

actively enhanced, enabling adaption to rising concentrations of guidance cue (Ferrell, 2009; Kohout and Lefkowitz, 2003; Otero et al., 2006). Receptor motility within the cell membrane and active polarization of the receptor can influence chemotactic sensing as well. While many chemotaxis receptors are homogeneously distributed during chemotaxis (Parent et al., 1998), some cluster or localize to specific areas of the polarized cell (Nieto et al., 1997; Palczewski, 2010; Vicente-Manzanares et al., 1998). Receptor polarization in gradient direction, for instance can enhance directionality (Levine and Rappel, 2013). However, sensitivity towards rapid directional changes might be reduced in such systems.

A primary influence on signal detection consists in the affinity of the receptor to the respective ligand. This affinity depends on the chemical and structural properties of the ligand and the ligand-binding domain of the receptor. In chemical equilibrium, it is characterized by the dissociation constant K_d and disassembly of the receptor/ligand complex depends solely on K_d . Whether a receptor binds a ligand also depends on the local concentration of the respective ligand. In this way, for a cell covered with receptors, changes of the ligand concentration across the cell diameter induce differential receptor activation and therefore polarized signaling (Parent, 1999). The probability of a single receptor in a given concentration c to be occupied is $\frac{c}{c+K_d}$ (Levine and Rappel, 2013), such that the change in external concentration leads to a difference in bound receptors that ultimately has to be recognized by the cell to induce directional motion.

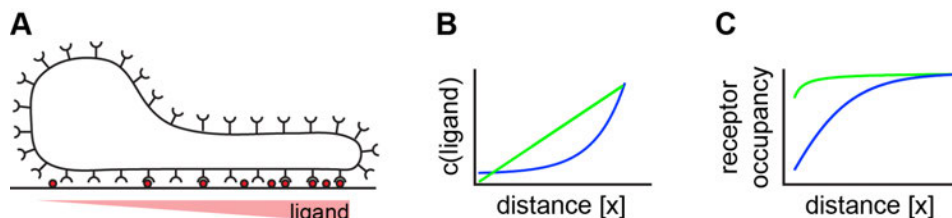


Figure 7.: Signal detection. A) Receptor distribution on the cell surface. Differential one dimensional ligand distribution. B) Linear (green) and exponential (blue) concentration gradient. C) Receptor occupancy calculated from linear (green) and exponential (blue) concentration gradients.

As ligand binding by a receptor is a stochastic process, the detection of the difference in bound receptors is subject to noise. The corresponding signal-to-

noise ratio (SNR) will, in this way, limit the cell's ability to detect the signal (Levine and Rappel, 2013). Apart from the binding/unbinding of ligands, receptor motility within the cell membrane and shape changes of the cell during migration constitute additional sources of noise that might influence gradient detection. Furthermore, differentiation of a gradient and subsequent induction of cell directionality will depend on intracellular signal interpretation (chapter 1.2.3.2).

How the fraction of bound receptors depends on the external concentration is shown in Figure 7. The fraction of bound receptors and the corresponding receptor occupancy across the cell depends on the diameter and the shape of the cell, the amount of available receptors and their distribution, as well as the shape of the gradient and its mean concentration ('background concentration'). In a simple example of a one-dimensional cell with fixed diameter and uniform receptor distribution, a local linear and exponential profile would lead to different receptor occupancies across the cell. For linear gradients for example, the receptor occupancy decreases rapidly with rising ligand concentration (Figure 7B and C). In contrast, exponential gradients offer lower receptor occupancy and can therefore instruct cell migration over a larger concentration range (Figure 7B and C). Based on the difference in receptor occupancy across the cell, models for the corresponding signal recognition have been proposed to explain a directional response in chemotactic organisms (Amselem et al., 2012; Mortimer et al., 2009; Ueda and Shibata, 2007).

1.2.3.2. Signal interpretation models

Exposed to local sources of the formylated tri-peptide fMLP (*N*-Formylmethionyl-leucyl-phenylalanin), unpolarized granulocytes generate local protrusions eventually leading to directed migration in direction of the fMLP source. The site of protrusion herein is determined by proximity to the source of fMLP (Gerisch and Keller, 1981). The same holds true for *D. discoideum* cells polarized in the presence of local pulses of cyclic adenosine monophosphate (cAMP). Instead of polarizing the chemoattractant receptor, cells localize and therefore polarize receptor signaling in the direction of highest chemoattractant

concentration (Parent et al., 1998). Those initial findings and subsequent work led to a collection of conceptual and mathematical models for chemotaxis.

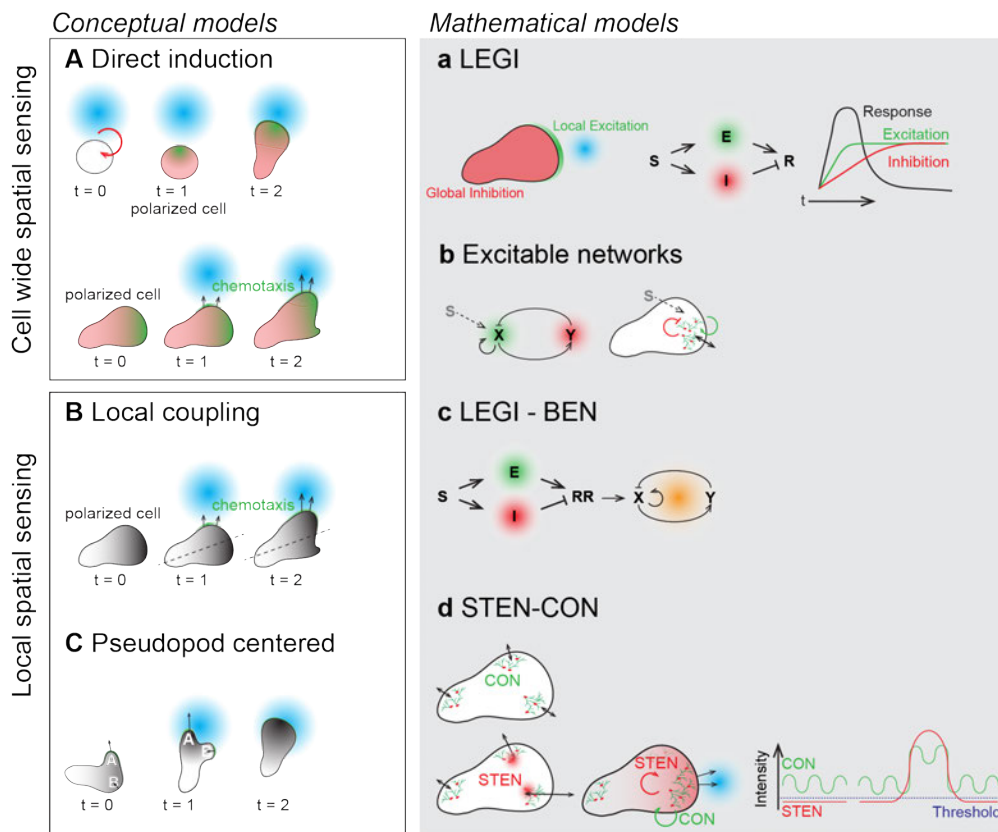


Figure 8.: Conceptual and mathematical models for chemotaxis. Left panels: Conceptual models; A) Cell wide signal integration; Direct induction. B) and C) Local signal integration; B) Local coupling. C) Pseudopod centered. Right panel: Mathematical models; a) Local excitation, global inhibition model (LEGI). b) Excitable networks and activator/inactivator models. c) LEGI-Biased excitable network model (BEN). d) Signal transduction excitatory network (STEN)-cytoskeleton oscillatory network (CON).

Rapid chemoattractant induced cell polarization is described through conceptual models summarized as *direct induction* models (Figure 8A, upper illustration). Receptor activation leads to *cell wide* signal integration. This integration step suggests a fast local activator, which is spatiotemporally confined to the area of highest activation by a slowly activated inhibitor. Mathematically, the model is described as ‘Local Excitation and Global Inhibition’, short LEGI model (Figure 8a) (Levchenko and Iglesias, 2002; Parent, 1999). Mathematical and experimental studies strengthen the idea of a global inhibition mechanism (Houk et al., 2012; Levine et al., 2006; Xu et al., 2007). LEGI explains static gradient sensing, adaption and relative sensitivity to

gradients, but fails to explain several features of chemotactic migrating cells like spontaneous polarization and migration in homogenous chemokine fields (Iglesias and Devreotes, 2008). Due to the local correlation of cell frontness and PIP_3 accumulation, the membrane bound signaling compound PIP_3 was a promising candidate for a local activator and therefore a cellular compass molecule (Parent et al., 1998; Rickert et al., 2000). However, it was shown that *D. discoideum* cells lacking PI_3K are still able to follow chemotactic signals (Hoeller and Kay, 2007). Motility though is severely impaired, arguing for a role of PI_3K and PIP_3 on migration itself and therefore for a separation of chemotaxis and cell migration modules, which is not considered in the LEGI model. To fill this gap, cell wide spatial chemoattractant sensing has to act on top of a cell intrinsic polarization and migration module (Figure 8A, lower illustration). The wave-like behavior of actin polymerization itself might represent such a migration module. The SCAR/WAVE complex component Hem1 is located at the plasma membrane inducing propagating actin waves which eventually, if pronounced enough, lead to membrane protrusion. Additionally, actin promotes removal of the complex from the membrane (Weiner et al., 2007). Therefore, actin polymerization would represent an excitable network, with Hem1 as an activator and actin itself as inhibitor (Figure 8b). Biased by external signals, the threshold for generating a protrusion is lowered, leading to localized protrusions and biased random motility (Biased excitable network, BEN) (Hecht et al., 2011). The mathematical LEGI-BEN model (Figure 8c) combines the random migration properties of an excitable network with the sensing and adaption properties of a LEGI model, accounting for the biased random walk often observed for migrating and chemotactic cells (Xiong et al., 2010). Persistent migration and cell intrinsic polarity as observed in migrating cells however, can't be explained using the LEGI-BEN model. Additionally, the strict separation of the cytoskeletal part (BEN) and signal transduction part (LEGI) was shown to be obsolete (Huang et al., 2013).

In the signal transduction excitable network (STEN) and the cytoskeletal oscillatory network (CON) model (STEN-CON model, Figure 8d) rapid cytoskeletal oscillations activate and are enhanced by slow signaling events.

Internal noise and cytoskeletal feedback can trigger local STEN activation leading to pronounced protrusion and random migration if a signal threshold is reached (Figure 8d, right graph). Accordingly, cell wide chemoattractant signal integration, e.g. following the LEGI model, can enhance the STEN network locally, promoting CON activation and therefore lamellipodial protrusion at the location of highest STEN activity (Figure 8d, left illustration). Recently cell polarity, manifested as cytoskeletal architecture instead of dynamics was shown to additionally influence the likeliness of local protrusions (Wang et al., 2014).

Two other conceptual chemotaxis models are based on intrinsic cellular polarity. Similar to the mathematical LEGI-BEN or STEN-CON models, the migratory- and signaling- modules are separated. Instead, pre-polarized cells do not spatially integrate signals in a *cell wide*, but *local* fashion. The *local coupling model* allows spatial sensing only at the leading edge of the polarized cell (Arriemerlou and Meyer, 2005). A “local-coupling” of extrinsic signals and intrinsic polarity steers the random migrating cell in small increments towards the chemoattractant gradient. (Figure 8B).

All models discussed above represent signal centered models assuming extracellular signals to *induce* formation of protrusions (Insall, 2010). The *pseudopod centered model* however, is based on constantly, dynamically forming and splitting pseudopods (Figure 8C). Here, chemotactic signals only influence the kinetics or positions of newly formed pseudopods (Chubb et al., 2002).

1.2.3.3. Signal interpretation strategies

The classical understanding of *taxis* is a strong directional bias of the migrating cell in direction imposed by the guidance cue. However, many guidance systems do not follow this paradigm. In order to locally bias random cell motility and to increase the probability of a cell to find its target, chemo- and haptotactic guidance cues can induce directional and kinetic effects (Krummel et al., 2016; Sarris and Sixt, 2015). Such a kinetic effect is the bias on directional speed. Here, cell velocity can be increased towards the maximal concentration of the

chemotactic cue (*othotaxis*) or reduced in close proximity to the source to avoid “overshooting” (Castellino et al., 2006; Sarris et al., 2012). Both mechanisms allow finding of the target area even in systems with noisy background. Furthermore, in geometrically constrained systems like naïve T-cell migration on the fibroblast reticular cell (FRC) network, kinetic effects are an efficient way to induce directionality (Mempel et al., 2005).

1.2.4. Gradient generation *in vivo*

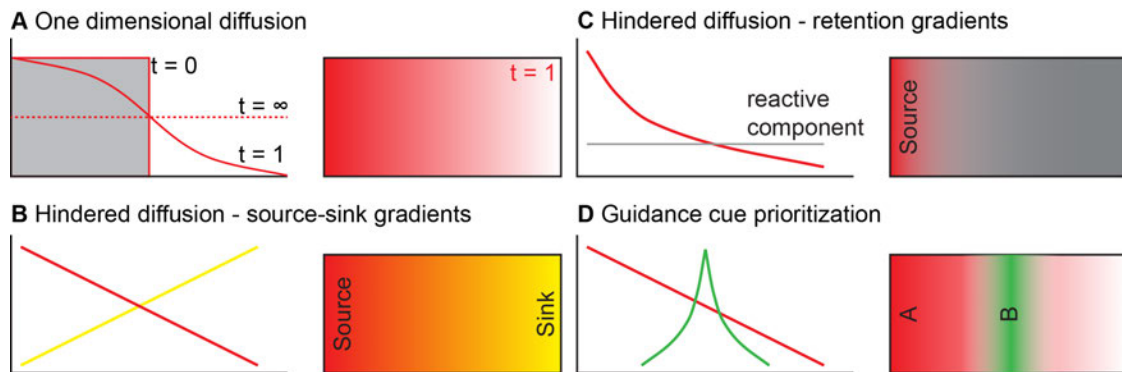


Figure 9.: Concentration gradient generation *in vivo*. Concentration c plotted against location x (left panels). Concentration depicted as intensity plot (right panels). A) One dimensional diffusion. At $t = 0$, the left compartment is full and right compartment empty. Diffusion from left to right compartment equilibrates concentration in both compartments at $t = \infty$. B) Hindered diffusion. Source-sink model. Concentration gradient is maintained by constant secretion from a source and depletion by a sink. C) Hindered diffusion. Retention by surface binding leads to accumulation close to the source. D) Guidance cue prioritization.

One of the few physiologically relevant examples for unbiased diffusing gradients is the transient diffusion of small molecular guidance cues (Figure 9A). Reactive oxygen species (ROS) such as hydrogen peroxide (H_2O_2) are able to diffuse nearly unbiased away from sites of wounded tissue in order to attract granulocytes (Niethammer et al., 2009).

In contrast, more *in vivo* evidence can be found for hindered diffusion, which enables the formation of short ranged, steep gradients shaped by external boundary conditions. Underlying principles can be depletion (sink) or concentration (reactive component) of diffusible factors at distinct distances from the source of secretion. In a source-sink model (Figure 9B), the environment (Boldajipour et al., 2008; Ulvmar et al., 2014) or the migrating cells themselves (Muinonen-Martin et al., 2014) deplete guidance cues by endocytosis (Boldajipour et al., 2008; Ulvmar et al., 2014) or degradation

(Garcia et al., 2009). Hence, a stable gradient of defined dimensions is formed. Some guidance cues bear reactive domains suggesting binding to reactive components in their environment (Figure 9C). Depending on the affinity or amount of secreted guidance cue, local immobilized spots or steep immobilized gradients are formed. Due to the charged nature of several chemokines, some bind to heparan sulfates or other charged ECM components in the interstitium, thereby forming immobilized gradients towards the area of secretion (Bao et al., 2010; de Paz et al., 2007; Hirose et al., 2002; Weber et al., 2013).

Competition with other guidance cues represents another layer of control. Here prioritization determines arrival of the cell at the predestined location in the organism (Figure 9D). Host derived, “intermediary” guidance cues act as long range or steady state signals to guide cells. Pathogen or host derived danger signals, so called “end target” guidance cues in turn can act on shorter range and are prioritized over intermediary signals. An example for such a prioritization system is used by granulocytes (Heit et al., 2002). Generally guided by chemokines like interleukin-8 or CXCL12 (intermediary signals), end target signals like C5A or pathogen derived fMLP are prioritized to successfully arrive at sites of infection (Heit et al., 2008).

1.3. Dendritic cells as a model for chemokine guided haptotaxis

1.3.1. Dendritic cell lifecycle

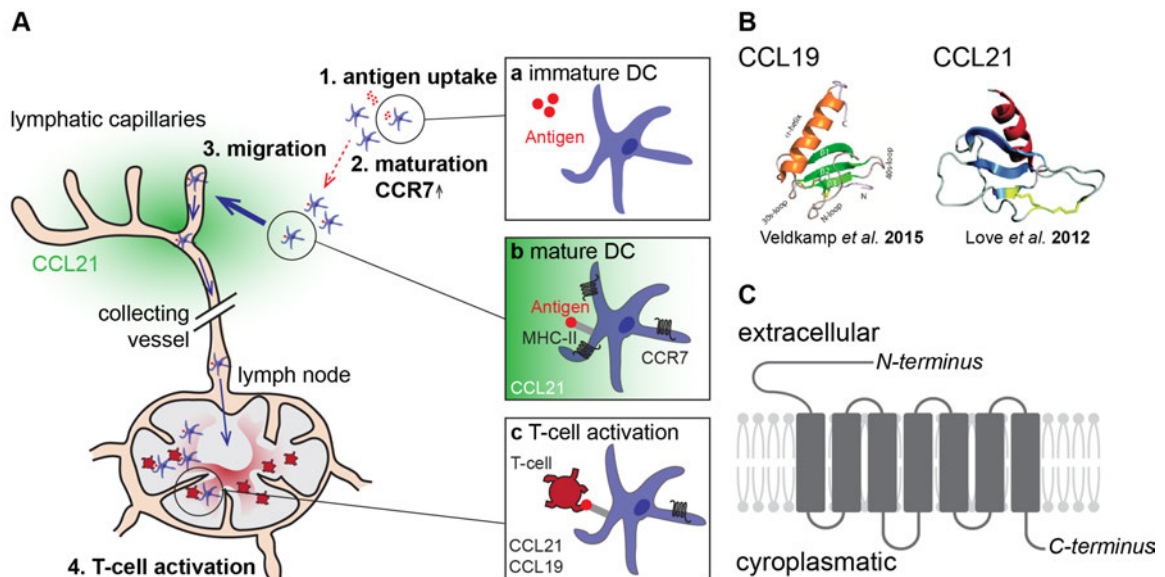


Figure 10.: DC lifecycle. A) 1. Antigen uptake in peripheral organs. 2. maturation and 3. haptotactic migration following CCL21 signals towards the lymphatic vessels. 4. Interaction with naïve T-cells in the parenchyma of the lymph node. (a) Immature DC. (b) Mature DC expressing CCR7 and presenting antigen on the cell surface via MHC class II complexes, following a concentration gradient of CCL21 (c) mature DC interacting with a lymphocyte in the parenchyma of the lymph node. B) NMR solution structures of the chemokines CCL19 and CCL21. C) CCR7, schematic illustration.

DCs are the most important antigen presenting cells (APC) of the adaptive immune response and therefore are decisive for triggering as well as dampening adaptive immunity (Steinman and Banchereau, 2007). In an immature, non-stimulated state, DCs scan peripheral tissues that are in close contact to the environment like skin, gut or mucaosa for internal and external danger signals, such as inflammatory stimuli or pathogens (Figure 10.A.a). Hereby, DCs constantly switch between local probing and random motility (Vargas et al., 2015). Intercepting an inflammatory stimulus, DCs pause random migration, become highly phagocytic, and thereby acquire antigens (Förster et al., 2008) (Figure 10.A.1). Pathogen encounter triggers a terminal differentiation program termed “maturation”. This includes the expression of co-stimulatory molecules, the production of cytokines and the externalization of major histocompatibility complex II (MHC-II) required for the priming of naive T cells (Figure 10.A.2). They eventually cease phagocytosis, return to the motile

state and up-regulate the C-C chemokine receptor 7 (CCR7). This imparts exclusive responsiveness towards the chemokines C-C motif ligand 19 (CCL19) and 21 (CCL21) while expression of other guidance cue receptors is downregulated (Figure 10.A.b). Following CCR7 signals, DCs migrate from the peripheral sites towards the lymphatic vessels, enter the vessels and eventually reach the draining lymph node (LN) (Russo et al., 2016; Weber et al., 2013). Within LNs, CCR7 signals guide DCs towards the T cell parenchyma where they physically encounter and eventually instruct T cells (Steinman and Banchereau, 2007) (Figure 10.A.4 and Figure 10.A.c).

1.3.2. CCR7 and its ligands - chemokines CCL19 and CCL21

The chemokine receptor CCR7 is expressed mainly by T-cells, B-cells, NK-cells, thymocytes and DCs (Figure 10C) (Müller et al., 2003). Its expression is differentially regulated in the aforementioned cell types and mainly depends on the respective maturation state or exogenous stimuli (Müller et al., 2003). CCR7 binds its two chemokines, CCL19 and CCL21, with similar affinities in the picomolar range (Sullivan et al., 1999). Although structurally and sequentially similar, CCL19 and CCL21 differ in expression, solubility and presentation and induce differential signaling (*ligand biased signaling*) (Rosenkilde, 2014) (Figure 10A and B) (Byers et al., 2008; Zidar et al., 2009). Both chemokines are constitutively expressed by stromal cells within lymphoid T-cell zones, but only CCL21 is secreted by high endothelial venules (HEVs) and lymphatic endothelial cells (Gunn et al., 1998; Luther et al., 2000).

1.3.2.1. Chemokine guided haptotaxis

While CCL19 does not significantly interact with ECM components and therefore is considered 'soluble', CCL21 does bind to charged heparan sulfates or other charged components of the ECM (de Paz et al., 2007). Binding is mediated by a 34 amino acid, basic, c-terminal extension (Veldkamp et al., 2015). Secreted by lymphatic endothelial cells, which are forming the lymphatic vessels, ECM binding retains CCL21 in close proximity to the vessels, forming an immobilized and stable haptotactic gradient towards the vessels (Weber et

al., 2013). Homing of antigen presenting DCs to secondary lymphoid tissues critically depends on the interpretation of this immobilized, haptotactic CCL21 gradient. However, how DCs interpret this gradient has not been addressed yet.

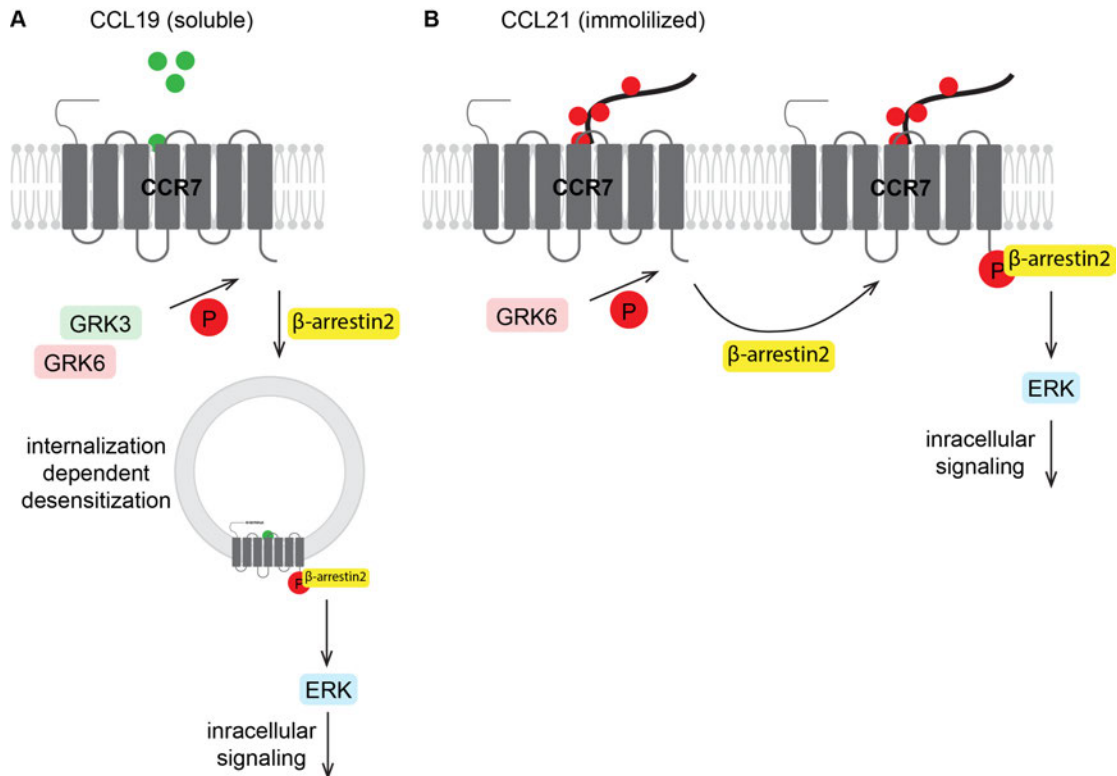


Figure 11.: Chemokine dependent CCR7 signal termination. A) Binding of soluble CCL19 leads to GRK3 and GRK6 dependent CCR7 phosphorylation followed by rapid β-arrestin2 dependent CCR7 internalization. GRK6 induced MAP kinase signaling. B) Binding of immobilized CCL21 leads to GRK6 dependent CCR7 phosphorylation and β-arrestin2 recruitment. Following GRK6 dependent CCR7 phosphorylation CCR7 is not internalized actively. GRK6 induced MAP kinase signaling.

1.3.2.2. CCR7 signaling and desensitization

Like all chemokine receptors, CCR7 belongs to the $G\alpha_{10}$ class of GPCRs. After CCL19/21 binding, the corresponding heterotrimeric G-proteins are activated, dissociate and induce signaling cascades including $PLC\beta$ and PI_3K pathways (Kohout et al., 2004). While G-protein induced Ca^{2+} and cAMP signaling is conserved for CCL19 or CCL21 dependent CCR7 activation, G-protein independent signaling differs significantly. (Kohout et al., 2004; Zidar et al., 2009) Upon G-protein dissociation, the CCL19/CCR7 complex recruits the G-Protein coupled receptor kinases GRK3 and GRK6 (Figure 11) (Zidar et al., 2009). GRK3 dependent CCR7 phosphorylation then leads to β-arrestin2

binding and rapid internalization of the CCL19/CCR7/ β -arrestin2 complex via clathrin coated pits (Figure 11A) (Byers et al., 2008; Otero et al., 2006). Following the classical GPCR sequestering pathway, CCL19 is degraded and CCR7 rapidly transported to the cell surface (Otero et al., 2006). This rapid recycling might facilitate responsiveness to wide concentration ranges of CCL19. Additionally, GRK6 dependent CCR7 phosphorylation and β -arrestin2 recruitment facilitates ERK activation and MAP kinase signaling. The surface immobilized CCL21/CCR7 complex recruits GRK6 only, resulting in reduced CCR7 phosphorylation compared to the CCL19/CCR7 complex (Figure 11B) (Zidar et al., 2009). Similarly, β -arrestin2 recruitment is reduced and the CCL21/CCR7 complex is not internalized via clathrin coated pits (Byers et al., 2008; Zidar et al., 2009). Hence, CCL21/CCR7 complexes are internalized only passively and CCR7 desensitization is mediated mainly by blocking heterotrimeric G-protein binding. As for CCL19, GRK6 induces ERK and MAP kinase activity to a similar extent. (Zidar et al., 2009)

Interpreting the haptotactic CCL21 gradient is crucial for homing of antigen presenting DCs to secondary lymphoid tissues (Russo et al., 2016; Weber et al., 2013) and CCR7 desensitization by GRK6 an essential part of the CCL21 induced signaling cascade (Zidar et al., 2009). However, the impact of CCR7 desensitization on DC migration and haptotaxis has not been addressed in a quantitative manner. Impaired receptor desensitization has been studied extensively for the chemokine receptor CXCR4. C-terminal phosphorylation of CXCR4 after CXCL12 ligation leads to rapid internalization and desensitization (Neel et al., 2005). Whereas deletion of the c-terminus reduced chemotaxis toward CXCL12 in HEK cells in an *in vitro* model (Roland et al., 2003), *in vivo* migration velocity and directionality of primordial germ cells (PGCs) were unchanged (Minina et al., 2007). However, persistence increased while PGCs reduced their tumbling behavior, thereby become more likely to miss their target. Similarly, human promyelocytic leukemia cells (HL60) with reduced GRK2 mediated formyl-peptide receptor (FPR1) desensitization reduced their tumbling phases leading to more persistent chemotaxis towards gradients of fMLP (Liu et al., 2012). In contrast, enhanced FPR1 desensitization by

increased GRK2 activity led to increased tumbling phases and hence reduced directionality.

In order to probe signal guided haptotaxis and desensitization of immobilized chemokine/receptor complexes in a controlled environment, *in vitro* assays are required which offer precise control over CCL21 presentation and ideal conditions for DC migration. For probing CCR7 ligand biased signaling, spatiotemporal control of both, immobilized CCL21 and diffusing CCL19 is required.

1.4. *In vitro* assay systems

1.4.1. Dendritic cell migration in confined environments

DCs must be able to migrate efficiently in diverse cellular environments to fulfill their function as sentinels of the adaptive immune response (Reis e Sousa, 2006). In an immature state they constantly scan their environment for danger signals by alternating random motility and local probing (Vargas et al., 2015). In a mature state, they traverse diverse cellular environments, like the cell and fiber network of the interstitium (Figure 12, *in vivo* situation), endothelial barriers or the dense compartments of the lymph node to eventually interact with specific naïve T-cells in the parenchyma of the lymph node.

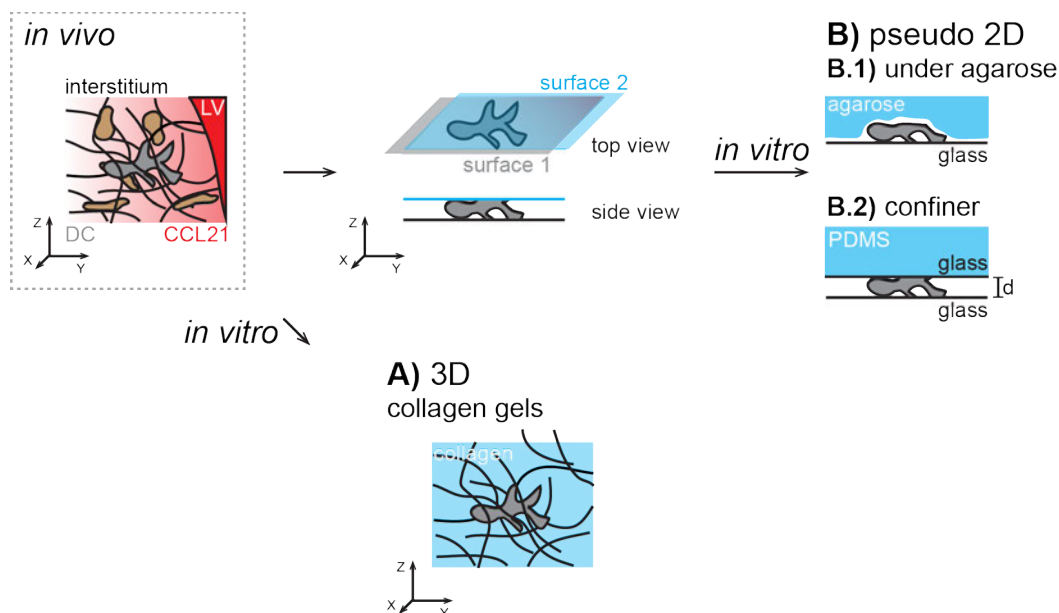


Figure 12.: Interstitial DC migration as an inspiration for *in vitro* migration assays. 3D *in vivo* situation: DC migrate in the dense fiber and cell network of the interstitium, following CCL21 signals (red) to the lymphatic vessel. A) 3D migration assay. DCs are embedded in a matrix (collagen or matrigel) mimicking the fiber network of the interstitium. B) Pseudo-2D migration assays. DCs are migrating in 2D confined conditions, using similar force transduction mechanisms as in 3D. B.1) Under agarose assay. DCs are migrating under a sheet of agarose. B.2) Cell confiner. DCs are migrating in a narrow migration chamber with defined, homogenous height.

Therefore, DC migration strategies have to be efficient and independent of specific adhesive cues and specialized topologies. Correspondingly, lacking strong lamellipodial FAs, they are able to migrate on highly adhesive substrates without the risk of stalling. In confined environments, they exploit diverse topological features, like fibrillar pores or other cells to generate traction force

despite not having any adhesive support (Lämmermann et al., 2008). Furthermore, without losing migration efficiency, DCs are able to migrate in environments with changing adhesiveness by adjusting their migratory machinery, such as the speed of actin polymerization (Renkawitz et al., 2009).

However, in artificial 2D environments offered by many commercially available *in vitro* assay systems, DCs migrate only in presence of chemokines which increase adhesiveness (Schumann et al., 2010). To ascertain DC migration, chemotaxis or haptotaxis at low chemokine concentrations or in the absence of chemokine, assays offering either confinement or a topologically complex environment are required:

Fibrillar gel based migration assays offer ideal conditions to enable DC migration in 3D through imitation of the dense cell and fiber network of the interstitium (Figure 12A). In these assays, migratory DCs are embedded in a gel matrix providing a meshwork of dense fibers. Cross-linked or just randomly oriented fibers create topological support and pores, which allow DCs to exert traction forces. Using collagen for matrix generation, pore size of the gel and therefore migration efficiency can be varied by polymerization conditions or collagen composition (Wolf et al., 2013). Furthermore, artificial hydrogels offer tight control over pore size, adhesiveness and even allow for ligand presentation (DeForest et al., 2009; Gould et al., 2012).

However, for imaging reasons, 2D conditions are often favored. Detailed tracking of cells migrating in 3D also requires 3D imaging and therefore complex image analysis. Furthermore, intracellular processes can be analyzed more efficiently if cell dynamics are limited to 2D. Thus, assay systems offering 3D migration conditions in a 2D framework are desired. Confining DC migration between two surfaces both provides support for traction force generation and limits the degree of freedom to 2D. It is hence termed 'pseudo-2D' environment. Specifically, cells migrate between a lower glass surface, which allows for cell imaging and a confining upper surface (Figure 12). This upper surface can be gel like (e.g. agarose or acrylamide), pushing the cell and lamellipodium onto the glass substrate and enabling detailed imaging of the sheet-like lamellipodium (Figure 12B.1) (Renkawitz et al., 2009). The surface

can also consist of another glass surface, positioned in a defined distance to the lower surface (Figure 12B.2) (Le Berre et al., 2014). In this case cell migration dynamics can be assessed. However, the lamellipodium is freely moving, impeding detailed imaging of lamellipodial dynamics (Eichner *et al.* unpublished data).

1.4.2. Diffusion-based gradients

A plethora of experimental setups are available to create diffusion-based chemotactic gradients and to assay the chemotactic behavior of migrating cells. To assess chemotaxis in 3D environments mainly gel-based assays are used (Figure 13A).

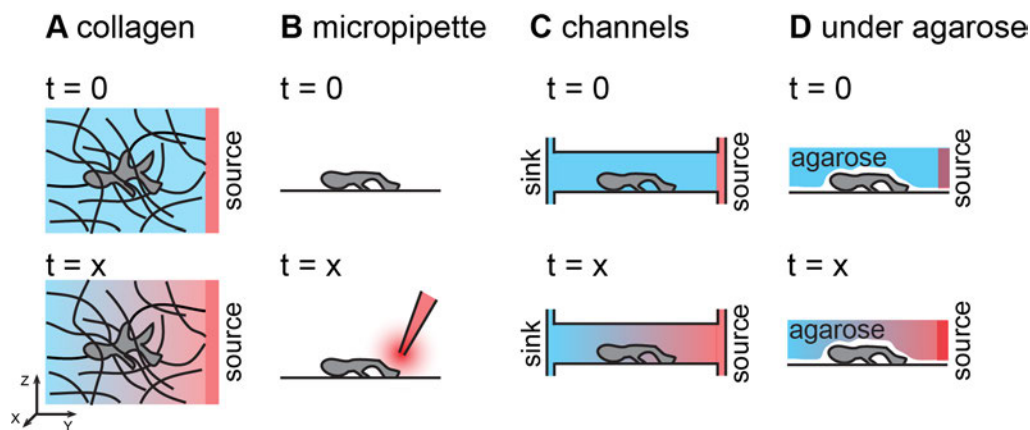


Figure 13.: Examples for diffusion generated gradients of guidance cue. $t = 0$ showing time before gradient generation and $t = x$ referring to a time during gradient generation. A) Collagen gel based assays. Guidance cue is freely diffusing in the aqueous collagen mixture from a source reservoir. Gradients reach equilibrated linear profiles after several hours. B) Micropipette assays. Guidance cue is applied with a micropipette. Steep, but transient gradients of guidance cue form rapidly. C) Chemotaxis channels. Gradient of guidance cue is formed in a channel connecting a source and a sink reservoir. D) Under agarose assays. Guidance cue is freely diffusing into the aqueous agarose mixture. Gradients reach a linear profile after several hours.

The guidance cue is applied in a reservoir connected to a gel matrix that contains cells (Figure 13A). Due to the fibrous structure of the matrix, almost unbiased diffusion of small molecules into the gel is possible, creating a linear gradient after a short build-up phase. This gradient can be stabilized if a sink reservoir is attached or continuously rising if the migration chamber is closed (chapter 5, Figure 47A). A classical and rather simple method to create steep chemotactic gradients is the pulsed release of guidance cue from a micropipette (Figure 13B). Here, cells can be embedded in a gel-matrix or migrate on

adhesive substrate. However, gradients formed through the pulsed release from a micropipette are transient and difficult to control (Arriemerlou and Meyer, 2005).

Commercial chemotaxis assays are mostly based on systems introduced by Dunn or Zigmond (Hodzic et al., 1991; Zigmond, 1977). Both systems use a narrow migration chamber connecting a cell suspension that contains a sink reservoir with a guidance cue that is kept in a source reservoir (Figure 13C). Adhesive migrating cells can enter the migration chamber and migrate towards the source reservoir. Manufactured from glass, both types of chambers allow live cell imaging during migration.

Agarose based pseudo-2D migration assays, as used for monitoring DC migration can easily be modified to also study chemotaxis. To this end, guidance cues are injected either into a reservoir or directly into the gel (Figure 13D). A concentration gradient is established by diffusion into the aqueous agarose gel and lamellipodial kinetics can be probed as mentioned in chapter 1.4.1.

The above-mentioned methods do not allow for spatiotemporal control of the diffusive gradients and gradient shape. Therefore, more advanced, sophisticated assays are required for a more precise quantification of chemotaxis. Fortunately, the rather new field of microfluidics is capable to fill this gap.

1.4.3. Microfluidics

In macroscopic systems, fluid flow is usually turbulent, with complex phenomena like chaotic eddies and vortices. We think of large systems such as water flowing around a ship or the wind near the surface of the earth (Figure 14a). In contrast, laminar flow is uniform with layers of fluid that are parallel to the direction of flow, hardly mixing laterally. (Figure 14b and c). Whether or not fluid flow is turbulent is characterized by a parameter termed the Reynolds number R (Purcell, 1977).

It is defined as

$$R = \rho L v / \eta .$$

The Reynolds number is a dimensionless quantity defined by the density ρ of the fluid, the viscosity η of the fluid, a characteristic length L of the traveled fluid and the flow velocity v . The transition from laminar to turbulent flow occurs for $R > 2000$.

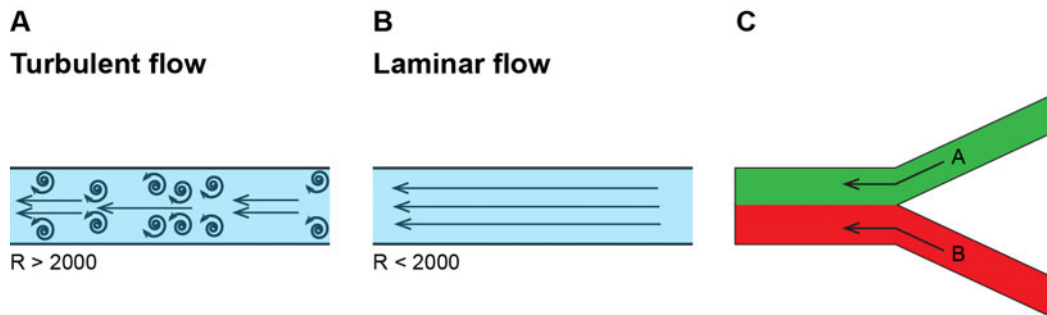


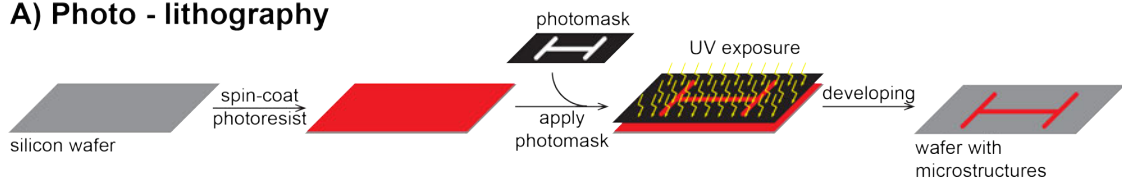
Figure 14.: Fluid flow patterns. A) Turbulent flow. Reynold's number > 2000 . B) Laminar flow. Reynold's number < 2000 . C) Colliding laminar flowing liquids. Mixing is turbulence free and therefore only occurs via diffusion.

For flow channels that have sub-millimeter diameter, termed “microfluidic channels”, the length L refers to the diameter (as long as the channel is circular). In a channel with diameter $L = 0.1 \text{ mm}$ filled with water traveling with velocity $v = 10^{-3} \text{ mm/s}$, the Reynolds number is

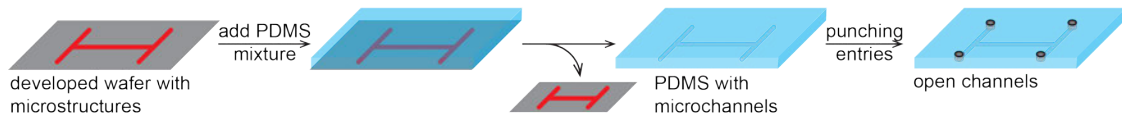
$$R = \rho L v / \eta = (10^3 \text{ kg / m}^3)(10^{-4} \text{ m})(10^{-3} \text{ mm / s}) / (0.01 \text{ Pas}) = 10^{-2} .$$

This is much smaller than the transition to turbulence and therefore microfluidic systems can be thought of as providing an environment that offers ‘life at low Reynold's number’, which is the typical environment for micron-sized cellular organisms (Purcell, 1977). Low Reynolds numbers refer to regimes of laminar flow, where mixing of fluid only occurs due to diffusion. Another aspect of low Reynolds number flow in a microfluidic channel is that drifting of cells is prevented due to drag forces. Therefore, microfluidic systems offer an environment with precise spatiotemporal control of chemical (e.g. soluble factors) and physical (e.g. confinement and localization) properties governing cellular sensing and migration on a microscopic scale (Adamo et al., 2012; Debs et al., 2012; Reynolds, 1883; Streets et al., 2014).

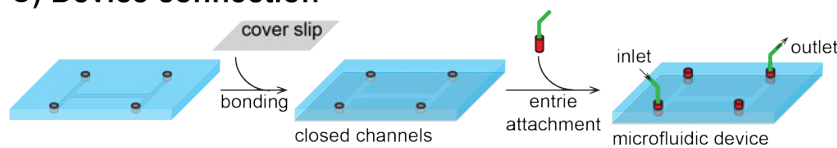
A) Photo - lithography



B) Replica molding



C) Device connection



D) Microfluidic valves

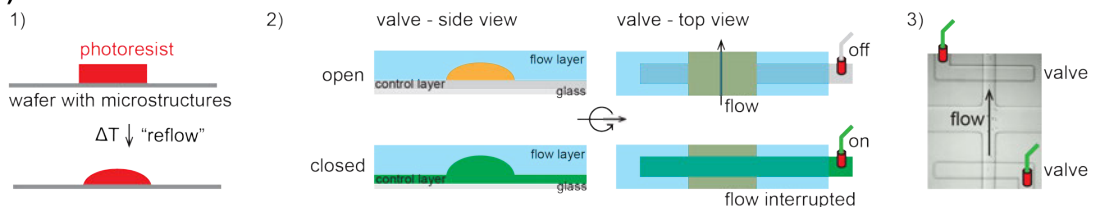


Figure 15.: Microfluidic chip production. A) Photo-lithography. Clean silicon wafers are spin coated with a UV curable photoresist in height of the future micro-channels. Photomasks confine UV exposure to generate microchannel structure. Developing dissolves uncured areas resulting in silicon wafers bearing the photographic negative of the microchannels (master). B) Soft-lithography or replica molding. PDMS mixture is poured onto the photographic negative. After curing, a photographic positive of the microchannels is imprinted in the PDMS block. Entry holes are punched at the designated positions. C) Device assembly and connection to a microfluidic system. Open PDMS imprints are closed with a plasma activated glass cover slip to create closed microchannels. Flow- and control channels are connected to cell- or reagent reservoirs and sink reservoirs. D) Microfluidic valves. D.1.) Reflowing of square channels for round channels which can be closed by microfluidic valves. D.2.) Schematic of microfluidic valves. Round flow channel (yellow) on control channel (grey) separated by thin PDMS membrane. Inflation of control channel in to the flow channel (green) closes flow channel at intersecting areas.

The fabrication of microfluidic devices requires the ability to reliably create and control sub-millimeter sized structures. Inspired by the semiconductor industry, micron sized features can be produced by photo-lithography (Figure 15A). Specifically, photoresists are spun on blank silicon wafers in a thickness corresponding to the desired channel height. Depending on the photoresist, channel features are cured by UV exposure through a photomask (negative photoresist, e.g. SU-8) or the photoresist surrounding the channel features is dissolved after UV exposure (positive photoresist, e.g. AZ 40 XT). This pattern bearing silicon wafer (master) is used as a photographic negative mold. In a

process termed “replica molding”, liquid elastomer, mostly transparent polydimethylsiloxane (PDMS) is poured onto the master and thermally cured (Figure 15B) (Whitesides et al., 2001). The cured features bearing PDMS (photographic positive) is then removed from the master and bonded to a plasma oxidized glass surface in order to close the channels. This allows for observation of fluids in the system of microfluidic channels. One method of flowing liquid through the channels is to connect ports to pressurized air (Figure 15C).

Microfluidic valves can be used to stop and direct fluid flows. This allows the construction of e.g. cell sorters and pumps (Unger, 2000). In detail, the elastomer block with channel features and opened channel entries (Figure 15B, last step) is bonded onto a thin, elastic second elastomer layer bearing microchannels perpendicular to the flow channels (control layer, Figure 15D 2. and 3.). Pneumatic pressurization of those control channels leads to inflation of the elastomer membrane under the flow channel. The inflated control channel locally displaces the fluid in the flow channel, thereby closing it (Figure 15B 2.). Valves can seal only rounded channels. Therefore rectangular AZ40-XT flow layer molds are reflowed by increasing the temperature (Figure 15D 1.). Simple microfluidic devices without valves can be controlled with pressure regulators. Pneumatic valve systems however use software and electronics to control the operation of multiple air pressurized solenoid valves.

1.4.3.1. Soluble gradient generation using microfluidic systems

A predestined application of microfluidic systems in life science is the controlled generation of concentration gradients. The ability to control the concentration of soluble factors both spatially and temporally through using microfluidic chips makes microfluidic setups an ideal tool to examine cellular processes like chemotaxis.

Utilizing the properties of laminar flow in microfluidic channels allows for flow based gradient generation. Instead of mixing, particles in fluids with laminar flow merge only by diffusion, leading to a slow and limited exchange of particles between layers of fluid. Therefore, smooth gradients of guidance cue

can be generated by parallel flows of different concentrations of that guidance cue (Figure 16A). Ricart *et al.* used chemokine flows of different concentrations to create opposing, soluble chemokine gradients to probe for the chemotactic potential of different CCR7 and CXCR4 ligands (Ricart *et al.*, 2010). A similar flow-based device, the “microfluidic wave generator” was used to create travelling waves of cyclic adenosine monophosphate (cAMP) (Skoge *et al.*, 2014). This study gave insights into the cellular memory of chemotactic *D. discoideum*.

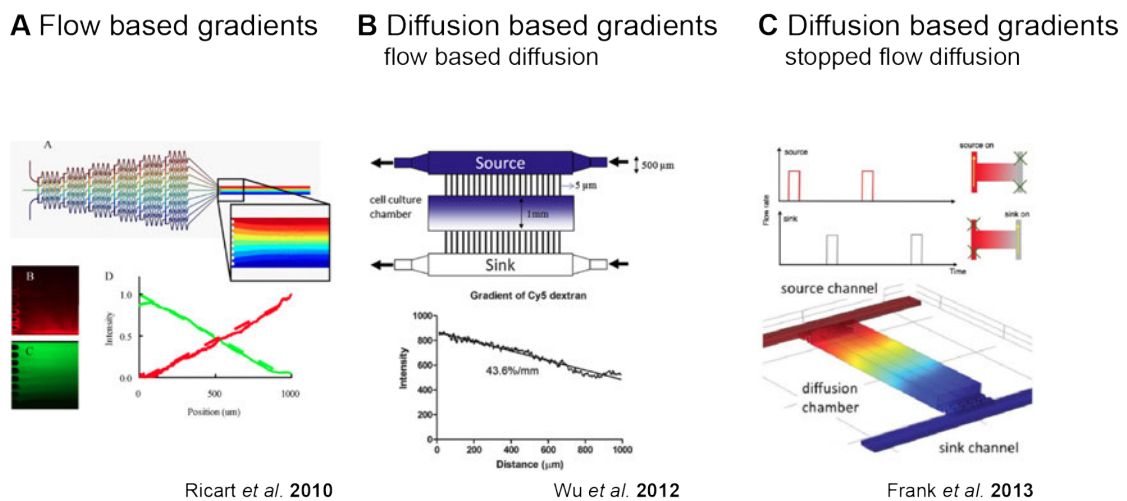


Figure 16.: Microfluidic gradient generation. A) Flow based microfluidic gradient generation. B) Diffusion-based gradient generation. C) Diffusion-based, stopped-flow gradient generation.

A disadvantage of flowing gradients is the influence of flow on migrating cells. Shear stress created by flow for example increases L-selectin dependent adhesion of leukocytes onto P-selectin glycoprotein ligand (Yago *et al.*, 2004). For flow critical applications, techniques for flow free gradient generation in microfluidic systems are available. Instead of mixing flows, source and sink channels can be connected with a central chamber. Diffusion from the source channel through the central chamber thereby generates a flow free linear gradient within the central migration chamber perpendicular to the flow (Figure 16B) (Wu *et al.*, 2012).

If diffusion into and out of the diffusion chamber is temporally controlled, arbitrary diffusion-based gradients can be generated (Figure 16C) (Frank and Tay, 2013). Specifically, sequentially opened pneumatic membrane valves restrict the flow into and from the migration chamber allowing for unidirectional

media exchange by diffusion only. Opening of the source channel feeds the concentration of guidance cue at one end of the migration chamber and opening of the sink channel depletes the concentration at the other end, hence keeping the profile at a constant steepness. Different gradient profiles can be generated by temporal modulation of source and sink opening/closing. Mehling *et al.* used stable, flow free CXCL12 gradients to induce human lymphocyte chemotaxis. In combination with a sorting device, they were able to sort and analyze cells according to their chemotactic potential (Mehling *et al.*, 2015).

1.4.4. Immobilized guidance cues

To assess haptotactic cell behavior, many different approaches to immobilize guidance or adhesive cues on surfaces have been developed (Ricoult *et al.*, 2015). Unlike diffusion generated, soluble gradients, immobilized gradients often require comprehensive surface chemistry techniques to *activate surfaces* in order to further modify them. Subsequently, the activated surfaces can be either *passivated* to prevent cell adhesion or signal activation or *functionalized with receptor ligands* to induce cell adhesion or signal activation. The requirements for such immobilized gradients differ significantly for *haptotactic integrin ligands* and *haptotactic GPCR ligands*. For haptotactic GPCR ligands, mechanical properties of the substrate in patterned and non-patterned areas have to be consistent to exclude mechanical influences. In contrast, when using haptotactic integrin ligands, non-patterned areas should prevent cell binding and therefore be passivated. Forces exerted by migrating cells or those probing adhesion are sufficient to pull adsorbed and non-covalently bound integrin ligands off the patterned surfaces. Therefore, for sustainable surface functionalization, adhesive integrin ligands must be immobilized in a covalent manner

1.4.4.1. Micropatterning

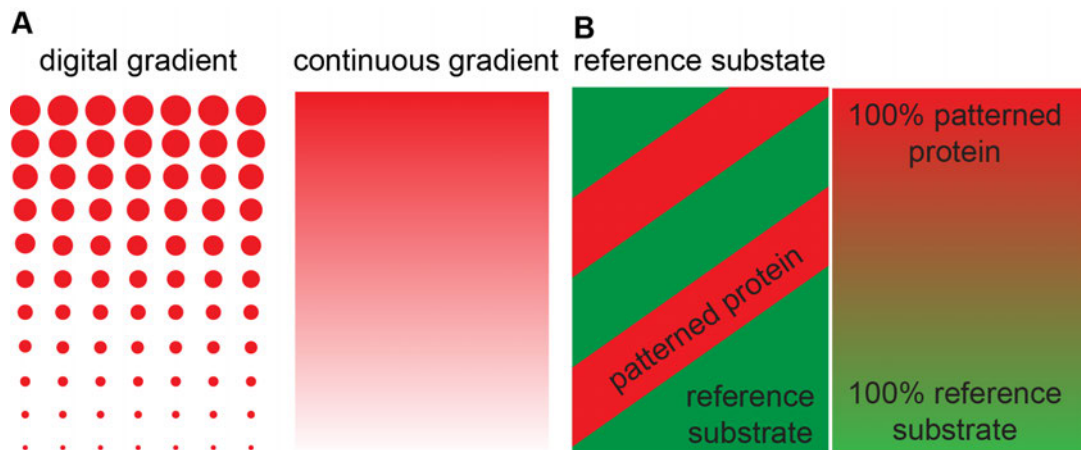


Figure 17.: Micropatterning. A) Digital and continuous gradients as examples for patterns with submicron resolution. B) Reference substrate. Surface properties of non-patterned areas are referred to as 'reference substrate'. The reference substrate covers the photographic negative of the respective pattern.

Methods to create surface bound gradients and shapes of bioactive molecules with subcellular resolution are termed 'micropatterning techniques' and represent an important tool in cell biology, development and medicine (Blawas and Reichert, 1998). For example, patterns of integrin ligands allow the control of cell attachment and shape (Freeman et al., 2016; Schiller et al., 2013). Guidance cue patterns like netrin-1 can influence axon growth and patterned signaling molecules or co-factors enable *in vitro* examination of basic cellular processes (Gressin et al., 2015; Mai et al., 2009). Some techniques result in digital patterns and shapes, others allow for the generation of homogenous gradients (Figure 17A). Yet, most micropatterning techniques are based on the same principles in a sense that a surface is locally modified by chemical or physical protein deposition. This deposition can be *additive* meaning that the surface is activated through local modification, or *subtractive*, meaning that the surface is activated through local ablation. Both types of deposition yield patterns of immobilized biomolecule, the photographic positive, and reference substrate, the photographic negative (Figure 17B).

1.4.4.2. Surface activation

In order to attach organic molecules on polymers, metal or glass surfaces in a controlled fashion, attachment sites need to be created. This attachment can be

achieved electrostatically or covalently. Electrostatically activated surfaces are obtained using strong bases, like potassium hydroxide or plasma treatment. Whereas inert gas plasma efficiently reduces organic impurities, air or oxygen plasma charges the surface by oxidation. Therefore, positively charged proteins or polymers, like poly-*L*-lysine (PLL, Table 1), can attach and mediate linker or non-charged protein binding (Figure 18A).

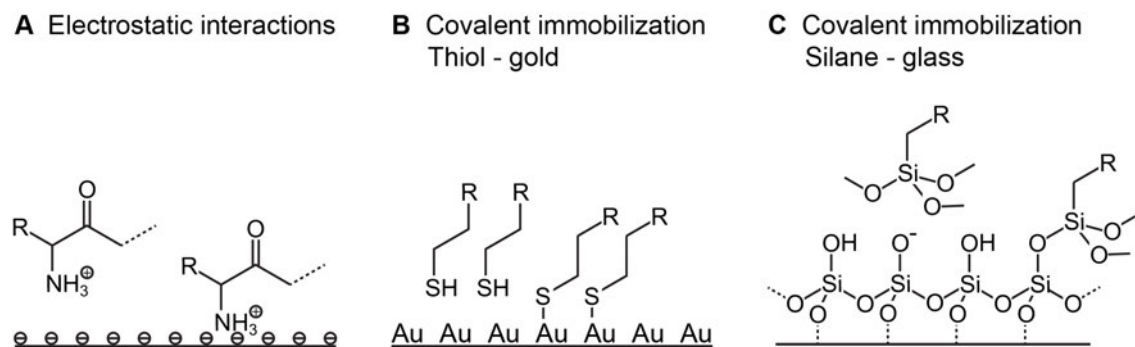


Figure 18.: Surface functionalization. A) Electrostatic interaction. Positively charged functional groups electrostatically interact with negatively charged surfaces B) Covalent immobilization: Thiol/gold interaction. Local oxidation and thereby covalent immobilization of alkanethiolates by gold particles or surfaces. C) Covalent immobilization: Silane/glass interaction. Free hydroxyl groups of the glass surface covalently replace alkoxy groups of oxalkylsilanes.

Electrostatic interactions mainly lead to multiple layers that do not allow control for thickness and stability. What is generally desired for specificity and sustainability is the covalent surface binding of only a single layer of active molecules. Self assembled monolayers, SAMs fulfill this demand (Mrksich and Whitesides, 1996). SAMs usually consist of an aliphatic tail and a reactive head domain. Applied as a solution or vapor, the head domain binds the surface specifically while the tail can be modified after monolayer formation. Many classical surface functionalization techniques are based on the formation of alkanethiolate SAMs on gold coated surfaces (Figure 18B) (Mrksich and Whitesides, 1996). In these techniques, the reactive thiol head group is oxidized at the gold surface, thereby being bound covalently. Depending on the modification, the aliphatic tail provides ordered SAM organization and determines polar or non-polar properties of the surface coating. Reactive adapters, like carboxylic groups or primary amines, in turn allow for further functionalization of the monolayer.

Applicable on hydroxyl bearing surfaces e.g. glass, silicon wafers or polymers like PDMS, oxalkylsilanes offer more versatile applications of SAMs (Figure 18C). The reactive oxalkyl-silane head forms covalent bonds with free hydroxyl groups and oxyanions of the surface. As for alkanethiolates, the tail determines polarity and can be modified after SAM formation.

1.4.4.3. Passivation of activated surfaces

Many protein micropatterning techniques are based on passivating surface coatings preventing biomolecule or cell adhesion in non-patterned regions. Therefore polar, hydrophilic or non-polar, hydrophobic polymers can be used.

Formula	Compound	Polarity	Attachment
	Polyethylene glycol (PEG)	polar	covalent/ electrostatic
	Polyhydroxymethyl methacrylate (polyHEMA)	polar	electrostatic
	Polyvinyl alcohol (PVA)	polar	covalent
 R = alkyl R = alkyl-NH ₂ R = alkyl-SH R = alkyl-COOH	Oxalkylsilanes	polar/non-polar	covalent
 R = alkyl R = alkyl-NH ₂ R = alkyl-SH R = alkyl-COOH	Alkanethiolates	polar/non-polar	covalent

Table 1.: Surface passivation reagents.

Polyethylene glycol (PEG) represents the most widely used passivation polymer (Table 1). Commonly, flexible PEG chains of approximately 2-5 kDa are surface immobilized via a reactive head functionalization. Due to their hydrophilicity, PEG chains are highly hydrated in aqueous environment, thereby preventing surface adsorption to a large extent. Long PEG - chains can be covalently

attached to functionalized surfaces and short PEG chains are widely used as intra - molecular spacers and linkers. However, due to practical and financial reasons, in many applications and experimental setups, PEG is electrostatically immobilized. Therefore positively charged PLL is grafted with PEG chains, mediating adsorption on oxidized and charged surfaces.

Polyhydroxymethyl methacrylate (poly-HEMA) is another hydrophilic polymer electrostatically immobilized on charged surfaces (Table 1). Like PLL-PEG, poly-HEMA forms a hydrated shell to prevent surface adsorption. Due to the chain character and the electrostatic immobilization, poly-HEMA and PEG coatings are highly flexible and, depending on the layer thickness, transient and often short lived.

Covalently attached to the surface, passivating SAMs are more stable than electrostatic immobilized reagents. Prolonging the aliphatic tail of oxalkylsilanes or alkanethiols (Figure 18B and C) creates a non-polar, hydrophobic SAM, preventing cell adhesion and protein adsorption (Table 1) (Mrksich and Whitesides, 1996). Modification of their reactive adapters with polar/hydrophilic polymers like PEG or polyvinyl alcohol (PVA, Table 1), creates polar/hydrophilic surface passivation. In contrast to the flexible, hydrated PEG chains, PVA forms a dense, hydrated polymer. PEG chains are binding surfaces with a reactive head domain. The PVA polymer however, is immobilized at various positions (hydroxyl groups) throughout the PVA chains and intra- and intermolecular hydrogen bonds form a stable polymer layer. This grants strong surface binding of the whole polymer and therefore sustainable surface passivation (Doyle, 2001).

1.4.4.4. Functionalization of activated surfaces

Due to the simplicity of the method and therefore the possibility to create large or repetitive patterns in a high throughput fashion, micro-contact printing is popular and widely used (Figure 19A). In these techniques, a photographic positive stamp is manufactured, for example of PDMS, using photoresist patterned silicon wafers or by heat embossing. This stamp is covered with the biomolecule solution and applied onto an activated or reactive surface, creating

a digital pattern (Figure 17A). The remaining, non-patterned areas can then, in turn, be covered with the reference substrate. For example, adhesive ligand modified alkanethiolates were patterned on gold vaporized surfaces using PDMS stamping techniques. Subsequently PEG-modified alkanethiolates were bound onto the non-patterned areas, thereby confining growth of bovine capillary endothelial cells (Mrksich and Whitesides, 1996).

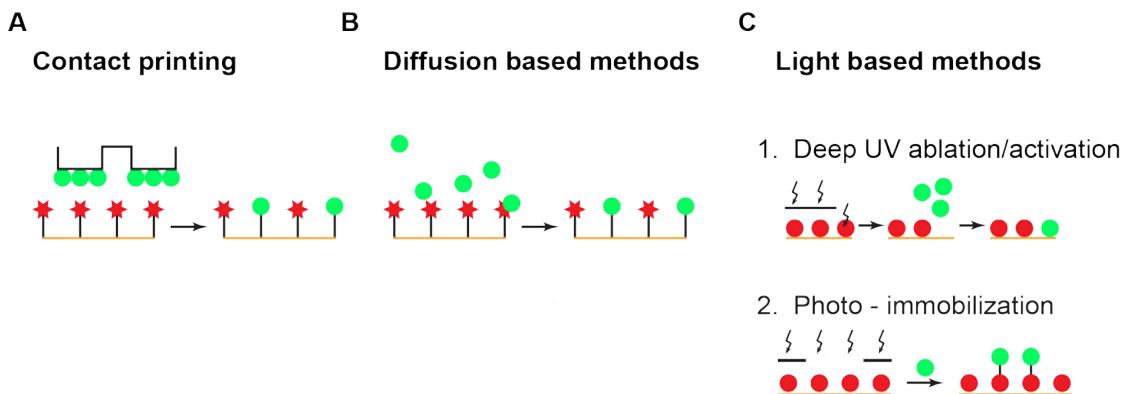


Figure 19.: Micropatterning techniques. A) Contact printing. B) Diffusion-based techniques. C) Light based techniques. 1) Subtractive; Photo-ablation of mostly passivating surface coating. 2) Additive; Photoactivation of surface or reagent for immobilization of reagent, linker or ligand.

To generate continuous immobilized gradients of biomolecules, mainly diffusion-based methods have been used. These methods are based on generation of a diffusion-based gradient of biomolecules on an activated or reactive surface (Figure 19B). After immobilization, the surface is washed and the reference substrate can be applied homogeneously. Diffusion-based gradients can be generated by microfluidic mixing devices fitted onto reactive surfaces (Wu et al., 2012). A simpler approach is the application of ligand soaked gel stamps on reactive surfaces. In order to examine directed axon growth from hippocampal neurons, Mai *et al.* generated a netrin-1 gradient on an epoxy and PLL covered glass slide using an agarose block equipped with flow channels (Mai et al., 2009). Ligand diffusion from the flow channels into the agarose block formed a gradient on the epoxy-coated surface. The pre-coated PLL represented the reference substrate on which the cells were growing by integrin independent adhesion.

A major drawback of diffusion-based methods is that they do not allow for sharp borders or elaborate shapes. Light based immobilization methods

have the potential of offering the generation of both digital and continuous patterns and gradients. For digital pattern generation, light can be used to ablate the reference substrates, thereby activating the patterned surface for biomolecule binding (Figure 19C). Deep UV irradiation locally confined by a photomask can be used to ablate PLL-PEG on glass surfaces and simultaneously charge the ablated surface (Azioune et al., 2009). After irradiation, the ablated and activated areas can be incubated with adhesive ligand, thereby creating digital adhesive patterns for cell attachment.

For digital and continuous pattern and gradient generation, photo-catalyzed de-protection or coupling reactions can be utilized (Figure 19C). Many of those reactions are light dose dependent, therefore enabling the generation of continuous gradients as well as sharp borders. Instead of using highly energetic deep UV light, PLL-PEG ablation can be carried out using a UV laser exciting a photo-initiator like 4BzBTMA (Figure 20, Radical photoinitiators). Here, the excited initiator radically cleaves the surface passivating PEG chains in a dose dependent manner allowing the adsorption of immobilized protein gradients in the cleaved areas (Strale et al., 2016).

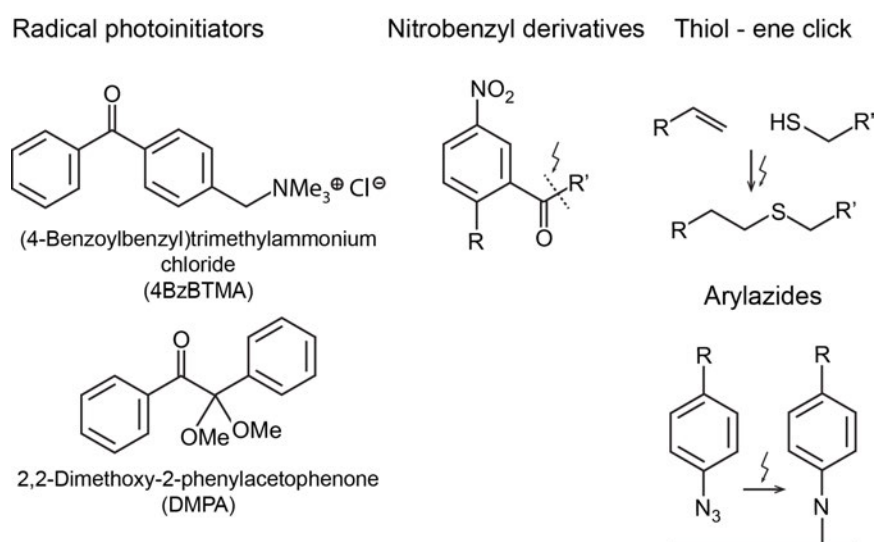


Figure 20.: Photopatterning reagents and techniques. Radical photo-initiators used for light dose dependent photo-ablation (4BzBTMA and DMPA). Photo-labile linker or caging groups, e.g. nitrobenzyl derivatives. Photo-reactive functional groups for specific (thiol-ene click) and non specific (arylazides) photo-immobilization.

Nitrobenzyl and its derivatives are widely used as photo-cleavable tags and linkers (Figure 20, Nitrobenzyl derivatives). As such, they allow for UV light

induced uncaging and activation of gel-soaked soluble ligands like fMLP (Collins et al., 2015). Furthermore, non-adhesive patches for cell attachment assays can be created by UV induced RGD de-attachment from RGD modified PEG chains (Wegner et al., 2015).

In addition, several photo-catalyzed methods to directly immobilize tagged proteins or biomolecules on surfaces are available. Thiol-ene click reactions for instance are widely used in surface-patterning and hydrogel modification (Figure 20, Thiol-ene click). Thiols chemically add to alkenes in a radical, UV induced manner (DeForest et al., 2009). This for instance allows UV induced, dose dependent patterning of acrylamide gels and alkene or thiol labeled surfaces.

Arylazides and other nitrene intermediate forming reagents covalently bind to any organic surface in a UV catalyzed manner (Figure 20, Arylazides). For instance, arylazide tagged RGD peptide has been immobilized on PVA coated surfaces using a UV lamp and a photomask (Sugawara and Matsuda, 1995). The created RGD patterns then provided integrin binding sites for endothelial cell growth.

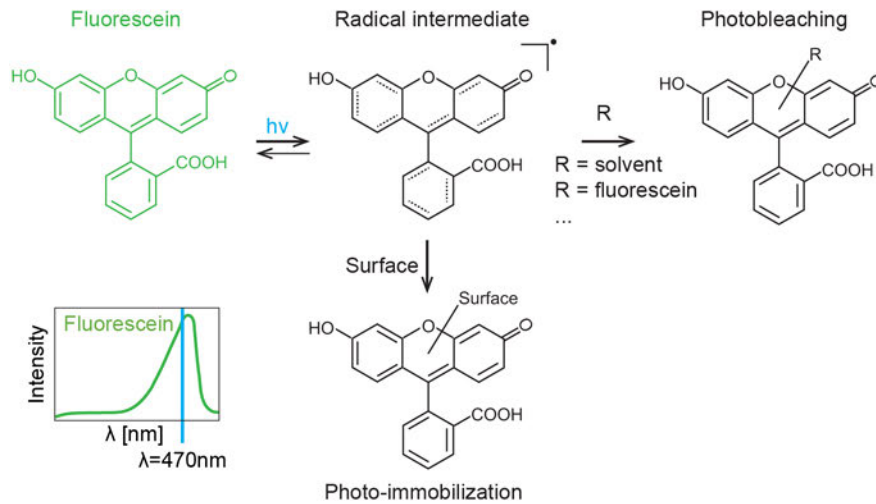
Generally, adsorption or photo-radical based photo-patterning techniques lack the possibility of reliable quantification of the patterned biomolecules. Additionally, usage of highly energetic UV light and direct ligand binding destroys and chemically alters ligand structure, thereby reducing the concentration of bioactive ligand on the surface.

1.4.4.5. Patterning by photobleaching

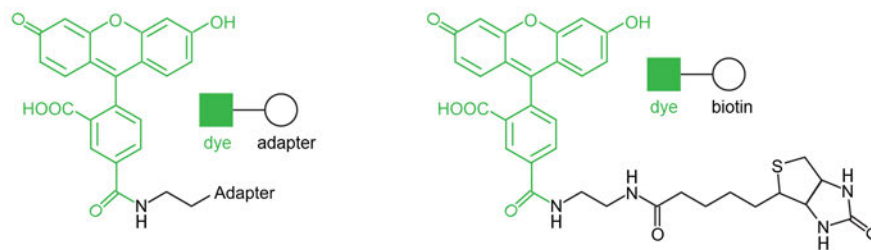
Photobleaching of fluorescent dyes is highly dependent on the excitation spectrum of the respective dye and the wavelength and intensity of the light source used for excitation. Once excited, radical intermediates form within the π -system of the dye. Those intermediates can either recover to the initial excitation state, thereby regaining their fluorescent properties, or be scavenged by either solvent molecules or other dye molecules. Hereby, covalent bonds between fluorescent dye-molecules or fluorescent dye and solvent molecules

are created and the conjugated π -system is interrupted, losing its fluorescent properties. This phenomenon is referred to as 'photobleaching' (Figure 21A).

A Photo-immobilization



B Adapter



C Protein immobilization by photo-bleaching

Photo-immobilization

Ligand binding

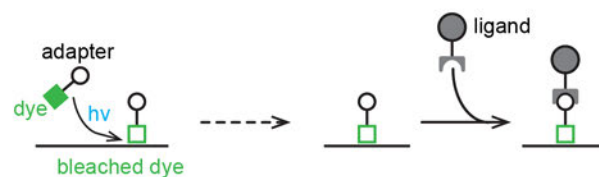


Figure 21.: Protein immobilization by photobleaching. A) Photobleaching of fluorescent dyes. Photo-excitation of fluorescent dye molecules generates radical intermediates. Those can either relax back to the fluorescent state or covalently bind other dye molecules (R = fluorescein) or solvent components (R = solvent), thereby losing or altering their fluorescent properties (photobleaching). Bleaching at surfaces induces covalent binding of the dye molecule to the surface (photo-immobilization). B) Modification of dye molecules with adapter functionalization (e.g. biotin for streptavidin binding). C) Adapter aided protein immobilization by photobleaching. Precise dosage dependent photopatterning of fluorescent dye-adapter heterodimers. A monolayer of active and accessible adapter is functionalized by adapter binding ligands.

Similarly, photobleaching in close proximity to surfaces results in the formation of covalent bonds between the surface and the bleached dye (Figure 21A 'Photo-immobilization') (Holden and Cremer, 2003). Photobleaching at surfaces is highly wavelength and dosage dependent, enabling immobilization of dye molecules according to their excitation properties and in homogeneously graded efficiencies. If the dye is coupled to an adapter molecule (Figure 21B), surfaces can be functionalized with adapter binding ligands after photo-immobilization (Figure 21C)

Due to the separation of photoreaction and ligand binding, only intact ligands are presented on the surface and can be quantified (Holden and Cremer, 2003). The additive nature of the photo-immobilization reaction allows modification of any surface without changing the reference system for example by ablation. Therefore it is ideally suited for applications in which consistency of the substrate properties are favored. Such applications include the immobilization of haptotactic guidance cues like chemokines. Like other photo-immobilization methods, it allows the generation of digital, as well as defined, homogenous gradients. Photo-excitation can be performed using a photomask or a digital mirror device illuminated with a mercury lamp and a filter set selected for the specific excitation spectrum of the used dye molecule (Holden and Cremer, 2003; Waldbaur et al., 2012). A focused laser beam with high z-resolution for dye excitation limits photo-immobilization to the illuminated areas on the surface thereby reducing background binding (Bélisle et al., 2008). Restricting the excitation wavelength to the excitation maximum of the respective dye enables the printing of multiple patterns sequentially from a single dye mixture (Bélisle et al., 2009; Holden and Cremer, 2003). Following a radical mechanism, the immobilization reaction allows homogenous overlap of printed lines, thereby creating homogenous gradients of patterned proteins.

Bleaching prone dye tagged molecules or proteins are often commercially available. Therefore, for most adapters photo-immobilization by photobleaching does not necessitate custom synthesis or chemical expertise. Adapter molecules should enable subsequent binding of target molecules like receptor ligands or amplifying connectors. Biotin/streptavidin or

antibody/antigen binding represent well established, non-covalent adaptor-connector pairs suitable for protein immobilization (Figure 22A) (Bélisle et al., 2009; 2011; Holden and Cremer, 2003).

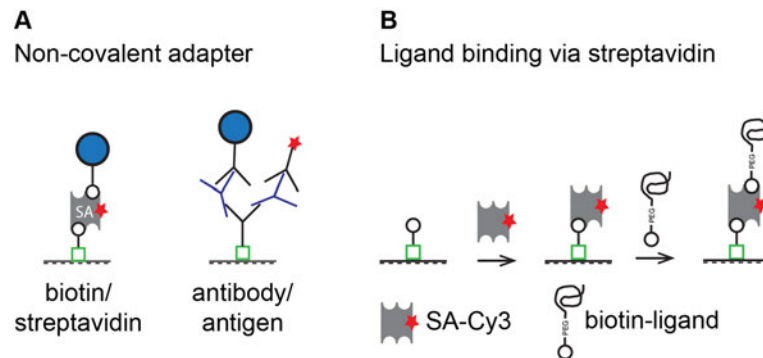


Figure 22.: Examples for adapter-connector pairs. Ligand in blue. Fluorescent dyes indicated as red star. A) Left: Biotin-streptavidin connector pair. Biotinylated ligands are immobilized on biotinylated surfaces using quadrivalent streptavidin as connector. Right: Antibody-antibody connector pair. Fluorescent dye and/or ligand labeled antibodies are immobilized on surface immobilized antibodies by multivalent secondary antibodies as connector. B) Workflow: Ligand binding via streptavidin. Biotinylated proteins, like chemokines are surface immobilized via dye labeled streptavidin linkers.

Surface-immobilized antibodies proved to efficiently bind multivalent secondary antibodies (Bélisle et al., 2009). In turn, those can immobilize ligand or dye labeled primary antibodies allowing for ligand functionalization and visualization of the patterned areas (Figure 22A). Surface-immobilized biotin-4-fluorescein (B4F, Figure 21A and B) binds streptavidin with femtomolar affinity (DeChancie and Houk, 2007). As a connector, streptavidin can bind four biotin molecules and therefore connect immobilized and ligand-bound biotin (Figure 22B). This allows for immobilization of biotinylated ligands on any streptavidin-functionalized surface. Commercially available dye-labeled streptavidins enable visualization of the protein patterns without interfering with or limiting the presentation of the biotinylated ligands (Figure 22B).

Streptavidin and antibody based photo-immobilization methods as introduced above hold several disadvantages regarding concentration and presentation. A major problem represents the size of the connector molecules. In case of CCL21, the immobilized biotinylated ligand is approximately 12 kDa in size. The connector, streptavidin, however is comparably big with a molecular weight of approximately 60 kDa, therefore determining maximal

deposition density of the monolayer. Antibodies, specifically IgG molecules offer with approximately 150 kDa similar problems. Hence, the maximally immobilized ligand concentration is heavily dependent on the size and globularity of the connector.

Furthermore, streptavidin binds biotin in a pocket like structure consisting of an 8-stranded β -barrel (Livnah et al., 1993). Small biotin-bound ligands like fMLP or RGD peptide may not be easily accessible for cell surface receptors if buried in this barrel-like cavity thereby evoking the necessity of elaborated linkers. Additionally, although in the femtomolar affinity-regime, biotin-streptavidin interactions are non-covalent and antibody-antigen interactions are even weaker. For some applications, e.g. patterning of integrin ligands like RGD peptide, a covalent immobilization of the ligand is necessary to avoid a gradual depletion of the ligand.

2. Project description

Haptotaxis is a widely applied mechanism to guide or concentrate cells within tissues of an organism. Cell binding ligands, such as the ECM component fibronectin (Carter, 1965) or tissue immobilized chemokines (Middleton et al., 1997) hereby act as cues that influence cell migration. Despite the relevance of haptotactic cell migration in key organismal processes that govern embryonic development (Thiery, 1984) or adequate immune responses (Middleton et al., 1997; Sarris et al., 2012; Weber et al., 2013), quantitative studies of haptotactic cell behavior are largely missing. This shortfall is to a large extent due to the lack of *in vitro* assays enabling such studies.

In this thesis, we aim to develop new experimental strategies to surface immobilize haptotactic chemokines or integrin ligands, that maintain the bioactive state and allow for arbitrarily graded depositing patterns / shapes. We set out to develop a series of *in vitro* haptotaxis assays by combining surface immobilization of the respective guidance cue with the corresponding experimental framework:

(i) Combining immobilized gradients of the chemokine CCL21 with physical cell confinement fostering DC migration *in vitro* allows us to quantitatively study the migratory behavior of CCL21 guided, haptotactic DCs. In addition, we intend to reveal the potential role of CCR7 signal termination for CCL21 guided haptotaxis by studying DCs lacking GRK6 mediated CCR7 desensitization. (chapter 3.1, Quantitative analysis of dendritic cell haptotaxis and chapter 3.2, Dendritic cells interpret interstitial CCL21 gradients in a signal-to-noise ratio governed, GRK6 dependent manner.)

(ii) We aim to immobilize CCL21 in a microfluidic chip that grants precise control of soluble guidance cue presentation. This approach enables us to study migratory cell behavior in the presence of soluble, chemotactic and immobilized, haptotactic chemokines. (chapter 3.3, A microfluidic device for measuring cell migration towards substrate bound and soluble chemokine gradients)

(iii) Eventually, we set out to quantitatively assess adhesion guided haptotactic cell behavior, by the development of a photo-patterning strategy granting covalent and precise surface immobilization of integrin ligands. Combined with a highly cell repellent surface coating we will be able to control for integrin guided haptotaxis. This approach should also allow us to control cell growth and shape by patterns of integrin ligands on cell scale. (chapter 3.4, Covalent, adapter based protein patterning by photobleaching)

In the following section of this thesis, each of the abovementioned chapters will be presented as either publication or publication draft including the respective introduction, results and materials and methods. Subsequently, each chapter is discussed in the discussion part of the thesis.

3. Results

3.1. Quantitative analysis of dendritic cell haptotaxis

Jan Schwarz¹ and Michael Sixt¹

¹*Institute of Science and Technology Austria (IST Austria), Klosterneuburg, Austria*

In: Tracy M. Handel, editor, *Methods in Enzymology*, Vol. 570, Burlington:

Academic Press, 2016, pp. 567-581.

ISBN: 978-0-12-802171-2

© Copyright 2016 Elsevier Inc.

3.1.1. Abstract

Chemokines are the main guidance cues directing leukocyte migration. Opposed to early assumptions chemokines do not necessarily act as soluble cues but are often immobilized within tissues. E.g. dendritic cell (DC) migration towards lymphatic vessels is guided by a haptotactic gradient of the chemokine CCL21. Controlled assay systems to quantitatively study haptotaxis *in vitro* are still missing. In this chapter, we describe an *in vitro* haptotaxis assay optimized for the unique properties of DCs. The chemokine CCL21 is immobilized in a bioactive state, using laser assisted protein adsorption by photobleaching. The cells follow this immobilized CCL21 gradient in a haptotaxis chamber, which provides three dimensionally confined migration conditions.

3.1.2. Introduction

As the main antigen presenting cells of the adaptive immune response, DCs play a crucial role in regulation and activation of adaptive immunity (Mellman

and Steinman, 2001). Under homeostatic conditions, DCs reside in peripheral tissues and continuously scan their environment for internal and external danger signals. After intercepting an inflammatory stimulus, DCs pause random migration and become highly phagocytic, thereby acquiring antigen (Reis e Sousa, 2006). Pathogen encounter then triggers a terminal differentiation program that is termed maturation. Maturation is accompanied by the production of cytokines, up-regulation of co-stimulatory molecules and the presentation of major histocompatibility complex (MHC)-peptide complexes which are required to prime naïve T cells in the lymph node (Steinman and Banchereau, 2007). Additionally, the chemokine receptor CCR7 is highly increased, imparting responsiveness towards the CCR7 ligands CCL19 and CCL21 (Sallusto et al., 1998). In order to reach the lymphatic vessel and to eventually arrive in the T cell area of the lymph node, the cells follow immobilized CCL21 gradients towards the vessels (Weber et al., 2013). This haptotactic migration is a rate-limiting step in the initiation of adaptive immune responses.

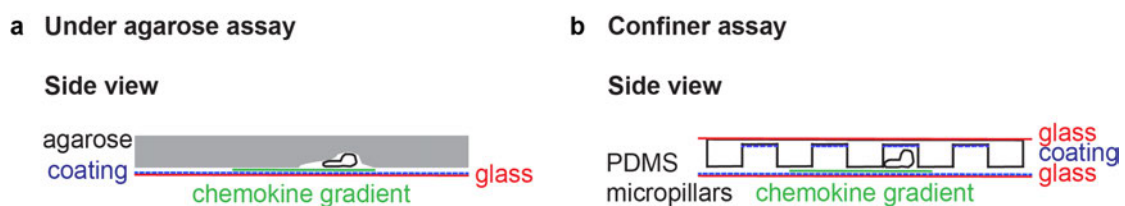


Figure 23.: 3D migration assays. A) Under agarose assay. Cells migrating under a sheet of agarose. B) Confiner assay. Cells migrating between two glass slides. The spacing between glass slides is determined by polydimethylsiloxane (PDMS) micropillars.

DCs feature a special type of amoeboid migration. In contrast to other leukocytes, migratory DCs exhibit even less adhesion to most substrates. This makes migration on 2D surfaces inefficient, but allows fast locomotion in 3D confined environments (reviewed in (Renkawitz and Sixt, 2010)). The 3D meshwork conditions of the interstitium have been mimicked *in vitro* for example by collagen gel migration assays (Lämmermann et al., 2008). To examine DC migration in a qualitative and quantitative manner *in vitro*, it is advantageous to limit the dimensions of migration. Confinement from the top, for example with an agarose layer (Figure 23a) allows the cells to migrate in a 3D-like configuration while pressed to a plane surface (Renkawitz et al., 2009).

The surface can be covered with adhesive or non-adhesive surface-coatings or functionalized specifically with chemokines to mimic haptotactic interstitial gradients.

The Piel group replaced the agarose layer with a second plane surface. Unlike agarose, that can be deformed by the cells and forms a soft cover, the stiff surface is positioned in a defined distance to the lower surface using PDMS micropillars as spacers (Figure 23b) (Le Berre et al., 2014). This setup provides a defined and controllable 3D migration chamber, which is ideally suited for the construction of a haptotaxis chamber, since both surfaces can be functionalized before chamber assembly. Furthermore, the cells can migrate without losing contact to the functionalized substrate and will not migrate out of the focal imaging plane.

In vivo, interstitial CCL21 gradients are continuous, steep and static gradients with lengths of about 100 μm (Weber et al., 2013). Many protein micropatterning techniques like mask bound photolithography (Azioune et al., 2009; Blawas and Reichert, 1998) or micro-contact printing (Whitesides et al., 2001) offer too low spatial resolution to mimic those homogenous, continuous gradients. Another disadvantage of some micropatterning techniques is the necessity of background blocking in the non-patterned regions. This changes important substrate properties like adhesiveness between patterned and non-patterned regions.

Laser assisted protein adsorption by photobleaching (LAPAP) is one of the few techniques able to generate gradients in micro-scale resolution without the need for background blocking (Bélisle et al., 2008). The principle underlying LAPAP is the covalent immobilization of dye molecules, e.g. fluorescein, on surfaces by photoactivation (bleaching) (Figure 24a). With light intensity determining the amount of immobilized fluorescein, homogenous, continuous gradients can be generated using photo-masks or movable lasers. Using a biotin - fluorescein heterodimer (B4F), any transparent surface can be biotinylated with arbitrary patterns and gradients (Figure 24a). Streptavidin (SA) offers four binding sites for biotin and binds it with extremely high affinity. Therefore, the biotin pattern can be further functionalized by streptavidin that, if

fluorescently labeled, can be used to simultaneously visualize the gradient. Biotinylated chemokines (e.g. CCL21) are then attached to the streptavidin-functionalized patterns (Figure 24b). CCL21 is immobilized to lymphatic endothelial cells and negatively charged extracellular matrix components by electrostatic interaction via its basic C-terminus (Figure 24c). The N-terminal part of the chemokine is involved in receptor ligation and activation (Love et al., 2012). To avoid unspecific CCL21 binding we use a truncated version of CCL21. This version only contains the region responsible for receptor ligation (amino acids 24-98) and is lacking the basic C-terminus. In order to maximize chemokine binding to the patterned B4F/SA areas, the truncated CCL21 24-98 is mono-biotinylated at the C-terminus.

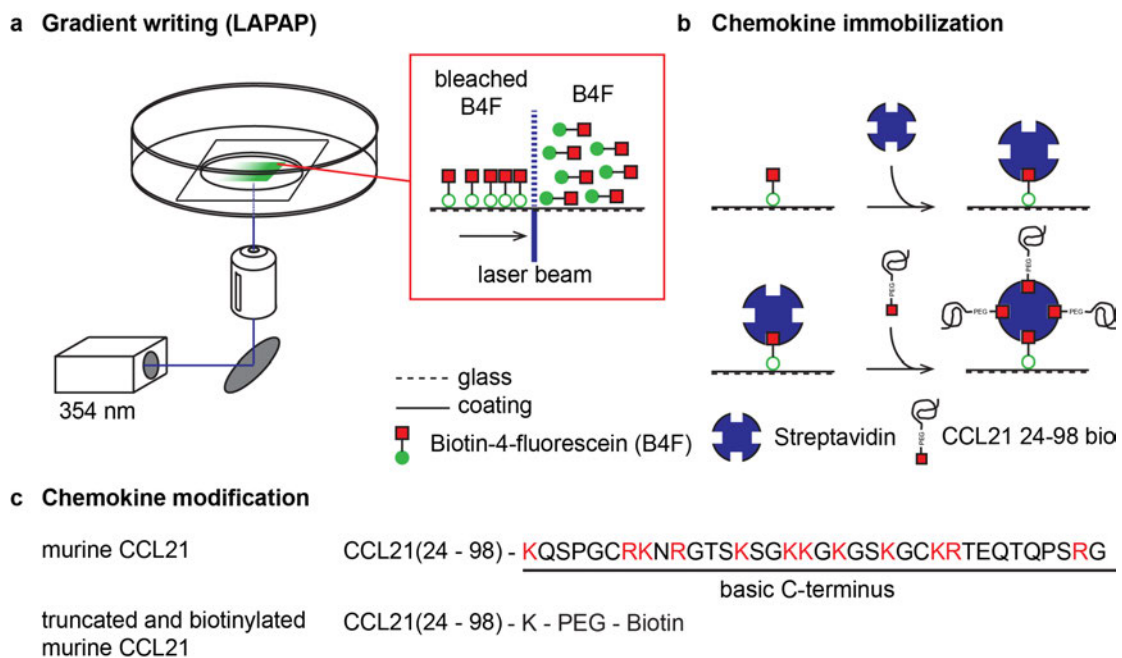


Figure 24.: Chemokine micropatterning. A) Gradient writing using laser assisted protein adsorption by photobleaching (LAPAP). Biotin-4-fluorescein (B4F) is immobilized on a coated glass surface by a movable UV laser ($\lambda = 354$ nm). B) Chemokine immobilization. Binding of streptavidin-Cy3 (SA-Cy3) functionalizes the B4F pattern. Free biotin binding sites of the immobilized SA-Cy3 bind biotinylated CCL21 24-98 and presents it in a bioactive state. C) Chemokine modification. Basic CCL21 c-terminus is replaced by biotin attached to a polyethylene glycol (PEG) linker.

3.1.3. Methods

In this chapter we will explain in detail how both, top and bottom part of the chamber are manufactured, how migratory DCs are differentiated from bone

marrow cultures and how the haptotaxis chamber is assembled. Some parts are adapted from published sources. In those cases the description will focus on the details we specifically changed. The respective basic methods are described in detail in the cited publications.

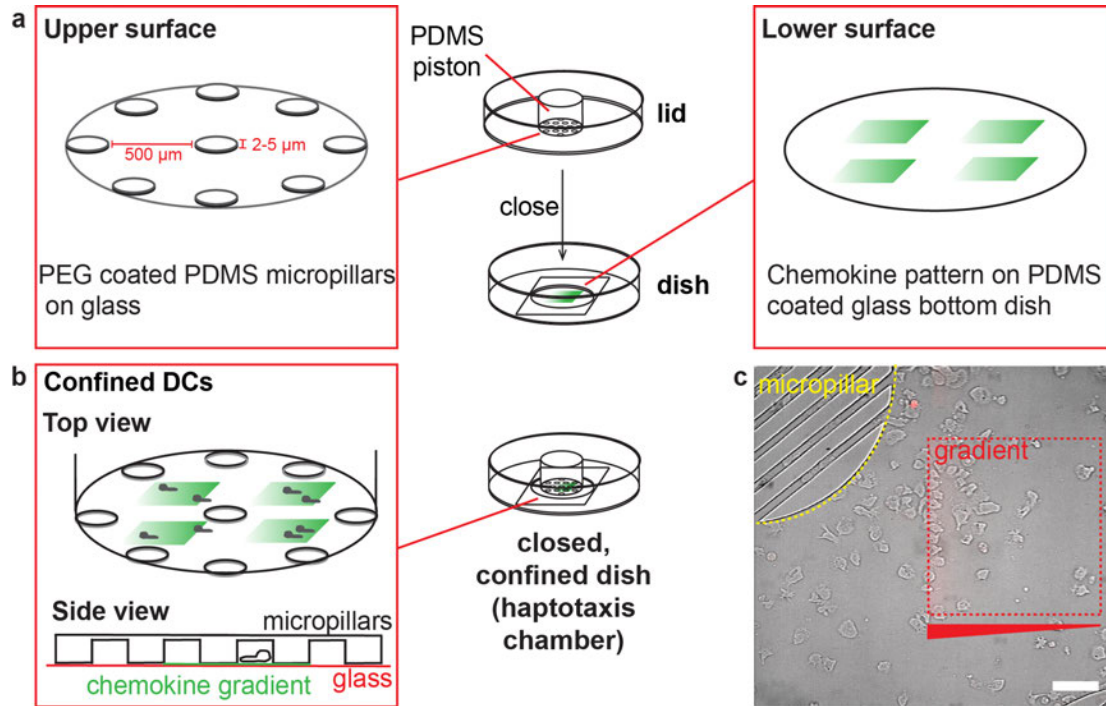


Figure 25.: Haptotaxis chamber. a) Upper and lower surface of the haptotaxis chamber. Lid with elastic PDMS piston and PEG coated PDMS micropillars on a round glass slide and the glass-bottom dish with CCL21 24-98 bio micropattern. Left magnified box: Round glass slide with PEG coated PDMS micropillars. The distance of the pillars is $500 \mu\text{m}$. The height of the micropillars is 2 to $5 \mu\text{m}$. Right magnified box: CCL21 24-98 bio micropattern on the glass of a glass-bottom dish. b) Closed haptotaxis chamber. Top view and side view of the closed haptotaxis chamber. c) Brightfield image of DCs migrating on a printed CCL21 24-98 bio gradient in the haptotaxis chamber. Micropillar and gradient are indicated with dashed lines. Scale bar represents $50 \mu\text{m}$.

The haptotaxis chamber consists of two glass surfaces that are spaced by polydimethylsiloxane (PDMS) micropillars. The upper surface bears the PDMS micropillars to define the height of the chamber (Figure 25a. upper surface). For the lower surface, a glass bottom dish is used which offers the chemokine pattern the cells are migrating on (Figure 25a. lower surface). The lower surface and the PDMS micropillar bearing upper surface are pressed onto each other by a big, elastic PDMS piston which is glued into the lid of a the glass bottom dish. Depending on the assay conditions, the lower surface can be PEG or BSA coated to avoid specific binding before LAPAP is used for functionalization with a haptotaxis inducing chemokine pattern. To avoid cell adhesion to the upper

surface, the PDMS micropillars are PEG coated. After fabrication of the top and bottom part, the cells are added and the chamber is closed (Figure 25b). The cells show haptotactic response within seconds and can be imaged directly after chamber assembly.

3.1.3.1. A. Lower surface preparation

3.1.3.1.1. A.1 Glass slides treatment and dish preparation

The lower surface of the haptotaxis chamber is a glass coverslip modified version of a 60 x 15 mm tissue culture dish. This setup allows convenient functionalization and washing of the cover slip, facilitates confinement and enables imaging of the migrating cells. Commercially available glass bottom dishes can be used as well, however they are less versatile than the custom-made version.

Required materials:

iso-propanol (Sigma Aldrich)

ethanol (Sigma Aldrich)

MΩ H₂O

Spin coater (Laurell Technologies Corporation, WS 650-MZ-23NPP)

Planetary centrifugal mixer (Thinky, ARE250)

22mm x 22mm, #2 glass slides (Mentzel Gläser, Thermo Scientific)

PDMS Sylgard 184 Elastomere Kit (Dow Corning)

Transparent aquarium silicone sealant (Marina)

60 x 15mm style non-pyrogenic polystyrene tissue culture dish (Falcon)

Plasma Cleaner (Harrick Plasma)

Oven (80 °C)

(optional) PBS (pH 7.2 without CaCl₂, without MgCl₂, GIBCO)

(optional) *PLL-PEG* (SuSos)

(optional) BSA (3 % m/v) in PBS (Sigma Aldrich)

(optional) Bovine fibronectin (Sigma Aldrich)

1. Sonicate coverslips in *iso*-propanol and ethanol (each 20 min, sweeping sonication).
2. Rinse cover slips with MΩ water without letting them dry and blow-dry them with N₂ or wipe them carefully with tissues.
3. Mix silicone elastomer and curing reagent in a 10:1 ratio using a planetary centrifugal mixer.
4. Plasma clean dishes (2 min, high intensity) and immediately add 500 μL of the well mixed, bubble free silicone elastomer/curing reagent mixture on the plasma cleaned side of a glass cover slip.
5. Spin at 4000 rpm for 40 s with a prior acceleration of 200 rpm/s using the spin coater. The PDMS thickness is about 17 μm. If slides will be imaged using a TIRF microscope thinner PDMS layers should be used.
6. Bake slides for 6 h at 80 °C in an oven (A.1.6).
7. Drill a hole with a diameter of 17 mm in the middle of the bottom of a 60 x 15mm Falcon Tissue culture dish (Figure 26a). A diameter of 17 mm is ideal for gluing 22 x 22 mm cover slips onto the hole.
8. Glue the PDMS coated glass slides on the bottom of the dishes using clear silicone aquarium sealant. The PDMS covered side has to face the dish.
9. Dry dishes over night (min. 6 h) at rt or 1 h at 80 °C.
10. (Optional for coated surfaces) plasma clean dishes (2 min, high intensity) and immediately incubated with PLL-PEG (0.5 mg/mL in HEPES), BSA or fibronectin (100 μg/mL in PBS) for at least 1 h (drying of the solution is allowed).
11. (Optional for coated surfaces) wash with PBS (3x) and store under PBS at 4 °C (A.1.11).

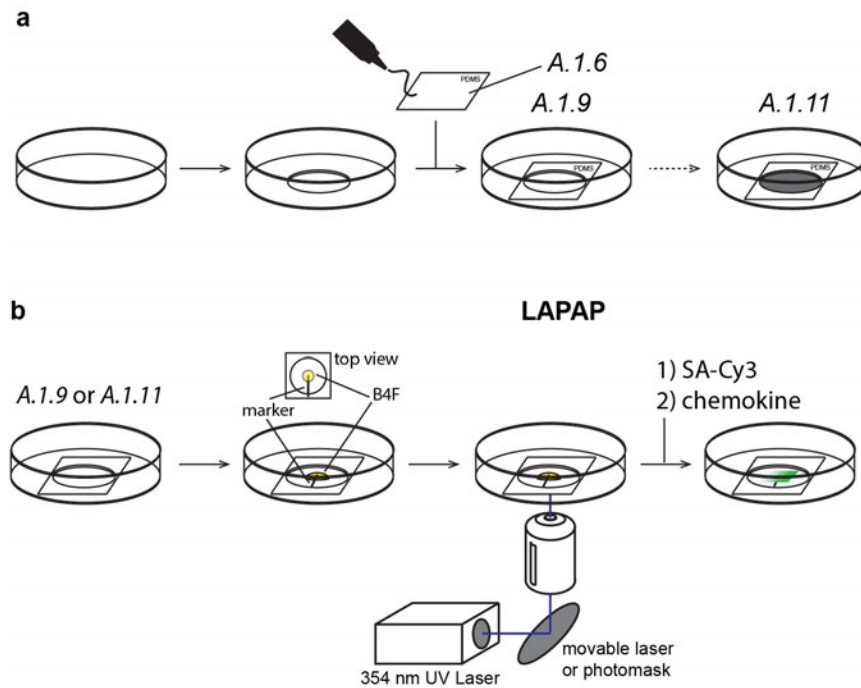


Figure 26.: Production of the CCL21 24-98 bio patterned glass-bottom dish. a) Glass-bottom dish production and modification. A hole is drilled into a 60 x 15 mm Falcon Tissue culture dish. A PDMS coated coverslip (A.1.6) is glued onto the hole with the PDMS coated surface facing into the dish (A.1.9). Surface coatings can be applied to the manufactured dish (A.1.11) b) Chemokine micropatterning. A droplet of B4F is placed on the marked area of the glass-bottom dish. Patterns are generated using LAPAP. SA-Cy3 and CCL24-98 bio are immobilized on the written B4F pattern.

3.1.3.1.2. A.2. Chemokine printing

This part partially depends on the microscope setup used for writing. See original publication by Belisle *et al.* for detailed description of possible laser writing setups (Bélisle *et al.*, 2008). We will focus on the staining and chemokine binding/handling procedures.

Required materials:

Microscope equipped with a movable laser or photomask and the corresponding software for gradient writing.

PBS (pH 7.2 without CaCl_2 , without MgCl_2 , GIBCO)

Biotin-4-Fluorescein (B4F, Sigma Aldrich)

Parafilm (Bemis)

BSA (0.1 % m/v) in PBS (Sigma Aldrich)

CCL21 24-98 bio (custom synthesized from ALMAC; for more detailed information see section D. Troubleshooting)

Streptavidin-Cy3 (SA-Cy3, Sigma Aldrich)

1. Take prepared dish out of the oven and let them cool down to room temperature. If coated dishes are used, aspirate PBS.
2. Place 20 μL of B4F solution (150 $\mu\text{g}/\text{mL}$ in PBS) in the middle of the PDMS coated glass slide of the previously prepared dish (Figure 26b). Close dish and seal it with parafilm to avoid drying of the B4F solution during laserwriting.
3. Mark the middle of the B4F droplet with a marker on the glass side of the cover slip. (Figure 26b).
4. Focus on the PDMS surface next to the marked spot. Write gradients/patterns (Figure 26b).
5. Aspirate B4F and wash 3 three times with PBS.
6. Add 20 μL of SA-Cy3 solution (10 $\mu\text{g}/\text{mL}$) and incubated at room temperature for 20 min in the dark.
7. Aspirate SA-Cy3 solution and wash three times with PBS. B4F/SA-Cy3 patterned dishes can be stored under PBS for up to one week at 4 $^{\circ}\text{C}$ in the dark. Seal the dishes with parafilm to avoid evaporation of the PBS.
8. Reconstitute the lyophilized CCL21 24-98 bio in 0.1 % BSA in PBS to a final concentration of 25 $\mu\text{g}/\text{mL}$. Aliquots can be stored at -20 $^{\circ}\text{C}$. Prior to use, the stock solution is diluted to 250 ng/mL in PBS.
9. Incubate SA-Cy3 patterned dishes with CCL21 24-98 bio (250 ng/mL) for 30 min at room temperature, subsequently washed three times with PBS and assemble haptotaxis chamber immediately.
This step needs to be timed well with the recovery period of the DCs. Only start incubation of the dishes with chemokine when the cells were recovered for at least 30 min.

3.1.3.2. B. Upper surface preparation

The haptotaxis chamber represents a modified version of the cell confiner established by the Piel group. Therefore we will only briefly discuss how the individual components are manufactured. For a detailed description please refer to Le Berre *et al.* (Le Berre et al., 2014).

3.1.3.2.1. B.1. Micropillar preparation:

Required materials

PDMS Sylgard 184 Elastomere Kit (Dow Corning)

Planetary centrifugal mixer (Thinky, ARE250)

Round cover glasses, #1, 12 mm diameter (Mentzel Gläser, Thermo Scientific)

Silicon wafer with micropillars of desired height and spacing (Le Berre et al., 2014).

iso-propanol

ethanol

Oven (80 °C)

Plasma Cleaner (Harrick Plasma)

Heating plate (95 °C)

PBS (pH 7.2 without CaCl₂, without MgCl₂, GIBCO)

PLL-PEG (SuSos, stock solution 2 mg/mL in HEPES; working solution 0.5 mg/mL)

1. Mix silicone elastomer and curing reagent in a 7:1 ratio using a planetary centrifugal mixer.
2. Carefully clean the silicon wafer with canned air. Then add about 4 mL of the bubble free silicone elastomer/curing reagent mixture on the wafer.
3. Plasma clean round cover glasses at high intensity for 2 min. Then place them with the plasma cleaned surface facing the silicone elastomer/curing reagent mixture on the wafer. Press them down to the silicon wafer and make sure to get rid of all the bubbles.
4. Bake PDMS on a heating plate for 15 min at 95 °C.
5. Remove PDMS coated cover glasses carefully with *iso*-propanol using a razor blade.
6. Plasma clean PDMS micro pillar containing surface of the round cover glass for 2 min at high intensity.

7. Add 50 μL PLL-PEG (100 $\mu\text{g}/\text{mL}$) and incubate at rt for at least 1 h (let it dry). Before usage wash at least five times with PBS and store under PBS.

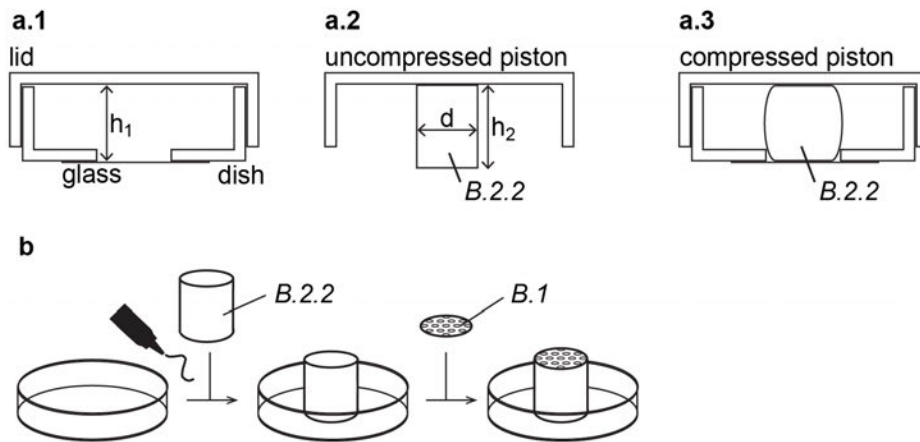


Figure 27.: Lid production. a.1) Side view of a closed glass-bottom dish. h_1 is the distance between glass slide and inner surface of the lid. a.2) Side view of lid with soft PDMS piston. Elastic PDMS piston B.2.2 glued into the lid of the glass-bottom dish. h_2 is the height of the piston B.2.2; d is the diameter of the piston B.2.2; $h_2 = h_1 + 1 \text{ mm}$. a.3) Closed glass-bottom dish with compressed PDMS piston B.2.2. Compression of the elastic piston B.2.2 presses PDMS micropillar coated round glass slide B.1 on the glass of the glass bottom dish. b) Lid with soft PDMS piston preparation. Piston B.2.2 is glued in the center of the inner part of the lid of the glass bottom dish. PDMS micropillar coated round glass slide B.1 is placed on the elastic PDMS piston B.2.2 with the micropillars facing away from the piston B.2.2.

3.1.3.2.2. B.2. Lid with soft PDMS piston

Required materials:

PDMS Sylgard 184 Elastomere Kit (Dow Corning)

Planetary centrifugal mixer (Thinky, ARE250)

Aluminum mold for soft PDMS pistons

Vacuum pump (Vacubrand, RZ6)

Vacuum desiccator

Oven (80 °C)

60 x 15mm style non-pyrogenic polystyrene tissue culture dish lid (Falcon)

iso-propanol (Sigma Aldrich)

Transparent aquarium silicone sealant (Marina)

To produce the soft PDMS piston (B.2.2) needed for confinement, the dimensions of the dish need to be considered. The pillar-height (h_2 Figure

27a.2) has to be 1mm longer than the distance between glass surface and lid (h_1 Figure 27a.1). This guarantees that the exerted force on the two surfaces is in an ideal range. The diameter of the pillar (d Figure 27a.2.) depends on the diameter of the hole and the glass slide used to produce the micropillar coated upper surface. For a 17 mm hole we use pillars of 10 or 12 mm diameter. To produce pillars with the correct dimensions it is advantageous to use an aluminum mold (Le Berre et al., 2014).

1. Mix silicone elastomer and curing reagent in a 30:1 ratio using a planetary centrifugal mixer.
2. Pour mixture in the aluminum mold and degas in a vacuum desiccator until bubbles are completely gone.
3. Bake PDMS for 6 h at 80 °C, then remove soft PDMS pistons carefully using *iso*-propanol.
4. Glue soft PDMS piston (B.2.2) in the middle of the lid of the 60 x 15mm non-pyrogenic polystyrene tissue culture dish using silicone aquarium sealant (Figure 27b).
5. Place micropillar coated, PEG coated cover glass (B.1) with the glass side facing the soft PDMS piston on the piston. The glass sticks to the PDMS without fixation.

3.1.3.3. C. Haptotaxis chamber assembly

3.1.3.3.1. C.1. Cell preparation

DCs are generated from mouse bone marrow according to Lutz *et al.* (Lutz et al., 1999). In this work we will focus on the isolation and enrichment of highly migratory DCs from bone marrow DC cultures.

Required materials:

LPS (Sigma Aldrich)

R10 cell culture medium (GIBCO RPMI medium with 10 % heat inactivated FCS, P/S and Glutamine)

GM-CSF supernatant from hybridoma cell culture

Tissue culture dishes, 15 cm (VWR)

PBS (pH 7.2 without CaCl₂, without MgCl₂, GIBCO)

Table centrifuge

1. Harvest the cell containing supernatant earliest at day 8 of the bone marrow DC culture and concentrate them (5 min at 300 g).
2. Resuspend approximately two million immature DCs in 25 mL 10 % GM-CSF supernatant containing R10 medium. Transfer cell suspension in a 15 cm tissue culture dish.
3. For maturation, stimulate immature DCs by incubation with LPS (200 ng/mL) for at least 6h (or over night) at 37 °C and 5 % CO₂.
4. After maturation, harvest cells containing supernatant without scratching or washing off non-migratory, adhesive DCs and concentrate them (5 min at 300 g).
5. Aspirate LPS containing supernatant thoroughly and resuspend DCs in 1 mL R10. Incubate at 37 °C and 5 % CO₂ for at least 1 h.
6. After chemokine incubation of the lower surface (A.2.), harvest the migratory DCs containing supernatant and centrifuge for 5 min at 300 g. Resuspend in R10 to a concentration of about 4x10⁴ cells/μL.

3.1.3.3.2. C.2. Chamber assembly

Required materials:

Dish with CCL21 patterned surface (A.2.)

Lid with PEG coated micropillars on soft PDMS pillar (B.2.)

Cell suspension (C.1.)

Fabric tape (Tesa, extra power perfect)

1. Aspirate PBS from the dish (A.2.) and add 4 μL of the migratory DC suspension (C.1.) on the marked area. Add 2 mL of R10 to the rim of the plastic dish. Avoid mixing with the cell suspension (Figure 28b).
2. Aspirate PBS from the PDMS micropillars (B.2.) and add 4 μL of the migratory DC suspension (C.1.) (Figure 28b).

3. Lower the lid quickly, but in a parallel fashion onto the dish. Hold the soft pillar pressed down onto the patterned coverslip without creating shear stress. The lid should now touch the rim of the dish, closing it completely (Figure 28c and Figure 28d).
4. Fix lid on dish with stripes of fabric tape. Lid and dish should stay in touch and the soft PDMS pillar should visibly be compressed to connect the micropillars (upper surface) on the cover glass (lower surface). Always place tape at opposite sites to generate homogenous pressure on the micropillars (Figure 28e).
5. Carefully shake the dish to wet the micropillars with the previously added R10 (Figure 28f).
6. Image at 37 °C and 5 % CO₂

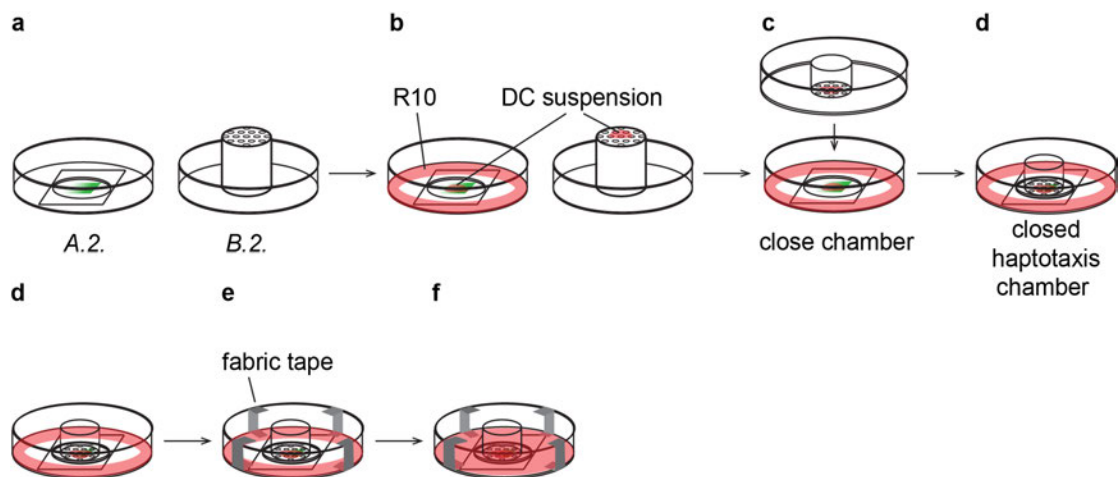


Figure 28.: Haptotaxis chamber assembly. A) Glass-bottom dish with CCL21 24-98 bio patterned surface (A.2) and lid with PEG coated micropillars on soft PDMS piston (B.2). B) DC suspension is placed on the micro pillars on soft PDMS piston (B.2) and on the gradient patterned area of the glass-bottom dish (A.2). R10 cell culture medium is placed on the rim of the glass-bottom dish (B.2). c) The glass bottom dish is closed to close the chamber. D) Fabric tape is attached to keep the PDMS piston under pressure.

3.1.4. Troubleshooting

The preparation of the assay involves many single manufacturing steps, which lead to the risk of small mistakes hampering success. In this section we will focus on some sensitive parts of the protocol and how to avoid mistakes.

3.1.4.1. *The haptotaxis chamber*

Homogenous confinement is crucial to guarantee similar migration conditions under the whole confinement surface. This is especially important if multiple gradients are imaged. The soft PDMS pistons exert pressure on the lower glass slide and the plastic lid of the dish. This pressure can, if too high, deform one or both of them leading to confinement only at the rim of the micropillar coated slide. Deformation of the lower glass can be avoided by using glass thicker than $190\ \mu\text{m}$ (coverslips thicker than #1.5). Replacement of the thin plastic lid by a thicker and more rigid plastic or glass lid can improve confinement homogeneity as well.

In some cases medium or air bubbles can be stuck between both surfaces, preventing proper confinement. Gentle tapping with a pen or tweezers on the lower glass of the freshly confined chamber can remove the excessive air/medium.

PEG coating of the micropillars is important to avoid cell attachment to the upper, not chemokine functionalized surface. In our protocol we advise using PLL-PEG although it can be toxic for the cells if present at high concentrations in cell suspensions. Therefore careful washing of the PEG coated micropillars is recommended.

3.1.4.2. *Cell treatment*

A high quality of cells is essential for optimal migration behavior in the haptotaxis chamber. To guarantee stable conditions and to minimize cell

heterogeneity it is advantageous to use cells that have been frozen at day 8 of the bone marrow culture.

After maturation it is crucial to remove all the LPS containing media and recover the cells for at least 1 h in fresh R10 and at high cell number. Recovery periods longer than 4 h reduce viability.

Depending on micropillar height, the volume between both surfaces is rather small and medium exchange with the surrounding medium reservoir is limited. If cell number is too high, toxic metabolites can harm the cells and influence their migration. Ideal cell numbers are dependent on the quality of the bone marrow culture and need to be titrated.

3.1.4.3. LAPAP/chemokine presentation

Upon CCL21 encounter, DCs start to spread their lamellipodium on the surface, adapting a “fried egg” like morphology. Stressed cells however contract and retract their protrusions. If cells contract instead of spreading after confinement, exchange all LAPAP reagents. B4F and SA-Cy3 decompose after a few months at 4 °C.

The success of the chemokine immobilization can be evaluated by antibody staining of the immobilized CCL21 (mouse CCL21 antibody; R&D, 10 µg/mL, 1 h at rt). Even without a background block, the unspecific binding of truncated CCL21 to the PDMS surface is extremely low. However, to evaluate background levels, antibody staining of each batch of coverslips is recommended. Proper cleaning of the slides is necessary if glass slides without PDMS coating are used.

For immobilization, the chemokine needs to have a biotin tag. Considering the size of the chemokine (~12 kDa) versus streptavidin (~50 kDa) it is beneficial to introduce a short PEG spacer between chemokine and the streptavidin binding

biotin tag. Furthermore, monobiotinylation can increase the chemokine concentration on the streptavidin pattern.

3.1.5. Perspectives

LAPAP enables printing of chemokine patterns of arbitrary shape and intensity on a wide range of surface coatings. This opens a plethora of new possibilities to the field of haptotaxis, but also chemotaxis. With LAPAP not only defined gradients can be generated. The ability to create sharp borders allows the printing of even more complex patterns like staircase functions or sudden steps in gradients enabling to address fundamental mechanisms like cellular memory or polarization. The ability to immobilize guidance cues to many surface coatings opens up new perspectives on the role of adhesion during haptotaxis. Our haptotaxis assay was not only established to satisfy the requirements of DC haptotaxis. CCL19-biotin, CCL21-biotin or CXCL12-biotin patterns allow us to probe the migratory behavior of naïve or activated CD4⁺ T-cells. Using other biotinylated ligands allows to employ other types of leukocytes. For example immobilization of biotinylated fMLP is suited to test the haptotactic guidance of granulocytes, which is well explored in the chemotactic regime.

3.1.6. Acknowledgements

This work was supported by the Boehringer Ingelheim Fonds, the European Research Council (ERC StG 281556) and a START Award of the Austrian Science Foundation (FWF). We thank Robert Hauschild, Anne Reversat and Jack Merrin for valuable input and the Imaging Facility of IST Austria for excellent support.

3.1.7. Author contributions

M.S. and J.S. initiated and designed the project. J.S. established the assay; J.S. and M.S. wrote the manuscript.

3.2. Dendritic cells interpret interstitial CCL21 gradients in a signal-to-noise ratio governed, GRK6 dependent manner.

Jan Schwarz¹, Veronika Bierbaum¹, Kari Vaathomeri^{1,2}, Robert Hauschild¹, Marcus Brown³, Alexander Leithner¹, Anne Reversat¹, Teresa Tarrant⁴, Tobias Bollenbach¹, Michael Sixt¹

¹*Institute of Science and Technology Austria (IST Austria), Klosterneuburg, Austria.*

²*Wihuri Research Institute, Translational cancer biology program, Helsinki, Finland.*

³*Medizinische Universität Wien, Vienna, Austria.*

⁴*Thurston Arthritis Research Center, Department of Medicine, Division of Rheumatology, Allergy and Immunology, University of North Carolina School of Medicine, Chapel Hill, USA.*

- in preparation -

3.2.1. Abstract

Haptotactic dendritic cell (DC) guidance by gradients of tissue bound chemokine (CCL21) represents a rate-limiting step in adaptive immune response. Although experimentally confirmed *in vivo*, the mechanisms underlying immobilized CCL21 gradient sensing remain elusive. Here, we use an *in vitro* system allowing for precise control of CCL21 immobilization to analyze haptotactic behavior of DCs in a quantitative manner.

We find haptotactic sensing to be dependent on the absolute CCL21 concentration and the local steepness of the gradient, a scenario in which DC directionality is governed by the signal-to-noise ratio of CCL21 binding to its receptor CCR7. Moreover, we observe that those conditions are perfectly matched by the gradient provided *in vivo*. Furthermore, we find CCR7 signal termination by the G-protein coupled receptor kinase 6 (GRK6) to be crucial for

haptotactic CCL21 gradient sensing *in vitro* and confirm those observations *in vivo*. These findings suggest that stable, tissue bound CCL21 gradients act as sustainable 'roads' to ensure optimal guidance *in vivo*.

3.2.2. Introduction

The concept of cell guidance by substrate immobilized guidance cues, such as chemokines, is termed haptotaxis (Carter, 1967; Middleton et al., 1997; Weber et al., 2013). It allows for effective cell guidance at sites where diffusive gradients can't be maintained, are disadvantageous or where gradients need to be stable and maintained without external stimuli (Middleton et al., 1997; Russo et al., 2016; Sarris et al., 2012; Weber et al., 2013). Accordingly, DC migration towards the lymphatic vessel (LV) is guided by a haptotactic gradient of the chemokine CCL21. Secreted by lymphatic endothelial cells, CCL21 is retained by charged components of the interstitium thereby forming a stable, immobilized gradient decaying from the LVs (de Paz et al., 2007; Weber et al., 2013). Stimulated by pathogens or danger signals in the periphery, DCs use those stable 'routes' to efficiently find LVs, enter them and eventually instruct naïve T-cells in the parenchyma after reaching the draining lymph node (Mellman and Steinman, 2001). Whereas haptotactic migration is guided by tissue immobilized CCL21, migration in the lymph node is partially instructed by soluble CCL19 (Luther et al., 2002). Both chemokines bind the same receptor, CCR7 and promote differential desensitization after ligation. CCR7 desensitization is mediated by two G-protein couple kinases (GRKs) GRK 3 and -6. CCL19 induces GRK3 and -6 activation and rapid β -arrestin2 dependent CCR7 internalization (Byers et al., 2008; Otero et al., 2006). Therefore, CCL19 signals lead to rapid receptor recycling and allow for signal adaption (Byers et al., 2008; Kohout and Lefkowitz, 2003; Otero et al., 2006; Zidar et al., 2009). CCL21, usually presented in an immobilized fashion, induces GRK6 binding of CCR7, blocking further heterotrimeric G-protein activation. CCL21 induced GRK6 binding does not lead to CCR7 internalization and thereby is terminating GPCR signaling without the possibility to adapt (Kohout et al., 2004; Zidar et al.,

2009). Although tissue bound CCL21 induced desensitization is purely GRK6 dependent, its influence on DC haptotaxis has not been addressed yet.

For efficient haptotactic gradient sensing DCs have to detect the surface bound CCL21, interpret the detected spatial signal and evoke a cellular response, e.g. in form of increased adhesion and directional migration (Schumann et al., 2010). Generally, to establish a directional response, cells have to detect a concentration difference across their cell diameter. Hereof, Berg and Purcell have formulated theoretical limits (Berg and Purcell, 1977). Recently, those limits have been extended to explicitly include receptor-binding (Bialek and Setayeshgar, 2005; Kaizu et al., 2014; Rappel and Levine, 2008). By observing gradient-induced chemotactic responses *in vitro*, models based on detection of a spatially varying concentration by differential receptor binding could be evaluated (Amselem et al., 2012; Mortimer et al., 2009). Using similar *in vitro* systems, chemotactic interpretation models have been developed to explain how cells integrate signals into directional response and how signal differences on a receptor level lead to cell polarization and directed migration (Arriemerlou and Meyer, 2005; Iglesias and Devreotes, 2008). Although several *in vitro* systems for immobilized gradient generation have been established (Ricoult et al., 2015), chemokine guided haptotaxis has not been addressed quantitatively.

In this study, we use an *in vitro* system allowing for precise control of CCL21 immobilization while offering optimal DC migration conditions, to address how DCs detect haptotactic gradients of CCL21 (Schwarz and Sixt, 2016). We quantitatively assess the influence of different gradient properties such as steepness, functional form and total CCL21 concentration on DC haptotaxis *in vitro* and show that absolute CCL21 concentration and local steepness of the gradient generate a spatial signal whose quality is reflected by DC directionality and velocity. Furthermore, haptotactic CCL21 gradients found *in vivo* comply those quality prerequisites. Moreover, we address how CCR7 signal termination by GRK6 influences haptotactic gradient sensing and find DC haptotaxis being GRK6 dependent *in vitro* and in an *in vivo* model.

3.2.3. Results

3.2.3.1. *Characterization of immobilized CCL21 gradients in vivo*

Immunofluorescence data of the endogenous CCL21 distribution in the dermal interstitium of explanted mouse ears showed gradients of tissue immobilized CCL21 steeply decaying from the lymphatic vessels (Weber et al., 2013). To understand gradient shape and chemokine concentration dependency for DC haptotaxis, we quantified the CCL21 distribution within the perilymphatic interstitium and found similar gradient shapes in all analyzed dermal explants (Figure 29A-E). To this end, ear preparations of membrane labeled mice (mTmG) were enhanced for lymphatic vessels by staining of the lymphatic vessel endothelial hyaluronan receptor 1 (LYVE-1, Figure 29A) and murine CCL21 (Figure 29B).

The CCL21 staining showed a diffusive distribution of CCL21 associated with lymphatic vessels, but excluding blood vessels (Figure 29C), and cellular accumulations near lymphatic vessels (Figure 29B). As observed earlier (Weber et al., 2013), interstitial CCL21 concentration decreased with distance from the lymphatic vessels. Quantification of the CCL21 signal decay starting at the edge of each vessel revealed a non-linear gradient of CCL21 *in vivo* (Figure 29E). The normalized concentration of CCL21 could be fitted with an exponential function of the form $c_0 + a \cdot \exp(-x/\delta)$, where c_0 is the background concentration originating from unspecific background staining or detector offset, δ is a decay length and a the maximal concentration of bound chemokine, to a decay length $\delta = 54.3 \pm 2.8 \mu\text{m}$ (Figure 29E).

3.2.3.2. *Haptotaxis Assay*

In order to understand how DCs follow those tissue immobilized, haptotactic CCL21 gradients we sought to mimic haptotactic migration conditions *in vitro*. Gradient shape or absolute CCL21 concentration can't be altered easily in an *in vivo* setup. Micro-patterning, however allows the generation of arbitrary shapes and gradients *in vitro*.

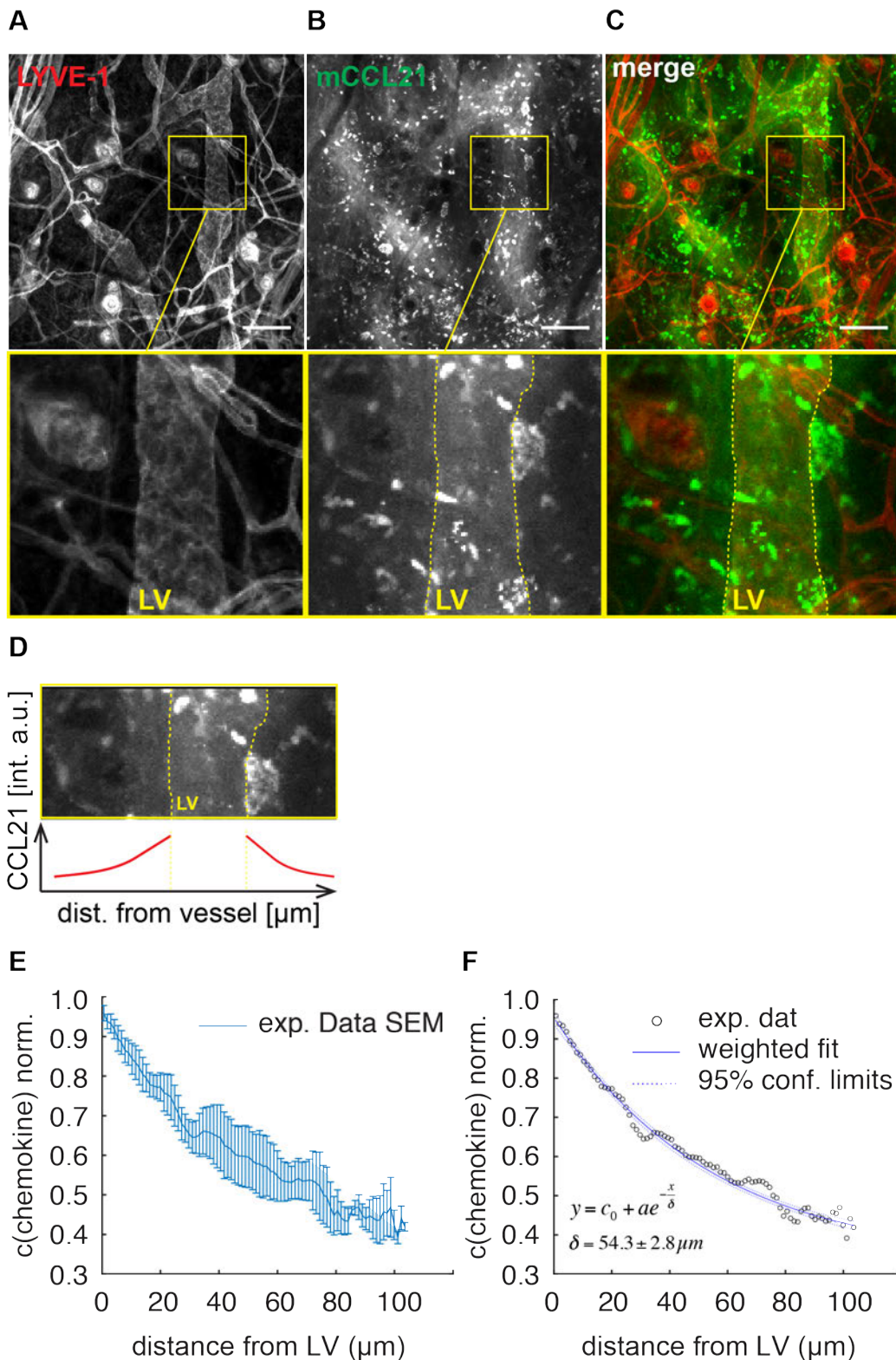


Figure 29.: Visualization and quantification of the interstitial CCL21 gradient. A) – C) CCL21 distribution in mouse ear dermal explants. Z-projections of explanted ear dermis of membrane labeled mice (mTmG) stained for lymphatic vessels (LYVE-1, A) and CCL21 (anti-mCCL21 ,B). Overlay (merge, C). Areas in the yellow boxes are enlarged and the borders of the lymphatic vessels indicated by dotted, yellow lines. Scale bar 100 μm . D) – F) Quantification of the interstitial CCL21 gradient. D) Schematic of CCL21 quantification.. CCL21 staining intensities were averaged as a function of distance from the lymphatic vessels (yellow, dotted lines). E) Normalized intensities of CCL21 stainings plotted against the distance from the lymphatic

vessel (SEM, n = 4). F) Fit of an exponential decay to the experimentally acquired data shown in (E) with background signal c_0 , and decay length $\delta = 54.3 \pm 2.8 \mu\text{m}$.

To be able to migrate with high velocity in a packed cellular environment, migratory DCs adhere only weakly and rather migrate in a contraction and protrusion governed manner (Lämmermann et al., 2008). However, high concentrations of CCL21 induce β_2 integrin dependent adhesion and migration (Schumann et al., 2010) whereas in the presence of low CCL21 concentrations, DCs detach after a short global adhesion phase and switch to short-lived, local adhesions which allow for rapid migration. The migration of DCs can thus be probed in either a 3D environment that consists of an extracellular matrix (Lämmermann et al., 2008), or by exploiting physical confinement that promotes DC migration and allows the examination of haptotaxis for low concentrations of CCL21 (Le Berre et al., 2014).

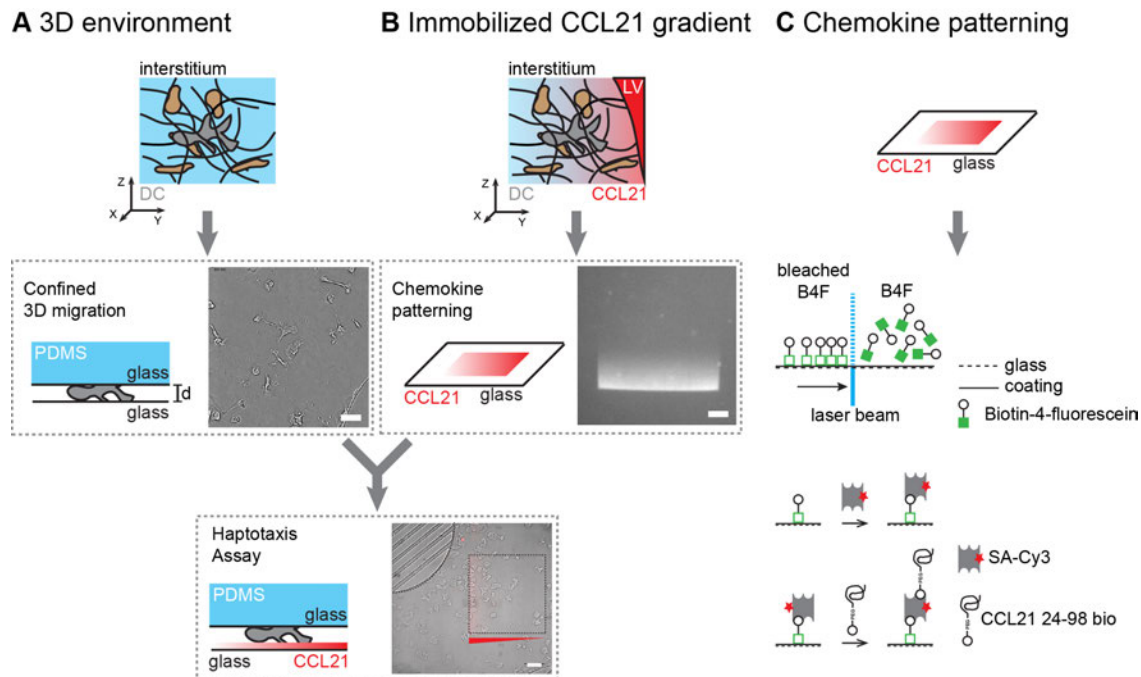


Figure 30.: Haptotaxis assay. A) and B) Confining dendritic cells on surface immobilized gradients of CCL21 (Haptotaxis assay). A) 3D environment: Conditions of interstitial 3D migration are mimicked by physical confinement of dendritic cells between two glass surfaces with distance d . B) Immobilized CCL21 gradient: Haptotactic, immobilized CCL21 gradient is created by chemokine patterning. Scale bar $50 \mu\text{m}$.

C) Schematics of chemokine patterning. Biotin-4-fluorescein (B4F) is surface immobilized by laser assisted photobleaching. CCL21 24-98 bio is surface immobilized on the B4F gradient via dye labeled streptavidin (SA-Cy3).

Through confinement of DCs on defined immobilized gradients of CCL21, we created an assay allowing us to test for haptotaxis of DCs in a highly controlled fashion (Schwarz and Sixt, 2016). To allow for 3D type migration as in the interstitium, cells were confined between two glass slides with a defined spacing of 4 μm (Figure 30A) (Le Berre et al., 2014). Confinement only was enough to induce random migration of mature DCs (Figure 32E, R10). In order to mimic the tissue immobilized haptotactic gradient of CCL21 (Figure 30B), we used a photo-immobilization technique which allows the generation of homogenous surface immobilized gradients and digital patterns (Figure 30C) (Schwarz and Sixt, 2016). Specifically, using a steerable ultra violet (UV) laser ($\lambda = 355 \text{ nm}$) with adjustable intensity, gradients of biotinylated fluorescein (B4F) were immobilized on polydimethylsiloxane (PDMS) coated glass slides in an additive manner (Holden and Cremer, 2003). Therefore, background adhesiveness is identical for patterned and non-patterned regions excluding signal differences originating from integrin ligands (King et al., 2016). Subsequently, biotinylated CCL21 was attached to the immobilized biotin gradients in a bioactive state via streptavidin (SA) (Figure 30C). Visualization of gradient location and properties without interfering with the receptor binding affinity of the immobilized CCL21 was achieved by using dye labeled streptavidin (SA-Cy3). To avoid unspecific binding of CCL21 to non-patterned regions, we decided to use a truncated, biotinylated version of CCL21 (CCL21 24-98 bio) that is lacking the highly charged c-terminal extension responsible for heparan sulfate binding *in vivo* (Weber et al., 2013). The truncated, biotinylated version of CCL21 was chemotactically functional and exhibited similar chemotactic activity in a 3D chemotaxis assay compared to full length CCL21 (Supplemental Figure 1).

Antibody staining against CCL21 confirmed the successful immobilization of CCL21 24-98 bio on the PDMS surface (Figure 31A). To quantify the efficiency of CCL21 24-98 bio surface deposition, we used a fluorescently labeled version of the biotinylated chemokine and compared the gradient intensity with fluorescence intensities of titrated concentrations (Figure 31B and C). In the haptotaxis assays, we have maximal concentrations of

immobilized CCL21 24-98 bio of 180 ± 58 molecules/ μm^2 including a background of 5 ± 2 molecules/ μm^2 (Figure 31C).

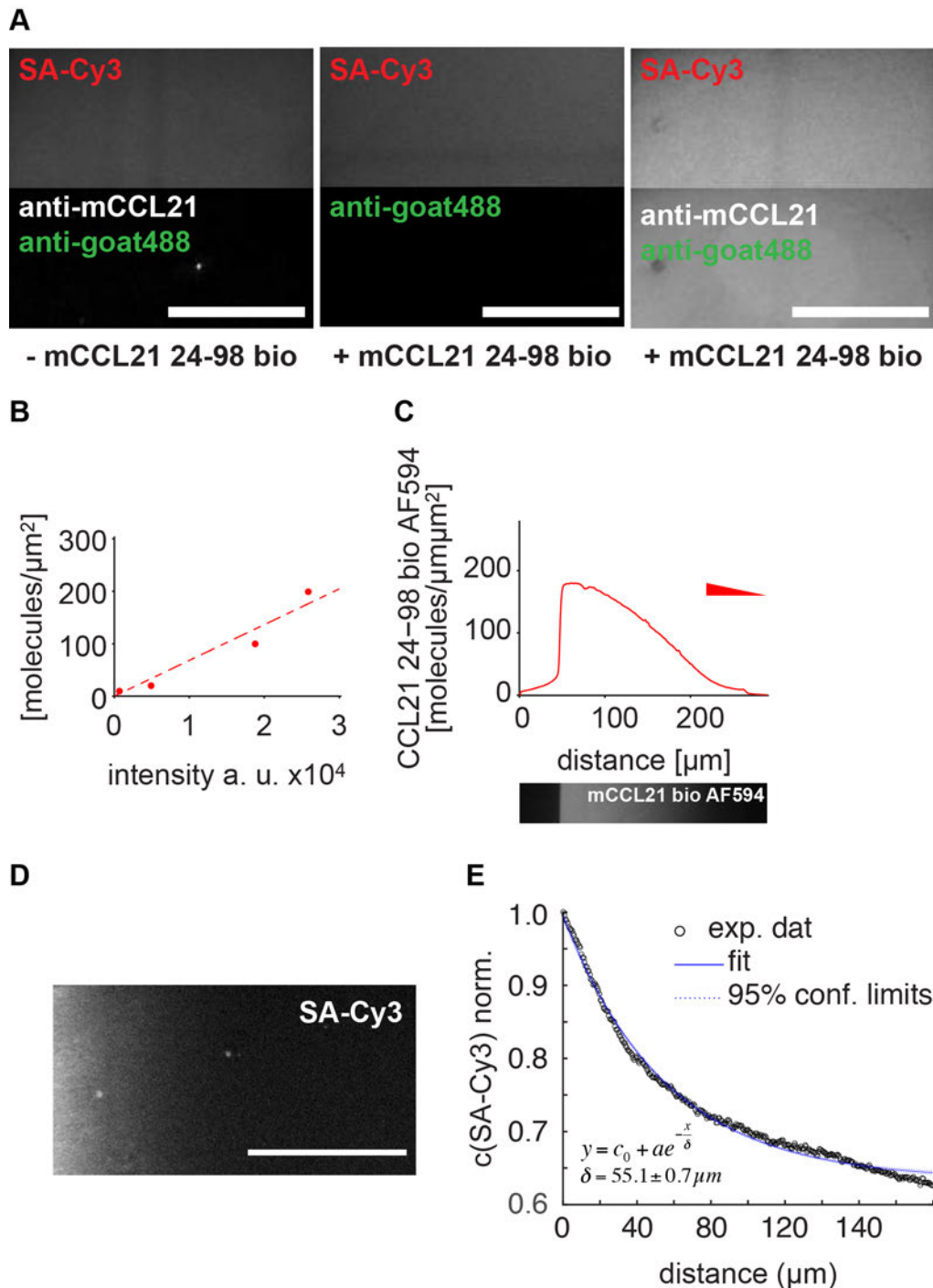


Figure 31.: Analysis of surface immobilized CCL21 24-98 bio and *in vitro* reconstruction of the interstitial CCL21 gradient. A) Visualization of CCL21 24-98 bio bound to surface immobilized B4F via dye labeled streptavidin (SA-Cy3). Left panel: B4F/SA-Cy3 only; no unspecific binding of the anti-CCL21 and 2nd antibody. Middle panel: B4F/SA-Cy3/CCL21 24-98 bio; no unspecific binding of the 2nd antibody. Right panel: B4F/SA-Cy3/CCL21 24-98 bio; specific binding of the anti-CCL21 and 2nd antibody to surface immobilized CCL21 24-98 bio. Scale bar 50 μm . B) and C) Quantification of surface immobilized chemokine using AF594 labeled CCL21 24-98 bio. B) Fluorescence intensity of different concentrations of CCL21 24-98 bio AF594 solution. C) Quantification of surface immobilized CCL21 24-98 bio AF594; c_{MAX} (CCL21 24-98 bio

AF594) = 180 ± 58 molecules/ μm^2 , background = 5 ± 2 molecules/ μm^2 D) and E) *In vitro* reconstruction of the interstitial CCL21 gradient measured *in vivo* (Figure 29). D) SA-Cy3 image of the patterned gradient. Scale bar 100 μm . E) Fit of an exponential decay to the printed gradient (D). Background signal c_0 , and decay length $\delta = 55.1 \pm 0.7 \mu\text{m}$.

Taken together, our assay consists of a confiner with a height of 4 μm that contains arrays of immobilized CCL21 of size 350 x 350 μm . The CCL21 concentrations in these arrays can have any continuous shape in the range of 5 to 180 molecules/ μm^2 .

To reproduce the gradient observed *in vivo* in our *in vitro* assay, we printed an exponential-like SA-Cy3 gradient (Figure 31D) with a function that was modified for technical reasons but lead to a gradient that, with a decay length of $\delta = 55.1 \pm 0.7 \mu\text{m}$, was identical to the one observed *in vivo* in the range of 100 μm , the typical distance for reliable detection of CCL21 *in vivo* (Figure 31E).

The remaining unknown property of the observed exponential interstitial CCL21 gradient in mouse ear explants is the absolute concentration $c_0 + a$ of tissue immobilized CCL21. Hence, we explored exponential gradients with a decay length of roughly 54 μm for different absolute concentrations.

3.2.3.3. Characterization of DC migration in haptotaxis assays

To elucidate the impact of gradient shape and concentration on the recognition of haptotactic CCL21 gradients by DCs, we printed exponential-like (Figure 32A, blue profiles) and linear (green profiles) gradients of CCL21 24-98 bio, using the decay length δ observed *in vivo* in the exponential-like gradients (Figure 29F and Figure 31D and E). We printed both shapes with two types of steepness. In the first type, the maximal concentration of 180 molecules/ μm^2 allowed by the system was set to be the maximum of the gradient, and in the second type, we chose half of this maximal concentration, i.e., 90 molecules/ μm^2 (Figure 32A, Intensities $I = 1$ and $I = \frac{1}{2}$). The shades of the profiles in Figure 32A indicate the standard deviation among different prints ($n \geq 5$, for each gradient type), underlining the high reproducibility of the photo-patterning technique. After cell loading and assembly of the haptotaxis chamber (Figure 30) (Schwarz and Sixt, 2016), we collected trajectories of migrating cells

for times ≥ 100 min (Figure 32B). Cell directionalities and velocities were determined by comparing displacements within trajectories for time steps of 20 s. This timing was chosen because it was the smallest time that should still show a displacement of the cell for most of the steps. Using these intervals, the instantaneous velocity of each cell is then given by the displacement per unit time. The instantaneous directionality or haptotactic index HI of the cell is given by $HI = \cos \theta$, where θ is the angle formed between the current direction of the cell and the direction of the gradient (Figure 32C). Here, we have defined the haptotactic index in analogy to the chemotactic index. An index equal to one, $HI = 1$, represents migration along the direction of the gradient, and $HI = -1$ migration against gradient direction. As we are interested in the alteration of cell migration as a function of the external concentration, we pool all cell tracks according to a given region. This means that each gradient is divided into eight equally spaced bins (Figure 32D). In this way, each bin has a size of $350/8=43 \mu\text{m}$, which corresponds to roughly 1.5 cell diameters. We chose this bin size to account for the fact that DCs tend to reshape continuously and stretch out significantly upon migration. As a consequence, each bin has an average concentration which is determined by the shape of the respective gradient. The overall directionality in a given bin is then given by the average haptotactic index, $\langle HI \rangle$, in that bin across all cell tracks. Average velocities are determined in the same way.

An average $\langle HI \rangle$ close to one indicates high directionality, and a zero average $\langle HI \rangle$ indicates that cells move randomly without any preferred direction. Throughout this paper, we present both average $\langle HI \rangle$ and average cell speeds a function of the corresponding average concentration per bin (Error bars show the standard deviation of the respective average determined by bootstrapping).

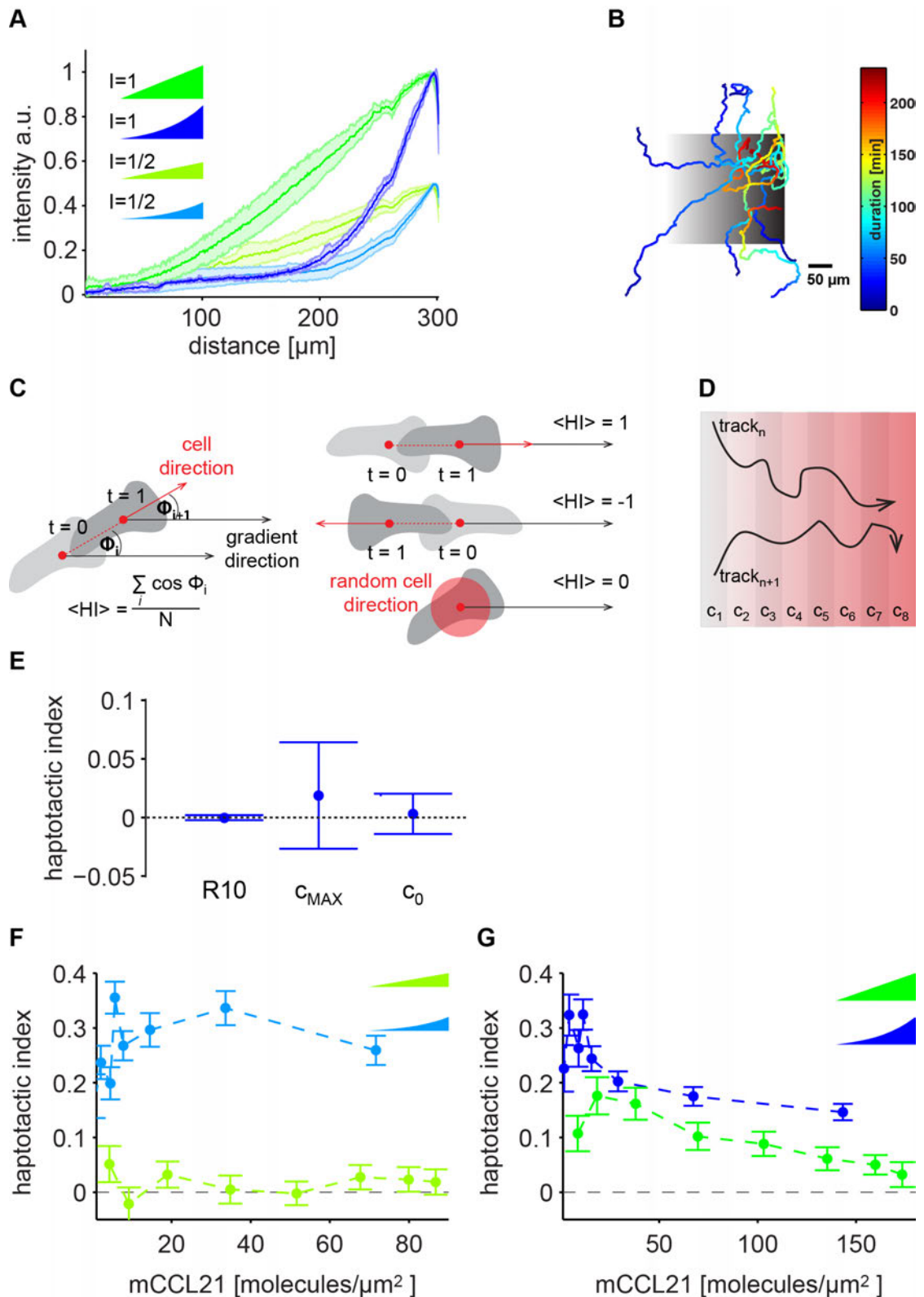


Figure 32.: Analysis of dendritic cell haptotaxis on defined gradients of surface immobilized CCL21. A) Gradient profiles (SA-Cy3 staining) of linear (green profiles) and *in vivo* like, exponential (blue profiles) gradients of CCL21 24-98 bio. $I = 1$ represents maximal printable concentration, $I = \frac{1}{2}$ represents half maximal printable concentration. $n \geq 5$ profiles for each gradient type. B) DC trajectories of a representative experiment of dendritic cells migrating on an $I = \frac{1}{2}$ exponential like gradient of surface immobilized CCL21 24-98 bio. CCL21 24-98 bio gradient indicated in black. Trajectories are color-coded with duration of the track, where blue

represents early times, and red late times. Scale bar 50 μm . C) Schematic of haptotactic index. Analogously to the chemotactic index, the haptotactic index $\langle\text{HI}\rangle$ shown here as an average over one cell trajectory is calculated as an average of the cosines of the angle between cell direction and gradient per time step. $\langle\text{HI}\rangle = 1$ represents perfect migration in direction of gradient, $\langle\text{HI}\rangle = -1$ migration against the gradient direction and $\langle\text{HI}\rangle = 0$ random migration. D) Schematic of cell trajectories (black) on a gradient of CCL21 (red). Cell trajectories in each concentration bin ($c_1 - c_8$, grey bins) were pooled for each gradient- or genotype condition. E) Haptotactic indices $\langle\text{HI}\rangle$ of dendritic cells migrating in the absence of chemokine (R10 cell culture medium), on areas of maximal chemokine deposition (c_{MAX}) or next to areas with chemokine patterns (c_0). Error bars represent bootstraps from resampling 200 times. F) and G) Haptotactic indices of dendritic cells migrating on gradients reaching half maximal CCL21 24-98 bio deposition ($I = 1/2$, F) and maximal CCL21 24-98 bio deposition ($I = 1$, G), with linear gradients in green and exponential like gradients in blue. Each bin ($c_1 - c_8$) of the respective gradients is represented by its mean haptotactic index. Haptotactic indices are shown as a function of the average concentration of each condition within the respective bin. Haptotactic indices are calculated for all trajectories within one condition ($n = 8-19$ independent experiments for each gradient condition)

3.2.3.4. Gradient shape and steepness influences recognition of haptotactic CCL21 gradients

After an initial polarization phase, DCs started to migrate in the haptotaxis chamber. In chambers without immobilized CCL21 24-98 bio (Figure 32E, R10), in chambers offering maximal concentration of homogenous surface immobilized CCL21 24-98 bio (Figure 32E, c_{MAX}) and in areas outside of surface immobilized CCL21 4-98 bio with background concentration c_0 (Figure 32E, c_0) cells migrated randomly showing haptotactic indices of zero within error (Figure 32E). However, cells migrating on a shallow exponential-like gradient (Figure 32A, blue profile with $I = 1/2$) exhibited a high positive haptotactic response throughout the whole gradient (Figure 32F, blue symbols). In contrast, a linear gradient covering the same concentration range (Figure 32A, $I=1/2$, green profile) was not able to induce haptotactic behavior (Figure 32F, green symbols), suggesting that the ability of DCs to perform haptotaxis depends on the shape of the gradient.

In the exponential-like gradients, a significant portion of the gradient falls below concentrations of ~ 10 molecules/ μm^2 of CCL21 24-98 bio which is very close to the background. In these concentrations, cells show a strong haptotactic response, with fluctuations in the data, which are due to the increased variations in the pattern compared to high concentrations. For

concentrations exceeding ~ 30 molecules/ μm^2 , haptotactic response was reduced as the concentration increased (Figure 32F).

Cells on gradients exploring the full range of concentration (Figure 32A, $l=1$), clearly showed directional cell migration for both linear and exponential gradients (Figure 32G). Again, cells on exponential-like gradients showed significantly higher haptotactic response compared to cells migrating on linear gradients. In contrast to the shallow linear gradient ($l = 1/2$), the steep linear gradient ($l = 1$) did induce a haptotactic response also in regimes of low CCL21 24-98 bio concentration. As for shallow gradients (Figure 32F), directionalities did exhibit fluctuations for CCL21 24-98 bio concentrations close to the background. However, exploiting the full range of concentrations, led to curves that decayed smoothly as concentration increased (Figure 32G).

In all cases where cells showed a haptotactic response, cell directionality decreased towards higher concentrations, with concentrations below 40 molecules/ μm^2 leading to the highest directionalities. Our results suggest a strong dependence on gradient shape, with the *in vivo* type exponential gradients leading to overall higher cell directionalities compared to linear gradients. In addition, we find that shallow gradients fall below a threshold of detection if they are linear while recognition is still possible in exponential gradients spanning the same concentration.

3.2.3.5. Dendritic cell haptotaxis reflects signal-to-noise-ratio of immobilized chemokine gradient

The experimentally obtained directionalities indicate a mechanism of CCL21 recognition that depends on both the shape of the gradient and total chemokine concentration. The smooth decay of directionality towards increasing concentrations across the different gradient shapes suggests a root-type scaling with the inverse concentration. We will demonstrate this scaling to be in agreement with the signal-to-noise ratio of CCL21 recognition by its receptor CCR7, the details of which outline in the following:

In order to move directionally, a cell has to recognize the difference in concentration across the cell diameter, a mechanism referred to as spatial

gradient recognition (Berg and Purcell, 1977). This recognition process is mediated through binding of chemokine to the respective receptor with a dissociation constant K (Figure 33A). Under the assumption of equilibrium binding and a fixed number of receptors, the linear and exponential type gradients (Figure 33B, left panel) will result in a given receptor occupancy (Figure 33B, middle panel). The signal that the cell has to interpret to move directionally, in this way, is the average difference of bound receptors across the cell diameter. As activation of CCR7 with CCL21 does not lead to β -arrestin 2 dependent receptor internalization (Zidar et al., 2009), we assume receptor numbers to be constant for each cell. The signal-to-noise ratio (SNR) of signal recognition on the receptor level is given by the average difference in receptor occupancy divided by the variance of this difference. Different profiles will then lead to different SNRs (Figure 33B, right panel). For a homogenous distribution of receptors, the SNR on the receptor level takes a particularly simple form and is given by $\sqrt{K_D R} / 2(K + c) \frac{\Delta c}{\sqrt{c}}$, where K_D is the dissociation constant, R is the total number of receptors, c the concentration, and Δc the difference in concentration across the cell diameter (Ueda and Shibata, 2007).

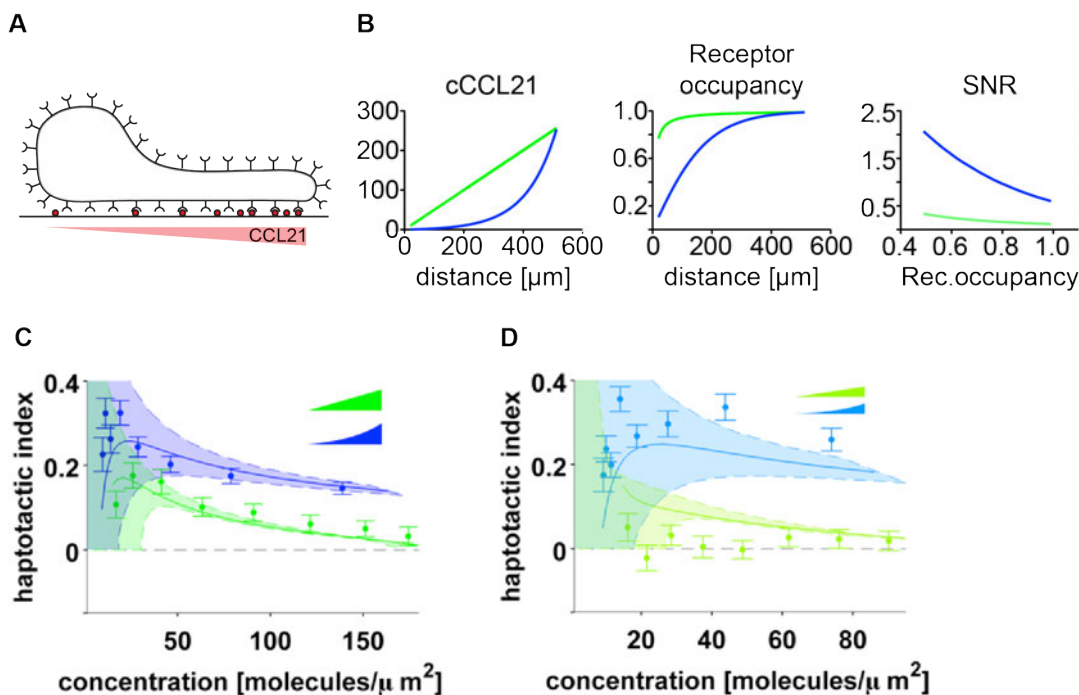


Figure 33.: Dendritic cell haptotaxis reflects SNR of immobilized chemokine gradient. A) Schematic of differential CCL21 binding to CCR7, homogenously distributed over the cell surface. B) Left panel: Linear (green) and exponential like (blue) gradients of CCL21. CCL21

concentration plotted against the location on the respective gradient. Middle panel: Illustration of receptor occupancy plotted against location on the respective gradient for linear (green) and exponential like (blue) gradients assuming equilibrium binding and a fixed number of receptors. Right panel: SNR of signal recognition on receptor level of linear (green) and exponential like (blue) gradients. SNR plotted against the distance of the respective gradient. C) and D) SNR matched to the haptotactic response ($\langle HI \rangle$) of dendritic cells migrating on linear (green) or exponential like (blue) gradients of CCL21 ($l = 1$, C and $l = 1/2$, D). SNR (solid lines) are fitted using a single dissociation constant K_D and different scaling factors (α_{lin} and α_{exp}) for linear and exponential like gradients. Shading indicates variations in the SNR computed from corresponding standard deviations in the gradient profiles (Figure 32).

This simple form of SNR turns out to match the functional behavior of cell directionality (Figure 33C and D), where we compare the SNR (solid lines) with an overall dissociation constant K_D to the cell directionality (symbols) for the different input concentrations from the linear and exponential masks. For comparison of directionality and SNR, we allow for rescaling of the SNR such that $HI = \alpha \cdot SNR$. We have fitted a single dissociation constant $K_D = 0.1$ nM to the data that span the full range of concentration ($l=1$, linear and exponential), albeit allowing for different rescaling factors $\alpha_{exp} = 1$ and $\alpha_{lin} = 0.58$. The results are shown in Figure 33C, where the shading indicates the variation of the fitted SNR with variations of the mask as given by the standard deviation shown in Figure 32C. Our value for K_D is in the range of the values reported previously (Haessler et al., 2011; Sullivan et al., 1999). Figure 33D shows the SNR where we have used the input masks for shallow gradients ($l=1/2$), and have imposed both the dissociation constant and the respective scaling factor from the fits for the steep gradients ($l=1$) onto the SNR. Again, the shading indicates variations in the SNR arising from the corresponding standard deviations in the input masks.

Although the value of the dissociation constant in the data can not be determined accurately due to the high sensitivity of SNR to the input concentrations for concentrations below ~ 30 molecules/ μm^2 , our results agree with various features of a SNR that is based on recognition of CCL21 by the receptor. First, the SNR is higher or equal to the exponential compared to the linear profiles irrespective of the dissociation constant. We clearly observe this behavior throughout the conditions measured. Second, in the limit of $K_D \ll c$, the SNR scales as $\frac{\Delta c}{\sqrt{c^3}}$. The tails of our distributions follow this scaling behavior (Figure 33). Importantly, the ratio of SNRs for different gradient steepness

shows that the SNRs in this limit are proportional as roughly 1 (steep exp): 0.97 (shallow exp): 0.37 (steep lin): 0.18 (shallow lin), with the SNR of the shallow linear gradient being the lowest one. Note that the ratios were evaluated at a concentration of 85 ± 3 molecules/ μm^2 but do not change significantly for concentrations exceeding 50 molecules/ μm^2 . Hence, in a scenario where SNR governs gradient recognition, the shallow linear gradient seems to fall below a threshold of detection.

3.2.3.6. Influence of immobilized CCL21 gradients on cell speed

In order to probe for kinetic effects of surface immobilized gradients of CCL21 in DC haptotaxis, we analyzed the influence of CCL21 on DC velocity. The presence of soluble CCL21 24-98 bio with a concentration comparable to the maximal concentration in the immobilized assays significantly enhanced both cell speed and persistence compared to cells migrating in pure cell culture medium (Figure 34Aa and Supplemental Figure 1D). This result suggests that soluble CCL21 has a chemokinetic effect on mature DC migration.

Surprisingly, this effect does not seem to be present in the case of immobilized CCL21 24-98 bio, at least in the case of cell velocities, where we do not observe such a speeding up. We compared the velocities of cells migrating on patches of homogenous immobilized CCL21 24-98 bio concentrations (c_{MAX}), with cells migrating in the background concentration (c_0 , Figure 34Ab). In both concentrations, cell velocities were comparable to the velocity in cell culture medium only (Figure 34Aa, R10). For DCs migrating on immobilized CCL21 24-98 bio, we are not able to access alterations of persistence, as cell trajectories are not sufficiently long to allow for extraction of persistence.

In assays of immobilized CCL21, cells sped up only when migrating on gradients of CCL21 24-98 bio. In both linear and exponential gradients, cells showed increased cell velocity in regions of low concentrations of CCL21 24-98 bio, while velocities in maximal concentrations was comparable to the case of R10 (Figure 34Ac).

Figure 34B and C show the full dependence of average cell velocity of haptotactic DCs for both steep and shallow gradients. Cells migrating on steep ($l=1$) linear and exponential-like gradients showed highest velocities at low concentration regimes and slowed down towards the maximum of the immobilized CCL21 24-98 bio gradients (Figure 34B).

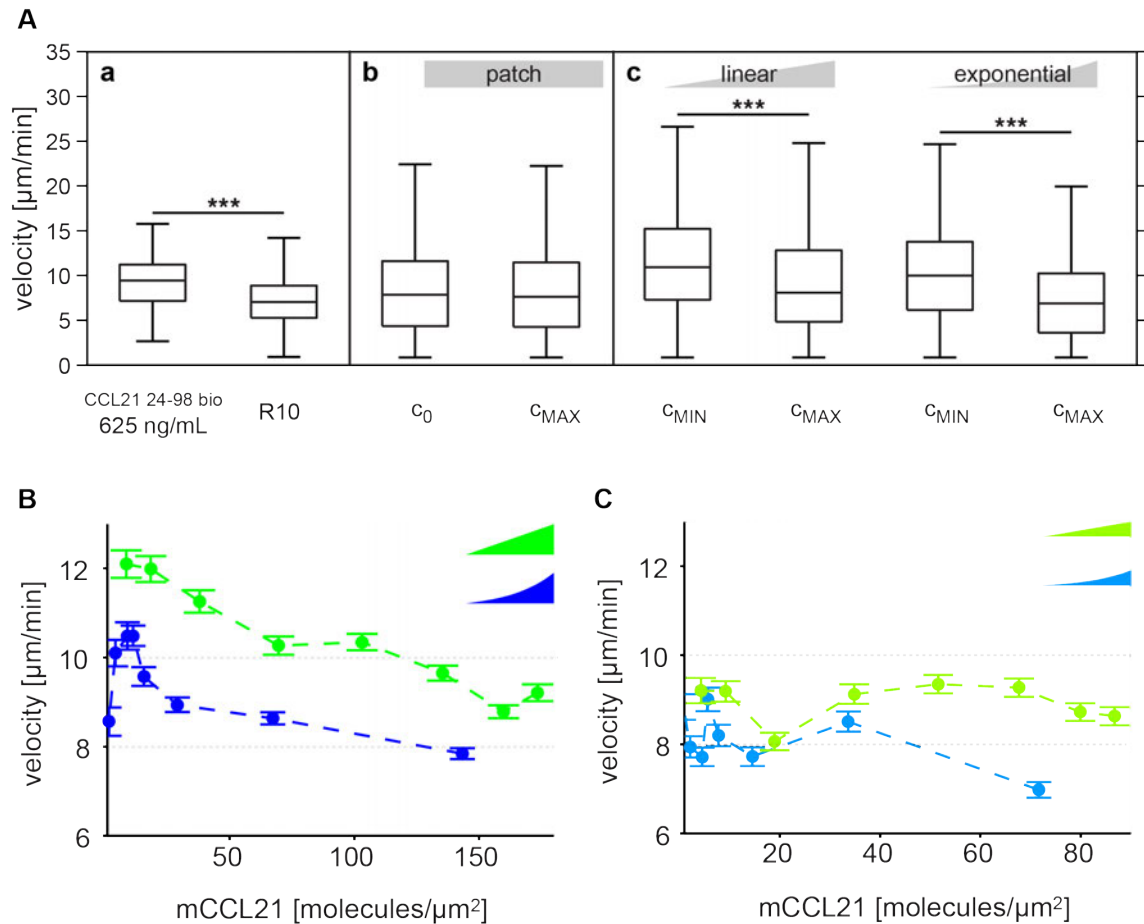


Figure 34.: Influence of immobilized CCL21 gradients on cell speed. A) DC velocities in presence or absence of areas and gradients of CCL21 24-98 bio. a) DC velocities in cell culture medium with (CCL21 24-98 bio, 625 ng/mL) and without CCL21 24-98 bio (R10). b) DC velocities on areas of homogenous surface immobilized CCL21 24-98 bio (maximal CCL21 24-98 bio deposition, c_{MAX}) and next to areas of surface immobilized CCL21 24-98 bio (c_0). c) DC velocities at low concentrations (c_{MIN} , bins c_1 - c_4) and high concentrations (c_{MAX} bins c_5 - c_8) of linear (left graphs) and exponential (right graphs) gradients of surface immobilized CCL21 24-98 bio. B) and C) Average velocities of DCs migrating on gradients reaching maximal CCL21 24-98 bio deposition ($l=1$, B) and half maximal CCL21 24-98 bio deposition ($l=1/2$, C). Linear gradients in green and exponential like gradients in blue. The velocities are shown as a function of the average concentration in each bin ($c_1 - c_8$) for the respective profile ($n=8-19$ independent experiments for each gradient condition).

Cells migrating on shallow ($l=1/2$) linear and exponential-like gradients showed a peak of velocities in a concentration regime of up to 40 molecules/ μm^2 , followed by a second, plateau-type peak with a decay towards higher

concentrations of immobilized CCL21 24-98 bio (Figure 34C). Generally, cells migrating on linear gradients of CCL21 24-98 bio were faster than on exponential-like gradients at similar concentrations (Figure 34B and C). In addition, gradient steepness ($I=1$) seemed to have an enhancing effect on migration velocity for linear but also exponential gradients (Figure 34B and C) compared to shallow gradients ($I=1/2$). The average cell velocity, to some extent, follows cell directionality (Supplemental Figure 2) in the sense that cell velocity in low concentrations is maximal and decreases with increasing concentration in a fashion similar to the haptotactic index (Figure 32F and G). On the other hand, the overall cell velocity is enhanced more in linear gradients compared to exponential ones. To present, we cannot conclude what mechanism drives this connection between cell speed and directionality.

3.2.3.7. *G-protein coupled receptor kinase 6 is important for shallow haptotactic gradient sensing*

The response of DCs to immobilized gradients of CCL21 reflects the quality of signal transduction in a sense that WT DCs with a fully functioning signaling pathway rely on the SNR of bound CCL21 in order to move directionally. In this way, perturbations in the signaling pathway may result in hindrance of haptotaxis, and, as a consequence, an impaired efficiency of reaching the lymphatic capillaries *in vivo*.

G-protein coupled receptor kinases (GRKs) play an important role in signal modulation and desensitization close to the receptor level of the GPCR signaling hierarchy (Kohout and Lefkowitz, 2003). GRK6 hereby was shown to be responsible for CCR7 phosphorylation exclusively after activation by CCL21 (Zidar et al., 2009). In contrast, CCL19 binding of CCR7 led to recruitment of GRK3 and GRK6, leading to completely different signal modulation, including rapid receptor internalization (Byers et al., 2008; Zidar et al., 2009). GRK6 dependent CCR7 phosphorylation therefore is a promising candidate for perturbing CCL21 induced CCR7 signaling and gradient sensing characteristics. Therefore, we analyzed directionalities and velocities of DCs lacking the G-protein coupled receptor kinase GRK6^{-/-}.

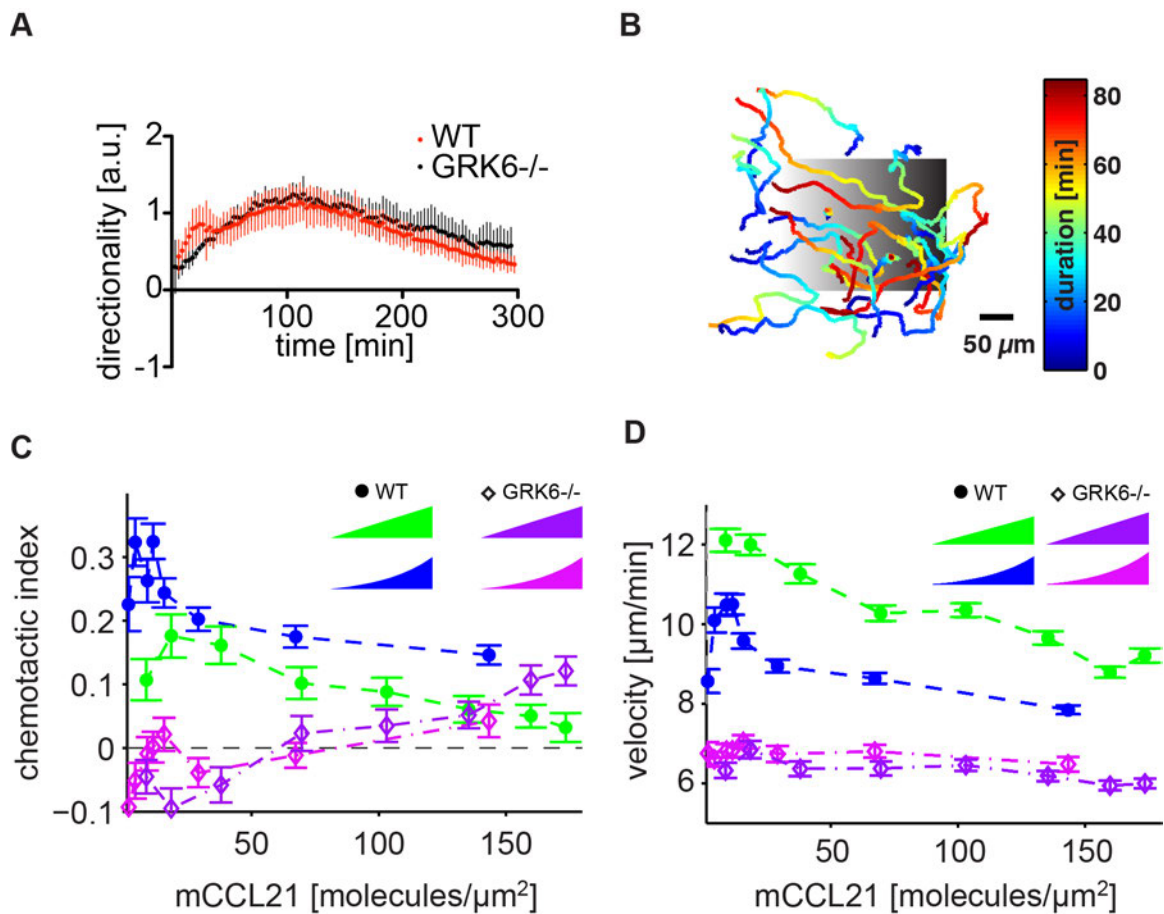


Figure 35.: CCL21 guided DC haptotaxis is GRK6 dependent *in vitro*. A) Collagen gel based chemotaxis assay. Average directionality of WT (red) and GRK6^{-/-} (black) dendritic cells towards a diffusion generated gradient of CCL21 24-98 bio plotted against the corresponding time (n = 9 independent experiments; frame rate 3 min). B) DC trajectories of a representative experiment of GRK6^{-/-} dendritic cells migrating on an exponential like (I=1) gradient of surface immobilized CCL21 24-98 bio. CCL21 24-98 bio gradient indicated in black. Trajectories are color-coded for duration, with early times in blue and late times in red. Scale bar 50 μm . C) – D) Haptotactic indices (C) and average velocities (D) of WT (dots, blue and green) and GRK6^{-/-} (diamonds, purple and pink) of dendritic cells migrating on linear (green and purple) and exponential like (blue and pink) gradients (I = 1) of CCL21 24-98 bio. The haptotactic indices (B) and velocities (C) are shown as a function of the average concentration in each bin ($c_1 - c_8$) for the respective profile (n=8-19 independent experiments for each gradient condition).

Surprisingly, GRK6^{-/-} DCs did not show any impairment in their ability to chemotax when exposed to soluble (diffusion generated) gradients of CCL21 24-98 bio (Figure 35A). However, when exposed to an immobilized, haptotactic gradient covering similar concentrations of CCL21, GRK6^{-/-} cells showed a severe decline in directionality (Figure 35B and C) and velocity (Figure 35D) compared to wild type cells. For most concentrations, GRK6^{-/-}

cells did not exhibit any directionality in neither linear nor exponential-like gradients (Figure 35C). Directional sensing of GRK6^{-/-} DCs on both gradients was partially restored in high concentrations, reaching directionalities comparable to wild type cells at similar concentrations (Figure 35C). GRK6^{-/-} cells migrated more slowly than wild type cells over the entire range of concentration in both the linear and exponential gradients (Figure 32A, I=1). In contrast to wild type cells, the velocities of GRK6^{-/-} DCs did not differ on linear and exponential gradients and remained almost constant throughout the entire range of concentration (Figure 35D).

Our *in vitro* results from observing haptotactic GRK6^{-/-} DCs suggest that signaling precision, facilitated by receptor desensitization is crucial for interpretation of static, immobilized gradients, however is negligible for chemotaxis or cell migration as such. GRK6^{-/-} cells migrating on immobilized gradients of CCL21 24-98 bio do not move directionally over a wide range of concentrations. The recognition of CCL21 24-98 bio seems, at least partially, to be shifted to higher absolute concentrations of CCL21 24-98 bio.

3.2.3.8. *G-protein coupled receptor kinase 6 is important for shallow haptotactic gradient sensing in vivo.*

To test our *in vitro* finding in an *in vivo* environment, we used dermal explants of split mouse ears and added labeled, exogenous DCs on the exposed dermal tissue bearing endogenous haptotactic CCL21 gradients. The exposed CCL21 gradient induced invasion of DCs into the dermal interstitium and after 20 min cells that didn't enter the interstitium were washed away (Scheme Figure 36D). After additional time that allowed for further interstitial migration towards the lymphatic vessel, the explants were analyzed.

After the initial invasion step, less GRK6^{-/-} cells entered the ear explants compared to WT DCs (Figure 36A, B and E). Furthermore, GRK6^{-/-} DCs were located closer to the lymphatic vessels than WT DCs, in regions where the endogenous CCL21 concentration is higher (Figure 36F, 35 min and Figure 29A - E). Moreover, at early time points GRK6^{-/-} DCs showed similar alignment with lymphatic vessels as WT cells (Figure 36G, 35 min), suggesting a similarly

random cell distribution for GRK6^{-/-} and WT DCs in CCL21 presenting areas. As shown under *in vitro* conditions, DCs lacking GRK6 did not react directionally to low

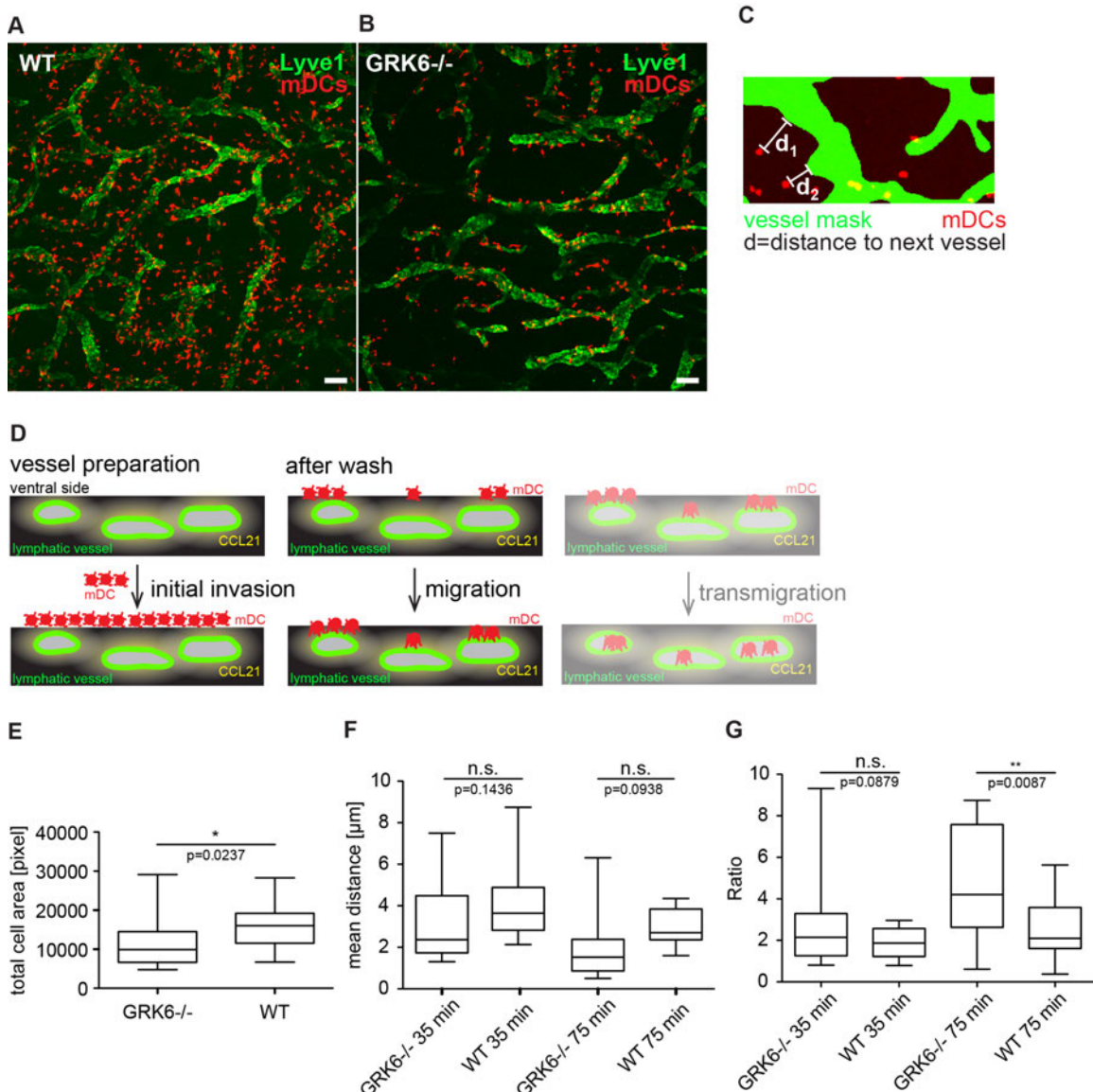


Figure 36.: DC haptotaxis on *in vivo* CCL21 gradients is GRK6 dependent. A) and B) Z-stack projections of DCs (red) and lymphatic vessel immunostaining (green) after a 35 min co-incubation of DCs with mouse ear dermal explants. A) WT DCs and B) GRK6^{-/-} DCs. Scale bar 100 µm. C) Schematic of dermal explant analysis. Lymphatic vessels (LV) are represented by binary masks (vessel mask). DC numbers are determined by red and yellow pixel counts (total cell area). DC distances to the next vessel measured as distances of each red pixel to the respective vessel mask. Cells aligned to vessels (yellow) are excluded. Cell alignment with lymphatic vessels calculated as ratio of cells inside LV compared to an image with the LV rotated by 90° (this value is ~1 if the cell distribution is random. The value is high if the cells localize very well to the vessel). D) Schematic of *in vivo* adhesion and crawl in assay. Left panel: DC suspension is incubated on mouse ear dermal explants with exposed LV and CCL21 gradients. Middle panel: DCs adhere and invade tissue in a CCL21 dependent manner (Tal et al., 2011; Weber et al., 2013). Right panel: DCs reaching LV transmigrate into the vessel. E) Number of adhering and tissue entering WT (n = 21 analyzed regions of ear explants) of n ≥ 4

mice) and GRK6^{-/-} (n = 18 analyzed regions of ear explants of n \geq 4 mice) DCs after 20 min of incubation with mouse ear dermal explants. Cell number is presented as total cell area. F) Average distance of WT and GRK6^{-/-} DCs to the next LV after 35 min (WT n = 13, GRK6^{-/-} n = 13 regions of ear explants of n \geq 4 mice) or 75 min (WT n = 13, GRK6^{-/-} n = 10 regions of ear explants of n \geq 4 mice) of incubation with mouse ear dermal explants. G) Alignment (ratio see C) of WT and GRK6^{-/-} DCs with LVs after 35 min (WT n = 13, GRK6^{-/-} n = 13 regions of ear explants of n \geq 4 mice) or 75 min (WT n = 13, GRK6^{-/-} n = 10 regions of ear explants of n \geq 4 mice) of incubation with mouse ear dermal explants. Ratios \gg 1 represent high alignment with vessels.

endogenous CCL21 concentrations resulting in invasion into the explanted dermal interstitium only in areas close to the source of chemokine secretion.

In vitro, at homogenous concentrations of CCL21, the CCL21 induced adhesion of GRK6^{-/-} DCs to a cell culture dish was similarly efficient as that of WT DCs (Supplemental Figure 1F) suggesting that perturbed directional sensing is responsible for impaired invasion in areas presenting low concentrations of CCL21. After 75 min, both GRK6^{-/-} and WT DCs were localized closer to the lymphatic vessels than after 35 min and both showed similar migration towards the lymphatic vessels (Figure 36F and Supplemental Figure 4F). However, significantly more GRK6^{-/-} were aligned with the lymphatic vessels after 75 min of migration (Figure 36G). Consequently, in high CCL21 concentrations, as found close to the CCL21 secreting lymphatic endothelial cells, GRK6^{-/-} DCs managed to migrate towards the lymphatic vessels as well as WT cells. Starting closer, more GRK6^{-/-} DCs manage to align with the lymphatic vessels than WT DCs starting further away. Once GRK6^{-/-} DCs reached the LV we could not detect any difference regarding their ability to transmigrate into the vessel and subsequently reach the lymph node (Supplemental Figure 3).

Taken together, our *in vitro* and *in vivo* results suggest that DCs lacking GRK6 are not able to react on shallow immobilized CCL21 gradients, but react directionally to high concentration gradients of immobilized CCL21.

3.2.4. Discussion

In this paper, we have set up *in vitro* haptotactic environments with different shapes to probe for the properties of mature DC migration guided by surface-immobilized CCL21. By analysis of hundreds of cell trajectories in different gradients of CCL21, we determined the directionality of the cells, their

corresponding speed, and the dependence of these quantities on the corresponding gradient profile. Our experiments show that cells are most directional in concentration profiles that resemble those observed in vivo, with exponentially varying concentrations of CCL21 (Figure 32F and G). Recognition of linearly rising concentrations is possible as long as the rise of the concentration exceeds a given threshold. In all cases where cells recognize the gradient, low concentrations of CCL21 lead to higher directionality as opposed to high ones.

These observations are consistent with a scenario where the SNR of gradient detection on the receptor level governs cell directionality (Figure 33C and D). In other words, DC directionality reflects the quality of the signal, which poses a limit to haptotaxis irrespective of the specific mechanism of signal integration. What we cannot quantify here is the extent to which the SNR is influenced by intrinsic noise further downstream the signaling cascade. While a SNR including second messenger dynamics has been discussed for *D. discoideum* (Amselem et al., 2012), the corresponding numbers are not available for DCs. Our experiments provide strong evidence that cells interpret the concentration difference incorporated by the difference in bound receptors at the front and the back of the cell, an assumption exploited by many models of signal recognition in chemotaxis (Bagorda and Parent, 2008). The mechanisms cells possibly exploit to interpret the difference in bound receptors has been discussed theoretically but not fully clarified experimentally (Arriemerlou and Meyer, 2005; Iglesias and Devreotes, 2008; Swaney et al., 2010; Xiong et al., 2010).

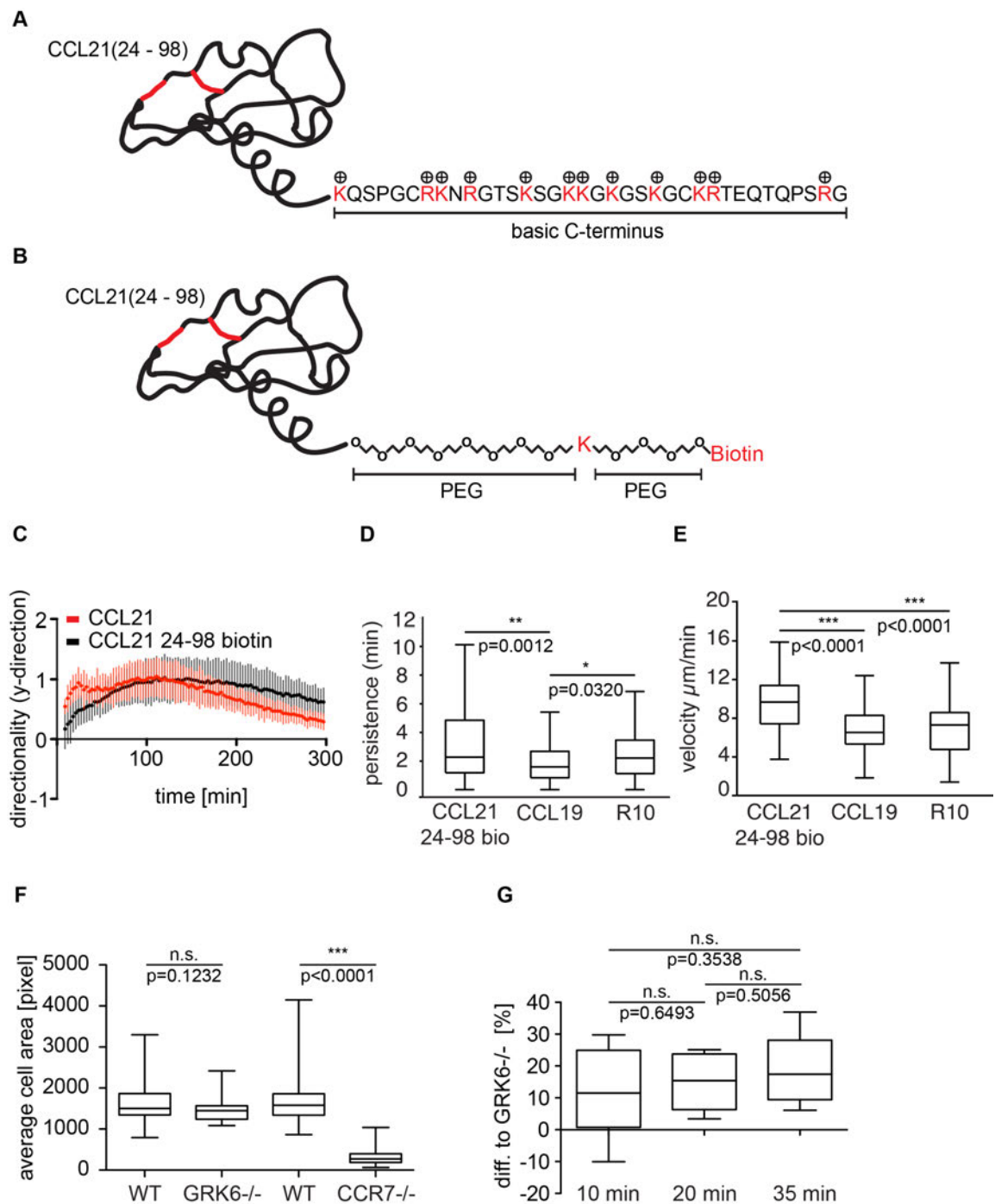
Another feature that influences cell directionality but is not included in the SNR are memory effects such as e.g. cell persistence. As cells tend to maintain their direction to a certain extent, directionality data across a few cell diameters are likely to not be entirely independent. A possibility to test for the interrelation between elements of cell motion and signal recognition would be using cells with altered motility.

Along with a dependence of cell directionality on CCL21 concentration, DCs alter their velocity accordingly (Figure 34B and C). This alteration could point to

DCs exploiting kinetic guidance, a phenomenon that has been observed in different cell types: Chemotactic CD8⁺ T-lymphocytes increase directionality and velocity towards sites of CD4⁺ T-lymphocyte/DC interactions (Castellino et al., 2006). Haptotactic zebrafish neutrophils are guided exclusively kinetically towards tissue bound zCXCL8 sources through increasing their migration velocity while migrating towards and slowing down in close proximity to the source (Sarris et al., 2012; Weber et al., 2013). For these cells, zCXCL8 functions as a kinetic trap at the source of zCXCL8 secretion. Similarly, DCs slow down when reaching the LV (Weber et al., 2013). Hence, for homing DCs, a kinetic trap at the lymphatic vessel could be favorable as well, as a slow down in high CCL21 concentrations in proximity of the lymphatic vessels would serve as a trigger for DCs to accumulate at the vessels and prevent “overshooting”.

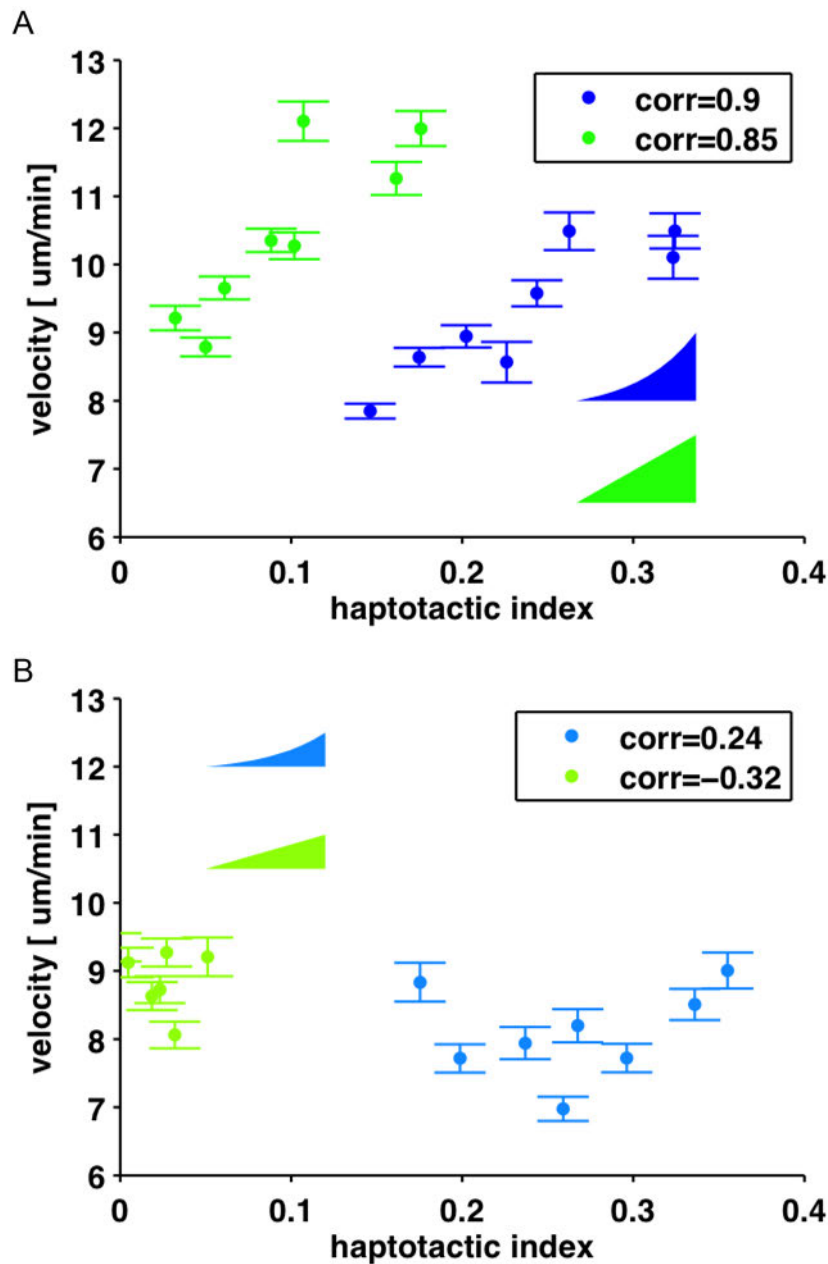
Furthermore, we have addressed, for the first time, the motile properties of GRK6 deficient DCs. It turns out that impaired GRK6 signaling addressed in biochemical experiments (Zidar et al., 2009) considerably hinders haptotaxis in terms of directionality and velocity, while not affecting chemotaxis in similar concentration regimes (Figure 35C and D). Signal termination of CCR7 after CCL21 activation is solely dependent on GRK6 and mainly occurring via an internalization independent mechanism (Byers et al., 2008; Otero et al., 2006; Zidar et al., 2009). Hence, impaired signal termination might increase intracellular ‘noise’ and shift haptotactic response in the direction of higher CCL21 concentrations (Ueda and Shibata, 2007). According to biochemical studies (Zidar et al., 2009), GRK6 deficient cells show severely reduced ERK activity. The decline in migration velocity of GRK6 deficient cells was reminiscent of cancer cells with impaired ERK signaling (Mendoza et al., 2015). Therefore, reduced ERK signaling of GRK6 deficient DCs might be an explanation for reduced DC migration efficiency, independently of CCL21 concentration and gradient shape (Figure 35D).

3.2.5. Supplemental figures

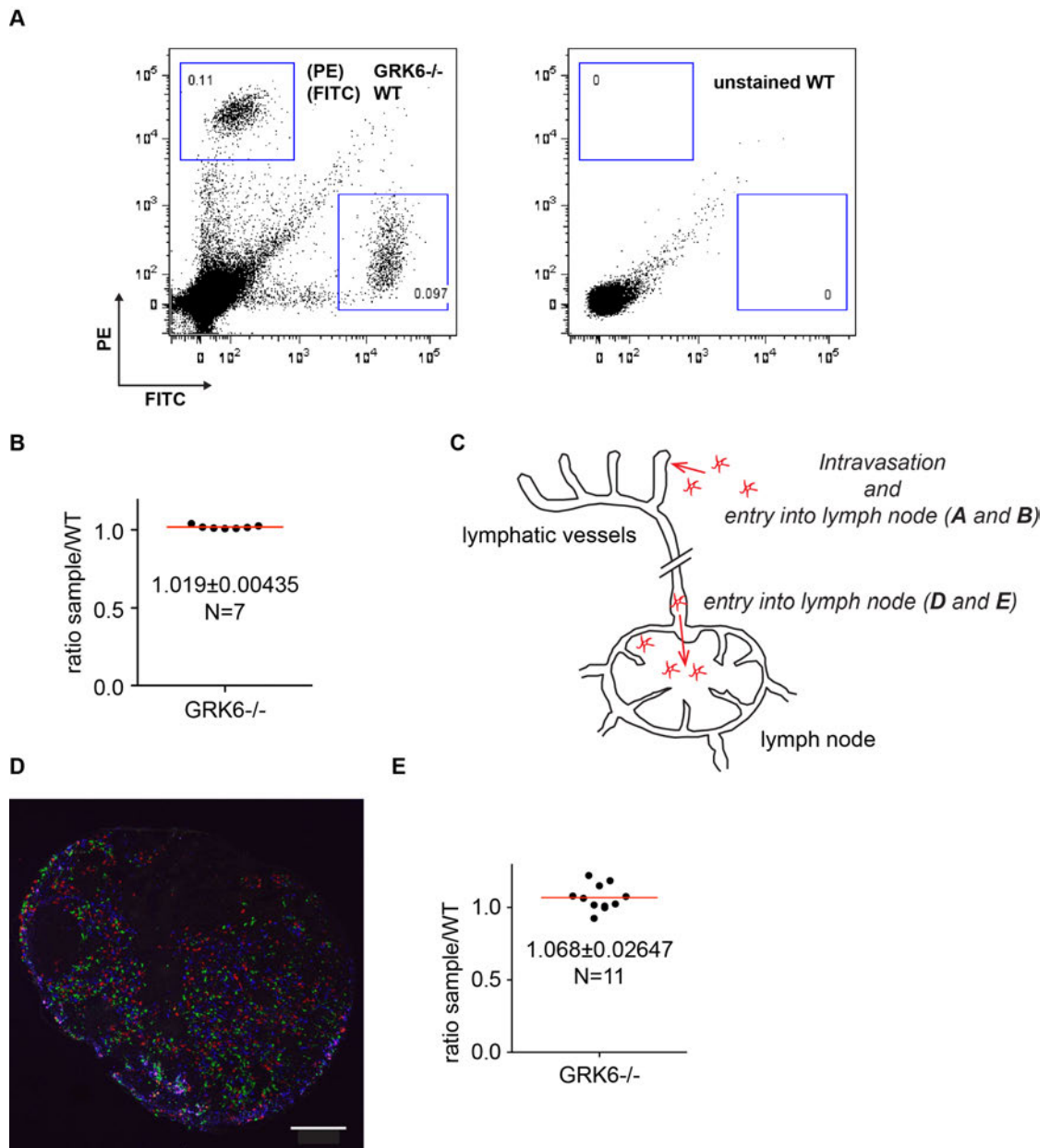


Supplemental Figure 1.: CCL21 24-98 bio. A) Schematic of full length murine CCL21 including the basic c-terminus. B) Schematic of CCL21 24-98 bio. Biotin tag including PEG linker. C) Collagen gel based chemotaxis assay. Average directionality of WT DCs evoked by a diffusion generated gradient of full length murine CCL21 (red) or CCL21 24-98 bio (black) Average directionalities plotted against the corresponding time (n = 6 independent experiments, frame rate 3 min). D) Persistence of DCs migrating in 2D confinement; n = 110, goodness of fit (gof) ≥ 0.95 . E) Persistence of DCs migrating in 2D confinement; n = 110, gof ≥ 0.95 . F) CCL21 induced adhesion/cell spreading assay. WT DCs and DCs of the respective genotype were mixed in a 1:1 ratio and allowed to spread on CCL21 coated glass surfaces. $n_{\text{WT}} = 39/n_{\text{GRK6}^{-/-}} = 38, n_{\text{WT}} = 48/n_{\text{CCR7}^{-/-}} = 40$. G) Distance difference towards the LV of WT DCs

compared to GRK6^{-/-}. Distance [difference in %] of a 1:1 mixture of WT and GRK6^{-/-} DCs for 10, 20 and 35 min of adhesion on dermal explants. n = 6 for each timepoint.



Supplemental Figure 2.: Velocity as a function of haptotactic index for WT DCs in A) full linear and exponential profile and B) half linear and exponential profile, with correlation coefficients as indicated in the legend. A) For a large span of concentrations, velocity and haptotactic index are highly correlated, indicating a tight coupling between cell velocity and direction. Once below the detection threshold (B), as is the case for the linear profile (light green), this relation no longer holds true. In the exponential profile (light blue), the coupling appears to be weaker because of high uncertainty in the profile for small concentrations that make up a substantial fraction of the data set.



Supplemental Figure 3.: GRK6^{-/-} DCs do not show impaired entry into the lymphatic vessels or *intra nodal* migration *in vivo*. A) and B) Intravasation into the LV of GRK6^{-/-} DCs. A) FACS analysis of WT and GRK6^{-/-} DCs recovered from draining (popliteal) lymph nodes 24 h after injection into the footpad of WT recipient mice. Representative dot plots of recovered PE or FITC positive DCs and unstained, non injected control DCs B) Quantification of DC arrival in the LN. Cell ratios were calculated from the absolute BMDC numbers arrived in the lymph node and normalization to the initially injected ratio to correct for unequal injection ratios. Dots represent relative ratios acquired from a single experiment. Red line mean, n = 7. Fluorescent labeling for each injection pair was inverted in half of the experiments to exclude labeling influences. C) Schematic of tested *in vivo* DC migration routes in D) and E) Intra lymphatic DC migration. D) Representative image of LN sections from lymph nodes recovered 3 h after intra lymphatic injection of WT (green) and GRK6^{-/-} (cyan) and GRK3^{-/-} (red) DCs. Scale bar 200 μ m. E) Quantification of intra nodal DC migration towards the center of the respective LN by measuring the distance of each cell to the edge of the respective LN. Migrated distance of GRK6^{-/-} DCs is compared to WT DCs and each other (Ratio). Red line mean, n = 11. Fluorescent labeling for each injection was shuffled in during the experiments to exclude labeling influences.

3.2.6. Materials and methods

3.2.6.1. Cell culture

DCs were generated from the bone marrow extracted from femur and tibia of mice in R10 culture medium (RPMI 1640 supplemented with 10 % fetal calf serum (FCS), 2 mM L-Glutamin, 100 U/mL Penicillin, 100 µg/mL Streptomycin and 50 µM 2-Mercaptoethanol, all Invitrogen) supplied with 10 % granulocyte-macrophage colony stimulating factor (GM-CSF) hybridoma supernatant. DCs were maintained at 37 °C in a humidified incubator with 5 % CO₂ and frozen on day 9 of the culture in 10 % DMSO in FCS. For experimental use, frozen DCs were thawed and stimulation overnight with 200 ng/mL Lipopolysaccharide (LPS) prior to usage.

3.2.6.2. Mice

C57BL/6J and B6Cd45.1, Pep Boy mice used in this study were bred and maintained according to the Austrian law for animal experiments (“Österreichisches Tierschutzgesetz”) and sacrificed at 4 to 10 weeks of age for use in experiments. Permission was granted by the Austrian federal ministry of science, research and economy (identification code: BMWF-66.018/0005-II/3b/2012).

3.2.6.3. GRK6^{-/-} bone marrow chimera generation

Bone marrow of GRK6^{-/-} mice (B6.129S4-Grk6^{tm1Mca}/J) was provided by Teresa Tarrant, Thurston Arthritis Research Center, UNC Chapel Hill. For GRK6^{-/-} bone marrow chimera generation, 5-8 weeks old B6Cd45.1, Pep Boy recipient mice were irradiated with a dose of 11 Gy. After 24 h 5x10⁶ CD45.2 positive GRK6^{-/-} donor cells were injected retro-orbitally in a total volume of 150 µL PBS. After 6 weeks, DCs were generated from the bone marrow extracted from femur and tibia of the recipient mice. Efficiency of the bone marrow transfer was quantified by FACS analysis. Briefly, matured DCs of recipient mice were stained for MHC-II to identify DCs, CD45.1 to identify recipient WT DCs and CD45.2 to identify donor GRK6^{-/-} DCs. Fc receptors were blocked to avoid

unspecific antibody binding. Stainings were carried out in FACS Buffer (1xPBS, 2 mM EDTA, 1 % BSA). All samples were kept on ice until data acquisition on a FACS Aria III Cell sorter (Becton Dickinson)

3.2.6.4. Chemokine

Biotinylated, truncated murine CCL21 (mCCL21 24-98 bio) was synthesized by ALMAC (Craigavon, UK). Desiccated mCCL21 24-98 bio was reconstituted to a concentration of 25 $\mu\text{g}/\text{mL}$ in PBS and stored at $-20\text{ }^\circ\text{C}$. Prior to use, mCCL21 24-98 bio was diluted to a working concentration of 250 ng/mL in PBS.

Peptide	Sequence	Notes
Mouse CCL21 (24-98) Biotin	SDG GGQ DCC LKY SQK KIP YSI VRG YRK QEP SLG CPI PAI LFS PRK HSK PEL CAN PEE GWV QNL MRR LDQ PPA PG-PEG-PEG- K(PEGBiotin)- OH	12-atom PEG spacer between Lys98 and biotin. 2 x 12-atom PEG spacer between Gly97 and Lys98.

Table 2.: Biotinylated, truncated murine CCL21 (CCL21 24-98 bio).

DyLight 594 (Thermo Fisher Scientific) labeled mCCL21 24-98 bio was prepared following the manufacturers protocol. Briefly, 100 μg mCCL21 24-98 bio was reconstituted in 100 μL phosphate buffer containing 0.1 M Na_2HPO_4 , 0.15 M NaCl adjusted to pH 7.2-7.5. 65 μg DyLight 594 NHS ester (Thermo Fisher Scientific) were added and the mixture was allowed to react for 1h at room temperature. Then 500 μL of Tris/HCl pH 7.6 were added to the reaction mixture to quench excessive DyLight 594 NHS ester. The mixture was allowed to react for 1h at rt. mCCL21 24-98 bio DL595 was purified using MW10 kDa spin columns (Amicon Ultra-2 Centrifugal Filter devices, Millipore) and stored at $-80\text{ }^\circ\text{C}$.

3.2.6.5. Haptotaxis chamber production

The haptotaxis chamber was manufactured as described earlier (Schwarz and Sixt, 2016). Specifically it consists of two glass surfaces that are spaced by polydimethylsiloxane (PDMS) micropillars. The upper surface bears the PDMS

micropillars to define the height of the chamber. For the lower surface, a PDMS coated glass bottom dish is used. Lower surface and the PDMS micropillar bearing upper surface are pressed onto each other by an elastic PDMS piston which is glued into the lid of a the glass bottom dish. To avoid cell adhesion to the upper surface, the PDMS micropillars are PEG coated. After fabrication of top and bottom part the cells are added and the chamber is closed. PDMS micropillars and piston are manufactured as published earlier (Le Berre et al., 2014).

Micropillar production - For micropillar production silicone elastomer and curing reagent (PDMS Sylgard 184 Elastomere Kit; Dow Corning) were mixed in a 7:1 ratio and degassed using a planetary centrifugal mixer (ARE250, Thinky). The micropillar bearing silicon wafer (produced as described by Le Berre *et al.* (Le Berre et al., 2014)) was cleaned carefully with canned air before 4 mL of the bubble free silicone elastomer/curing reagent mixture were poured carefully on the wafer without generating bubbles. Following plasma activation at high intensity for 2 min (Plasma Cleaner, Harrick Plasma), round cover glasses (#1, 12 mm diameter; Mentzel Gläser, Thermo Fisher Scientific) were place with the activated surface facing the silicone elastomer/curing reagent mixture on the wafer. The PDMS covered wafer was cured on a heating plate for 15 min at 95 °C before the micropillar coated glass slides were removed with a razor blade and *iso*-propanol. For PEG coating, micropillars were plasma activated and incubated with 50 μ L PLL-PEG (100 μ g/mL in HEPES, SuSos) at rt for at least 1 h. Before usage PEG coated PDMS micropillars were washed with PBS to remove excessive PLL-PEG.

Lid with soft PDMS lid production - For PDMS piston production, silicone elastomer and curing reagent (PDMS Sylgard 184 Elastomere Kit; Dow Corning) were mixed in a 30:1 ratio and degassed using a planetary centrifugal mixer (ARE250, Thinky). Then the PDMS mixture was poured carefully in an aluminum mold offering the correct dimensions of the needed PDMS piston and degassed in a vacuum desiccator (Le Berre et al., 2014). PDMS mixture was

cured for 6h at 80 °C before they could be removed carefully using *iso*-propanol.

Soft PDMS pistons were glued in the middle of the lid of the 60 x 15 mm non-pyrogenic polystyrene tissue culture dish (Falcon) using silicone aquarium sealant (Marina). Micropillars are placed on the piston with the glass side facing the soft PDMS piston.

PDMS coated glass dish production-For dish production coverslips (22mm x 22mm, #2 glass slides, Mentzel Gläser, Thermo Fisher Scientific) were sonicated in *iso*-propanol and ethanol to remove impurities on the glass surface (each 20 min, sweeping sonication) followed by rinsing with MΩ water without letting them dry. After rinsing, cover slips were blow-dried with canned N₂. Silicone elastomer and curing reagent (PDMS Sylgard 184 Elastomere Kit; Dow Corning) were mixed in a 10:1 ratio using a planetary centrifugal mixer (ARE250, Thinky). Cleaned glass slides were plasma activated (2 min, high intensity, Plasma Cleaner, Harrick Plasma) and immediately 500 μL of the PDMS mixture were added on the plasma cleaned side of the glass cover slip. Glass slides were spin coated at 4000 rpm for 40 s with a prior acceleration of 200 rpm/s (spin coater, WS 650-MZ-23NPP, Laurell Technologies Corporation) and subsequently baked for 6h at 80 °C in an oven.

For easier handling, a hole with a diameter of 17 mm was drilled in the middle of the bottom of a 60 x 15 mm Tissue culture dish (Falcon) and PDMS coated glass slides were glued on the bottom of the dishes using transparent silicone aquarium sealant (Marina). Dishes were cured over night at rt.

3.2.6.6. Laser writing and mCCL21 24-98 bio immobilization

For chemokine micropatterning, 20 μL biotin-4-fluorescein (B4F, 150 μg/mL, Sigma Aldrich, St. Louis, Missouri) were placed in the middle of a PDMS coated glass dish and patterns were written using a steerable, pulsed UV laser ($\lambda = 355$ nm) as described before (Bélisle et al., 2008). Briefly, the UV laser was focused into the interface between the bottom of the PDMS coated glass slide and the biotin-4-fluorescein solution with a long working distance 20x objective

(Zeiss LD Plan Neo 20x 0.4). A pair of high-speed galvanometric mirrors, controlled by a custom program, was moving the focal spot within the B4F droplet.

The gradient pattern was specified by an image whose pixel values determined the light dose used for bleaching. Careful calibration allowed compensating for the off-center drop-off of numerical aperture of the objective as well as the geometric distortions from the imperfect imaging of the scan mirrors into the back aperture of the objective. This allowed gradient writing in the full field of view of the objective. For each spot, the total light dose was split up into multiple laser pulses in order to average out the pulse-to-pulse power variability of the laser. The gradient was written one spot at a time with the scanning mirrors moving the laser focus by about half the diameter of the focus spot in order to create a continuous pattern. In this fashion, crosstalk between different locations in the pattern was minimized since the scattered light from one spot did not reach the threshold of bleaching elsewhere unlike projector based systems where the entire area is exposed simultaneously. The low wavelength of the UV laser lead to a high lateral resolution ($\sim 0.7 \mu\text{m}$) and the low crosstalk to a high dynamic range ($\sim 100:1$) of the gradient pattern. The writing speed was limited by the laser's pulse frequency of 1 kHz. A full description of the hardware employed can be found in Behrndt *et al* (Behrndt et al., 2012).

Following laser writing, the slide was washed with PBS, incubated for 20 min at room temperature with streptavidin-Cy3 (SA-Cy3, 10 $\mu\text{g}/\text{mL}$ in PBS with 3 % BSA, Sigma Aldrich, St. Louis, Missouri). After washing with PBS the slide was incubated for 30 min at 37 °C with CCL21 24-98 bio followed by an additional washing step. CCL21 24-98 bio patterned glass slides should be used directly in haptotaxis experiments.

To reproduce the gradient observed *in vivo* in our *in vitro* assay, we printed an exponential-like SA-Cy3 gradient that was designed to fit the full range of print intensity determined by grayscale values and possible extension for patterning. The function used for patterning is given by

$$c = ((\exp(s \cdot (x-1)/512) - 1) \cdot 255 / (\exp(s) - 1)),$$

where c is the concentration, x the position, and s is the steepness. The profile is printed in a range of 512 px, resulting in a patch of size 512 x 512 px that is constant along one axis and spans grayscale values in an exponential fashion such that starting at high intensities, the pattern in a range of $\sim 100 \mu\text{m}$ agrees with the profile observed in vivo.

3.2.6.7. Imaging

All in vitro haptotaxis assays were recorded with a 20x/0.5 PH1 air objective on a inverted widefield Nikon Eclipse microscope equipped with a light source with flexible excitation band selection (green 549/15, red 632/22; Lumencor). Confocal microscopy images were obtained with a 10x/0.3 PH1 objective on a Leica SP5 upright laser-scanning confocal microscope equipped with 488, 561 and 633 nm laser lines and with a 20x/0.8 air objective on a inverted Zeiss LSM 700 with 405, 488 and 640 nm laser lines. For mCCL21 24-98 bio quantification, images were obtained using a 20x/0.8 air objective on a Zeiss Axio Observer microscope equipped with an external light source (Leica). B4F patterns were written using a 40x/1.2 W Korr UV-Vis-IR water immersion objective on a inverted Zeiss Observer microscope equipped with 355 nm pulsed laser and a motorized piezo stage.

3.2.6.8. Antibody staining (immobilized mCCL21 24-98 bio)

Printed B4F patches were stained with SA-Cy3 for 20 min at room temperature in the dark. After washing with PBS patches were incubated with PBS only or with CCL21 24-98 bio in PBS (250 ng/mL). Subsequently, patches were stained with goat anti mouse CCL21 (R&D) and rabbit anti goat 488 (Molecular Probes), goat anti mouse CCL21 (R&D) only or rabbit anti goat 488 (Molecular Probes) only. Patches were imaged using a Zeiss Axio Observer widefield microscope.

3.2.6.9. Collagen migration assays

The assay was performed as previously described in (Lämmermann et al. (Lämmermann et al., 2008)). For one standard collagen gel, 150 µl PureCol® (stock: 3,1 mg/ml, bovine Collagen I, Advanced Biomatrix) was carefully mixed with 20 µl MEM (10x, Sigma Aldrich) and 10 µl NaHCO₃-solution (7.5%, Sigma-Aldrich) avoiding bubbles. A 2:1 ratio, 150 µl of the collagen solution was mixed with 75 µl DC suspension (3x10⁶ cells/ml in R10 medium) resulting in a final gel concentration of 1.7 mg/ml and a cell concentration of 1x10⁶ cells/ml gel. 125 µl of the collagen-cell mixture was casted into a round custom-made migration chamber (diameter 12 mm, thickness 2 mm). For collagen polymerization and buffer equilibration, the gels were incubated at 37 °C and 5 % CO₂ for 45 minutes. Afterwards, the gels were overlaid with 40 µl of CCL19 (625 ng/mL final conc. Diluted in R10 medium, R&D Systems), CCL21 (850 ng/mL final conc. Diluted in R10 medium, R&D Systems) or CCL21 24-98 bio (850 ng/mL final conc. Diluted in R10 medium). DC migration was observed via time-lapse video microscopy.

3.2.6.10. Adhesion assays

Glass dishes (MaTek, USA) were plasma act activated using a plasma cleaner (Harrick Plasma, 2 min, high Intensity). Following activation, glass dishes were PLL-PEG-Biotin coated (0.5 mg/mL in HEPES, SuSos, Switzerland). CCL21 24-98 bio was surface immobilized via streptavidin (SA-Cy3). WT and GRK6^{-/-} DCs were stained with either TAMRA (3 µM, Thermo Fisher Scientific) and oregon green (3 µM, Thermo Fisher Scientific) and vice versa to avoid dye induced effects and mixed in a 1:1 ratio in cell culture medium (R10). 200 µL cell suspension was applied to the CCL21 24-98 bio coated surface and cells were imaged while spreading. Movies were binarized (Fiji (Schindelin et al., 2012)) and the maximal total area of each movie was calculated.

3.2.6.11. In vivo staining of interstitial CCL21 gradients

Dermal ear sheets of ROSAmTmG mice were prepared as described before

(Weber and Sixt, 2012). The ventral ear sheets were fixed immediately in 4 % PFA at room temperature for 25 min, blocked with 1 % BSA in PBS for 1 h, stained with biotinylated anti-CCL21 (R&D systems, BAF457) and anti-Lyve1 (R&D systems, clone 223322) antibodies, which were diluted in blocking buffer, at rt for 2 h followed by incubation with streptavidin-Alexa fluor 647 (Jackson ImmunoResearch, 016-600-084) and anti-rat DyLight 549 (Jackson ImmunoResearch, 712-506-150) for 1.5 h. The stained ear sheets were imaged with a Zeiss LSM700 upright microscope with W Plan-Apochromat 20x objective (numerical aperture 1.0) and Zen2011 software.

3.2.6.12. Image analysis of in vivo and in vitro gradients

Gradients are analyzed as described before (Weber et al., 2013). In short: a mask identifying the LVs is drawn by hand (Gimp, www.gimp.org) for each point in the image the distance from the LV is calculated. Distance represents the length of the shortest possible path to the LV. The chemokine concentration as a function of the distance is calculated by averaging over each experiment separately excluding the image borders. The results from 4 experiments which were performed with identical settings are pooled and $c(\text{distance}=0)$ is normalized to 1. The chemokine concentration as a function of distance from the LV can be fitted accurately with a simple exponential decay. c_0 is the background signal (background staining, detector offset, etc.). Exactly the same was done for in vitro gradients of SA-Cy3.

3.2.6.13. Ex vivo crawl in assay (endpoint analysis)

Mouse ear sheets were prepared as previously described (Weber and Sixt, 2012). Briefly, mouse ears of 4-6 weeks old mice were split into dorsal and ventral halves. Ear sheets were mounted dermis side up on the lid of a 0.5 mL Eppendorf tube and R10 medium was added. LPS stimulated WT and GRK6^{-/-} DCs were stained with TAMRA (3 μM , Thermo Fisher Scientific) or eFluor670 (1.5 μM , eBioscience) respectively and vice versa. A total of 6×10^5 fluorescently labeled DCs were added at a 1:1 ratio or one genotype only in R10 supplemented with 10 mM HEPES (Life Technologies) on the ear

preparation and allowed to adhere for 10 or 20 min at 37 °C and 5 % CO₂ before non-adherent cells were washed away. Adhering cells were fixed with 4 % paraformaldehyde in PBS (32 %, Electron Microscopy Science) immediately after washing (10 min timepoint) or after 10, 15 and 55 min incubation at 37 °C and 5 % CO₂ after washing (20, 35 and 75 min timepoints). After fixation, lymphatic vessels were immunostained using rat anti-mLYVE-1 (R&D Systems) primary antibody and anti rat-488 secondary antibody (Jackson ImmunoResearch). Labeled DCs and lymphatic vessels in the explants were visualized by confocal imaging. Image analysis: A custom Fiji script was used to calculate the closest distance from the LV for each pixel of hand-drawn binary masks of the LV network. Cell images were segmented by manual intensity thresholding followed by size filtering. The mean distance was then calculated as the mean of the product of the cell segmentation image and the distance map. Likewise the LV mask and cell segmentation was used to calculate the fraction of cells that migrated into the LV. The effective migration is calculated as the mean distance from the LV normalized to the corresponding value derived from the original cell segmentation but with the LV mask rotated by 90°. This procedure provided a measure that was independent of cell number and local density of the LV network. In any case the borders of the images were excluded from the analysis because this lead to an overestimation of the distance.

3.2.6.14. *In vivo migration assay*

Both, WT and GRK6^{-/-} DCs were fluorescently labeled with 3 μM Oregon Green (Thermo Fisher Scientific) or 3 μM TAMRA (Invitrogen) and vice versa and mixed in a 1:1 ratio yielding a final concentration of 1x10⁶ cells/mL in PBS. A volume of 25 μL of the DC suspension was injected subcutaneously into the hind footpads of C57BL/6J mice. Draining popliteal lymph nodes were harvested 24 h after injection and mechanically opened in DMEM, supplied with 2.5 % FCS, 100 U/ml Penicillin, 100 μg/ml Streptomycin, 2 mM L-Glutamin (all Invitrogen) and 10 mM HEPES (Sigma-Aldrich). The enzymatic digestion of the opened lymph node was carried out with collagenase D (0.5 mg/ml collagenase

D, Roche) and DNaseI (40 µg/ml DNase I, Roche) in the presence of CaCl₂ (3 mM CaCl₂, Sigma-Aldrich) at 37 °C and stopped after 30 min by adding 0.5 M EDTA (Sigma Aldrich). DCs were identified by immunostaining for CD11c and MHC-II, different genotypes additionally by their fluorescent labeling by flow cytometry. DC ratios were calculated as the absolute number of fluorescently labeled WT DCs divided by the absolute number of GRK6^{-/-} DCs.

3.2.6.15. Cell tracking

For image processing and cell tracking Fiji (Schindelin et al., 2012) and a plugin for manual tracking (“Manual Tracking”, Cordelieres 2005) were used. Images and tracking data were analyzed using Matlab 2013 (MathWorks Inc. MA, US).

3.2.6.16. Statistical analysis

The position of cell tracks relative to the pattern of CCL21 was determined through comparison with a snapshot of the pattern, to ~ 10 pixel precision, corresponding to ~ 6 µm. Tracks were then binned according to their location on the pattern, with using 8 ~40 µm sized bins per pattern along the axis with varying CCL21 concentration. Cells outside the pattern were combined for characterization of cell behavior in R10 only. The bin size was chosen larger than a typical cell diameter to ensure a sufficient amount of data per bin and to account for persistent motion. Diminishing the bin size changed averages but did not influence the results qualitatively.

From cell tracks, the direction of the cells was calculated through the angle Θ between the direction of the respective gradient and the (current) cell direction. The direction of each cell was determined every 20 s. This time interval was chosen as small as possible to determine instantaneous cell speed. Smaller intervals lead to numerous events without any cell motion and artifacts from tracking, by an overrepresentation of angles of 90, 180, 270 and 360° which correspond to neighbouring pixels. In all tracks, events without any cell motion were excluded from further analysis. The overall directionality of cells is then given by $\langle HI \rangle = \langle \cos(\Theta) \rangle$, where the average is over all times and all events in a given bin. Accordingly, the average instantaneous speed is

calculated by averaging over all frame-to-frame displacements in a given bin divided by the time between frames. The concentration in each bin is calculated as an average of the concentration within that bin from the corresponding profile. Error bars represent the standard deviation of $\langle \cos(\Theta) \rangle$ determined with a bootstrapping method, where we resampled 200 times with the original sample size. For fitting of the dissociation constant, the experimental profiles were used as an input concentration. The linear profiles were approximated with a polynomial of degree 4, and for the exponential profiles, the original input function for patterning was used.

The persistence and speed data in Supplementary Figure 2 C,D were obtained as follows:

As cell speed is subject to large heterogeneity, the persistence was determined for each cell separately. This restricts analysis to long trajectories to ensure sufficient statistics. Cell trajectories with minimal length of 200 frames were used to determine mean square displacement per cell. To obtain the persistence, the MSD of each trajectory was averaged for each frame-to-frame duration τ from 1 to 20 frames, and the resulting curves were fitted to the analytical expression of the MSD for a persistent random walk in 2D,

$$MSD(\tau) = 2 * p^2 s^2 e^{-\tau/p} + \frac{\tau}{p} - 1.$$

Persistences were evaluated for a goodness of fit > 0.95 , and the data set was cropped to have the same amount of data for CCL21, CCL19, and R10. The same data were used to determine the corresponding distributions of the velocities.

3.2.7. Author contributions

J.S. performed the experiments; M.S. and J.S. initiated the project and designed the experiments. V.B. was responsible for the theoretical part of the manuscript and data analysis; V.B. and T.B. contributed the theoretical model. K.V. contributed dermal AB stainings; K.V., M.B. and A.L. helped with *in vitro* experiments; R.H. built the Laser writing microscope, wrote the LabView protocol and was responsible for analysis of *in vivo* experiments; J.M. helped

with microfabrication; A.R. helped with confinement assays and T.T. supplied the GRK6^{-/-} mice; All authors were involved in interpretation of results and preparation of the manuscript.

3.2.8. Acknowledgements

This work was supported by the Boehringer Ingelheim Fonds, the European Research Council (ERC StG 281556) and a START Award of the Austrian Science Foundation (FWF). We thank Jack Merrin for valuable input and the Imaging Facility of IST Austria for excellent support.

3.3. A microfluidic device for measuring cell migration towards substrate bound and soluble chemokine gradients

Jan Schwarz¹, Jack Merrin¹, Tino Frank², Robert Hauschild¹, Veronika Bierbaum¹, Tobias Bollenbach¹, Savaş Tay^{2 3}, Michael Sixt¹, Matthias Mehling^{1 2 4}

¹*Institute of Science and Technology Austria (IST Austria), Klosterneuburg, Austria.*

²*Department of Biosystems Science and Engineering, ETH Zürich, Basel, Switzerland.*

³*Institute for Molecular Engineering, The University of Chicago, Chicago, IL, 60637.*

⁴*Department of Biomedicine and Neurology Department, University Hospital Basel, Basel, Switzerland.*

- in submission -

3.3.1. Abstract

Cellular locomotion is a central hallmark of eukaryotic life. It is governed by cell-extrinsic molecular factors, which can either emerge in the soluble phase or as immobilized, often adhesive ligands. To encode for direction every cue must present as a spatial or temporal gradient. Here, we developed a microfluidic chamber that allows us to measure cell migration in response to a combination of surface immobilized and soluble molecular gradients. As a proof of principle we study the response of dendritic cells (DCs) to their major guidance cues, chemokines. The majority of data on chemokine gradient sensing is based on *in vitro* studies employing soluble gradients. Despite evidence suggesting that *in vivo* chemokines are often immobilized to sugar residues, limited information is available of how cells respond to immobilized chemokines. We tracked the migration of DCs towards immobilized gradients of the chemokine CCL21 and

varying superimposed soluble gradients of CCL19. Differential migratory patterns illustrate the potential of our setup to quantitatively study the competitive response to both types of gradients. Beyond chemokines our approach is broadly applicable to alternative systems of chemo- and haptotaxis such as cells migrating along gradients of adhesion receptor ligands vs. any soluble cue.

3.3.2. Introduction

The ability of cells to migrate is fundamental to many physiological processes, such as embryogenesis, regeneration, tissue repair and protective immunity (Horwitz and Webb, 2003). Cell migration is mainly governed by the adhesion of cells to substrates (other cells or connective tissue) and by extracellular signaling molecules acting as motogenic stimuli or directional guidance cues (Ridley, 2003). The specific impact of these factors differs considerably between cell types. While mesenchymal and epithelial cells are dominated by adhesive interactions the amoeboid crawling of leukocytes is largely controlled by guidance cues of the chemokine family (Bear and Haugh, 2014; Thelen, 2001). The prevailing paradigm of chemokine function is that spatial diffusion-based gradients of chemokines induce polarization and directed migration of the responding cells towards the chemokine source (Roca-Cusachs et al., 2013). However, the scarce information available for *in vivo* chemokine gradients suggests that the situation is often more complex and that chemokines are unlikely to distribute by free diffusion only. Like most growth factors chemokines bind to different degrees to cell surface or connective tissue glycosaminoglycans (Bao et al., 2010; Patel et al., 2001; Sarris et al., 2012). Such interactions restrict chemokine distribution and thereby can shape gradients. For chemokines binding with high affinity to sugar residues, immobilization can even lead to the formation of stable solid phase gradients, which induce a variant of haptotaxis (Weber et al., 2013). Although it is conceivable that cells can equally respond to gradients of soluble and/or immobilized chemokines, almost all available cell biological information about gradient sensing is based on *in vitro* studies employing soluble gradients.

The best understood example for the significance of immobilized vs. soluble chemokine gradients is the trafficking of DCs. After having captured antigen in non-lymphoid tissues, DCs migrate along immobilized gradients of the high affinity sugar-binding chemokine (C-C motif) ligand 21 (CCL21) towards lymphatic vessels, from where they are flushed into the sinus of lymph nodes. Once in the lymph node, the cells experience a second chemokine, (C-C motif) ligand 19 (CCL19), which interacts with the same receptor (C-C chemokine receptor 7, CCR7) but interacts only weakly with sugars. It has been shown *in vitro* that the directionality of DCs migrating on homogeneously immobilized CCL21 can be biased by gradients of soluble CCL19 (Schumann et al., 2010). Additionally, exposed to competing soluble gradients of CCL19 and CCL21, DCs displayed higher sensitivity towards CCL19 (Ricart et al., 2010). In contrast, if CCL21 diffusion was influenced by unspecific binding to charged extracellular matrix components, CCL21 induced directionality prevailed when opposed by a soluble CCL19 gradient (Haessler et al., 2011). How DCs respond to immobilized and co-existing immobilized and soluble chemokine gradients remains elusive.

Here we developed an *in vitro* setup to study the significance and interaction of co-existing bound and soluble chemokine gradients for directed cell migration. To this end we engineered a microfluidic device to generate diffusion-based chemokine gradients, which allows simultaneous surface-immobilization of arbitrarily graded chemokine patterns. We used DCs as a model to track migration in response to soluble and immobilized chemokine on a single cell level in real time.

3.3.3. Results and discussion

3.3.3.1. *Microfluidic system to probe chemotactic and haptotactic migration at the single cell level*

To quantitatively track immune cell migration in simultaneous response to chemotactic and haptotactic gradients we developed a microfluidic device that allows (i) patterning of bound chemokine gradients, (ii) precise positioning of immune cells on these haptotactic gradients and (iii) the generation of flow-free soluble chemokine gradients superimposed on haptotactic gradients in small microfluidic migration chambers. Specifically, the two-layer PDMS microfluidic device (overview in Figure 37a) consists of 9 inlets for reagents and media, 1 cell loading inlet, 3 waste outlets and 6 migration chambers (Figure 37b). The core component of this microfluidic device are these 6 migration chambers ($l = 1100 \mu\text{m}$, $w = 200 \mu\text{m}$, $h_{\text{max}} = 28 \mu\text{m}$) containing one side port at the middle of the long ends of the chamber while the ports at the two short ends of the chamber are connected to supporting sink and source channels (Figure 37b). For the controlled flow of fluids and cells all ports are equipped with independently controllable PDMS membrane valves. Support channels connect the reagent inlets with the migration chambers and the outlets. Cells can be loaded via the ports at the short ends resulting in a distribution along the chamber as shown in Figure 37c. Alternatively, cells can be loaded via the ports at the long ends resulting in a localized distribution in the center of the chamber (Figure 37c). As described earlier (Frank and Tay, 2013; Mehling et al., 2015), the flow of different molecules (e.g. chemokines) through the supporting source and sink channels and coordinated opening of the respective ports to individual chambers after having stopped fluid flow allows the generation of flow-free diffusion-based chemokine gradients in which the steepness, mean concentration and duration can be independently controlled. For example, spatially opposing gradients can be generated in parallel (Figure 37c, chamber 1 vs. chamber 3) and the polarity or ligand type of the gradients can be switched when needed.

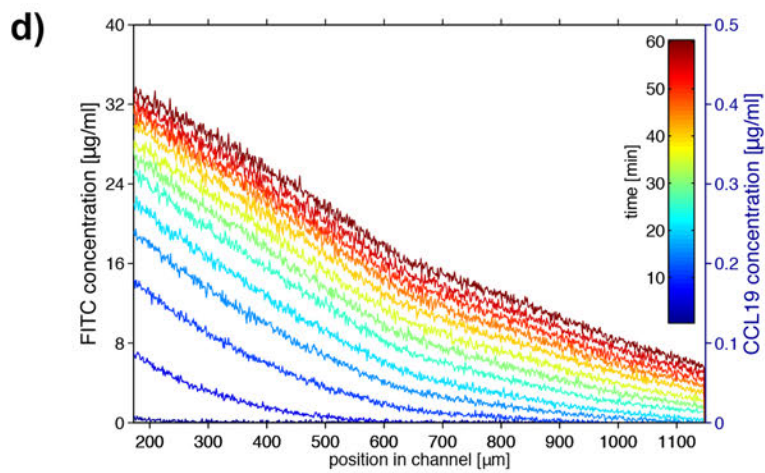
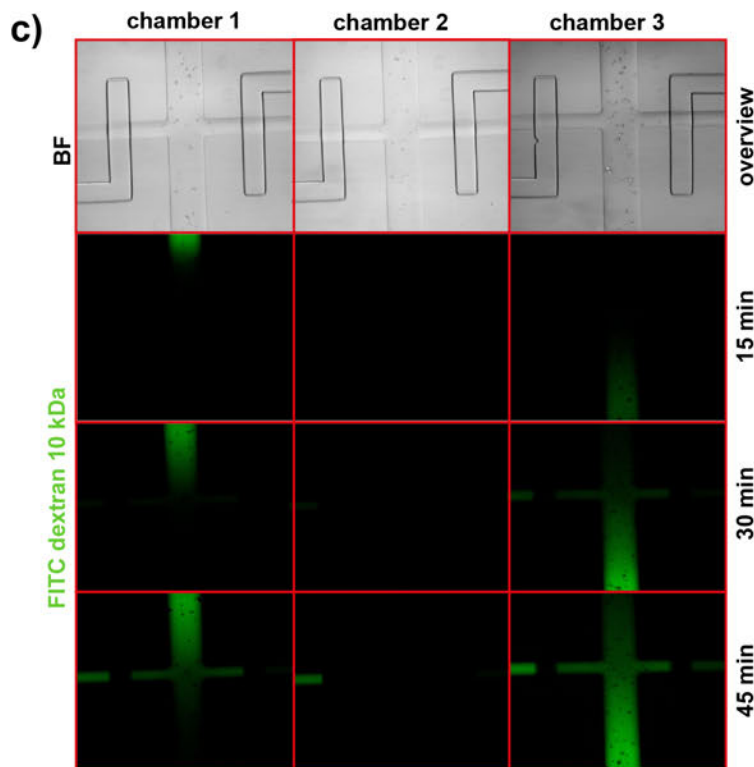
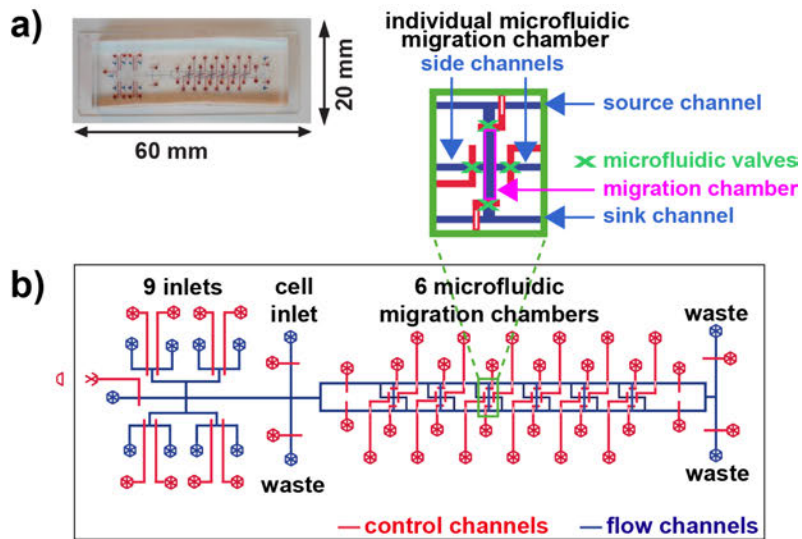


Figure 37.: Overview of the set up and functionality of the microfluidic migration device. a) Photograph of the device with flow channels filled with blue liquid and control channels filled with red liquid. b) Schematic overview of the geometry of the entire device and an individual migration chamber (inset). Flow channels are shown in blue, and control channels are shown in red. c) Overview of three migration chambers loaded with bone marrow derived DCs (upper row) and dynamics of formation of opposing diffusion-based gradients visualized with FITC-dextran (10kDa) in chambers one and three. In chamber two, cell culture medium is exchanged as a control. d) Diffusion profiles averaged over the width of the channel as a function of the location in the channel for different times, with the intensity mapped to the concentration of FITC dextran (10 kDa) (left axis) and CCL19 (right axis). Time is colour-coded from blue (short times) to red (long times), with each line separated by 5 min. The image is cropped at the end of the valve.

As the generation of chemotactic gradients in our device is based on diffusion for mass transport and not fluid flow, migration characteristics of individual cells can be quantified without physical disturbances of cells. For our chemokine CCL19 migration experiments, a continuously rising linear gradient was induced, reaching a CCL19-concentration of approximately $0.4 \mu\text{g/mL}$ at its maximum after 1 h (Figure 37d).

Our PDMS-based microfluidic system with closed channels requires bonding of one channel-sustaining PDMS part to either glass or a second PDMS layer. This bonding involves activation and heating steps, which preclude protein deposition before chamber assembly. We developed a protocol allowing protein patterning on pre-assembled chips. For protein patterning, we employed a photo-patterning technique to covalently surface-deposit fluorescently tagged molecules in arbitrary shapes and, most importantly, with graded intensity distributions (Holden and Cremer, 2003).

We patterned biotinylated fluorescein (B4F) using a focused and movable 355 nm ultra-violet laser (Figure 38a and b). While laser positioning enables the generation of arbitrary B4F patterns, regulation of intensity and dwell time additionally allows for quantitative control of local deposition with diffraction-limited resolution. Following exposure, unbound B4F was washed out and chambers were filled with streptavidin (SA), which, upon binding to B4F, serves as an adapter for biotin-coupled reagents. Next, we loaded the chambers with the chemokine CCL21 carrying a c-terminal PEG-biotin tag (CCL21 24-98 bio). After washout, this yielded a surface bound CCL21 pattern, which corresponded to the initial laser pattern.

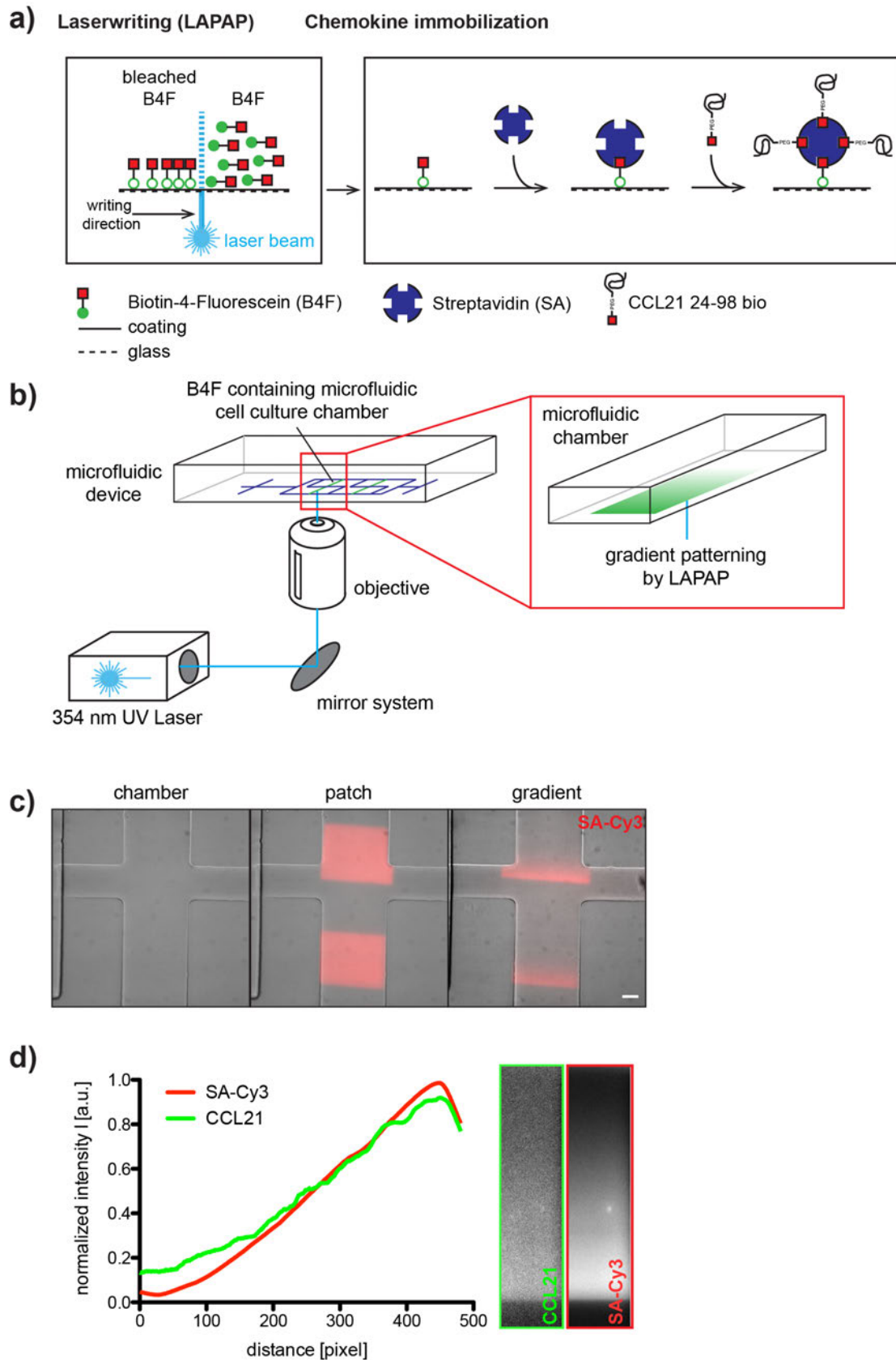


Figure 38.: Manufacturing of haptotactic chemokine gradients in a microfluidic migration chamber. a) Schematic of biotin-4-fluorescein patterning by photobleaching (B4F, left panel) and the chemokine immobilization protocol (right panel). b) Schematic of laser writing into a

microfluidic migration chamber. PDMS block with microfluidic chip (left panel). Microfluidic migration chamber with B4F gradient (enlarged region). c) SA-Cy3 staining of different laser written B4F patterns in microfluidic migration chambers overlaid with the respective bright field image of the chamber. From left to right: chamber without pattern ('chamber'), chamber with two printed patches ('patch') and a chamber with two gradients ('gradient') as used in the migration experiments (Figure 39 and Figure 40). Scale bar represents 100 μm . d) Immunostaining of a linear CCL21 gradient printed in a migration chamber. SA-Cy3 image (red line and right image) and anti-CCL21/anti-goat AF 488 image (green line and left image). Fluorescence intensities were normalized to the respective maximum.

The use of fluorescently labelled SA such as SA-Cy3 allowed visualization of printed patterns (Figure 38c). Importantly, the SA-Cy3 pattern correlated closely with the amount of biotinylated CCL21 bound to SA as shown with anti-CCL21 antibody staining (Figure 38d).

Taken together, we reconfirm previous reports which describe the generation of highly controllable diffusion-based chemokine gradients in microfluidic devices (Frank and Tay, 2013; Mehling et al., 2015). We then integrated the immobilization of chemokines with high spatial resolution in this microfluidic device. The chemokine immobilization procedure involves several binding and washing steps, which are usually executed manually on a dish or cover slip. Our device not only allows patterning within the cell culture chamber but also enables automatization of all binding and washing steps because it features 10 inlets for different solutions. This accelerates the procedure of protein patterning significantly.

3.3.3.2. *Immobilized CCL21 gradients induce DC haptotaxis in a microfluidic migration chamber*

The defined, surface-immobilized and bioactive CCL21 patterns and gradients obtained by photo-patterning (Figure 38) allowed us to quantify haptokinetic and haptotactic migration of DCs in our microfluidic device. Figure 39 illustrates the migration of DCs in the presence and absence of immobilized CCL21. Under control conditions DCs adhere loosely to the fibronectin-coating, show a round morphology with constant protrusions (Supplemental movie S1, no chemokine) and migrate spontaneously and without direction (Figure 39a). In contrast, DCs exposed to a patch with a homogenous concentration of CCL21 start to adhere more tightly to the immobilized chemokine (Supplemental movie S1, CCL21

patch) while migrating more efficiently but without direction (Supplemental figure S4, CCL21 patch). This demonstrates the haptokinetic effect of evenly immobilized CCL21 (Figure 39b). While exposure to a gradient of immobilized CCL21 also resulted in more pronounced adherence of DCs to the substrate (Supplemental movie S1, CCL21 gradient), this additionally induced directed migration of the cells towards higher concentrations of the gradient (Figure 39c). This migration pattern demonstrates the haptotactic effect of CCL21 when immobilized as a gradient. Taken together, we show that CCL21 immobilized in our microfluidic device impacts the migration of DCs. Specifically, CCL21 induces chemokinesis when immobilized as a patch or chemotaxis when immobilized as a gradient.

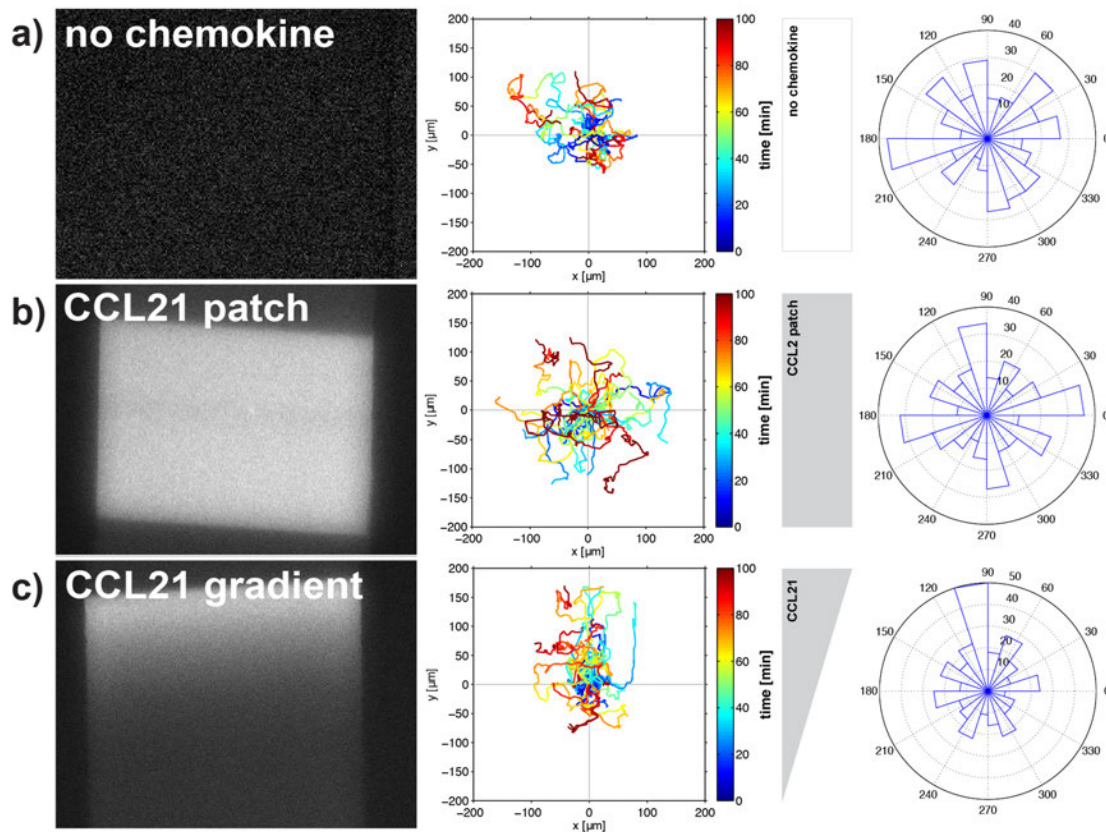


Figure 39.: DCs migrating on immobilized CCL21 24-98 bio. a) DCs migrating in a microfluidic channel treated with SA-Cy3 and CCL21 24-98 bio without B4F laser-writing. b) DCs migrating on a SA-Cy3 stained CCL21 24-98 bio patch printed in a microfluidic channel. c) DCs migrating on a SA-Cy3 stained CCL21 24-98 bio gradient printed in a microfluidic channel. Left panels: Representative images of the SA-Cy3 stained patterns. Middle panel: Corresponding cell track analysis [dimensions in μm ; time is colour-coded]. Gradient direction and pattern shape are indicated in grey. Right panel: Rose plot visualizing the distribution of angles of all tracks in an angular sector field (3 min intervals).

3.3.3.3. *CCL19 gradients induce DC chemotaxis in a microfluidic migration chamber*

We have previously shown that chemotaxis can be induced in T cells by exposure to a soluble gradient of the chemokine CXCL12 generated in a microfluidic migration device (Mehling et al., 2015). To recapitulate this finding for other immune cells, we exposed DCs to a continuously rising gradient of CCL19 or control conditions in migration chambers of our microfluidic device (Figure 40). Specifically, we loaded the DCs via the ports at the short ends of the chamber resulting in a distribution of the cells along the chamber. Cells adhered loosely to the fibronectin-coated PDMS surface (Supplemental movie S2) with some cells starting to migrate randomly within approximately 30 min. (Supplemental movie S2, 1800 s). Following attachment, we exposed the cells to fresh cell-culture medium diffusing into the chamber from both short ends as a control without generating a CCL19-gradient (Figure 40a). This resulted in the undirected migration of the cells (Figure 40a). In parallel we exposed DCs in another migration chamber to a diffusion-based gradient of CCL19 by sequentially refilling the channels at the top and the bottom of the microfluidic migration chamber with fresh medium either containing CCL19 or cell culture medium (Figure 40b-d). This resulted in a CCL19-gradient along the entire chamber and accordingly to exposure of DCs to low, intermediate, or high concentrations of CCL19 (CCL19_{ow}, CCL19_{medium}, CCL19_{high}; Figure 40b-d).

Compared to control cells, exposure of DCs to low concentrations of chemokine resulted in faster migration (Figure 41, CCL19_{ow}) while overall migration remained undirected (Figure 40b), reflecting the chemokinetic effect of CCL19. The preferential distribution of tracks towards the short ends of the chamber relates to the fact that migration towards the long ends of the chamber is impeded by the rectangular geometry of the chambers. Exposure of DCs to intermediate concentrations of the CCL19-gradient resulted in a significantly increased directionality of single cell trajectories towards higher concentrations of the chemokine (Figure 40c). While higher CCL19 concentrations did not enhance cell velocity (Figure 41, CCL19_{high}), directionality was further

augmented when DCs were exposed to high concentrations of the CCL19-gradient (Figure 40d).

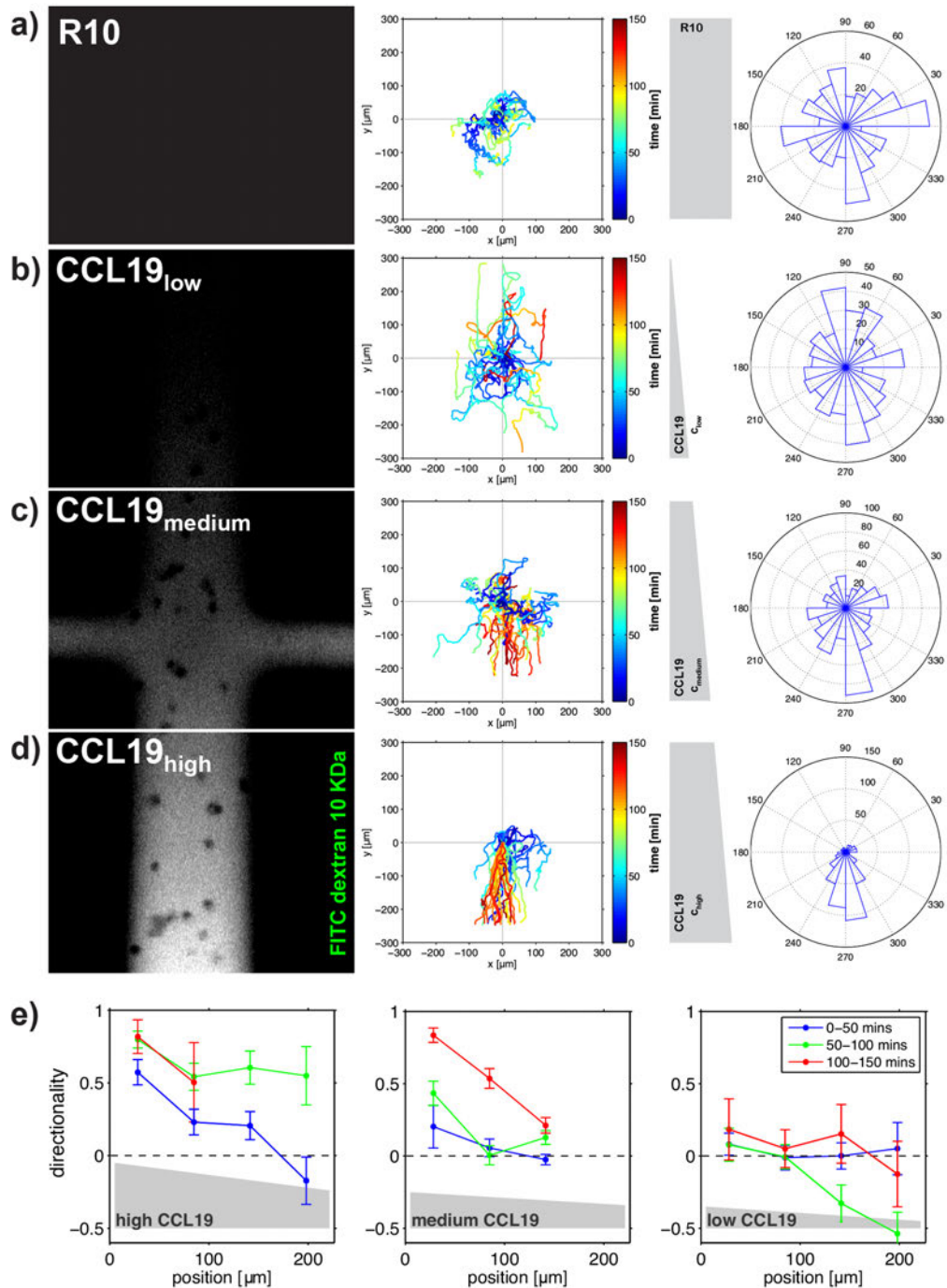


Figure 40.: CCL19 gradients induce DC chemotaxis in a microfluidic migration chamber. a) DCs migrating in a diffusion-based gradient of cell culture medium (R10). b - d) DCs migrating in a diffusion-based CCL19/FITC dextran 10kDa gradient. e) Directionalities as a function of the position in the microfluidic assay for low (left panel) intermediate (middle panel) and high (right panel) average concentrations of CCL19. The zero position corresponds to the lower edge of the field of view in (b-d), where the respective concentration is maximal. The directionalities are shown for short, intermediate, and long times, shown in blue, green, and red, respectively. b)

and e.1) Lower third of the migration chamber; low CCL19 concentration regime. c) and e.2) Middle third of the migration chamber; medium CCL19 concentration regime. d) and e.3) Upper third of the migration chamber; high CCL19 concentration regime. Left panel: Representative images of the CCL19/FITC dextran 10kDa and the cell culture media (R10) gradient at $t = 60$ min. Middle panel: Corresponding cell track analysis [dimensions in μm ; time is colour-coded]. Gradient direction and pattern shape are indicated in grey. Right panel: Rose plot visualizing the distribution of angles of all tracks in an angular sector field (3 min intervals).

Our microfluidic migration device allows tracking of individual cells with high spatial and temporal resolution. This is exemplified in Figure 40e, which shows the directionality of DCs during the build-up phase of the CCL19 gradient as a function of time and the position in the chamber. As shown in Figure 40b-d, the chamber was divided into three sections containing high, intermediate and low concentrations of the CCL19-gradient.

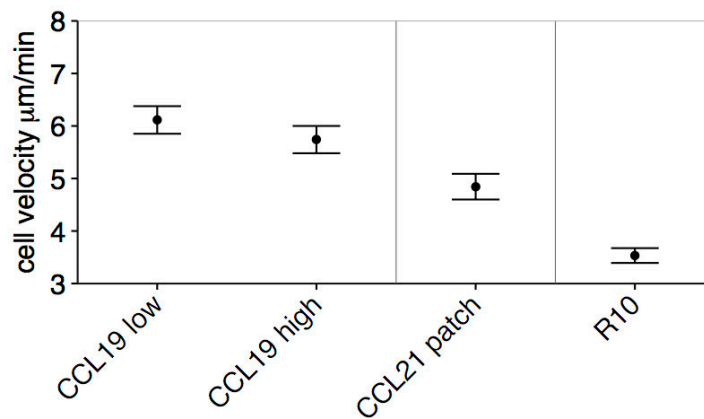


Figure 41.: Velocities of DCs for different conditions. Cells migrate with increased velocity in presence of both CCL19 and CCL21 in comparison to medium only (R10). Velocities are increased even if the cells do not move directionally, as it is the case at low concentrations of soluble CCL19 and on the patch of CCL21.

These data show that DCs migrate in high concentrations of the chemokine gradient more directionally than in intermediate concentrations while migration in low concentrations was non-directional. Specifically, we also observed within the given sections of the chemokine gradient - i.e. in low, intermediate and high CCL19-concentrations - a correlation between the directionality of cell migration and increasing chemokine concentrations. Taken together, these data indicate that the directionality of DC migration correlated with increasing concentrations of CCL19 in the gradient. In summary we show that diffusion-based chemokine gradients in microfluidic devices can induce directed migration also in DCs. The finding that directed migration can also be induced in myeloid cells expands

previous reports on the induction of directed migration in T lymphocytes (Mehling et al., 2015) and emphasizes the potential of microfluidics for assessing biologically relevant properties on a single cell level.

3.3.3.4. Migration of DC in competing chemotactic and haptotactic chemokine gradients

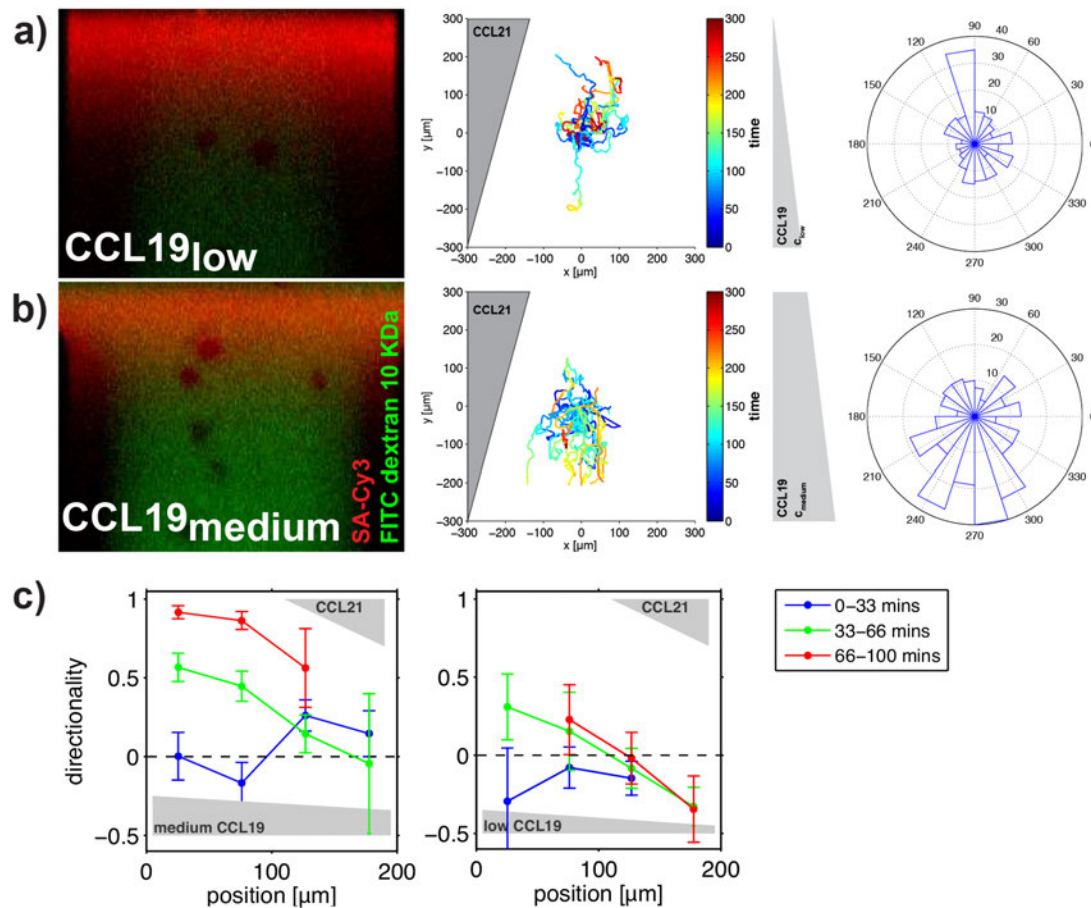


Figure 42.: DCs migrating on opposing chemotactic CCL19 and haptotactic CCL21 gradients. a) CCL19_{low}/CCL21 area of the chamber. b) CCL19_{medium}/CCL21 area of the chamber. Left panel: Representative images of the soluble CCL19/FITC dextran 10kDa gradient (green) after 45 min superimposed with immobilized CCL21/SA-Cy3 gradients (red) of the respective areas. Middle panel: Tracks of migrated DCs in the respective areas [dimensions in μm ; time is colour-coded]. Gradient directions are indicated in grey. Right panel: Rose plot visualizing the distribution of angles of all tracks in an angular sector field (3 min intervals). c) Directionalities as a function of the position in the channel for intermediate and low average concentrations of CCL19 (from left to right). Zero position corresponds to the lower edge of the field of view, and the directionalities are shown in blue, green, and red for short, intermediate, and long times.

After having shown that our microfluidic device allows us to expose DCs to chemotactic and haptotactic guidance cues we next quantified migration of DCs simultaneously exposed to diffusion-based and immobilized chemokine gradients. Specifically, we assessed the migration of DCs when exposed to

competing gradients of soluble CCL19 on the one side and immobilized CCL21 on the other side. To this end CCL21-gradients were printed into the lower and middle area of the migration chamber. After washing, DCs were positioned in the chamber including the two CCL21-gradients (Supplemental movie S3). After 30 min of cell recovery, an opposing diffusion-based CCL19 gradient was generated as described above. By doing so, one of the CCL21-gradients was superimposed with a low-concentration CCL19-gradient (CCL19_{ow}/CCL21 gradients; Figure 42a), while the other was superimposed with a medium-concentration CCL19-gradient (CCL19_{med um}/CCL21 gradients; Figure 42b). DCs positioned in CCL19_{ow}/CCL21 gradients migrated towards higher concentrations of the haptotactic CCL21-gradient (Figure 42a). Specifically, cells migrate in a haptotactic fashion towards the higher concentrations of the CCL21-gradient at all times as indicated by the colour code (cold colours: early time-points, hot colours: later time-points) in Figure 42a. In contrast to this, DCs positioned in CCL19_{med um}/CCL21 gradients migrated towards higher concentrations of the chemotactic CCL19-gradient (Figure 42b).

As for the chemotactic gradient profiles, we plotted the average directionalities of DCs in the CCL19_{ow}/CCL21 and the CCL19_{med um}/CCL21 gradients as a function of time (Figure 42c). These data indicate that the presence of the CCL19_{ow}/CCL21 gradients induced preferential migration towards the haptotactic gradient. By contrast, exposure of DCs to CCL19_{med um}/CCL21 gradients resulted, after build-up of the CCL19-gradient, in highly directional chemotaxis. Our findings suggest that haptotactic CCL21 gradients in the presence of a soluble CCL19-gradient induce directed migration only at low CCL19 concentrations. Increasing concentrations of the CCL19-gradient resulted in directed migration along the soluble gradient while overriding the effect of the opposing haptotactic CCL21-gradient.

Taken together, we show that the use of microfluidics allows superimposing chemotactic on haptotactic chemokine gradients and that DCs respond differentially to these guidance cues in relation to the respective signal strength. As the characteristics of these soluble and immobilized chemokine

gradients can be precisely controlled, this approach has the potential to address fundamental questions of directional cell migration.

3.3.4. Conclusion

Much of our understanding of directed cell migration is based on data from animal models. Some of the findings have been recapitulated *in vitro* by either chemotactic or haptotactic migration assays. These data have added substantially to our understanding of the mechanisms underlying guided cell migration. However, the likely possibility that both chemotactic and haptotactic gradients exist simultaneously *in vivo* was not addressed in such setups.

The setup described here allows the generation of haptotactic gradients by photo-patterning and the flow-free generation and maintenance of diffusion-based gradients. The integration of these assays into a microfluidic device allows the positioning of cells in specific regions of the respective gradients and assessing responses to a multitude of guidance cues in parallel. As a proof of concept we compared quantitatively the migration characteristics of DCs on immobilized chemokine gradients while varying the superimposed chemotactic gradients and found differential migratory responses. Hence, our microfluidic setup is suited to study processes in which co-existing immobilized and soluble gradients impact on cell migration. In addition to being suited for immobilization of chemokines, our approach also permits the study of migration characteristics of cells in haptotactic gradients of cellular adhesion sites – e.g. along gradients of integrin-ligands and co-existing gradients of any conceivable soluble guidance cue.

An example for co-existing immobilized and soluble chemokine gradients is the mobilization of mesenchymal stem cells during tissue regeneration by soluble chemokines such as CCL19 on the one side and chemokines that bind to extracellular glycans such as CCL2, CXCL12 or CCL5 on the other side (Fox et al., 2007; Hocking, 2015). Also, guided cell migration presumably mediated by chemotactic and haptotactic signals are of importance in the pathogenesis of autoimmune diseases such as multiple sclerosis (MS) (Holman et al., 2011) an

assumption that is underlined by the fact that potent drugs for the treatment of MS target immune cell migration (Derfuss et al., 2013; Mehling et al., 2011). Taken together, the combination of chemo- and haptotactic guidance cues plays a fundamental role during various physiological processes such as protective immunity and tissue regeneration but also in the pathogenesis of diseases like cancer and autoimmunity. In light of the capability of our microfluidic device to control co-existing chemotactic and haptotactic guidance cues and assess the migratory response of cells on a single cell level in real time our setup has the potential to significantly contribute to a better understanding of migration-related aspects of the above-mentioned processes.

3.3.5. Material and methods

3.3.5.1. Design and fabrication of microfluidic chips

The microfluidic photomask design was drawn with Coreldraw X6 (Corel corporation, US) and printed on transparency at a resolution of 8 μm (JD Photo Data & Photo Tools, UK). A control and flow mold were produced by photolithography on a silicon wafer as described earlier with minor modifications (Mehling et al., 2015). In brief, the flow layer mold was spin-coated with hexamethyldisiloxane at 3000 rpm for 30 s and then baked at 110 $^{\circ}\text{C}$ for 1 min. Next, the wafer was spin-coated with AZ-40XT (Microchemicals, Germany) at 3000 rpm for 30 s and soft baked at 110 $^{\circ}\text{C}$ for 5 min. Photoresist was then exposed to ultra violet (UV) light for 15 min using a beam expanded 365 nm UV LED, (M365L2-C1–UV, Thorlabs GmbH, Germany). After UV exposure, the wafer was post-baked for 2 min at 110 $^{\circ}\text{C}$. The wafer was developed in AZ-726-MIF developer for 5-7 min, rinsed in water and was then reflowed for valve closing at 110 $^{\circ}\text{C}$ for 10 min. The 100 μm wide parabolic AZ40XT channels had a central height of 26.3 μm .

The control layer silicon wafer mold was spin-coated with GM1070 SU-8 (Gersteltec, Switzerland) at 3100 rpm for 40 s to reach a final height of 25 μm . The wafer was then baked for 15 min at 65 $^{\circ}\text{C}$ and then 35 min at 95 $^{\circ}\text{C}$. The wafer was exposed for 10 min with the UV-LED. The post exposure bake was

15 min at 65 °C, then 45 min at 95 °C. The wafer was then developed in SU-8 developer (Gersteltec, Switzerland). Finally, both flow and control wafers were non-stick functionalized with trichlorosilane for 1 h in a vacuum desiccator. Microfluidic chips were fabricated by multi-layer polydimethylsiloxane (PDMS) soft-lithography as described previously (Frank and Tay, 2013; Mehling et al., 2015).

3.3.5.2. Chip set-up, operation and control

The glass slide carrying the microfluidic chip was cleaned and taped on a slide holder. Control channels were connected to miniature pneumatic solenoid valves (Festo, Switzerland) that were controlled via an established control box system (Gomez-Sjöberg et al., 2007) with a custom Matlab (MathWorks, US) graphical user interface. Optimal closing pressures of push-up PDMS membrane valves were determined individually for each chip the pressure in control channels was increased by 0.5 bar. Flow lines were connected to inlets, pressurized with 0.2-0.4 bar and the whole chip was filled with phosphate buffered saline (PBS). The cell culture chambers were incubated with human plasma fibronectin ($c = 250 \mu\text{g/mL}$, Millipore, Austria) for 1 h while fibronectin remaining in the flow channels was flushed off the flow channels with PBS. Following incubation of cell culture chambers for 1 h with fibronectin, the entire chip was flushed with cell culture medium for 10 min.

3.3.5.3. Generation of stable soluble chemokine gradients

Stable diffusion-based chemokine gradients were generated and maintained as previously described by using a switching source-sink flow pattern. (Frank and Tay, 2013; Mehling et al., 2015) Briefly, the channels at the short ends of the cell culture chambers were sequentially refilled with fresh R10 medium (RPMI 1640 supplemented with 10 % fetal calf serum, L-Glucose and Penicillin/Streptomycin, all from Life Sciences, Austria) or with a mixture of murine CCL19 ($2.5 \mu\text{g/mL}$ in R10; Almac, UK) and FITC-dextran 10 kDa ($200 \mu\text{g/mL}$ in R10; hydrodynamic radius: 2.3 nm; Sigma Aldrich, US). By doing so, a local high concentration (source) and a low concentration (sink) is

established between which a chemokine gradient is built up and maintained by diffusion. We used FITC-dextran as a proxy to monitor the chemokine gradient within the chamber. The diffusion profiles of FITC-dextran 10 kDa and the chemokines CCL19 and CCL21 are expected to be very similar for similar hydrodynamic radii. These radii can be estimated empirically (Wilkins et al., 1999) and read (1.7 +/- 0.4) nm for CCL19 (9 kDa) and (1.9 +/- 0.4) nm for CCL21 (12.5 kDa), which is comparable to the 2.3 nm of FITC-dextran 10 kDa.

3.3.5.4. Generation of bound chemokine gradients by laser-assisted adsorption by photobleaching

For *on-chip* chemokine patterning, each chamber was washed with PBS for 10 s to remove unbound fibronectin. Next, chambers were filled with biotin-4-fluorescein (B4F, 150 $\mu\text{g}/\text{mL}$, Sigma Aldrich, US) and patterns were written using a steerable, pulsed UV laser ($\lambda = 355 \text{ nm}$) Specifically, a long working distance 20x objective (Zeiss LD Plan Neo 20x 0.4) focused the UV laser at the interface between the bottom of the microfluidic chamber and the B4F. A custom program controlled a pair of high-speed galvanometric mirrors that moved the focus spot within the chamber. The gradient pattern was specified by an image whose pixel values determined the light dose used for bleaching. Careful calibration allowed compensating for the off-center drop of numerical aperture of the objective as well as the geometric distortions arising from the imperfect imaging of the scan mirrors into the back aperture of the objective. Hence, the full field of view of the objective could be utilized for gradient writing. For each spot, the total light dose was split up into multiple laser pulses in order to average out the pulse-to-pulse power variability of the laser. The gradient was written into the bottom of the chambers one spot at a time with the scanning mirrors moving the laser focus by about half the diameter of the focus spot in order to create a continuous pattern. The low wavelength of the UV laser resulted in a high lateral resolution ($\sim 0.7 \mu\text{m}$) and the low crosstalk to a high dynamic range ($\sim 100:1$) of the gradient pattern. The writing speed was limited by the laser's pulse frequency of 1 kHz. A full description of the hardware employed can be found in Behrndt *et al.* (Behrndt et al., 2012).

Following laser writing, the chamber was washed with PBS for 10 s and subsequently incubated for 20 min at room temperature with streptavidin-Cy3 (SA-Cy3, 10 μ g/mL in PBS with 3% BSA, Sigma Aldrich, US). After 10 s of washing with PBS, the chamber was incubated for 30 min at 37 °C with biotinylated CCL21 (CCL21 24-98 bio; custom synthesized, 250 ng/mL in PBS, Almac, UK). Apart from loading steps, the supporting source and sink channels were kept constantly under flow with PBS (0.2 bar) to reduce unspecific adsorption of any reagent outside the cell culture chambers. Following washing for 10 s with PBS the DC suspension (10x10⁶ cells/mL in R10 medium) was loaded into the cell culture chambers.

3.3.5.5. *Mice, dendritic cell isolation, culture and maturation*

C57BL/6J mice used in this study were bred and maintained according to the Austrian law for animal experiments (“Österreichisches Tierschutzgesetz”) and sacrificed at 4 to 10 weeks of age for use in experiments. Permission was granted by the Austrian federal ministry of science, research and economy (identification code: BMWF-66.018/0005-II/3b/2012).

DCs were generated from bone marrow cells extracted from femur and tibia of C57BL6 mice. In brief, bone marrow cells were collected by spinning distally capped bones in an upright position with 4500 rpm for 5 min. Next, 2x10⁶ bone marrow cells were cultured in 10 mL R10 medium containing 1 mL supernatant from a granulocyte-macrophage colony-stimulating factor (GM-CSF) hybridoma cell line in a non-adhesive petri dish. On day 4, 10 mL of R10 medium containing 2 mL supernatant from a GM-CSF hybridoma cell line were added. On day 7, 10 mL of cell culture medium was replaced by 10 mL of R10 medium containing 2mL supernatant from a GM-CSF hybridoma cell line. DCs were harvested on day 8-10 of the culture and matured overnight with lipopolysaccharide (LPS, 200 ng/mL).

3.3.5.6. *Imaging, Cell-tracking and data analysis*

Cells were imaged using an automated inverted microscope (Nikon Ti, 10x/NA 0.3 Air Plan Fluor Ph1 and 20x/NA 0.5 Air Plan Fluor Ph1 objective; Nikon,

Japan) equipped with a stage-top incubator controlling for temperature (37 °C), CO₂-concentration (5 %) and humidity (90 %), a digital EMCCD camera (EMCCD C9100-02; Hamamatsu photonics, Japan) and the imaging software Nikon NIS-AR (Nikon, Japan). For evaluation of migration properties, cells were tracked in an area of 300 x 200 μm, which corresponds to the size of the chemokine pattern. Cell tracks are represented on a x-y coordinate system, with the origin of each trajectory aligned to (0,0). Each track is colour-coded for time, such that cold colours represent early and hot colours later time points. For image processing and cell tracking, Fiji (Schindelin et al., 2012) and a plugin for manual tracking (“Manual Tracking”, Cordelieres 2005) were used. Images and tracking data were analyzed using Matlab 2013 (MathWorks Inc., US).

3.3.5.7. Statistical analysis

From cell tracks, the direction of the cells was calculated through the angle Θ between the direction of the respective gradient and the (current) cell direction. The direction of each cell was determined every 3 min. This time interval was chosen so that most cells have moved by roughly their typical diameter. Events, without any motion, were excluded from the analysis. The overall directionality of cells is then given by $\langle \cos(\Theta) \rangle$, where the average is over both time and location of the cells, with time spans and regions as indicated in the main text. Error bars represent the standard deviation of $\langle \cos(\Theta) \rangle$ determined with a bootstrapping method, where we resampled 200 times with the original sample size.

3.3.6. Author contributions

M.S., M.M. and J.S. initiated the project. J.S. and M.M planned and performed the experiments. J.M. built the pneumatic control unit for microfluidic valve operation and produced silicone wavers for microfluidic chip production. R.H. built the laserwriting microscope setup and wrote the LabView script operating it. T.F. wrote MatLab scripts to operate the microfluidic valves. V.B and T.B. were responsible for statistical data analysis. S.T. contributed to data

discussion. M.M, J.S, V.B. and M.S. wrote the main manuscript text. All authors reviewed the manuscript.

3.3.7. Acknowledgement

This work was supported by the Swiss National Science Foundation (Ambizione fellowship; PZ00P3_154733 to M.M.), the Swiss Multiple Sclerosis Society, a fellowship from the Boehringer Ingelheim Fonds (BIF) to J.S., the European Research Council (grant ERC GA 281556) and a START award from the Austrian Science Foundation (FWF) to M.S.

3.3.8. Supplemental movies

Supplemental movie S1: Representative movie of DCs migrating in the microfluidic migration chamber. Left panel: DCs migrating on fibronectin. Middle panel: Haptokinetic migration of DCs on fibronectin functionalized homogenously with CCL21 24-98 bio. Right panel: Haptotactic migration of DCs on fibronectin functionalized with an exponential gradient of CCL21 24-98 bio. Scale bars represent 50 μm .

Supplemental movie S2: Representative movie of DCs following a gradient of CCL19 in the microfluidic migration chamber. The three different concentration regimes are indicated as black boxes (CCL19_{high}, CCL19_{medium} and CCL19_{low}). CCL19/TAMRA dextran 10 kDa gradient in red. Scale bar represents 50 μm .

Supplemental movie S3: Representative movie of DCs migrating on printed CCL21 24-98 bio gradients (red). Cells are challenged with a soluble CCL19/FITC dextran 10 kDa gradient in green. Tracked areas lie within the three different concentration regimes (CCL19_{high}, CCL19_{medium} and CCL19_{low}) and are indicated as black boxes. Scale bar represents 50 μm .

3.4. Covalent, adapter based protein patterning by photobleaching

Jan Schwarz¹, Maria Nemethova¹, Remy Chait¹, Robert Hauschild¹, Calin Guet¹ and Michael Sixt¹

¹*Institute of Science and Technology Austria (IST Austria), Klosterneuburg, Austria.*

- in preparation -

3.4.1. Abstract

We introduce a UV-independent building block based photo-patterning technique, allowing for covalent immobilization of tagged molecules on arbitrary surfaces. Using a sustainable passivating surface coating, we tested our method for zero-background patterning of cell-adhesive integrin ligand, controlling cell shape, growth and migration. Our approach is versatile, requires only basic tagging chemistry and is independent of specific light sources.

3.4.2. Introduction

Controllable deposition of extracellular signaling or adhesion molecules on cell culture surfaces (also described as micropatterning) became an essential tool in all experimental fields operating with cultured cells (Ricoult et al., 2015; Théry, 2010). The goal is, to “print” molecules on surfaces to gain spatial control over signaling and/or adhesion thereby influencing cell growth (Bélisle et al., 2011; Gray et al., 2008), motility (Brandley and Schnaar, 1989; Schwarz and Sixt, 2016) or morphology (Schiller et al., 2013).

One of the main challenges in such surface engineering is to be able to print independent of the reference substrate. Patterning needs to be possible on surfaces with passivating as well as adhesive, cell culture compatible properties in order to cover a wide range of applications. Especially passivating surfaces represent a challenge, since they have to offer high reactivity for patterning but also sustainable background passivation.

In order to facilitate versatility, patterning has to enable quantitative digital patterns (Azioune et al., 2009) but also continuous gradients (Wu et al., 2012) with submicron-sized resolution. Furthermore, surface immobilization needs to be based on covalent modifications. This allows for stable and sustainable patterns for long-term applications e.g. well-free cell-culture systems, where cells adhere to a coated area but not to the passivated surroundings.

Until now, a robust and simple method combining all those features is missing. Here, we introduce a covalent, building block-based and therefore versatile photo-immobilization technique. It comprises a light dosage dependent patterning step, which is feasible on arbitrary surfaces enabling the production of sustainable patterns and gradients. We validate the method by photo-patterning of adhesive ligands on a cell repellent surface coating, thereby confining cell growth and migration to the designated areas and gradients.

3.4.3. Results and discussion

Building block based patterning combines two orthogonal reaction steps in order to surface immobilize molecules in a bioactive monolayer. In a first step, a fluorescent dye labeled adapter is covalently immobilized on any surface by photo-bleaching (Figure 43Aa) (Holden and Cremer, 2003). In a second step, the adapter binding ligand is covalently attached to the surface bound adapter (Figure 43Ab). Separation of the photobleaching and the ligand binding step hereby prevents degradation of ligand during the photobleaching step. Thus, only active and accessible ligands are presented on the surface.

Due to its covalent character, versatility and specificity, we chose the alkyne/azide 'click' system as a chemical adapter system to connect the surface immobilized adapter with the respective ligand (Figure 43B) (Rostovtsev et al., 2002). Here, azide labeled molecules or proteins are covalently attached to photo-immobilized alkynes or *vice versa*. Azide- or alkyne-modified dyes, amino acids, proteins and nucleic acids as well as labeling reagents and kits are commercially available and inexpensive due to the rising importance of click-chemistry related techniques like immunofluorescence methods.

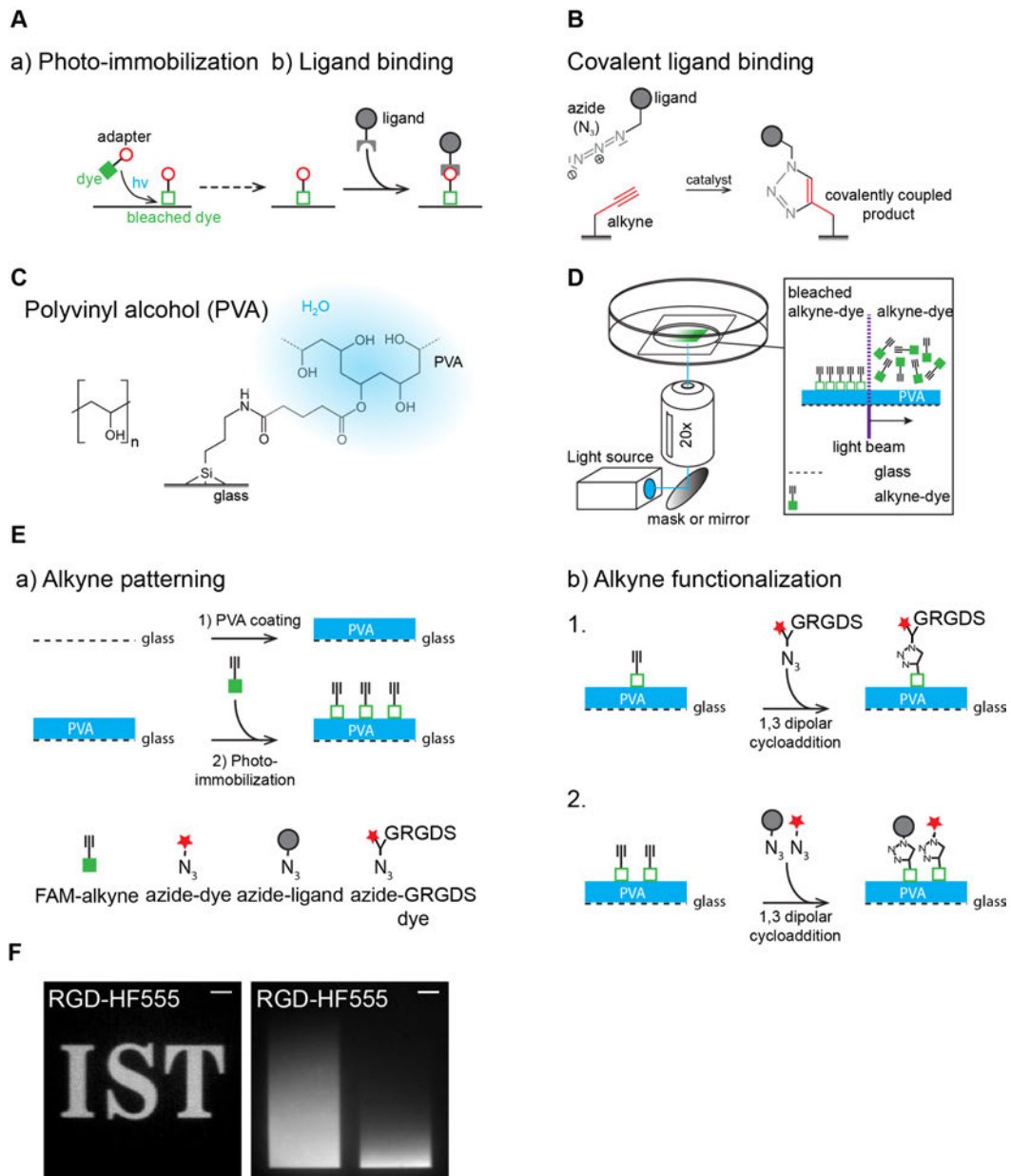


Figure 43.: Covalent protein patterning by photobleaching. (A) Schematic of building block based photo-patterning. a) Surface immobilization of dye labeled adapter molecules by photobleaching. b) Immobilization of adapter binding ligands. (B) Cu(I) catalyzed 1,3 dipolar cycloaddition of soluble, ligand bearing azides (N_3) and photo-immobilized alkynes for covalent ligand binding. Small, ~70 Da triazole linker between surface immobilized dye. (C) Polyvinyl alcohol (PVA). PVA polymer covalently bound to the aminosilane surface, forming a hydrated, passivating layer. The layer thickness is determined by PVA spin coating. (D) Schematic of alkyne-dye surface immobilization by photobleaching. Dye bleaching in close proximity to the surface leads to covalent bond formation between the bleached dye and the surface. (Holden and Cremer, 2003) Subsequently, if intact, the alkyne-functionalization can undergo 1,3 dipolar cycloaddition with a 1,3 dipole. (E) Photopatterning protocol a) Alkyne patterning: Photo-immobilization of fluorescein labeled alkyne (FAM-alkyne) on PVA coated glass slide. b) Alkyne functionalization: Immobilization of azide labeled GRGDS peptides (RGD-HF555) via 1,3 dipolar cycloaddition. Co-immobilization of azide labeled ligands and dyes. (F) Fluorescence images of RGD-HF555 patterns and gradients on PVA surfaces. Scale bar 50 μm .

As a proof of principle, we covalently immobilized the integrin ligand (GRGDS) on passivated, cell repellent surfaces to control for cell shape, growing conditions and migration. Especially for surface immobilization of adhesive ligands, like GRGDS, covalent attachment is crucial to enable proper force transduction of the cells onto the substrate. Similarly, sustainable passivation is necessary to avoid uncontrolled background adhesiveness. For surface passivation, we chose polyvinyl alcohol (PVA), a hydrophilic and passivating polymer that is bound covalently to the glass surface (Figure 43C). PVA films offer anti-adhesive properties over long time periods and can be efficiently modified by photo-bleaching (Doyle, 2001; Sugawara and Matsuda, 1995). After PVA coating, we immobilized fluorescein labeled alkyne (FAM-alkyne) on the PVA surface by photobleaching (Figure 43D and Ea). Subsequently, azidylated GRGDS can be attached to gradients and patterns of photo-immobilized FAM-alkyne via click reaction (Figure 43Eb.1). Here, we used a dye labeled version of azide-GRGDS (RGD-HF555, Supplemental Figure 4A), allowing for direct visualization and quantification of the patterns and gradients. (Figure 43F). Alternatively, azidylated ligands can be co-immobilized with inexpensive azidylated dyes (Figure 43Eb.2).

Photobleaching efficiency and therefore alkyne-dye immobilization efficiencies are maximal at the excitation maximum of the respective dye already at low light intensities (Holden and Cremer, 2003). Thus, any fluorescence microscope can be modified for patterning by photobleaching without the necessity of specific light sources (e.g. UV light). To illustrate this, we used two different microscopy setups to create patterns and gradients of FAM-alkyne/RGD-HF555 and addressed major differences: An epi-fluorescence microscope, equipped with a 470 nm LED light source. Here, patterns and gradients were generated by a controllable LCD panel inserted into the light-path of the microscope (Figure 44A) (Stirman et al., 2012). And a microscope equipped with a steerable 355 nm UV laser (Figure 44A) (Behrndt et al., 2012; Weber et al., 2013). For the LCD panel masked 470 nm LED, immobilization efficiency correlates with exposure time (Supplemental Figure

4B-D). Accordingly, laser power correlates linearly with the light intensity of the UV laser (Supplemental Figure 4D and Weber et al. (Weber et al., 2013)).

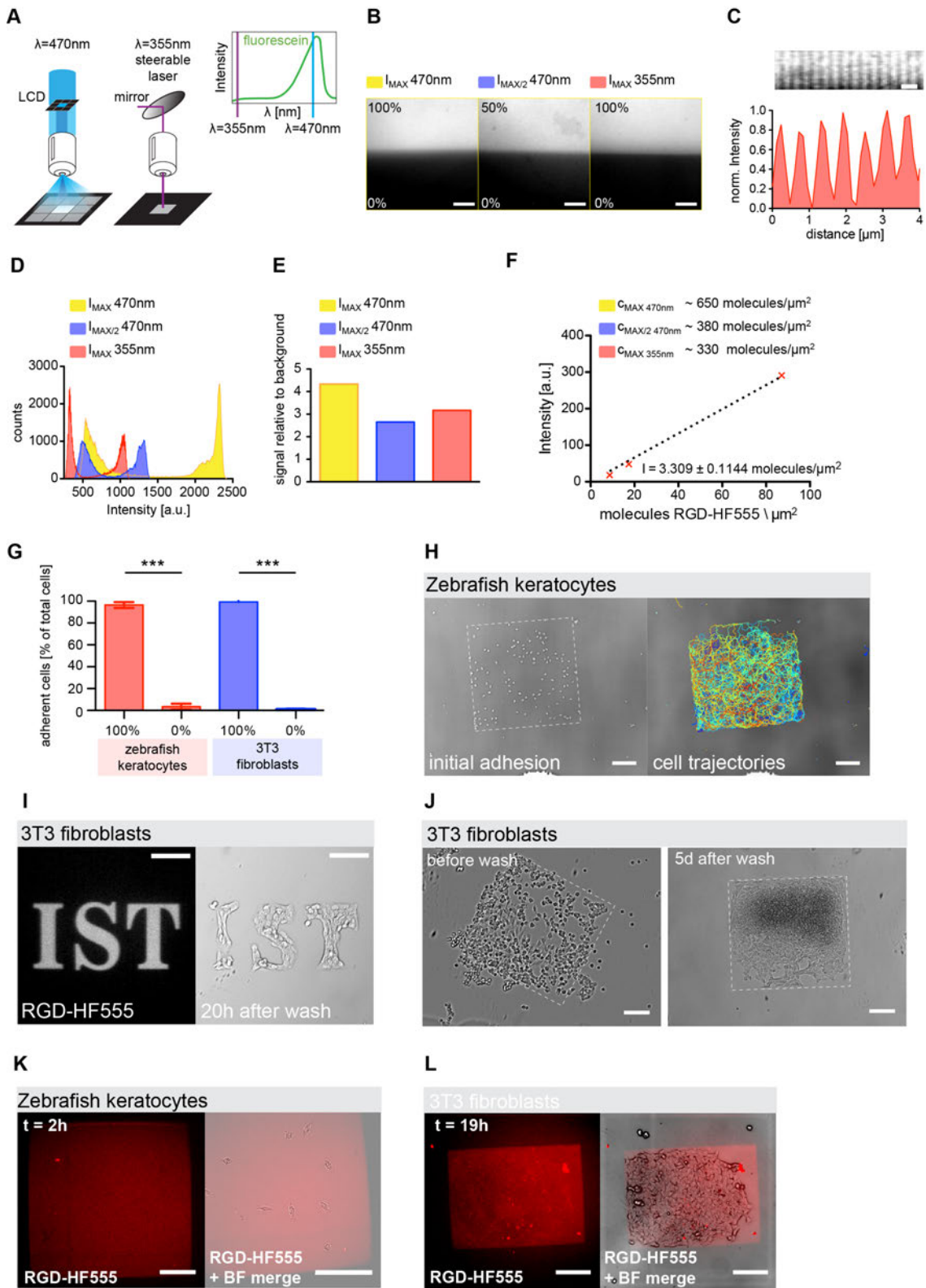


Figure 44.: Characterization of RGD-HF555 photopatterning on passivating PVA coating. A) Schematic of microscopy setups used for photo-bleaching. Left: 470 nm LED light source. Pattern generation by a controllable LCD mask in the light path of the microscope (measured contrast ratio 297:1). LED exposure time and mask dependent deposition efficiency (c_{MAX}).

Right: 355 nm laser writing. Pattern generation by pixel wise illumination. Laser intensity dependent deposition efficiency. Both setups use 8 bit greyscale images as templates with white (255) = maximal illumination and black (0) = minimal (LCD) or no illumination (laser). Excitation spectrum of fluorescein in relation to the excitation wavelengths of both microscope setups. B) Fluorescence images of maximal (100 %) and minimal (0 %) deposition of alkyne-FAM / RGD-HF555 using both patterning setups. Half maximal (50 %) deposition of alkyne-FAM / RGD-HF555 using the 470 nm/LCD setup. Scale bar 10 μm . C) Maximal resolution of alkyne-FAM / RGD-HF555 photo-immobilization. 20 x objective, 355 nm laser writing. Scale bar 1 μm . D) Intensity histograms of fluorescence images of 2B. E) Mean fluorescent signal intensity on patterned regions (100 %) relative to mean background fluorescence next to patterned regions (0 %). $n \geq 6$ images for each condition. F) Quantification of RGD-HF555 immobilization efficiency by comparison with a RGD-HF555 fluorescence intensity standard curve. $n \geq 6$ images for each condition. G) Fraction of zebrafish keratocytes (red bars, $p < 0.0001$) or 3T3 fibroblasts (blue bars, $p < 0.0001$) adhering on (100 % Intensity) or next to (0 % Intensity) 450 μm x 450 μm square patches of RGD-HF555. Patterns for highly RGD sensitive zebrafish keratocytes were generated with the 355 nm steerable laser. Patterns for less sensitive 3T3 fibroblasts were generated with the 470 nm LED light source. H) Zebrafish keratocytes migrating on a patch of RGD-HF555 printed on PVA background. Cell trajectories after $t = 2$ h. Scale bar 100 μm . I) 3T3 fibroblasts adhering on demanding shapes of RGD-HF555; $t = 20$ h after rinsing with cell culture medium to remove non-adhering cells. Scale bar 100 μm . J) Brightfield images of 3T3 fibroblasts adhering and growing on square patches of RGD-HF555; $t = 3$ h after seeding (before wash) and $t = 5$ d after washing. Scale bar 100 μm . (K) and (L) Fluorescence images of RGD-HF555 after $t = 2$ h keratocytes migration K) or $t = 19$ h 3T3 fibroblast adhesion L). Scale bar 100 μm .

Operating at the excitation maximum of fluorescein (Figure 44A), the 470 nm LED light source allowed higher maximal FAM-alkyne deposition than the 355 nm UV laser. (Figure 44B and histograms in D). However due to the contrast ratio dependency of the projector dependent system, laser based patterning showed a reduced background for similar deposition efficiencies (Figure 44D and E). We quantified surface immobilized RGD-HF555 and measured a maximal concentration of 653 ± 24 molecules/ μm^2 with the 470 nm LED and 334 ± 12 molecules/ μm^2 with the 355 nm laser (Figure 44F). The minimal spacing between single lines of RGD-HF555 was 0.58 ± 0.045 μm for patterning with a 20x objective (Figure 44C).

Next we tested the bioactivity of immobilized RGD-HF555 and the effectivity of the cell repellent PVA coating. Therefore we printed RGD-HF555 patches offering ideal adhesiveness for migrating zebrafish keratocytes and adhesive growing 3T3 mouse embryonic fibroblasts (3T3 fibroblasts) respectively. Zebrafish keratocytes only adhered in the RGD-HF555 patterned areas (100 % relative light intensity). Adhesion in non-patterned areas (0 % relative light intensity) could rarely be observed (Figure 44G, zebrafish keratocytes).

Similarly, growing 3T3 fibroblasts only grew on patterned regions, avoiding non-patterned areas (Figure 44G, 3T3 fibroblasts). This behavior could also be observed for 3T3 fibroblast growth on demanding shapes (Figure 44I). Similar to adhesion, zebrafish keratocytes migration was confined to RGD-HF555 patterned regions, as illustrated by cell trajectories (Figure 44H). Although highly motile, the cells were not able to cross the RGD-HF555/PVA interface and were forced to repolarize and change direction (Supplemental movie SM1).

To test whether the covalent PVA surface passivation is stable and therefore suited for long-term experiments like well free cell culture, we grew 3T3 fibroblasts on RGD-HF555 patches beyond confluency. Even after 5 days we could not observe cells growing or attaching outside the patterned area (Figure 44J). Accordingly, RGD-HF555 immobilization on PVA needs to be stable in order to promote sustainable cell adhesion. We imaged RGD-HF555 localization at late time-points of the respective experiments in order to test whether RGD-HF555 is consumed by migrating or growing cells. Here, we did not observe any depletion in the homogenous RGD-HF555 patch after 2 h of zebrafish keratocyte migration (Figure 44K) or 19 h of 3T3 fibroblast growth (Figure 44L). Additionally, cells did not accumulate the adhesive ligand intracellularly, as was observed for zebrafish keratocytes migrating on fibronectin patterns on surface bound PLL-PEG (Supplemental Figure 4F).

Precise control of concentration gradient properties, such as shape and steepness (c_{MAX}) of signaling or adhesive cue gradients is essential for understanding processes like haptotaxis (Brandley and Schnaar, 1989; Wu et al., 2009). To illustrate the ability to generate arbitrary homogenous gradients, we printed concentration gradients of RGD-HF555 differing in their maximal concentration (Figure 45A) and shape (Figure 45B). 3T3 fibroblasts adhering to linear and exponential RGD-HF555 gradients migrated and grew in a polarized fashion in direction of maximal RGD-concentration (Figure 45C and Supplemental movie SM2). Similarly, highly motile zebrafish keratocytes migrated preferentially in areas of a linear RGD-HF555 gradient where adhesiveness was highest for the assayed concentration range (Figure 45D

and E and Supplemental movie SM3). Hereby, cell trajectories shifted to highest RGD-HF555 concentrations

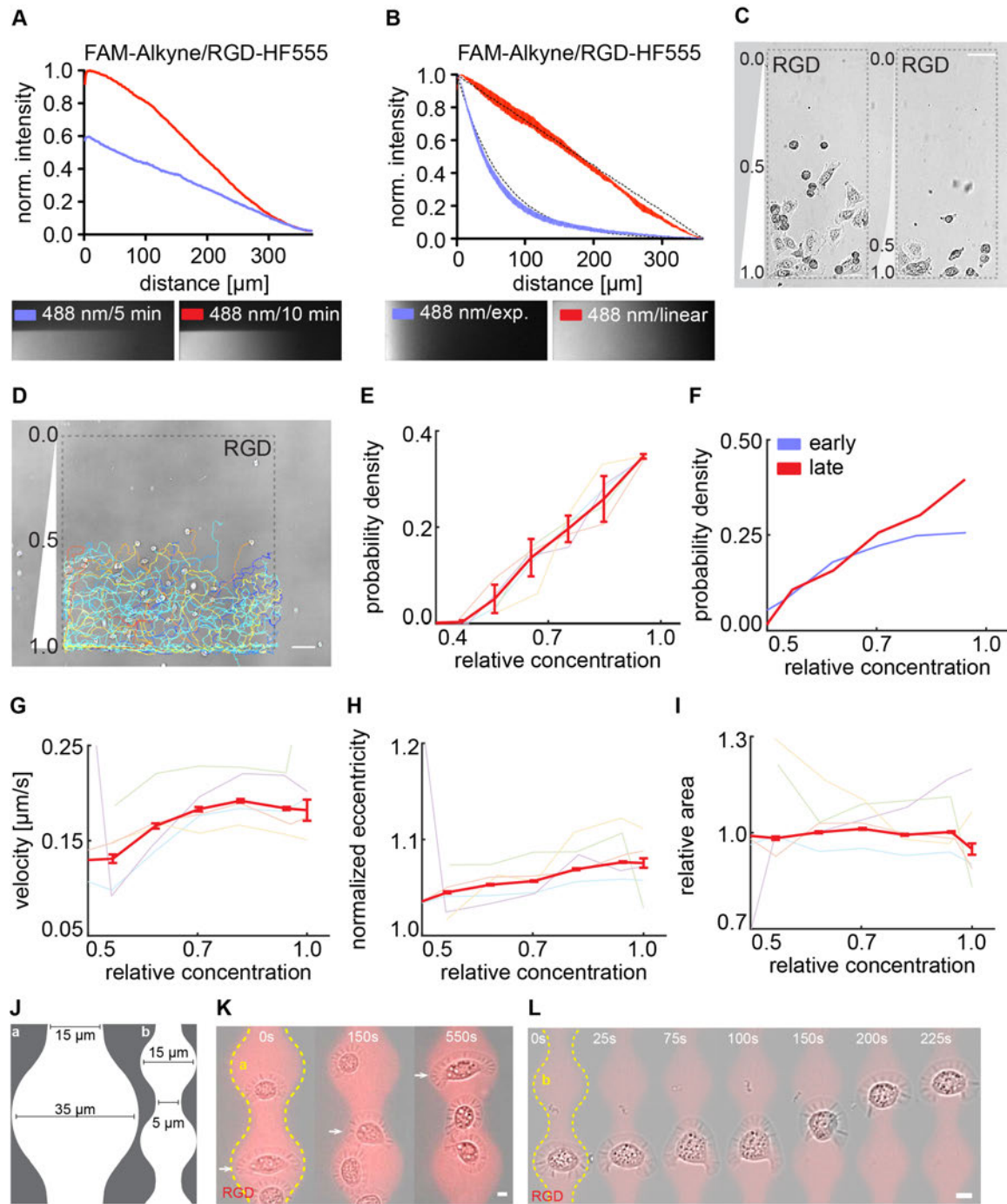


Figure 45.: Covalent, low background protein patterning as tool for probing haptotaxis and cell migration. A) Normalized intensity profiles of linear gradients of RGD-HF555. Gradient steepness dependent on 470 nm LED exposure time. Blue profile: 5 min exposure time. Red profile: 10 min exposure time. B) Normalized intensity profiles of linear and exponential like gradients of RGD-HF555. Blue profile: 5 min exposure time, exponential mask. Red profile: 5 min exposure time, linear mask. For (C)-(I) Relative RGD-HF555 concentration is given as relative light intensity. C) Brightfield image of 3T3 fibroblasts adhering and migrating on linear (left) and exponential (right) gradients of RGD-HF555. Scale bar 50 μm . D) Brightfield image of zebrafish keratocytes migrating on a linear gradient of RGD-HF555. Scale bar 50 μm . E) Distribution of zebrafish keratocyte trajectories within a linear gradient of RGD-HF555 ($t = 2$ h;

n = 5 independent experiments). F) Time dependent zebrafish keratocyte trajectory distribution within a linear gradient of RGD-HF555. Early: t = 0 - 60 min and late: t = 61 - 120 min (n = 5 independent experiments). G) Zebrafish keratocyte velocities dependent on relative RGD-HF555 concentration (n = 5 independent experiments). H) Zebrafish keratocyte shape (measured by eccentricity) dependent on relative RGD-HF555 concentration (n = 5 independent experiments). I) Total cell area of zebrafish keratocytes dependent on relative RGD-HF555 concentration (n = 5 independent experiments). J) Template for alternating wide and narrow adhesive areas influencing cell shape changes during migration. K) Zebrafish keratocyte migrating on 35 μm wide areas of RGD-HF555 with 15 μm constrictions. Scale bar 5 μm . (L) Zebrafish keratocyte migrating on 15 μm wide areas of RGD-HF555 with 5 μm constrictions. Scale bar 5 μm .

over time (Figure 45F) demonstrating the haptotactic behavior of zebrafish keratocytes on gradients of RGD-HF555. Next we tested if we are able to replicate keratocyte morphologies and migration efficiencies, obtained by migration experiments on homogenous fields of defined RGD concentration (Barnhart et al., 2011), on a single, linear gradient. As observed on homogenous fields of adhesive ligand, migration efficiency (measured by velocity) increased with adhesiveness and decreased at high RGD-HF555 concentrations (Figure 45G). Additionally, with adhesiveness, cell eccentricity increased as cells adopted the oval, fan-shaped morphology characteristic for migrating fish keratocytes (Figure 45H) (Theriot and Mitchison, 1991). However, migrating on concentration gradients, the total cell area remained constant in the observed RGD-HF555 concentration range (Figure 45I), which was not observed on homogenous fields of defined RGD concentration (Barnhart et al., 2011).

Instead of changing adhesiveness, cell spreading and eccentricity can also be influenced by available adhesive area. To illustrate this, we spatially confined migration of fish keratocytes on alternating wide and narrow regions of RGD-HF555 (Figure 45J-L). In 35 μm wide areas, cells showed a fan like lamellipodium that collapsed in narrow, 15 μm wide constrictions (Figure 45K and Supplemental movie SM4). In 15 μm wide areas with 5 μm constrictions (corresponding half a cell diameter), parts of the lamellipodium protruded along the constriction, trailing the bigger cell body to the next, wide area (Figure 45L and Supplemental movie SM5). For both patterns, cells moved only on patterned areas, avoiding passivated background areas.

due to light scatter and LCD dark pixel light leakage just outside of the pattern ($r_{ex} = -0.02$) that is about an order of magnitude slower than that at the pattern center ($r_{ex} = -0.02$). E) Linear input power - laser intensity correlation of the steerable 355 nm laser. F) Fibronectin-biotin immobilized on streptavidin-Cy3 (SA-Cy3). SA-Cy3 immobilized on PLL-PEG-biotin adsorbed glass surface. Scale bar 50 μm .

In summary, we introduce a versatile building block based, covalent photo-patterning technique, able to produce digital patterns and homogenous concentration gradients on arbitrary surfaces. Without the necessity of strong UV light, patterning can be carried out on standard fluorescence microscopes with minor modifications. In combination with a cell repellent PVA surface coating, we were able to confine cell growth and migration on patterned areas and induce haptotactic behavior on gradients of covalently patterned adhesive ligand.

3.4.4. Materials and methods

3.4.4.1. PVA coating

Glass bottom dishes (MaTek, USA) were polyvinyl alcohol (PVA) coated as described earlier. (Doyle, 2001) Briefly, the glass surface of a MaTek dishes was activated for 25 min at room temperature with 50 % nitric acid (Sigma Aldrich, St. Louis, Missouri). After activation, the dish was rinsed over night in ddH₂O. Subsequently, the glass surface was deprotonated by incubation for 15 min at room temperature with 200 mM NaOH (Sigma Aldrich, St. Louis, Missouri). The deprotonated and washed glass surface (ddH₂O) was blow-dried using canned nitrogen. By incubation with 1 % aqueous solution of APTES (w/v, Sigma Aldrich, St. Louis, Missouri), the glass surface was amino-silanized for 5 min and carefully washed with ddH₂O for 10 min. The amino-silanized glass surface was then cured at 65 °C for 3 h. For aldehyde activation, surfaces were incubated with 0.5 % aqueous glutaraldehyde (Sigma Aldrich, St. Louis, Missouri) solution for 30 min at room temperature. A ~ 200 nm thick poly-vinyl alcohol (PVA, 6 % aqueous solution with 0.1 % 2N HCl) film was bound to the glutaraldehyde activated surface by spin coating (40 s at 7000 rpm; 550 rpm acceleration within 18 s). Prior to use, dishes were washed carefully with ddH₂O.

3.4.4.2. Photo-immobilization of FAM-alkyne

3.4.4.2.1. Laser writing

Approximately 20 μ L FAM-alkyne (6-isomer, Lumiprobe, Hannover, Germany) were placed in the middle of a PVA coated glass dish and patterns were written using a steerable, pulsed UV laser ($\lambda = 355$ nm) as described before (Bélisle et al., 2008). Briefly, the UV laser was focused into the interface between the bottom of the PVA coated glass slide and the FAM-alkyne solution with a long working distance 20x objective (Zeiss LD Plan Neo 20x 0.4). A pair of high-speed galvanometric mirrors, controlled by a custom program, was moving the focal spot within the FAM-alkyne droplet. The gradient pattern was specified by an image whose pixel values determined the light dose used for bleaching. Careful calibration allowed compensating for the off-center drop-off of numerical aperture of the objective as well as the geometric distortions from the imperfect imaging of the scan mirrors into the back aperture of the objective. This allowed gradient writing in the full field of view of the objective. For each spot, the total light dose was split up into multiple laser pulses in order to average out the pulse-to-pulse power variability of the laser. The gradient was written one spot at a time with the scanning mirrors moving the laser focus by about half the diameter of the focus spot in order to create a continuous pattern. In this fashion, crosstalk between different locations in the pattern was minimized since the scattered light from one spot did not reach the threshold of bleaching elsewhere unlike projector based systems where the entire area is exposed simultaneously. The low wavelength of the UV laser lead to a high lateral resolution (~ 0.7 μ m) and the low crosstalk to a high dynamic range ($\sim 100:1$) of the gradient pattern. The writing speed was limited by the laser's pulse frequency of 1 kHz. A full description of the hardware employed can be found in Behrndt *et al.* (Behrndt et al., 2012).

3.4.4.2.2. Projector

Projector-based photo patterning was accomplished using a microscope-coupled LCD projector similar to one designed by Stirman, *et al.* (Stirman et al., 2011). Briefly, the light source of an LCD-based overhead projector (Panasonic

PT AE6000E; contrast ratio $297\pm 1:1$) is replaced by a 470 nm LED source (Thorlabs M470L3). The projection lens is removed and the projected image coupled by a relay lens (Thorlabs AC508-100-A-ML, $f = 100$ mm) into the rear port of an Olympus IX83 inverted microscope. A 50/50 beamsplitter (Thorlabs BSW10R) directs half of the incident light through a 20X objective (Olympus LUCPLFLN20XPh) to the substrate surface. The reflection of the projected pattern from the substrate-air interface is imaged on a digital camera (Hamamatsu Orca Flash4.0v2). With the microscope focused on the substrate surface, the projector is adjusted to bring the projected image and microscope focal planes into alignment. Custom software utilizing MATLAB and MicroManager (Edelstein et al., 2010) is used to generate and project patterns, and to control LED illumination and the microscope. When exposing patterns, a prepared substrate is washed and dried by aspiration before mounting securely on the microscope's stage. The microscope focus is then adjusted to bring a projected target pattern into focus at the substrate surface. When multiple patterns are to be exposed on a single substrate, focal offsets are manually determined at the extremities of the pattern array and offsets at intermediate locations estimated by least squares fitting of a plane through the measured points. The LED is extinguished and a small volume of FAM-alkyne is carefully deposited onto the target surface without displacing the substrate. The system then automatically cycles sequentially through the pattern locations, at each exposing specified patterns for corresponding durations.

3.4.4.3. 1,3 dipolar cycloaddition

Volume	Component
2.2 μL	Click-it cell reaction buffer (Thermo)
19.8 μL	ddH ₂ O
2.5 μL	Reaction buffer additive (Thermo)
0.5 μL	CuSO ₄
5 μL	RGD-HF555 (30 μM)

Table 3.: Click reaction mixture.

GRGDS-HF555-Azide (RGD-HF555) was custom synthesized by Eurogentec (Serain, Belgium). Following laser writing or projector based patterning, the alkyne patterned PVA surfaces were washed with PBS and incubated for 30 min in the dark with the reaction mixture (Table 3). After washing with PBS, RGD-HF555 patterns can be stored for up to a month under PBS.

3.4.4.4. Quantification of immobilization efficiency

Fluorescence intensities of a dilution series of RGD-HF555 (0.8 ng/mL, 0.16 ng/mL and 0.08 ng/mL) were measured in a defined volume of a 12.87 μm high PDMS chamber (4.2×10^{-8} mL; $57.1 \mu\text{m} \times 57.1 \times 12.87 \mu\text{m}$) and a standard curve was calculated (Fluorescence intensity = 3.309 ± 0.1144 molecules/ μm^2). Fluorescence intensities of patches of surface immobilized RGD-HF555-Azide were measured using the same imaging settings as for the dilution series. Immobilized RGD-HF555 concentrations were calculated from measured fluorescence intensities using the obtained standard curve.

3.4.4.5. Design and fabrication of the PDMS chamber

The photomask design for the polydimethylsiloxane (PDMS) chamber was drawn with Coreldraw X6 (Corel corporation, US) and printed on an emulsion film transparency at a resolution of 8 μm (JD Photo Data & Photo Tools, UK). A mold of the chamber was produced by photo-lithography on a silicon wafer as described earlier with minor modification (Mehling et al., 2015). In brief, the chamber mold was spin-coated with hexamethyldisiloxane (HMDS) at 3000 rpm for 30 s and then baked at 110 °C for 1 min. Following this, the wafer was spin-coated with SU 8 GM1040 (Gersteltec, Switzerland) at 450 rpm for 45 s. The wafer was soft baked at 110 °C for 5 min. Photoresist was then exposed to ultra violet (UV) light for 15 min using a beam expanded 365 nm UV LED, (M365L2-C1–UV, Thorlabs GmbH, Germany). After UV exposure, the wafer was post-baked for 2 min at 110 °C. The wafer was developed in AZ-726-MIF developer for 5-7 min and then rinsed in water.

The chamber was fabricated by soft-lithography as described previously (Kellogg et al., 2014; Mehling et al., 2015). In brief, a PDMS mixture (RTV615, Momentive, US) of 10:1 (potting-agent:cross-linking agent) was mixed and degassed by using a mixing machine (Thinky ARE-250, Japan). Next, the PDMS mixture (70 g) was poured over the wafer, degassed for 20 min in a dessicator, and cured for 1 h at 80 °C. Following this, PDMS was peeled off the mold and holes were punched for fluidic inlets using a 22-gauge mechanical puncher. The PDMS chamber and a glass slide were exposed to air plasma for 30 s for bonding and were then baked at 80 °C for at least 12 h. The 300 µm wide chamber had a height of 12.87 µm as measured by confocal microscopy.

3.4.4.6. Cell culture and primary cells

Swiss 3T3 mouse fibroblasts were maintained in high-glucose Dulbecco's modified eagle medium (DMEM+GlutaMAX) supplemented with 1% penicillin, 1% streptomycin, 1% glutamine and 10% fetal bovine serum (Gibco Life Technologies) at 37 °C.

Zebrafish used in this study were bred and maintained according to the Austrian law for animal experiments (“Österreichisches Tierschutzgesetz”). For preparation of keratocytes, scales from wild type zebrafish (strain AB) were transferred to plastic cell culture dishes containing start medium as described previously (Anderson, K. S. & Small, J. V. Preparation and fixation of fish keratocytes. *Cell Biology: A laboratory Handbook*, Vol. 2, 372–376 (Academic, 1998). After 1 day incubation at 28 °C monolayers of cells were treated with 1 mM EDTA in running buffer for 45-60 min to release individual cells.

3.4.4.7. Adhesion assays and migration assays

3.4.4.7.1. 3T3 Fibroblasts

Confluent 3T3 fibroblasts were detached with 0.05 % trypsin-EDTA. Depending on the experiment, 10^4 - 10^5 cells were plated onto GRGDS functionalized coverslip and incubated 3-4h at 37 °C to allow for attachment. Prior recording on the microscope, unattached cells were removed by gentle washing with medium.

3.4.4.7.2. Zebrafish keratocytes

EDTA released zebrafish keratocytes were washed with PBS, detached with 0.05 % trypsin-EDTA and replated on GRGDS functionalized coverslips. After 30 min incubation at rt nonattached cells were washed away.

3.4.4.8. *Imaging*

Adhesion and migration assays were recorded on a Leica DMIL LED with 10x/0.22 High Plan I objective. For RGD-HF555 imaging and quantification, images were obtained using 20x/0.8 air and 63x/1.4 oil immersion objectives on a Zeiss Axio Observer microscope equipped with an external light source (Leica).

3.4.4.9. *Cell tracking, image processing and statistical analysis*

For image processing and cell tracking, Fiji (Schindelin et al., 2012) and a plugin for manual tracking (“Manual Tracking”, Cordelieres 2005) were used. Images and tracking data were analyzed using Matlab 2013 (MathWorks Inc., US). Brightfield movies were preprocessed by normalizing the brightness of each frame. Then the time averaged median was subtracted to remove non-motile particles such as dirt, dead cells etc. from the images. Subsequently a pixel classifier (Ilastik (Sommer et al., 2011)) was manually trained on one data set to distinguish cell from non-cell pixels. The time projection of cell pixels was used to visualize the printed area and the RGD-HF555 gradient was manually added to the movies as an extra channel. All cells were manually tracked using Fiji (Schindelin et al., 2012) and its plugin for manual tracking (TrackMate). The position of the cells' center was used to determine the concentration by means of the extra channel. Furthermore the localization of the cells' center is used as a seed point for a seeded watershed segmentation which in turn yields the outline, shape, and area of the cells. The probability density was defined as the number of localizations obtained through the tracking at a specific concentration divided by the total number of localizations. Likewise the velocity distribution is derived. Cell eccentricity was measured as the euclidian length of the cell

perimeter divided by the length of the circumference of a circle with the same area. 1= circle, >1 more line like.

3.4.5. Supplemental movies

3.4.5.1.1. Supplemental movie SM1

Zebrafish keratocytes migration spatially confined to a square of RGD-HF555. Left panel: Fluorescence image of a square patch of RGD-HF555. Middle panel: Brightfield movie of zebrafish keratocytes migrating on a square patch of RGD-HF555. Right panel: Cell trajectories of zebrafish keratocytes migrating on a square patch of RGD-HF555. Scale bar 50 μm .

3.4.5.1.2. Supplemental movie SM 2

3T3 fibroblast growth and migration spatially confined to gradients of RGD-HF555. Left panel: Fluorescence image of linear (left) and exponential (right) gradients of RGD-HF555. Right panel: Brightfield movie of 3T3 fibroblast growth and migration spatially confined to a linear (left) and exponential (right) gradient of RGD-HF555. Scale bar 50 μm .

3.4.5.1.3. Supplemental movie SM 3

Zebrafish keratocytes migration spatially confined to a linear gradient of RGD-HF555. Left panel: Fluorescence image of a linear gradient of RGD-HF555. Middle panel: Brightfield movie of zebrafish keratocytes migrating on a linear gradient of RGD-HF555. Right panel: Cell trajectories of zebrafish keratocytes migrating on a linear gradient of RGD-HF555. Scale bar 50 μm .

3.4.5.1.4. Supplemental movie SM 4

Zebrafish keratocyte migrating on an alternating concave/convex pattern of RGD-HF555. Width convex area: 35 μm , width concave area: 15 μm . Scale bar 5 μm .

3.4.5.1.5. Supplemental movie SM 5

Zebrafish keratocyte migrating on an alternating concave/convex pattern of RGD-HF555. Width convex area: 15 μm , width concave area: 5 μm . Scale bar 5 μm .

3.4.6. Author contributions

J.S. and M.N. performed the experiments; M.S. and J.S. initiated the project and designed the experiments. R.H. built the Laser writing microscope, wrote the LabView protocol and was responsible for data analysis; R.C. supported by C.G. built the projector based photo-printing microscope and helped with pattern generation. All authors were involved in interpretation of results and preparation of the manuscript.

3.4.7. Acknowledgements

This work was supported by the Boehringer Ingelheim Fonds, the European Research Council (ERC StG 281556) and a START Award of the Austrian Science Foundation (FWF). We thank the Imaging Facility of IST Austria for excellent support.

4. Discussion

Throughout this work, we utilized a photo-immobilization technique that allowed us to precisely control CCL21 gradient shape and total CCL21 concentration (chapter 3.1 Quantitative analysis of dendritic cell haptotaxis). With this system at hand, we were able to identify optimal gradient properties for perception of immobilized CCL21 and address the role of signal termination for haptotactic gradient sensing (chapter 3.2 Dendritic cells interpret interstitial CCL21 gradients in a signal-to-noise ratio governed, GRK6 dependent manner.). Furthermore, by chemokine photo-immobilization inside a microfluidic chip that in addition allows for control over diffusible gradient conditions we created an assay for coinciding immobilized and soluble guidance cues (chapter 3.3 A microfluidic device for measuring cell migration towards substrate bound and soluble chemokine gradients). Adapting the photo-immobilization technique for covalent surface immobilization on passivating surfaces enabled us to expand our method for integrin ligand induced, adhesion guided haptotaxis (chapter 3.4 Covalent, adapter based protein patterning by photobleaching).

4.1. DC haptotaxis assay

4.1.1. Photo-patterning

During the last decades, many protein micro-patterning techniques have been developed to spatially control for protein concentration and presentation, with varying maximal resolution, pattern size and differing in their ability to generate homogenous gradients or digital patterns (Ricoult et al., 2015). As any specialized application, the generation of surface immobilized chemokine gradients has to meet certain requirements: (1) The technique has to allow for the creation of homogenous gradients on the length scale of a DC. (2) Patterning needs to be additive in order to avoid perturbation from the reference substrate. (3) The chemokine has to be presented in a biologically active and quantifiable state.

Photo-patterning techniques turn out to be ideally suited for protein micropatterning allowing the generation of detailed shapes and light dosage dependent gradients (Bélisle and Costantino, 2010; Holden and Cremer, 2003; Strale et al., 2016; Sugawara and Matsuda, 1995). In general, light based techniques can be utilized in a subtractive or additive manner (Figure 19, chapter 1.4.4.4). Subtractive photo-ablation based techniques require reference substrates for blocking or passivating the non-patterned regions (Azioune et al., 2009; Strale et al., 2016). The resulting differences in adhesive properties of the reference substrate and the chemokine-patterned areas might add differential integrin signaling to chemokine receptor signaling during migration. Hence, for quantitative analysis of chemokine guided haptotaxis integrin signaling needs to be constant and therefore only additive photopatterning methods qualify for chemokine micropatterning.

Additionally, direct photo-immobilization of the ligand should be avoided. Photoreactions induce radical intermediates and yield by-products that are highly reactive. Depending on the light dosage used for unspecific immobilization, multiple layers of biologically inactive or inaccessible ligands are formed (Holden and Cremer, 2003; Sugawara and Matsuda, 1995). If specific, mainly UV dependent photoreactions are used, bearing the risk of altering or destroying the patterned ligand by light induced rearrangements (Hoyle and Bowman, 2010). Therefore such reactions might impede quantification of active, surface bound ligands.

In order to allow for quantification and to restrict surface presentation to bioactive and accessible ligand, functional monolayers are desired (Mrksich and Whitesides, 1996). Using photobleaching of fluorescent dyes as an UV independent photo-immobilization step and separating ligand immobilization from the photo-reaction allows formation of a functional monolayer of ligands (Holden and Cremer, 2003). Hereby, biotin tagged fluorescein is surface immobilized in a light dosage dependent manner creating digital patterns or homogenous gradients. Subsequently, functional surface immobilized biotin is bound by streptavidin, serving as mediator to immobilize biotinylated ligands, such as chemokines.

4.1.2. CCL21 modification

CCL21, like other haptotactic chemokines, exhibits a basic c-terminal extension (de Paz et al., 2007; Love et al., 2012). This highly charged tail enables tissue immobilization *in vivo* (Middleton et al., 1997; Patel et al., 2001; Weber et al., 2013). While being useful for micropatterning techniques based on unspecific surface immobilization (Girrbach et al., 2016), it mediates unspecific background binding in non-patterned and non-passivated areas. Therefore we used a c-terminally truncated version of CCL21 (CCL21 24-98) offering only the domains necessary for CCR7 activation (Hirose et al., 2002). Surface immobilization via streptavidin requires a c-terminal biotin tag for binding streptavidin (Bélisle et al., 2008). In order to avoid steric hindrance within the biotin binding pocket of streptavidin (Livnah et al., 1993) and to foster accessibility for receptor binding, we introduced 3 consecutive 12-atom PEG spacers between the c-terminus of the truncated CCL21 (CCL21 24-98) and the biotin (CCL21 24-98 bio). Problems with bioactive presentation of small peptidic ligands (fMLP and RGD, Jan Schwarz unpublished data) emphasize the necessity of such linkers for accessibility.

4.1.3. DC migration conditions

Effective DC migration requires the topological support of fibrillar gels (Lämmermann et al., 2008) or physical confinement (Renkawitz et al., 2009). In 3D collagen gels, migration conditions seem ideal, however to quantitatively assess migratory behavior, cell trajectories need to be analyzed in 3D. Confinement under an agarose sheet limits DC migration to 2D, while offering physical support (Renkawitz et al., 2009). However inhomogeneity of the agarose, concerning hydration and therefore stiffness does not allow quantitative analysis of cell speed and directionality. Therefore, we confined DCs between two homogeneously spaced PDMS covered glass slides offering constant confinement and therefore constant migration conditions throughout the whole migration chamber (Le Berre et al., 2014). That very confinement however impedes monitoring of intracellular, lamellipodial dynamics and protein or molecule distribution within the thin lamellipodium for example by total

internal reflection fluorescence (TIRF) microscopy. For such studies, agarose confined cells can be monitored during haptotactic cell migration (chapter 5, Figure 47C).

In vivo, CCL21 is immobilized on heparan sulfates (Bao et al., 2010; Weber et al., 2013). DCs encountering CCL21 *in vivo* therefore are embedded in chemokine and cell polarization induced by the experienced chemokine gradient can align with the gradient direction. In our *in vitro* setup, CCL21 is presented in 2D. Cells experiencing the chemokine gradient are exposed to the highest CCL21 signal on the side facing the surface whereas the rest of the cell is not in contact with the chemokine. Independently of gradient direction, surface immobilized CCL21 induces cell polarity in direction of the surface. Gradient direction therefore might induce weaker directional response than *in vivo*. As a tradeoff for precisely controlled gradient shapes, chemokine concentrations and quantitative imaging we thus measure lower directionalities *in vitro*.

4.2. DC haptotaxis and CCR7 desensitization

4.2.1. CCL21 gradient *in vivo*

For a rapid adaptive immune response but also for the induction of tolerance, DCs need to find the lymphatic vessels independently of only transiently induced stimuli (Reis e Sousa, 2006). Therefore, gradients of immobilized guidance cue that induce DC haptotaxis could represent 'stable routes' for trafficking DCs. Recently we were able to prove the existence of such immobilized 'routes' (Weber et al., 2013). Secreted by lymphatic endothelial cells, CCL21 binds to charged components of the ECM surrounding lymphatic vessels. It is accumulating in close proximity of the lymphatic vessels thereby forming a haptotactic gradient towards them. By obtaining detailed images of the CCL21 distribution within the lymphatic vessel network in the mouse ear dermis we were able to identify a conserved gradient shape originating from the vessels (Figure 29). The measured exponential decay of CCL21 most likely represents a result of hindered diffusion (1.2.4). Exponential and exponential-

like gradients, for a large range of concentrations, locally have a higher gradient steepness compared to the absolute concentration than linear ones, which might offer higher potential to induce directional response (Ferrell, 2009). If chemokine immobilization influences detection, for example by altered signal termination mechanisms, DCs might be dependent on such signal-optimized gradients.

4.2.2. DC haptotaxis

In vivo, trafficking DCs are subject to a variety of topological or mechanical constrain as well as diffusing factors (Del Prete et al., 2007). We isolated haptotactic behavior from external ‘distractions’ and varied topological constrain in a defined *in vitro* environment, allowing for control of gradient- and migration conditions. To this end, we offered homogenous physical confinement to migrating DCs providing constant migration conditions (Figure 30, Supplemental Figure 1D and E). We combined this confinement with a dose dependent chemokine photo-patterning technique that enables the presentation and quantification of immobilized, bioactive CCL21 (chapter 3.1). This enabled us to study the gradient dependency of DC haptotaxis by altering CCL21 gradient shape and concentration regimes in analogy to the gradients observed *in vivo* (Figure 29 and Figure 31).

Intriguingly, exponential-like immobilized CCL21 gradients, such as the one observed *in vivo* provided most potent haptotactic potential (Figure 32). Hereby, low CCL21 concentrations were perceived better than higher concentrations. For linear immobilized CCL21 gradients only a defined concentration range and steepness effectively induced haptotactic behavior. These observations reflect the quality of the signal provided on a cells scale (Figure 33). Consequently, haptotactic CCL21 sensing is limited already on the level of signal detection, irrespective of the underlying signal integration mechanism. Following this hypothesis, DCs expressing lower levels of CCR7, such as CCR7^{+/-} DCs should saturate already at lower concentrations of immobilized CCL21 and hence shift the haptotactic response towards lower concentrations.

4.2.3. Influence of chemokine immobilization on signal desensitization and haptotaxis

The observed dependency on signal quality for immobilized CCL21 might be a result of altered ligand accessibility and receptor motility within the membrane. Presentation of tissue immobilized CCL21 and therefore accessibility for the respective receptor differs compared to purely soluble and diffusing chemokine. Hence, mechanisms relying on mobility and accessibility of the ligand, like signal termination and signal adaptation – if existent – might differ for surface associated receptor/ligand complexes.

Internalization of the CCR7 signaling complex is not enhanced by CCL21 binding (Byers et al., 2008; Otero et al., 2006). Hence, signal adaptation in order to enhance low quality spatial CCL21 signals seems to be missing, explaining the signal quality dependency of haptotactic DCs observed *in vitro* (chapter 3.2). Internalization independent signal termination, as observed for CCL21 induced CCR7 desensitization (Byers et al., 2008; Kohout et al., 2004; Otero et al., 2006) is possible independently of the presentation state of the ligand and therefore probably well suited for surface bound and soluble presented CCL21 (Schumann et al., 2010). Additionally, a prolonged retention time of the activated receptor in the plasma membrane allows for prolonged accessibility of the receptor for kinetically slow or energetically unfavorable rearrangements or interactions. CCL21 biased signaling might therefore be a result of retention of activated CCR7 in the plasma membrane (Hauser et al., 2016). If immobilized ligands necessitate desensitization without rapid internalization, CCL21 biased signaling might have resulted from its immobilized presentation state. Therefore, the presentation state of the ligand itself would be able to influence receptor signaling. CCL19 induces rapid internalization of the CCR7/CCL19 complex and therefore effective signal adaptation (Kohout et al., 2004; Otero et al., 2006). Hence, surface immobilization of soluble CCL19 might allow us to draw conclusions if immobilization and therefore reduced accessibility of the ligand is influencing receptor recycling and hence migratory response.

4.2.4. Influence of CCR7 desensitization on haptotactic gradient sensing *in vitro*

If haptotactic gradient sensing is highly dependent on the quality of the chemokine gradient, perturbations of the signal detection mechanism might influence haptotactic gradient sensing more severely than chemotactic gradient sensing. Hereby, CCR7 signal termination by GRKs seems to be a promising candidate. Although CCR7 desensitization by GRK3- and 6 has been studied intensively in a biochemical context for cells lacking either the kinases or the kinase affected c-terminus of CCR7 (Kohout et al., 2004; Otero et al., 2006; Zidar et al., 2009), quantitative studies concerning migratory effects are missing. In our *in vitro* experiments, DCs lacking GRK6 and therefore CCR7 signal termination showed impaired haptotactic gradient sensing in low concentration regimes of the printed CCL21 gradients. However, gradient sensing was partially restored towards high concentrations of surface bound CCL21 (Figure 35). Thus, the haptotactic response of GRK6^{-/-} DCs seems to be shifted towards higher concentrations of CCL21. So far we cannot explain why high CCL21 concentrations are perceived better. The behavior was reminiscent of an intracellular concentration threshold, since both, linear and exponential like gradients evoked similar responses in similar concentration regimes. In analogy to a proposed GRK2 dependent desensitization mechanism (Penela et al., 2014), missing signal termination might hyperstimulate the cell, thereby rising the threshold for the induction of effective polarized signaling and eventually polarized the cytoskeletal response.

The migratory behavior of cells lacking desensitization of CXCR4 (Minina et al., 2007) or FPR1 (Liu et al., 2012) displayed changes in persistence rather than directionality (see introduction 1.3.2.2). Unfortunately, we were not able to assess migration persistence as measured by Maiuri *et al.* (Maiuri et al., 2015) due to the limited length of the cell trajectories. However, trajectories did not show obvious changes in persistence as shown by Liu et al. (Liu et al., 2012).

Surprisingly, GRK6^{-/-} DCs did not show impaired chemotaxis towards soluble gradients of CCL21 in concentration regimes similar to immobilized CCL21 *in vitro* (Figure 35). Additionally, preliminary experiments show that WT

DCs and DCs lacking GRK6 showed a similar reduction of the chemotactic response in shallow chemotactic gradients of CCL21 (chapter 5, Figure 47B). Therefore, GRK6 dependent CCR7 termination seems to be crucial for the interpretation of substrate-immobilized gradients of CCL21 and dispensable for soluble gradients within the range of CCL21 concentrations tested. However, to ultimately discuss the cause driving this difference in recognition, the detection and interpretation of chemokines presented in soluble and immobilized fashion need to be addressed in more detail. One possible explanation might be the impaired motility of the receptor/CCL21 complex within the plasma membrane due to the surface immobilization of CCL21. As a result CCR7 clustering, which was recently demonstrated to boost DC migration, can be impaired or kinetically hindered (Hauser et al., 2016).

4.2.5. Influence of CCR7 desensitization on haptotactic gradient sensing - *in vivo*

DCs lacking GRK6 had difficulties entering the interstitium of mouse ear dermal explants in low concentration areas of the ear preparation (Figure 36). Although initial adhesion to CCL21 covered substrate was unaffected by the lack of GRK6 (Supplemental Figure 1F), directional invasion seemed impaired. Hence, the *in vivo* observations support the data collected *in vitro* but also emphasize the signal termination dependency for effective haptotactic migration.

In vitro, chemotactic gradient sensing and migration efficiency of DCs lacking GRK6 was unaltered. Additionally, the ability of GRK6^{-/-} DCs to follow chemotactic signals might have an effect in our *in vivo* studies as well. Once GRK6^{-/-} DCs entered dermal explants at higher concentrations of CCL21 we could not detect any difference regarding their ability to reach the vessel and subsequently the lymph node (Supplemental Figure 3). Truncation of tissue bound CCL21 in the mentioned areas and thereby release of soluble CCL21 (shedding) might form areas and gradients of soluble CCL21 which can be interpreted and therefore additionally instruct GRK6^{-/-} DC migration (Schumann et al., 2010).

4.2.6. Kinetic effects of CCL21 immobilization and impaired desensitization

Our *in vitro* experiments show that velocities of haptotactic DCs correlate with their directionality (Supplemental Figure 2). In accordance with cell directionality, cells increase their speed at optimal concentrations of CCL21 and slow down at higher concentrations (Figure 34). Similarly *in vivo*, DCs increase their velocity and directionality towards the lymphatic vessel and slow down in close proximity (Weber et al., 2013). This mechanism is referred to as *orthotaxis* (Sarris et al., 2012). However, probably due to the topologically demanding cell and fiber network in the interstitium, DCs are considerably slower *in vivo* than in our *in vitro* assay (Weber et al., 2013; Wolf et al., 2013). Covering a wider spectrum of DC velocity under *in vitro* conditions, we are able to obtain a much more detailed view on changes in migration kinetics and directionality compared to observations *in vivo*. Reduction of DC velocity at high concentrations might offer a useful side effect to concentrate homing DCs at the lymphatic vessels. Subsequently, local signals on lymphatic endothelial cells induce transmigration into the lumen of the vessel (Pflücke and Sixt, 2009; Tal et al., 2011).

DCs lacking GRK6 showed reduced migration efficiency independently of gradient shape or CCL21 concentration (Figure 35D). In cancer cells, guidance cue induced ERK signaling enhances migration velocities by increased lamellipodial protrusions (Mendoza et al., 2015). ERK and other kinases of the MAP kinase pathway are a direct target of GRK6 signaling (Zidar et al., 2009). Analogously, reduced ERK signaling of GRK6 deficient DCs might be responsible for this decline in velocity. Since CCL19 induced CCR7 activation is inducing ERK signaling via GRK6 as well, we might be able to observe similar effects for DCs lacking GRK6 migrating on surface immobilized CCL19. Additionally, ERK1/2/ inhibition of WT DCs migrating in similarly confined environments could yield similar results.

4.3. Coinciding soluble and immobilized guidance cues

4.3.1. Microfluidic chip

The assay used in the previous chapter allows for precise control over immobilized CCL21 but is not suited for the generation of controlled, diffusive gradients of soluble guidance cues. However, *in vivo* haptotactic gradients rarely occur in an isolated fashion. DCs shed immobilized CCL21, releasing a soluble form of CCL21 (Schumann et al., 2010). Within the T-cell zones of the lymph node CCL19 coincides with both immobilized and truncated CCL21, organizing DC and lymphocyte interaction (Luther et al., 2000). Furthermore, mature DCs secrete a plethora of cytokines and secondary guidance cues like LTB₄ and CCL19. Some of those secreted molecules have the potential to alter DC behavior, morphology and migration (Del Prete et al., 2007). Mesenchymal cells, epithelial cells or cancer cells are influenced by mechanical guidance, e.g. changing adhesiveness or substrate stiffness. Additionally, RTK ligands, like growth factors chemotactically influence their morphology and migration (Yang and Weinberg, 2008).

To be able to address those systems, we developed an *in vitro* setup allowing us to study the interaction of co-existing bound and soluble gradients of guidance cue on directed cell migration (chapter 3.3). Specifically, we designed a microfluidic device to generate controllable diffusion-based chemokine gradients, enabling simultaneous surface-immobilization of arbitrarily graded chemokine patterns by photopatterning. We used DCs as a model system to track migration in response to soluble and immobilized chemokine on a single cell level in real time.

The microfluidic chip offers six migration chambers. Pneumatic valves adjacent to all chamber openings can control media exchange in each chamber independently. This grants simultaneous control over media exchange, drug or guidance cue application in a homogenous or graded fashion and control over gradient orientation and shape. Therefore, a variety of experimental conditions can be assayed simultaneously with the respective control conditions, thereby minimizing technical variations influencing the experimental outcome. To date,

microfluidic systems for probing chemotactic behavior in 3D environments allow only slow changes in gradient polarity and prohibit manipulation of gradient shape (Haessler et al., 2011). Loading of the migration chambers of our device with cells embedded in a gel matrix enables control of guidance cue gradients for cells migrating in a 3D matrix environment (chapter 5, Figure 47D and E). Hence, stable gradients and different gradient shapes are accessible and allow further insights into chemotactic cell behavior under physiological conditions.

4.3.2. DC migration in flow free 2D environments

Although the manufacturing steps to assemble a microfluidic chip impede most protein patterning techniques, we were able to immobilize chemokine in the migration chambers using protein patterning by photobleaching (chapter 3.1) (Holden and Cremer, 2003). Subsequently, we tested the migratory behavior of DCs in the migration chambers in the presence and absence of diffusion-based and surface immobilized chemokines. As expected, in the absence of chemokine, DCs adhered loosely to the fibronectin coated chamber and displayed a rolling migration type, with alternating attachment and detachment phases. However, due to the flow free environment migration was still effective. Experiencing CCL21, DCs should increase integrin dependent adhesion and show more persistent migration patterns than in the absence of CCL21 or in the presence of CCL19 (Supplemental Figure 1 and Schumann *et al.* (Schumann et al., 2010)). Accordingly, DCs adhered to the CCL21/fibronectin bearing areas of the microfluidic migration chamber, spread and followed gradients of CCL21. However, unlike in 3D- or confined conditions, cell morphology was reminiscent of haptotactic mesenchymal cells, showing multiple lamellipodia and reduced global polarity. Despite these changes in morphology, we are able to reproduce enhanced spreading and persistent migration in presence of immobilized CCL21 and can induce haptotactic migration on gradients of surface immobilized CCL21. Embedding of DCs in a gel matrix or limiting the height of the migration chamber can induce physical confinement and therefore foster amoeboid like cell morphology.

A low concentration of CCL19 applied as a rising linear gradient was not sufficient to induce directionality or spreading but increased cell speed and therefore induced haptokinetic migration. Interestingly, DCs exposed to homogenous fields of soluble CCL19 did not increase their velocity or persistence (Figure 34 and Supplemental Figure 1). Similar to immobilized presented CCL21, enhancement of migration efficiency seems to depend either on concentration or spatial signal.

Increasing CCL19 concentration in turn led to increased cell polarity and therefore more directional migration towards the maximal CCL19 concentration. However, as reported previously (Supplemental Figure 1E and Schumann *et al.* (Schumann et al., 2010)), rising concentrations of soluble applied CCL19 did not affect adhesion or DC speed. Taken together, although DCs do not show the typical amoeboid like morphology, we are able to reconstitute typical chemokine induced migration and adhesion phenotypes.

4.3.3. Competing gradients of soluble CCL19 and immobilized CCL21

Migrating on fibronectin-coated surfaces without physical confinement or matrix support, DCs show a directional bias towards CCL19 if both chemokines are offered in equimolar, opposing chemotactic gradients (Ricart et al., 2010). In contrast, if CCL21 is presented in a semi-immobilized fashion, partially adsorbed to charged ECM components of a matrigel matrix, DCs prefer CCL21 over soluble CCL19 gradients of equimolar concentration. (Haessler et al., 2011) In both studies, chemokine preference is concentration dependent and none of the two CCR7 ligands induces a dominant bias as seen for fMLP guiding granulocytes in opposing fMLP/CXCL12 gradients (Heit et al., 2002). Therefore, presentation and local gradient properties might be decisive for CCR7 ligand bias. However, both methods do not allow for precise control of the generated gradients. By generating precisely controlled opposing gradients of soluble CCL19 on defined gradients of surface immobilized CCL21 we confirm the concentration dependency for CCR7 ligands. Depending on the provided concentration, DCs preferred either immobilized, haptotactic CCL21 or soluble CCL19. Further experiments with matching concentrations and varying

gradient shapes will allow us to address the ligand preference of CCR7 guided DCs.

In combination with passivating PVA coating and building block based photopatterning (chapter 3.4), the scope of our setup expands beyond chemokine immobilization. Patterns, gradients or shapes of integrin ligands or other mechanical guidance cues, in combination with precisely controlled soluble factors will represent a versatile tool for basic research as well as diagnosis.

4.4. Spatial control over cell adhesion and integrin guided haptotaxis

4.4.1. Method and outlook

Mechanical cell guidance relies on signal feedback from adhesion sites to the cytoskeletal network, biasing cell polarization and eventually migration (Inoue and Meyer, 2008; Wu et al., 2012). Signal strength hereby depends on the amount of newly formed adhesion complexes (*haptotaxis*) or their mechanical properties (*durotaxis*) (Carter, 1965; Plotnikov et al., 2012). To accurately analyze *haptotactic* gradient sensing, mechanical substrate properties need to be constant while adhesiveness needs to be precisely controllable. The defined gradients of covalently immobilized RGD motif on PVA passivated surfaces we developed in the scope of this thesis (chapter 3.4), offer ideal conditions to dissect the molecular basis of integrin guided haptotaxis.

Specifically, using covalently immobilized PVA as surface coating, we are able to create effective, cell repellent surfaces. Each vinylalcohol unit can serve as an attachment site for either surface binding or inter-chain hydrogen bonds. Hence, strong covalent surface attachment of a single PVA chain and intra- and intermolecular hydrogen bonds form a stable, insoluble polymer, granting sustainable surface passivation. Additionally, the defined polymer surface allows for sharp borders for additive photopatterning techniques. In contrast, PEG chains are usually attached to the surface via their reactive head domain and the ether groups form weaker intra-molecular hydrogen bonds.

Therefore PEG chains are more flexible and depending on their length more delocalized on the surface. This impedes sharp borders for additive methods, however due to the increased surface allows the deposition of higher protein concentrations. Both, PEG and PVA surface coatings allow subtractive methods that rely on ablation of the passivating coating.

We combine PVA coating with covalent immobilization of fluorescently labeled RGD in arbitrarily graded shapes and submicron resolution. The fluorescently tagged RGD allows for precise localization and quantification of the patterned area (Figure 44). Submicron sized resolution assesses cell adhesion and cell shape on or below cell size and the possibility to create homogeneously graded patterns grants control of haptotactic migration on defined gradients of adhesive cue (Figure 45).

Due to its versatility, our building block based surface modification method allows for a plethora of applications beyond probing haptotactic migration. The relative simplicity of the method makes it applicable in many biological laboratories. Surface patterning techniques often require either complex chemistry (Escorihuela et al., 2015) or machinery like UV-O cleaners (Azioune et al., 2009) and microfluidics (Wu et al., 2012) such that these patterning techniques are out of reach for many researchers. As our setup does not depend on UV, our approach is available on any fluorescence microscope with only minor modifications required. Azide or alkyne labeled dyes for photo-immobilization or protein-labeling kits for ligand immobilization are commercially available and inexpensive. Therefore, building block based photo-patterning can be established without profound chemical expertise.

Furthermore, separation of the photoreaction from ligand immobilization and the small covalent linkage offer technical advantages compared to other photo-patterning techniques. Only intact ligands are surface immobilized and thus can be quantified. Replacement of bulky and inaccessible streptavidin or antibody linkers grants better accessibility of small ligands such as drugs or small peptides. Moreover, maximal patterning efficiency in the monolayer is determined by the ligand itself instead of streptavidin or antibody linkers which allows printing of higher concentrations of smaller ligands. The specificity of the

alkyne/azide click reaction allows for usage of a variety of linkers for orthogonal immobilization reactions (Patterson and Prescher, 2015). For instance, stiff DNA or flexible polymer linkers can be introduced for distance specification or to measure binding forces (Jurchenko and Salaita, 2015; Wang and Ha, 2013). The concentration of immobilized ligand can be increased in a controlled fashion by adding amplifying, dendrimeric linkers. Moreover, photolabile linkers enable precise removal of formerly patterned areas (Wegner et al., 2015). Consequently such linkers allow the reduction of the feature size and enable low background patterning even on non-passivated surfaces.

In combination with the passivating PVA coating, long term experiments like well free cell culture systems become feasible. Here, cell populations could be grown on varying biological active compounds, transfection reagents or receptor ligands and analyzed in a high throughput manner. Optogenetic or microfluidic based stimulation could further increase the stimulation precision between single populations. Additionally, gradients of compounds or transfection reagents within areas of homogenous adhesive cues enable fast titration of effective concentrations and adhesive gradients might allow classification of the metastatic potential of cancer biopsies (Guo and Giancotti, 2004).

Naïve T-cells utilize the FRC network within the lymph node as roads promoting effective migration *in vivo*. Next to haptotactic chemokines, integrin ligands, like ICAM-1 have been hypothesized to restrict and guide their migration (Bajénoff et al., 2006; Katakai et al., 2013). Here, integrin ligands could serve as attachment sites for haptotactic chemokine guided migration or the integrin ligand itself could promote migration efficiency and therefore kinetic guidance. To date, the existence of integrin guided haptotaxis has not been demonstrated for migrating leukocytes. Defined gradients of immobilized integrin ligand, as accessible by our technique, could answer the question if integrin ligands alone can induce directional or kinetic guidance in leukocytes. Additionally, opposing gradients of haptotactic chemokines and integrin ligands or chemokine gradients on integrin ligand networks could give insights into how

both haptotactic cues might interact or cooperatively instruct leucocyte migration.

4.4.2. Outlook haptotactic mesenchymal cell migration

The generation of defined adhesive patterns and gradients allowed us to confine the migration and the growth of 3T3 fibroblasts and migration of zebrafish keratocytes to defined areas of RGD. On RGD gradients, we confirmed the haptotactic behavior of 3T3 fibroblasts. We furthermore observed haptotaxis in rapidly migrating zebrafish keratocytes, which to our knowledge, has not been reported yet. In the method based approach discussed in chapter 3.4, we have established a proof of principle for haptotaxis in both aforementioned cell types. In the following, a few additional observations aiming at a quantitative characterization of haptotaxis in keratocytes and fibroblasts will be presented as an outlook:

Keratocytes represent a minimalistic model for acto-myosin driven cell motility since their migration is independent of microtubule activity (Cooper and Schliwa, 1986; Theriot and Mitchison, 1991). On adhesive gradients, haptotactic keratocytes contracted at low adhesiveness and spread towards higher adhesiveness exhibiting the keratocyte specific, fan like lamellipodium. Reaching the maximal RGD concentration in our setup (Figure 46A, 0 – 100 %), highly motile keratocytes did not stop as purely mechanical guidance might suggest. Keratocytes rather repolarized and migrated back in the direction of lower adhesiveness until the adhesion was too weak to facilitate efficient migration. At this point, cells repolarized again in the direction of higher adhesiveness (Figure 46H). Hence, keratocytes constantly circled around maximal adhesiveness, exhibiting a very dynamic haptotactic behavior (Figure 46D, 0 – 100 %). Accordingly, haptotaxis sensing seems to act on top of a random, intrinsic polarity, mainly biasing directionality.

Similarly, 3T3 fibroblasts, which represent slowly migrating cells compared to zebrafish keratocytes (~30 times slower (Johnson et al., 2015; Suraneni et al., 2015)) constantly displayed protrusions in the direction of lower adhesiveness when migrating along an adhesive gradient.

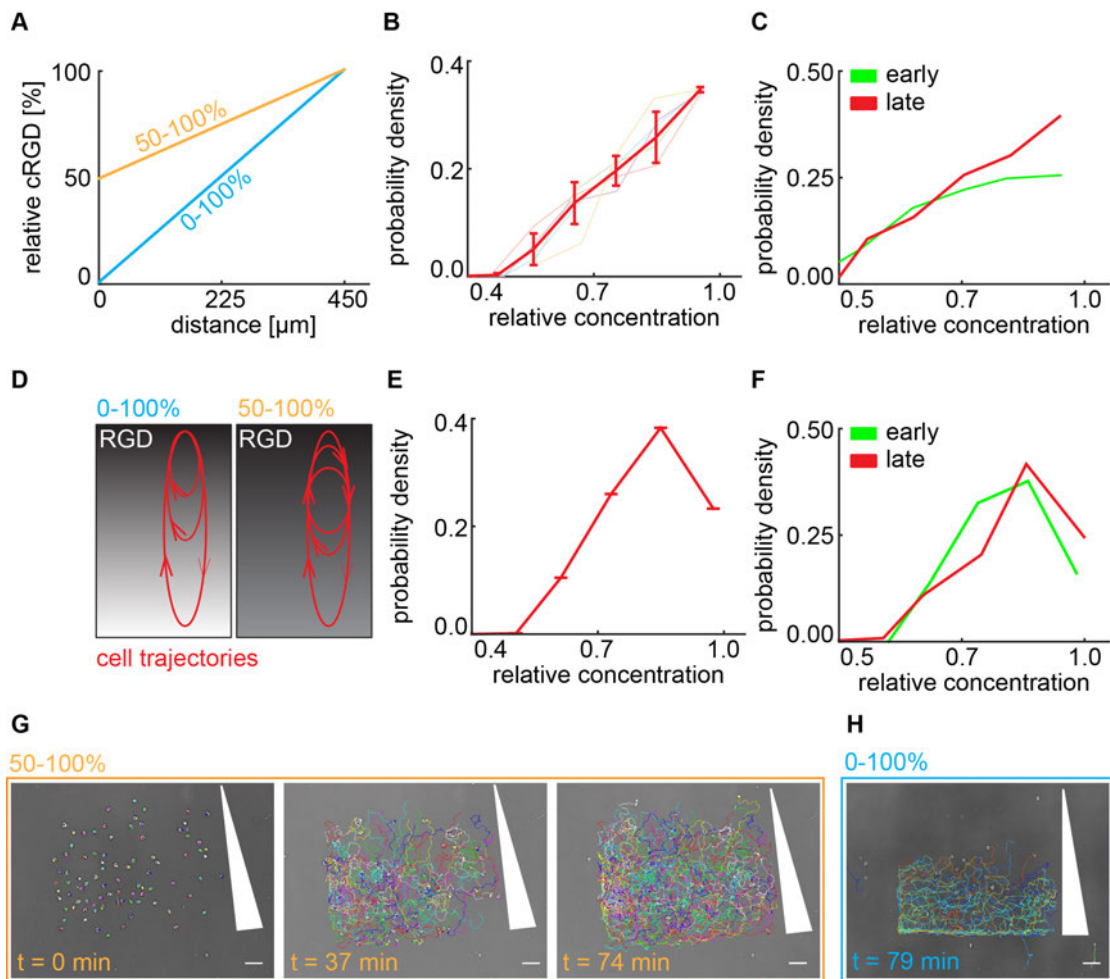


Figure 46.: Zebrafish keratocyte haptotaxis.

A) Tested gradients of RGD-HF555. Steep linear gradient: 0 to 100 % light intensity over the whole field of view ($450 \mu\text{m} \times 450 \mu\text{m}$). Shallow linear gradient: 50 to 100 % light intensity over the whole field of view ($450 \mu\text{m} \times 450 \mu\text{m}$). Cells cover $\sim 50\%$ of the patterned area. B) Probability of presence of zebrafish keratocytes on steep (0 to 100 % light intensity) gradients. Cells cover $\sim 100\%$ of the patterned area. C) Time dependency of probability of presence on steep linear gradients. Early: 0 – 40 min; Late: 41 – 79 min. D) Circling migratory behavior (red trajectories) on steep (0 – 100 %) and shallow (50 – 100 %) gradients of RGD-HF555 E) Probability of presence of zebrafish keratocytes on shallow (50 to 100 % light intensity) gradients. F) Time dependency of probability of presence on shallow linear gradients. Early: 0 – 37 min; Late: 38 – 74 min. G) Cell trajectories after $t = 0, 37, 74$ min on a shallow linear gradient. Gradient direction indicated in white. Scale bar $50 \mu\text{m}$. H) Cell trajectories after $t = 79$ min on a steep linear gradient. Gradient direction indicated in white. Scale bar $50 \mu\text{m}$.

This observation implies that due to the slower kinetics, fibroblasts seem to be less prone to random directional changes than keratocytes but exhibit a random component during migration as well.

Keratocyte migration is most efficient on substrates offering intermediate adhesiveness (Barnhart et al., 2011). Migrating on adhesive gradients, keratocytes showed a similar dependency with velocities increasing with adhesiveness and decreasing if adhesion was too high. This suggests a

kinetically driven mechanism of haptotaxis according to which cells would reside and distribute in areas offering ideal migration conditions rather than collect at highest adhesiveness. This view is supported by preliminary results of keratocytes migrating on a shallow gradient of RGD-HF555 (Figure 46A, 50 – 100 %). This gradient represents a spatially stretched version of the 0 – 100 % gradient, since cells only migrated on concentrations higher than 50 %. Although steep and shallow gradients shared the same maximal concentration (100 %), on the shallow gradient keratocytes seemed to avoid maximal adhesiveness (Figure 46G) and circle around ~80 % adhesiveness (Figure 46E and D, 50 - 100 %). This behavior can be explained by a kinetic haptotaxis model with ideal migration conditions at ~ 80 % adhesiveness. Additionally, the relative change in concentration ($\Delta c/c$) becomes small for increasing concentrations and/or shallow gradients. Another explanation might therefore be that cells are unable to interpret shallow gradients above 80 % adhesiveness any more. In fact, Brandley *et al.* observed $\Delta c/c$ dependent haptotactic behavior in migrating tumor cells (Brandley and Schnaar, 1989). However, this would not explain the peak in probability presence but would rather result in a plateau (Figure 46E). Further experiments with plateauing and exponential (high $\Delta c/c$) gradients will shed light on the $\Delta c/c$ dependency of haptotactic zebrafish keratocytes and the possibility of a kinetic haptotaxis model.

5. Appendix

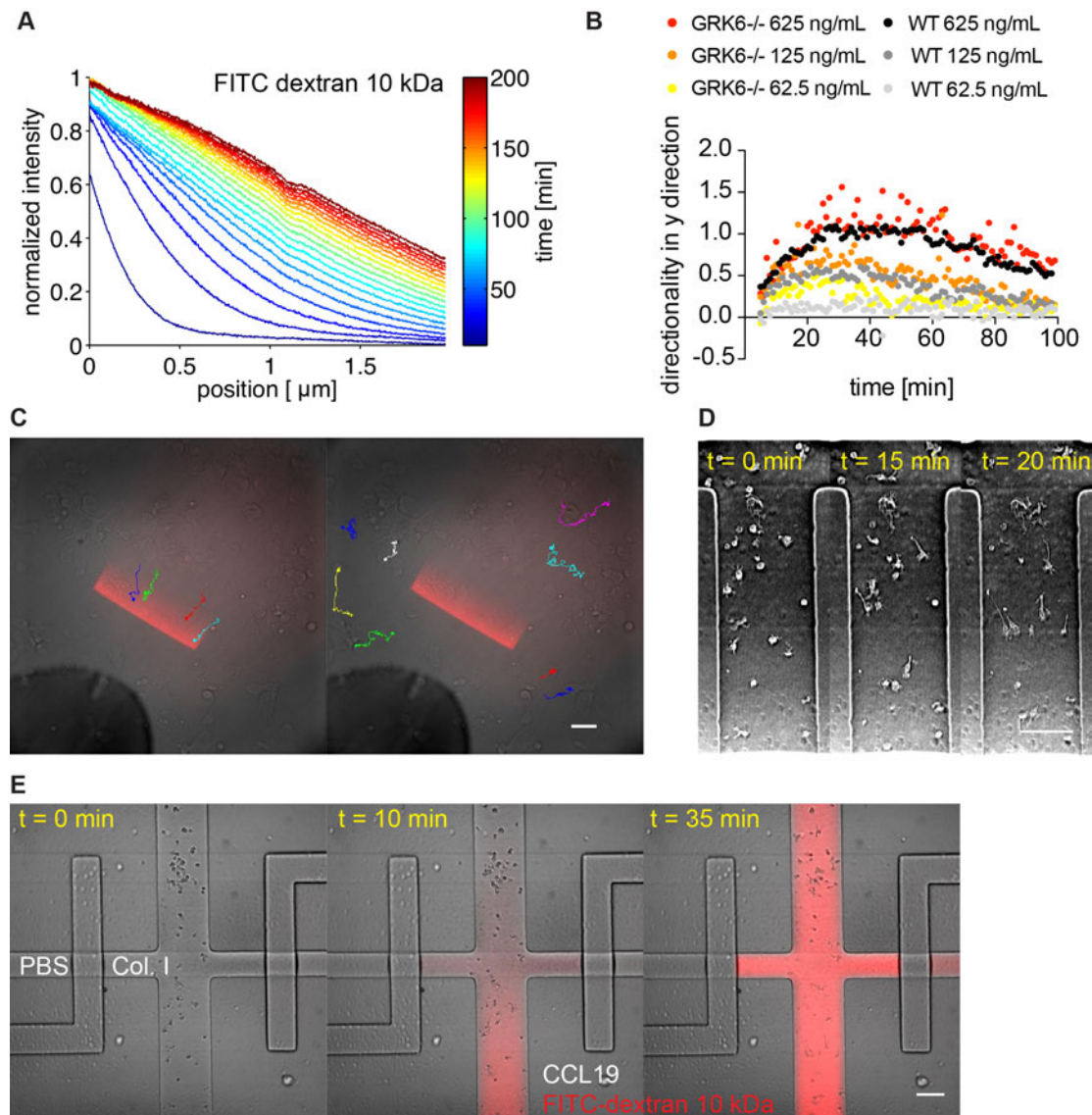


Figure 47.: Appendix. A) FITC dextran 10 kDa gradient developing in a collagen gel chamber. Each line represents 10 min. Time is color coded with cold colors representing early timepoints and warm colors representing late timepoints. FITC dextran 10 kDa concentration as fluorescence intensity against position in the gel in μm . 0 μm represents the gel/liquid interface. B) 3D chemotaxis assay (collagen assay). Directionality of GRK6^{-/-} and WT DCs at decreasing c_{MAX} ($c_{\text{MAX}1} = 625 \text{ ng/mL}$, $c_{\text{MAX}2} = 125 \text{ ng/mL}$, $c_{\text{MAX}3} = 62.5 \text{ ng/mL}$). C) DCs following a haptotactic gradient of CCL21 24-98 bio confined under an agarose layer. Gradient represented as SA-Cy3 staining. Scale bar 100 μm . D) and E) 3D chemotaxis assay (collagen assay) in the migration chambers of a microfluidic chip. Scale bar 100 μm . (E). The main chamber contains a collagen/DC suspension. Side channels and flow channels contain PBS or chemokine solution (CCL19, 625 ng/mL and FITC dextran 10 kDa). Chemokine gradient profile determined by sequential valve control. D) Enlarged view of (E). Cells show characteristic morphology while migrating within the collagen fibers of the gel.

6. Bibliography

- Abercrombie, M. (1961). The bases of the locomotory behaviour of fibroblasts. *Exp. Cell Res. Suppl 8*, 188–198.
- Abercrombie, M., Heaysman, J.E., and Pegrum, S.M. (1971). The locomotion of fibroblasts in culture. IV. Electron microscopy of the leading lamella. *Exp. Cell Res. 67*, 359–367.
- Adamo, A., Sharei, A., Adamo, L., Lee, B., Mao, S., and Jensen, K.F. (2012). Microfluidics-Based Assessment of Cell Deformability. *Anal Chem 84*, 6438–6443.
- Amselem, G., Theves, M., Bae, A., Beta, C., and Bodenschatz, E. (2012). Control parameter description of eukaryotic chemotaxis. *Phys. Rev. Lett. 109*, 108103.
- Andrew, N., and Insall, R.H. (2007). Chemotaxis in shallow gradients is mediated independently of PtdIns 3-kinase by biased choices between random protrusions. *Nat Cell Biol 9*, 193–200.
- Arriuermerlou, C., and Meyer, T. (2005). A Local Coupling Model and Compass Parameter for Eukaryotic Chemotaxis. *Developmental Cell 8*, 215–227.
- Asokan, S.B., Johnson, H.E., Rahman, A., King, S.J., Rotty, J.D., Lebedeva, I.P., Haugh, J.M., and Bear, J.E. (2014). Mesenchymal chemotaxis requires selective inactivation of myosin II at the leading edge via a noncanonical PLC γ /PKC α pathway. *Developmental Cell 31*, 747–760.
- Azioune, A., Storch, M., Bornens, M., Théry, M., and Piel, M. (2009). Simple and rapid process for single cell micro-patterning. *Lab Chip 9*, 1640.
- Bagorda, A., and Parent, C.A. (2008). Eukaryotic chemotaxis at a glance. *Journal of Cell Science 121*, 2621–2624.
- Bajénoff, M., Egen, J.G., Koo, L.Y., Laugier, J.P., Brau, F., Glaichenhaus, N., and Germain, R.N. (2006). Stromal cell networks regulate lymphocyte entry, migration, and territoriality in lymph nodes. *Immunity 25*, 989–1001.
- Bao, X., Moseman, E.A., Saito, H., Petryanik, B., Thiriot, A., Hatakeyama, S., Ito, Y., Kawashima, H., Yamaguchi, Y., Lowe, J.B., et al. (2010). Endothelial Heparan Sulfate Controls Chemokine Presentation in Recruitment of Lymphocytes and Dendritic Cells to Lymph Nodes. *Immunity 33*, 817–829.
- Barczyk, M., Carracedo, S., and Gullberg, D. (2009). Integrins. *Cell Tissue Res 339*, 269–280.
- Barnhart, E.L., Lee, K.-C., Keren, K., Mogilner, A., and Theriot, J.A. (2011). An Adhesion-Dependent Switch between Mechanisms That Determine Motile Cell Shape. *PLoS Biol 9*, e1001059.
- Bear, J.E., and Haugh, J.M. (2014). Directed migration of mesenchymal cells: where signaling and the cytoskeleton meet. *Current Opinion in Cell Biology 30C*, 74–82.
- Behrndt, M., Salbreux, G., Campinho, P., Hauschild, R., Oswald, F., Roensch, J., Grill, S.W., and Heisenberg, C.-P. (2012). Forces driving epithelial spreading in zebrafish gastrulation. *Science 338*, 257–260.
- Beningo, K.A., Dembo, M., Kaverina, I., Small, J.V., and Wang, Y.L. (2001). Nascent focal

adhesions are responsible for the generation of strong propulsive forces in migrating fibroblasts. *The Journal of Cell Biology* 153, 881–888.

Benovic, J.L., Pike, L.J., Cerione, R.A., Staniszewski, C., Yoshimasa, T., Codina, J., Caron, M.G., and Lefkowitz, R.J. (1985). Phosphorylation of the mammalian beta-adrenergic receptor by cyclic AMP-dependent protein kinase. Regulation of the rate of receptor phosphorylation and dephosphorylation by agonist occupancy and effects on coupling of the receptor to the stimulatory guanine nucleotide regulatory protein. *Journal of Biological Chemistry* 260, 7094–7101.

Berg, H.C., and Purcell, E.M. (1977). CHEMORECEPTION. *Biophysj* 20, 193–219.

Bélisle, J.M., and Costantino, S. (2010). Density amplification in laser-assisted protein adsorption by photobleaching. *Spie Lase*.

Bélisle, J.M., Correia, J.P., Wiseman, P.W., Kennedy, T.E., and Costantino, S. (2008). Patterning protein concentration using laser-assisted adsorption by photobleaching, LAPAP. *Lab Chip* 8, 2164.

Bélisle, J.M., Kunik, D., and Costantino, S. (2009). Rapid multicomponent optical protein patterning. *Lab Chip* 9, 3580.

Bélisle, J.M., Levin, L.A., and Costantino, S. (2011). High-content neurite development study using optically patterned substrates. *PLoS ONE* 7, e35911–e35911.

Bialek, W., and Setayeshgar, S. (2005). Physical limits to biochemical signaling. *Proceedings of the National Academy of Sciences of the United States of America* 102, 10040–10045.

Blawas, A.S., and Reichert, W.M. (1998). Protein patterning. *Biomaterials* 19, 595–609.

Boldajipour, B., Mahabaleswar, H., Kardash, E., Reichman-Fried, M., Blaser, H., Minina, S., Wilson, D., Xu, Q., and Raz, E. (2008). Control of chemokine-guided cell migration by ligand sequestration. *Cell* 132, 463–473.

Brandley, B.K., and Schnaar, R.L. (1989). Tumor cell haptotaxis on covalently immobilized linear and exponential gradients of a cell adhesion peptide. *Dev. Biol.* 135, 74–86.

Byers, M.A., Calloway, P.A., Shannon, L., Cunningham, H.D., Smith, S., Li, F., Fassold, B.C., and Vines, C.M. (2008). Arrestin 3 Mediates Endocytosis of CCR7 following Ligation of CCL19 but Not CCL21. *J. Immunol.* 181, 4723–4723.

Cai, H., Das, S., Kamimura, Y., Long, Y., Parent, C.A., and Devreotes, P.N. (2010). Ras-mediated activation of the TORC2-PKB pathway is critical for chemotaxis. *The Journal of Cell Biology* 190, 233–245.

Carter, S.B. (1965). Principles of cell motility: the direction of cell movement and cancer invasion. *Nature* 208, 1183–1187.

Carter, S.B. (1967). Haptotaxis and the mechanism of cell motility. *Nature* 213, 256–260.

Case, L.B., and Waterman, C.M. (2010). Adhesive F-actin waves: a novel integrin-mediated adhesion complex coupled to ventral actin polymerization. *PLoS ONE* 6, e26631–e26631.

Castellino, F., Huang, A.Y., Altan-Bonnet, G., Stoll, S., Scheinecker, C., and Germain, R.N. (2006). Chemokines enhance immunity by guiding naive CD8+ T cells to sites of CD4+ T cell-dendritic cell interaction. *Nature* 440, 890–895.

Choi, C.K., Vicente-Manzanares, M., Zareno, J., Whitmore, L.A., Mogilner, A., and Horwitz, A.R.

(2008). Actin and α -actinin orchestrate the assembly and maturation of nascent adhesions in a myosin II motor-independent manner. *Nat Cell Biol* *10*, 1039–1050.

Chubb, J.R., Wilkins, A., Wessels, D.J., Soll, D.R., and Insall, R.H. (2002). Pseudopodium dynamics and rapid cell movement in Dictyostelium Ras pathway mutants. *Cell Motil. Cytoskeleton* *53*, 150–162.

Chung, C.Y., Potikyan, G., and Firtel, R.A. (2001). Control of cell polarity and chemotaxis by Akt/PKB and PI3 kinase through the regulation of PAK α . *Molecular Cell* *7*, 937–947.

Clapham, D.E. (2006). Calcium Signaling. *Cell* *131*, 1047–1058.

Collins, S.R., Yang, H.W., Bongor, K.M., Guignet, E.G., Wandless, T.J., and Meyer, T. (2015). Using light to shape chemical gradients for parallel and automated analysis of chemotaxis. *Molecular Systems Biology* *11*, 804–804.

Cooper, M.S., and Schliwa, M. (1986). Motility of Cultured Fish Epidermal-Cells in the Presence and Absence of Direct-Current Electric-Fields. *J. Cell Biol.* *102*, 1384–1399.

Cox, E.A., Sastry, S.K., and Huttenlocher, A. (2001). Integrin-mediated adhesion regulates cell polarity and membrane protrusion through the Rho family of GTPases. *Molecular Biology of the Cell* *12*, 265–277.

de Paz, J.L., Moseman, E.A., Noti, C., Polito, L., Andrian, von, U.H., and Seeberger, P.H. (2007). Profiling heparin-chemokine interactions using synthetic tools. *ACS Chem Biol* *2*, 735–744.

Debs, B.E., Utharala, R., Balyasnikova, I.V., Griffiths, A.D., and Merten, C.A. (2012). Functional single-cell hybridoma screening using droplet-based microfluidics. *Proceedings of the National Academy of Sciences* *109*, 11570–11575.

DeChancie, J., and Houk, K.N. (2007). The origins of femtomolar protein-ligand binding: hydrogen-bond cooperativity and desolvation energetics in the biotin-(strept)avidin binding site. *J. Am. Chem. Soc.* *129*, 5419–5429.

DeForest, C.A., Polizzotti, B.D., and Anseth, K.S. (2009). Sequential click reactions for synthesizing and patterning three-dimensional cell microenvironments. *Nature Materials* *8*, 659–664.

Del Prete, A., Shao, W.-H., Mitola, S., Santoro, G., Sozzani, S., and Haribabu, B. (2007). Regulation of dendritic cell migration and adaptive immune response by leukotriene B₄ receptors: a role for LTB₄ in up-regulation of CCR7 expression and function. *Blood* *109*, 626–631.

Derfuss, T., Kuhle, J., Lindberg, R., and Kappos, L. (2013). Natalizumab therapy for multiple sclerosis. *Semin Neurol* *33*, 26–36.

Doyle, A.D. (2001). *Generation of Micropatterned Substrates Using Micro Photopatterning* (Hoboken, NJ, USA: John Wiley & Sons, Inc.).

Edelstein, A., Amodaj, N., Hoover, K., Vale, R., and Stuurman, N. (2010). Computer control of microscopes using μ Manager. *Curr Protoc Mol Biol* *Chapter 14*, Unit14–Unit20.

Escorihuela, J., Marcelis, A.T.M., and Zuilhof, H. (2015). Metal-Free Click Chemistry Reactions on Surfaces. *Advanced Materials Interfaces* *2*.

Fan, G., Shumay, E., Malbon, C.C., and Wang, H. (2001). c-Src tyrosine kinase binds the beta 2-adrenergic receptor via phospho-Tyr-350, phosphorylates G-protein-linked receptor kinase 2,

and mediates agonist-induced receptor desensitization. *Journal of Biological Chemistry* 276, 13240–13247.

Ferrell, J.E. (2009). Signaling motifs and Weber's law. *Molecular Cell* 36, 724–727.

Fox, J.M., Chamberlain, G., Ashton, B.A., and Middleton, J. (2007). Recent advances into the understanding of mesenchymal stem cell trafficking. *Br. J. Haematol.* 137, 491–502.

Förster, R., Davalos-Misslitz, A.C., and Rot, A. (2008). CCR7 and its ligands: balancing immunity and tolerance. *Nat Rev Immunol* 8, 362–371.

Franco, S.J., Rodgers, M.A., Perrin, B.J., Han, J., Bennin, D.A., Critchley, D.R., and Huttenlocher, A. (2004). Calpain-mediated proteolysis of talin regulates adhesion dynamics. *Nat Cell Biol* 6, 977–983.

Frank, T., and Tay, S. (2013). Flow-switching allows independently programmable, extremely stable, high-throughput diffusion-based gradients. *Lab Chip* 13, 1273.

Franz, C.M., Jones, G.E., and Ridley, A.J. (2002). Cell migration in development and disease. pp. 153–158.

Freeman, S.A., Goyette, J., Furuya, W., Woods, E.C., Bertozzi, C.R., Bergmeier, W., Hinz, B., van der Merwe, P.A., Das, R., and Grinstein, S. (2016). Integrins Form an Expanding Diffusional Barrier that Coordinates Phagocytosis. *Cell* 164, 128–140.

Friedl, P., Borgmann, S., and Brocker, E.B. (2001). Amoeboid leukocyte crawling through extracellular matrix: lessons from the Dictyostelium paradigm of cell movement. *J. Leukoc. Biol.* 70, 491–509.

Friedl, P. (2004). Preshpecification and plasticity: shifting mechanisms of cell migration. *Current Opinion in Cell Biology* 16, 14–23.

Fukui, Y., Hashimoto, O., Sanui, T., Oono, T., Koga, H., and Abe, M. (2001). Haematopoietic cell-specific CDM family protein DOCK2 is essential for lymphocyte migration. *Nature* 412, 826–831.

Garcia, G.L., Rericha, E.C., Heger, C.D., Goldsmith, P.K., and Parent, C.A. (2009). The group migration of Dictyostelium cells is regulated by extracellular chemoattractant degradation. *Molecular Biology of the Cell* 20, 3295–3304.

Gardel, M.L., Sabass, B., Ji, L., Danuser, G., Schwarz, U.S., and Waterman, C.M. (2008). Traction stress in focal adhesions correlates biphasically with actin retrograde flow speed. *The Journal of Cell Biology* 183, 999–1005.

Geiger, B., Spatz, J.P., and Bershadsky, A.D. (2009). Environmental sensing through focal adhesions. *Nature* 10, 21–33.

Gerisch, G., and Keller, H.U. (1981). Chemotactic reorientation of granulocytes stimulated with micropipettes containing fMet-Leu-Phe. *Journal of Cell Science* 52, 1–10.

Gilbert, S.H., Perry, K., and Fay, F.S. (1994). Mediation of chemoattractant-induced changes in [Ca²⁺]_i and cell shape, polarity, and locomotion by InsP₃, DAG, and protein kinase C in newt eosinophils. *The Journal of Cell Biology* 127, 489–503.

Girrbach, M., Rink, I., Ladnorg, T., Azucena, C., Heißler, S., Haraszti, T., Schepers, U., and Schmitz, K. (2016). Colloids and Surfaces B: Biointerfaces. *Colloids and Surfaces B: Biointerfaces* 142, 385–391.

- Gomez-Sjöberg, R., Leyrat, A.A., Pirone, D.M., Chen, C.S., and Quake, S.R. (2007). Versatile, fully automated, microfluidic cell culture system. *Anal Chem* *79*, 8557–8563.
- Goodman, O.B., Krupnick, J.G., Santini, F., Gurevich, V.V., Penn, R.B., Gagnon, A.W., Keen, J.H., and Benovic, J.L. (1996). Beta-arrestin acts as a clathrin adaptor in endocytosis of the beta2-adrenergic receptor. *Nature* *383*, 447–450.
- Gould, S.T., Darling, N.J., and Anseth, K.S. (2012). Small peptide functionalized thiolâ€ene hydrogels as culture substrates for understanding valvular interstitial cell activation and de novo tissue deposition. *Acta Biomaterialia* *8*, 3201–3209.
- Gray, D.S., Liu, W.F., Shen, C.J., Bhadriraju, K., Nelson, C.M., and Chen, C.S. (2008). Engineering amount of cell-cell contact demonstrates biphasic proliferative regulation through RhoA and the actin cytoskeleton. *Exp. Cell Res.* *314*, 2846–2854.
- Gressin, L., Guillotin, A., Gu rin, C., Blanchoin, L., and Michelot, A. (2015). Architecture dependence of actin filament network disassembly. *Curr. Biol.* *25*, 1437–1447.
- Gunn, M.D., Tangemann, K., Tam, C., Cyster, J.G., Rosen, S.D., and Williams, L.T. (1998). A chemokine expressed in lymphoid high endothelial venules promotes the adhesion and chemotaxis of naive T lymphocytes. *Proceedings of the National Academy of Sciences of the United States of America* *95*, 258–263.
- Guo, W., and Giancotti, F.G. (2004). Integrin signalling during tumour progression. *Nat Rev Mol Cell Biol* *5*, 816–826.
- Haessler, U., Pisano, M., and Wu, M. (2011). Dendritic cell chemotaxis in 3D under defined chemokine gradients reveals differential response to ligands CCL21 and CCL19. *Proceedings of the National Academy of Sciences of the United States of America* *108*, 5614–5619.
- Hauser, M.A., Schaeuble, K., Kindinger, I., Impellizzeri, D., Krueger, W.A., Hauck, C.R., Boyman, O., and Legler, D.F. (2016). Inflammation-Induced CCR7 Oligomers Form Scaffolds to Integrate Distinct Signaling Pathways for Efficient Cell Migration. *Immunity* *44*, 59–72.
- Hecht, I., Skoge, M.L., Charest, P.G., Ben-Jacob, E., Firtel, R.A., Loomis, W.F., Levine, H., and Rappel, W.-J. (2011). Activated membrane patches guide chemotactic cell motility. *PLoS Comput Biol* *7*, e1002044–e1002044.
- Heit, B., Robbins, S.M., Downey, C.M., Guan, Z., Colarusso, P., Miller, B.J., Jirik, F.R., and Kubes, P. (2008). PTEN functions to 'prioritize' chemotactic cues and prevent “distraction” in migrating neutrophils. *Nat Immunol* *9*, 743–752.
- Heit, B., Tavener, S., Raharjo, E., and Kubes, P. (2002). An intracellular signaling hierarchy determines direction of migration in opposing chemotactic gradients. *The Journal of Cell Biology* *159*, 91–102.
- Hirose, J., Kawashima, H., Willis, M.S., Springer, T.A., Hasegawa, H., Yoshie, O., and Miyasaka, M. (2002). Chondroitin sulfate B exerts its inhibitory effect on secondary lymphoid tissue chemokine (SLC) by binding to the C-terminus of SLC. *Biochim Biophys Acta* *1571*, 219–224.
- Hocking, A.M. (2015). The Role of Chemokines in Mesenchymal Stem Cell Homing to Wounds. *Adv Wound Care (New Rochelle)* *4*, 623–630.
- Hodzic, D., DUNN, G.A., and BROWN, A.F. (1991). A New Direct-Viewing Chemotaxis Chamber. *Journal of Cell Science* *99*, 769–775.
- Hoeller, O., and Kay, R.R. (2007). Chemotaxis in the absence of PIP3 gradients. *Current*

Biology 17, 813–817.

Hoeller, O., Toettcher, J.E., Cai, H., Sun, Y., Huang, C.-H., Freyre, M., Zhao, M., Devreotes, P.N., and Weiner, O.D. (2016). G β Regulates Coupling between Actin Oscillators for Cell Polarity and Directional Migration. *PLoS Biol* 14, e1002381.

Holden, M.A., and Cremer, P.S. (2003). Light activated patterning of dye-labeled molecules on surfaces. *J. Am. Chem. Soc.* 125, 8074–8075.

Holman, D.W., Klein, R.S., and Ransohoff, R.M. (2011). The blood-brain barrier, chemokines and multiple sclerosis. *Biochimica Et Biophysica Acta-Molecular Basis of Disease* 1812, 220–230.

Horwitz, R., and Webb, D. (2003). Cell migration. *Current Biology* 13, R756–R759.

Houk, A.R., Jilkine, A., Mejean, C.O., Boltyskiy, R., Dufresne, E.R., Angenent, S.B., Altschuler, S.J., Wu, L.F., and Weiner, O.D. (2012). Membrane Tension Maintains Cell Polarity by Confining Signals to the Leading Edge during Neutrophil Migration. *Cell* 148, 175–188.

Hoyle, C.E., and Bowman, C.N. (2010). Thiol-Ene Click Chemistry. *Angew. Chem. Int. Ed.* 49, 1540–1573.

Huang, C.-H., Tang, M., Shi, C., Iglesias, P.A., and Devreotes, P.N. (2013). An excitable signal integrator couples to an idling cytoskeletal oscillator to drive cell migration. *Nat Cell Biol* 15, 1307–1316.

Hynes, R.O. (1992). Integrins - Versatility, Modulation, and Signaling in Cell-Adhesion. *Cell* 69, 11–25.

Iglesias, P.A., and Devreotes, P.N. (2008). Navigating through models of chemotaxis. *Current Opinion in Cell Biology* 20, 35–40.

Inoue, T., and Meyer, T. (2008). Synthetic Activation of Endogenous PI3K and Rac Identifies an AND-Gate Switch for Cell Polarization and Migration. *PLoS ONE* 3, e3068.

Insall, R.H. (2010). Understanding eukaryotic chemotaxis: a pseudopod-centred view. *Nat Rev Mol Cell Biol* 11, 453–458.

Jaffe, A.B., and Hall, A. (2005). Rho GTPases: biochemistry and biology. *Annu. Rev. Cell Dev. Biol* 21, 247–269.

Johnson, H.E., King, S.J., Asokan, S.B., Rotty, J.D., Bear, J.E., and Haugh, J.M. (2015). F-actin bundles direct the initiation and orientation of lamellipodia through adhesion-based signaling. *The Journal of Cell Biology* 150, 807.

Jurchenko, C., and Salaita, K.S. (2015). Lighting Up the Force: Investigating Mechanisms of Mechanotransduction Using Fluorescent Tension Probes. *Mol. Cell. Biol.* 35, 2570–2582.

Kaizu, K., de Ronde, W., Paijmans, J., Takahashi, K., Tostevin, F., and Wolde, ten, P.R. (2014). The Berg-Purcell limit revisited. *Biophysical Journal* 106, 976–985.

Katakai, T., Habiro, K., and Kinashi, T. (2013). Dendritic cells regulate high-speed interstitial T cell migration in the lymph node via LFA-1/ICAM-1. *The Journal of Immunology* 191, 1188–1199.

Kellogg, R.A., Gomez-Sjöberg, R., Leyrat, A.A., and Tay, S.S. (2014). High-throughput microfluidic single-cell analysis pipeline for studies of signaling dynamics. *Nat Protoc* 9, 1713–1726.

King, S.J., Asokan, S.B., Haynes, E.M., Zimmerman, S.P., Rotty, J.D., Alb, J.G., Tagliatela, A., Blake, D.R., Lebedeva, I.P., Marston, D., et al. (2016). Lamellipodia are critical for haptotactic sensing and response. *Journal of Cell Science* 129, 2329-2342.

Kirchhausen, T. (1999). Adaptors for clathrin-mediated traffic. *Annu. Rev. Cell Dev. Biol.* 15, 705–732.

Kohout, T.A., and Lefkowitz, R.J. (2003). Regulation of G protein-coupled receptor kinases and arrestins during receptor desensitization. *Molecular Pharmacology* 63, 9–18.

Kohout, T.A., Nicholas, S.L., Perry, S.J., Reinhart, G., Junger, S., and Struthers, R.S. (2004). Differential Desensitization, Receptor Phosphorylation, -Arrestin Recruitment, and ERK1/2 Activation by the Two Endogenous Ligands for the CC Chemokine Receptor 7. *Journal of Biological Chemistry* 279, 23214–23222.

Krummel, M.F., Bartumeus, F., and Gérard, A. (2016). T cell migration, search strategies and mechanisms. *Nat Rev Immunol* 16, 193–201.

Lämmermann, T., Bader, B.L., Monkley, S.J., Worbs, T., Wedlich-Soldner, R., Hirsch, K., Keller, M., Förster, R., Critchley, D.R., Fässler, R., et al. (2008). Rapid leukocyte migration by integrin-independent flowing and squeezing. *Nature* 453, 51–55.

Lämmermann, T., Renkawitz, J., Wu, X., Hirsch, K., Brakebusch, C., and Sixt, M. (2009). Cdc42-dependent leading edge coordination is essential for interstitial dendritic cell migration. *Blood* 113, 5703–5710.

Le Berre, M., Zlotek-Zlotkiewicz, E., Bonazzi, D., Lautenschlaeger, F., and Piel, M. (2014). *Methods for Two-Dimensional Cell Confinement* (Elsevier Inc.).

Lefkowitz, R.J., Rajagopal, K., and Whalen, E.J. (2006). New roles for β -arrestins in cell signaling: not just for seven-transmembrane receptors. *Molecular Cell* 5, 643-652.

Levchenko, A., and Iglesias, P.A. (2002). Models of eukaryotic gradient sensing: application to chemotaxis of amoebae and neutrophils. *Biophysical Journal* 82, 50-62.

Levine, H., and Rappel, W.-J. (2013). The physics of eukaryotic chemotaxis. *Phys. Today* 66, 24.

Levine, H., Kessler, D.A., and Rappel, W.-J. (2006). Directional sensing in eukaryotic chemotaxis: A balanced inactivation model. *Proceedings of the National Academy of Sciences of the United States of America* 103, 9761–9766.

Leyme, A., Marivin, A., Perez-Gutierrez, L., Nguyen, L.T., and Garcia-Marcos, M. (2015). Integrins activate trimeric G proteins via the nonreceptor protein GIV/Girdin. *The Journal of Cell Biology* 210, 1165–1184.

Liu, X., Ma, B., Malik, A.B., Tang, H., Yang, T., Sun, B., Wang, G., Minshall, R.D., Li, Y., Zhao, Y., et al. (2012). Bidirectional regulation of neutrophil migration by mitogen-activated protein kinases. *Nat Immunol* 1–9.

Livnah, O., Bayer, E.A., Wilchek, M., and Sussman, J.L. (1993). Three-dimensional structures of avidin and the avidin-biotin complex. *Proceedings of the National Academy of Sciences of the United States of America* 90, 5076–5080.

Lo, C.M., Wang, H.B., Dembo, M., and Wang, Y.L. (2000). Cell movement is guided by the rigidity of the substrate. *Biophysj* 79, 144–152.

Love, M., Sandberg, J.L., Ziarek, J.J., Gerarden, K.P., Rode, R.R., Jensen, D.R., McCaslin,

- D.R., Peterson, F.C., and Veldkamp, C.T. (2012). Solution Structure of CCL21 and Identification of a Putative CCR7 Binding Site. *Biochemistry* *51*, 733–735.
- Luther, S.A., Bidgol, A., Hargreaves, D.C., Schmidt, A., Xu, Y., Paniyadi, J., Matloubian, M., and Cyster, J.G. (2002). Differing Activities of Homeostatic Chemokines CCL19, CCL21, and CXCL12 in Lymphocyte and Dendritic Cell Recruitment and Lymphoid Neogenesis. *The Journal of Immunology* *169*, 424–433.
- Luther, S.A., Tang, H.L., Hyman, P.L., Farr, A.G., and Cyster, J.G. (2000). Coexpression of the chemokines ELC and SLC by T zone stromal cells and deletion of the ELC gene in the *plt/plt* mouse. *Proceedings of the National Academy of Sciences of the United States of America* *97*, 12694–12699.
- Luttrell, L.M. (1999). -Arrestin-Dependent Formation of 2 Adrenergic Receptor-Src Protein Kinase Complexes. *Science* *283*, 655–661.
- Luttrell, L.M., and Lefkowitz, R.J. (2002). The role of beta-arrestins in the termination and transduction of G-protein-coupled receptor signals. *Journal of Cell Science* *115*, 455–465.
- Lutz, M.B., Kukutsch, N., Ogilvie, A.L., Rössner, S., Koch, F., Romani, N., and Schuler, G. (1999). An advanced culture method for generating large quantities of highly pure dendritic cells from mouse bone marrow. *J. Immunol. Methods* *223*, 77–92.
- Machacek, M., Hodgson, L., Welch, C., Elliott, H., Pertz, O., Nalbant, P., Abell, A., Johnson, G.L., Hahn, K.M., and Danuser, G. (2009). Coordination of Rho GTPase activities during cell protrusion. *Nature* *461*, 99–103.
- Machesky, L.M., and Insall, R.H. (1998). Scar1 and the related Wiskott–Aldrich syndrome protein, WASP, regulate the actin cytoskeleton through the Arp2/3 complex. *Current Biology* *8*, 1347–1356.
- Mai, J., Fok, L., Gao, H., Zhang, X., and Poo, M.M. (2009). Axon Initiation and Growth Cone Turning on Bound Protein Gradients. *Journal of Neuroscience* *29*, 7450–7458.
- Maiuri, P., Rupprecht, J.-F., Wieser, S., Rupprecht, V., Bénichou, O., Carpi, N., Coppey, M., De Beco, S., Gov, N., Heisenberg, C.-P., et al. (2015). Actin Flows Mediate a Universal Coupling between Cell Speed and Cell Persistence. *Cell* 1–14.
- Manahan, C.L., Iglesias, P.A., Long, Y., and Devreotes, P.N. (2004). Chemoattractant signaling in *dictyostelium discoideum*. *Annu. Rev. Cell Dev. Biol.* *20*, 223–253.
- Mehling, M., Frank, T., Albayrak, C., and Tay, S. (2015). Real-time tracking, retrieval and gene expression analysis of migrating human T cells. *Lab Chip* *15*, 1276–1283.
- Mehling, M., Hilbert, P., Fritz, S., Durovic, B., Eichin, D., Gasser, O., Kuhle, J., Klimkait, T., Lindberg, R.L.P., Kappos, L., et al. (2011). Antigen-specific adaptive immune responses in fingolimod-treated multiple sclerosis patients. *Ann. Neurol.* *69*, 408–413.
- Mellman, I., and Steinman, R.M. (2001). Dendritic Cells. *Cell* *106*, 255–258.
- Mempel, T.R., Junt, T., and Andrian, von, U.H. (2005). Rulers over Randomness: Stroma Cells Guide Lymphocyte Migration in Lymph Nodes. *Immunity* *25*, 867–869.
- Mendoza, M.C., Vilela, M., Juarez, J.E., Blenis, J., and Danuser, G. (2015). ERK reinforces actin polymerization to power persistent edge protrusion during motility. *Science Signaling* *8* ra47-ra47.
- Middleton, J., Neil, S., Wintle, J., Clark-Lewis, I., Moore, H., Lam, C., Auer, M., Hub, E., and

- Rot, A. (1997). Transcytosis and surface presentation of IL-8 by venular endothelial cells. *Cell* *91*, 385–395.
- Minina, S., Reichman-Fried, M., and Raz, E. (2007). Control of Receptor Internalization, Signaling Level, and Precise Arrival at the Target in Guided Cell Migration. *Current Biology* *17*, 1164–1172.
- Mitchison, T., and Kirschner, M. (1988). Cytoskeletal dynamics and nerve growth. *Neuron* *1*, 761–772.
- Mortimer, D., Feldner, J., Vaughan, T., Vetter, I., Pujic, Z., Rosoff, W.J., Burrage, K., Dayan, P., Richards, L.J., and Goodhill, G.J. (2009). From the Cover: A Bayesian model predicts the response of axons to molecular gradients. *Proceedings of the National Academy of Sciences* *106*, 10296–10301.
- Mrksich, M., and Whitesides, G.M. (1996). Using self-assembled monolayers to understand the interactions of man-made surfaces with proteins and cells. *Annu Rev Biophys Biomol Struct* *25*, 55–78.
- Muinonen-Martin, A.J., Susanto, O., Zhang, Q., Smethurst, E., Faller, W.J., Veltman, D.M., Kalna, G., Lindsay, C., Bennett, D.C., Sansom, O.J., et al. (2014). Melanoma Cells Break Down LPA to Establish Local Gradients That Drive Chemotactic Dispersal. *PLoS Biol* *12*, e1001966.
- Müller, G., Höpken, U.E., and Lipp, M. (2003). The impact of CCR7 and CXCR5 on lymphoid organ development and systemic immunity. *Immunol. Rev.* *195*, 117–135.
- Neel, N.F., Schutyser, E., Sai, J., Fan, G.-H., and Richmond, A. (2005). Chemokine receptor internalization and intracellular trafficking. *Cytokine & Growth Factor Reviews* *16*, 637–658.
- Nguyen, B.P., Ryan, M.C., Gil, S.G., and Carter, W.G. (2000). Deposition of laminin 5 in epidermal wounds regulates integrin signaling and adhesion. *Current Opinion in Cell Biology* *12*, 554–562.
- Nichols, J.M., Veltman, D., and Kay, R.R. (2015). ScienceDirect Chemotaxis of a model organism: progress with *Dictyostelium*. *Current Opinion in Cell Biology* *36*, 7–12.
- Niethammer, P., Grabher, C., Look, A.T., and Mitchison, T.J. (2009). A tissue-scale gradient of hydrogen peroxide mediates rapid wound detection in zebrafish. *Nature* *459*, 996–999.
- Nieto, M., Frade, J.M., Sancho, D., Mellado, M., Martínez-A, C., and Sánchez-Madrid, F. (1997). Polarization of chemokine receptors to the leading edge during lymphocyte chemotaxis. *J. Exp. Med.* *186*, 153–158.
- Oakley, R.H., Laporte, S.A., Holt, J.A., Barak, L.S., and Caron, M.G. (1999). Association of beta-arrestin with G protein-coupled receptors during clathrin-mediated endocytosis dictates the profile of receptor resensitization. *Journal of Biological Chemistry* *274*, 32248–32257.
- Otero, C., Groettrup, M., and Legler, D.F. (2006). Opposite fate of endocytosed CCR7 and its ligands: recycling versus degradation. *J. Immunol.* *177*, 2314–2323.
- Palczewski, K. (2010). Oligomeric forms of G protein-coupled receptors (GPCRs). *Trends Biochem. Sci.* *35*, 595–600.
- Palecek, S.P., Huttenlocher, A., Horwitz, A.F., and Lauffenburger, D.A. (1998). Physical and biochemical regulation of integrin release during rear detachment of migrating cells. *Journal of Cell Science* *111* (Pt 7), 929–940.
- Parent, C.A. (1999). A Cell's Sense of Direction. *Science* *284*, 765–770.

- Parent, C.A., Blacklock, B.J., Froehlich, W.M., Murphy, D.B., and Devreotes, P.N. (1998). G protein signaling events are activated at the leading edge of chemotactic cells. *Cell* *95*, 81–91.
- Patel, D.D., Koopmann, W., Imai, T., Whichard, L.P., Yoshie, O., and Krangel, M.S. (2001). Chemokines Have Diverse Abilities to Form Solid Phase Gradients. *Clinical Immunology* *99*, 43–52.
- Patterson, D.M., and Prescher, J.A. (2015). Orthogonal bioorthogonal chemistries. *Curr Opin Chem Biol* *28*, 141–149.
- Penela, P., Nogués, L., and Mayor, F. (2014). Role of G protein-coupled receptor kinases in cell migration. *Current Opinion in Cell Biology* *27*, 10–17.
- Peng, J., Wallar, B.J., Flanders, A., Swiatek, P.J., and Alberts, A.S. (2003). Disruption of the Diaphanous-related formin Drf1 gene encoding mDia1 reveals a role for Drf3 as an effector for Cdc42. *Current Biology* *13*, 534–545.
- Pflicke, H., and Sixt, M. (2009). Preformed portals facilitate dendritic cell entry into afferent lymphatic vessels. *Journal of Experimental Medicine* *206*, 2925–2935.
- Pitcher, J.A., Freedman, N.J., and Lefkowitz, R.J. (1998). G protein-coupled receptor kinases. *Annu. Rev. Biochem.* *67*, 653–692.
- Plotnikov, S.V., Pasapera, A.M., Sabass, B., and Waterman, C.M. (2012). Force fluctuations within focal adhesions mediate ECM-rigidity sensing to guide directed cell migration. *Cell* *151*, 1513–1527.
- Pollard, T.D., and Borisy, G.G. (2003). Cellular motility driven by assembly and disassembly of actin filaments. *Cell* *112*, 453–465.
- Ponti, A. (2004). Two Distinct Actin Networks Drive the Protrusion of Migrating Cells. *Science* *305*, 1782–1786.
- Purcell, E.M. (1977). Life at Low Reynolds-Number. *American Journal of Physics* *45*, 3–11.
- Rappel, W.-J., and Levine, H. (2008). Receptor noise limitations on chemotactic sensing. *Proceedings of the National Academy of Sciences* *105*, 19270–19275.
- Rasmussen, S.G.F., DeVree, B.T., Zou, Y., Kruse, A.C., Chung, K.Y., Kobilka, T.S., Thian, F.S., Chae, P.S., Pardon, E., Calinski, D., et al. (2011). Crystal structure of the β 2 adrenergic receptor-Gs protein complex. *Nature* *477*, 549–555.
- Reis e Sousa, C. (2006). Dendritic cells in a mature age. *Nature* *6*, 476–483.
- Renkawitz, J., and Sixt, M. (2010). Mechanisms of force generation and force transmission during interstitial leukocyte migration. *EMBO Rep* *11*, 744–750.
- Renkawitz, J., Schumann, K., Weber, M., Lämmermann, T., Pflicke, H., Piel, M., Polleux, J., Spatz, J.P., and Sixt, M. (2009). Adaptive force transmission in amoeboid cell migration. *Nat Cell Biol* *11*, 1438–1443.
- Reynolds, O. (1883). An Experimental Investigation of the Circumstances Which Determine Whether the Motion of Water Shall Be Direct or Sinuous, and of the Law of Resistance in Parallel Channels. *Proceedings of the Royal Society of London* *35*, 84–99.
- Ricart, B.G., John, B., Lee, D., Hunter, C.A., and Hammer, D.A. (2010). Dendritic Cells Distinguish Individual Chemokine Signals through CCR7 and CXCR4. *The Journal of Immunology* *186*, 53–61.

Rickert, P., Weiner, O.D., Wang, F., Bourne, H.R., and Servant, G. (2000). Leukocytes navigate by compass: roles of PI3Kgamma and its lipid products. *Trends in Cell Biology* 10, 466–473.

Ricoult, S.G., Kennedy, T.E., and Juncker, D. (2015). Substrate-bound protein gradients to study haptotaxis. *Front Bioeng Biotechnol* 3, 40.

Ridley, A.J. (2003). Cell Migration: Integrating Signals from Front to Back. *Science* 302, 1704–1709.

Roca-Cusachs, P., Sunyer, R., and Trepas, X. (2013). Mechanical guidance of cell migration: lessons from chemotaxis. *Current Opinion in Cell Biology* 25, 543–549.

Rohatgi, R., Ma, L., Miki, H., Lopez, M., KIRCHHAUSEN, T., Takenawa, T., and Kirschner, M.W. (1999). The interaction between N-WASP and the Arp2/3 complex links Cdc42-dependent signals to actin assembly. *Cell* 97, 221–231.

Roland, J., Murphy, B.J., Ahr, B., Robert-Hebmann, V., Delauzun, V., Nye, K.E., Devaux, C., and Biard-Piechaczyk, M. (2003). Role of the intracellular domains of CXCR4 in SDF-1-mediated signaling. *Blood* 101, 399–406.

Rosenkilde, M.M. (2014). Biased and G protein-independent signaling of chemokine receptors. *Front. Immunol.* 5, 1–13.

Rostovtsev, V.V., Green, L.G., Fokin, V.V., and Sharpless, K.B. (2002). A stepwise Huisgen cycloaddition process: copper(I)-catalyzed regioselective “ligation” of azides and terminal alkynes. *Angew. Chem. Int. Ed. Engl.* 41, 2596–2599.

Rot, A., and Andrian, von, U.H. (2004). Chemokines in innate and adaptive host defense: Basic chemokine grammar for immune cells. *Immunology* 22, 891–928.

Russo, E., Teijeira, A., Vaahromeri, K., Willrodt, A.-H., Bloch, J.S., Nitschké, M., Santambrogio, L., Kerjaschki, D., Sixt, M., and Halin, C. (2016). Intralymphatic CCL21 Promotes Tissue Egress of Dendritic Cells through Afferent Lymphatic Vessels. *Cell Reports* 7, 1723-1734.

Sallusto, F., Schaerli, P., Loetscher, P., Schaniel, C., Lenig, D., Mackay, C.R., Qin, S., and Lanzavecchia, A. (1998). Rapid and coordinated switch in chemokine receptor expression during dendritic cell maturation. *Eur. J. Immunol.* 28, 2760–2769.

Sarris, M., and Sixt, M. (2015). ScienceDirect Navigating in tissue mazes: chemoattractant interpretation in complex environments. *Current Opinion in Cell Biology* 36, 93–102.

Sarris, M., Masson, J.-B., Maurin, D., Van der Aa, L.M., Boudinot, P., Lortat-Jacob, H., and Herbomel, P. (2012). Inflammatory chemokines direct and restrict leukocyte migration within live tissues as glycan-bound gradients. *Curr. Biol.* 22, 2375–2382.

Sasaki, A.T. (2004). Localized Ras signaling at the leading edge regulates PI3K, cell polarity, and directional cell movement. *The Journal of Cell Biology* 167, 505–518.

Schiller, H.B., Hermann, M.-R., Polleux, J., Vignaud, T., Zanivan, S., Friedel, C.C., Sun, Z., Raducanu, A., Gottschalk, K.-E., Théry, M., et al. (2013). β 1- and α v-class integrins cooperate to regulate myosin II during rigidity sensing of fibronectin-based microenvironments. *Nat Cell Biol* 15, 625–636.

Schindelin, J., Arganda-Carreras, I., Frise, E., Kaynig, V., Longair, M., Pietzsch, T., Preibisch, S., Rueden, C., Saalfeld, S., Schmid, B., et al. (2012). Fiji: an open-source platform for biological-image analysis. *Nat Meth* 9, 676–682.

Schumann, K., Lämmermann, T., Bruckner, M., Legler, D.F., Polleux, J., Spatz, J.P., Schuler, M., et al. (2012). The chemokine CXCL12 is a chemoattractant for T cells. *Nat Cell Biol* 14, 1077–1085.

- G., Förster, R., Lutz, M.B., Sorokin, L., et al. (2010). Immobilized Chemokine Fields and Soluble Chemokine Gradients Cooperatively Shape Migration Patterns of Dendritic Cells. *Immunity* *32*, 703–713.
- Schwarz, J., and Sixt, M. (2016). Quantitative Analysis of Dendritic Cell Haptotaxis. In *Methods in Enzymology*, (Elsevier), pp. 567–581.
- Servant, G. (2000). Polarization of Chemoattractant Receptor Signaling During Neutrophil Chemotaxis. *Science* *287*, 1037–1040.
- Singer, A.J., and Clark, R.A. (1999). Cutaneous wound healing. *N. Engl. J. Med.* *341*, 738–746.
- Skoge, M., Yue, H., Erickstad, M., Bae, A., Levine, H., Groisman, A., Loomis, W.F., and Rappel, W.-J. (2014). Cellular memory in eukaryotic chemotaxis. *Proceedings of the National Academy of Sciences* *111*, 14448–14453.
- Small, J.V., Isenberg, G., and Celis, J.E. (1978). Polarity of actin at the leading edge of cultured cells. *Nature* *272*, 638–639.
- Smith, A., Carrasco, Y.R., Stanley, P., Kieffer, N., Batista, F.D., and Hogg, N. (2005). A talin-dependent LFA-1 focal zone is formed by rapidly migrating T lymphocytes. *J. Cell Biol.* *170*, 141–151.
- Sommer, C., Straehle, C., and Koethe, U. (2011). ilastik: Interactive learning and segmentation toolkit. *IEEEExplore* 230–233.
- Steinman, R.M., and Banchereau, J. (2007). Taking dendritic cells into medicine. *Nature* *449*, 419–426.
- Stirman, J.N., Crane, M.M., Husson, S.J., Gottschalk, A., and Lu, H. (2012). A multispectral optical illumination system with precise spatiotemporal control for the manipulation of optogenetic reagents. *Nat Protoc* *7*, 207–220.
- Stirman, J.N., Crane, M.M., Husson, S.J., Wabnig, S., Schultheis, C., Gottschalk, A., and Lu, H. (2011). Real-time multimodal optical control of neurons and muscles in freely behaving *Caenorhabditis elegans*. *Nat Meth* *8*, 153–158.
- Strale, P.-O., Azioune, A., Bugnicourt, G., Lecomte, Y., Chahid, M., and Studer, V. (2016). Multiprotein Printing by Light-Induced Molecular Adsorption. *Adv. Mater.* *28*, 2024–2029.
- Streets, A.M., Zhang, X., Cao, C., Pang, Y., Wu, X., Xiong, L., Yang, L., Fu, Y., Zhao, L., Tang, F., et al. (2014). Microfluidic single-cell whole-transcriptome sequencing. *Proceedings of the National Academy of Sciences* *111*, 7048–7053.
- Sugawara, T., and Matsuda, T. (1995). Photochemical surface derivatization of a peptide containing Arg-Gly-Asp (RGD). *J. Biomed. Mater. Res.* *29*, 1047–1052.
- Sullivan, S.K., McGrath, D.A., Grigoriadis, D., and Bacon, K.B. (1999). Pharmacological and signaling analysis of human chemokine receptor CCR-7 stably expressed in HEK-293 cells: high-affinity binding of recombinant ligands MIP-3beta and SLC stimulates multiple signaling cascades. *Biochemical and Biophysical Research Communications* *263*, 685–690.
- Suraneni, P., Ben Fogelson, Rubinstein, B., Noguera, P., Volkmann, N., Hanein, D., Mogilner, A., and Li, R. (2015). A mechanism of leading-edge protrusion in the absence of Arp2/3 complex. *Molecular Biology of the Cell* *26*, 901–912.
- Swaney, K.F., Huang, C.-H., and Devreotes, P.N. (2010). Eukaryotic Chemotaxis: A Network of Signaling Pathways Controls Motility, Directional Sensing, and Polarity. *Annu. Rev. Biophys.* *39*,

265–289.

Tal, O., Lim, H.Y., Gurevich, I., Milo, I., Shipony, Z., Ng, L.G., Angeli, V., and Shakhar, G. (2011). DC mobilization from the skin requires docking to immobilized CCL21 on lymphatic endothelium and intralymphatic crawling. *Journal of Experimental Medicine* 208, 2141–2153.

Tang, W., Zhang, Y., Xu, W., Harden, T.K., Sondek, J., Sun, L., Li, L., and Wu, D. (2011). A PLC β /PI3K γ -GSK3 signaling pathway regulates cofilin phosphatase slingshot2 and neutrophil polarization and chemotaxis. *Developmental Cell* 21, 1038–1050.

Thelen, M. (2001). Dancing to the tune of chemokines. *Nat Immunol* 2, 129–134.

Theriot, J.A., and Mitchison, T.J. (1991). Actin microfilament dynamics in locomoting cells. *Nature* 352, 126–131.

Théry, M. (2010). Micropatterning as a tool to decipher cell morphogenesis and functions. *Journal of Cell Science* 123, 4201–4213.

Thiery, J.P. (1984). Mechanisms of cell migration in the vertebrate embryo. *Cell Differ.* 15, 1–15.

Tsai, F.-C., and Meyer, T. (2012). Ca²⁺ Pulses Control Local Cycles of Lamellipodia Retraction and Adhesion along the Front of Migrating Cells. *Current Biology* 22, 837–842.

Tsai, F.-C., Seki, A., Yang, H.W., Hayer, A., Carrasco, S., Malmersjö, S., and Meyer, T. (2014). A polarized Ca²⁺, diacylglycerol and STIM1 signalling system regulates directed cell migration. *Nat Cell Biol* 16, 133–144.

Ueda, M., and Shibata, T. (2007). Stochastic Signal Processing and Transduction in Chemotactic Response of Eukaryotic Cells. *Biophysj* 93, 11–20.

Ulvmar, M.H., Werth, K., Braun, A., Kelay, P., Hub, E., Eller, K., Chan, L., Lucas, B., Novitzky-Basso, I., Nakamura, K., et al. (2014). The atypical chemokine receptor CCRL1 shapes functional CCL21 gradients in lymph nodes. *Nat Immunol* 15, 623–630.

Unger, M.A. (2000). Monolithic Microfabricated Valves and Pumps by Multilayer Soft Lithography. *Science* 288, 113–116.

Vargas, P., Maiuri, P., Bretou, M., Sáez, P.J., Pierobon, P., Maurin, M., Chabaud, M., Lankar, D., Obino, D., Terriac, E., et al. (2015). Innate control of actin nucleation determines two distinct migration behaviours in dendritic cells. *Nat Cell Biol* 18, 43–53.

Veldkamp, C.T., Kiermaier, E., Gabel-Eissens, S.J., Gillitzer, M.L., Lippner, D.R., DiSilvio, F.A., Mueller, C.J., Wantuch, P.L., Chaffee, G.R., Famiglietti, M.W., et al. (2015). Solution Structure of CCL19 and Identification of Overlapping CCR7 and PSGL-1 Binding Sites. *Biochemistry* 54, 4163–4166.

Vicente-Manzanares, M., Choi, C.K., and Horwitz, A.R. (2008). Integrins in cell migration - the actin connection. *Journal of Cell Science* 122, 199–206.

Vicente-Manzanares, M., Montoya, M.C., Mellado, M., Frade, J.M., del Pozo, M.A., Nieto, M., de Landazuri, M.O., Martínez-A, C., and Sánchez-Madrid, F. (1998). The chemokine SDF-1 α triggers a chemotactic response and induces cell polarization in human B lymphocytes. *Eur. J. Immunol.* 28, 2197–2207.

Vicente-Manzanares, M., Ma, X., Adelstein, R.S., and Horwitz, A.R. (2009). Non-muscle myosin II takes centre stage in cell adhesion and migration. *Nat Rev Mol Cell Biol* 10, 778–790.

- Waldbaur, A., Waterkotte, B., Schmitz, K., and Rapp, B.E. (2012). Maskless Projection Lithography for the Fast and Flexible Generation of Grayscale Protein Patterns. *Small* **8**, 1570–1578.
- Wang, M.-J., Artemenko, Y., Cai, W.-J., Iglesias, P.A., and Devreotes, P.N. (2014). The Directional Response of Chemotactic Cells Depends on a Balance between Cytoskeletal Architecture and the External Gradient. *CellReports* **9**, 1110–1121.
- Wang, X., and Ha, T. (2013). Defining Single Molecular Forces Required to Activate Integrin and Notch Signaling. *Science* **340**, 991–994.
- Wang, Y.L. (1985). Exchange of actin subunits at the leading edge of living fibroblasts: possible role of treadmilling. *The Journal of Cell Biology* **101**, 597–602.
- Weber, M., Hauschild, R., Schwarz, J., Moussion, C., de Vries, I., Legler, D.F., Luther, S.A., Bollenbach, T., and Sixt, M. (2013). Interstitial Dendritic Cell Guidance by Haptotactic Chemokine Gradients. *Science* **339**, 328–332.
- Weber, M., and Sixt, M. (2012). Live cell imaging of chemotactic dendritic cell migration in explanted mouse ear preparations. *Methods Mol Biol* **1013**, 215–226.
- Wegner, S.V., Sentürk, O.I., and Spatz, J.P. (2015). Photocleavable linker for the patterning of bioactive molecules. *Scientific Reports* **5**, 18309.
- Weiner, O.D., Marganski, W.A., Wu, L.F., Altschuler, S.J., and Kirschner, M.W. (2007). An Actin-Based Wave Generator Organizes Cell Motility. *PLoS Biol* **5**, e221.
- Wennerberg, K., Rossman, K.L., and Der, C.J. (2005). The Ras superfamily at a glance. *Journal of Cell Science* **118**, 843–846.
- Whitesides, G.M., Ostuni, E., Takayama, S., Jiang, X., and Ingber, D.E. (2001). Soft lithography in biology and biochemistry. *Annu Rev Biomed Eng* **3**, 335–373.
- Wilkins, D.K., Grimshaw, S.B., Receveur, V., Dobson, C.M., Jones, J.A., and Smith, L.J. (1999). Hydrodynamic radii of native and denatured proteins measured by pulse field gradient NMR techniques. *Biochemistry* **38**, 16424–16431.
- Wolf, K., Lindert, te, M., Krause, M., Alexander, S., Riet, te, J., Willis, A.L., Hoffman, R.M., Figdor, C.G., Weiss, S.J., and Friedl, P. (2013). Physical limits of cell migration: control by ECM space and nuclear deformation and tuning by proteolysis and traction force. *The Journal of Cell Biology* **201**, 1069–1084.
- Wong, S., Guo, W.-H., and Wang, Y.-L. (2014). Fibroblasts probe substrate rigidity with filopodia extensions before occupying an area. *Proceedings of the National Academy of Sciences* **111**, 17176–17181.
- Wu, C., Haynes, E.M., Asokan, S.B., Simon, J.M., Sharpless, N.E., Baldwin, A.S., Davis, I.J., Johnson, G.L., and Bear, J.E. (2012). Arp2/3 Is Critical for Lamellipodia and Response to Extracellular Matrix Cues but Is Dispensable for Chemotaxis. *Cell* **148**, 973–987.
- Wu, Y.I., Frey, D., Lungu, O.I., Jaehrig, A., Schlichting, I., Kuhlman, B., and Hahn, K.M. (2009). A genetically encoded photoactivatable Rac controls the motility of living cells. *Nature* **461**, 104–108.
- Wynn, T.A. (2008). Cellular and molecular mechanisms of fibrosis. *J. Pathol.* **214**, 199–210.
- Xiong, Y., Huang, C.-H., Iglesias, P.A., and Devreotes, P.N. (2010). Cells navigate with a local-excitation, global-inhibition-biased excitable network. *Proceedings of the National Academy of*

Sciences 107, 17079–17086.

Xu, J.S., Wang, F., Van Keymeulen, A., Herzmark, P., Straight, A., Kelly, K., Takuwa, Y., Sugimoto, N., Mitchison, T., and Bourne, H.R. (2003). Divergent signals and cytoskeletal assemblies regulate self-organizing polarity in neutrophils. *Cell* 114, 201–214.

Xu, X., Meier-Schellersheim, M., Yan, J., and Jin, T. (2007). Locally controlled inhibitory mechanisms are involved in eukaryotic GPCR-mediated chemosensing. *The Journal of Cell Biology* 178, 141–153.

Yago, T., Wu, J., Wey, C.D., Klopocki, A.G., Zhu, C., and McEver, R.P. (2004). Catch bonds govern adhesion through L-selectin at threshold shear. *The Journal of Cell Biology* 166, 913–923.

Yan, J., Mihaylov, V., Xu, X., Brzostowski, J.A., Li, H., Liu, L., Veenstra, T.D., Parent, C.A., and Jin, T. (2012). A G β ; γ Effector, ElmoE, Transduces GPCR Signaling to the Actin Network during Chemotaxis. *Developmental Cell* 22, 92–103.

Yang, H.W., Collins, S.R., and Meyer, T. (2016). Locally excitable Cdc42 signals steer cells during chemotaxis. *Nat Cell Biol* 18, 191–201.

Yang, J., and Weinberg, R.A. (2008). Epithelial-mesenchymal transition: at the crossroads of development and tumor metastasis. *Developmental Cell* 14, 818–829.

Zhang, J., Barak, L.S., Anborgh, P.H., Laporte, S.A., Caron, M.G., and Ferguson, S.S. (1999). Cellular trafficking of G protein-coupled receptor/ β -arrestin endocytic complexes. *Journal of Biological Chemistry* 274, 10999–11006.

Zidar, D.A., Violin, J.D., Whalen, E.J., and Lefkowitz, R.J. (2009). Selective engagement of G protein coupled receptor kinases (GRKs) encodes distinct functions of biased ligands. *Proceedings of the National Academy of Sciences* 106, 9649–9654.

Zigmond, S.H. (1977). Ability of polymorphonuclear leukocytes to orient in gradients of chemotactic factors. *The Journal of Cell Biology* 75, 606–616.